THE SEDIMENT DYNAMICS OF AHURIRI ESTUARY, NAPIER, NEW ZEALAND

A thesis
submitted in partial fulfilment
of the requirements for the joint degree of
Master of Science in Marine Geosciences
at the
University of Waikato
and
Universität Bremen

by

Tracey Michelle Eyre

2009

ABSTRACT

Ahuriri Estuary is a shallow, microtidal estuary located in Hawke's Bay, New Zealand. Sediment transport pathways and areas of potential erosion and accretion of Ahuriri Estuary are identified to enhance the understanding of the fate of contaminants entering the estuary and to provide a basis for future large-scale modelling applications. Fine sediments have a high adsorption capacity for heavy metals and nutrients, which may result in the accumulation of contaminants in estuarine environments. Extensive land claim of previously inundated areas uplifted by the 1931 Napier earthquake for industrial, urban and agricultural expansion has led to an increase in heavy metal and nutrient runoff into the estuary. Characterising the hydrodynamics and sediment transport of the estuary is imperative for the prediction and mitigation of sedimentation and contaminant accumulation.

A combination of hydrodynamic and sediment transport modelling using the DHI MIKE 21 suite was used to run a series of scenarios of sediment release into the estuary and subsequent dispersal. The MIKE 21 Flow model was calibrated and validated using field data from two field deployments conducted during a spring and neap tide. The hydrodynamic model predicted current direction and velocity patterns in concurrence with measured data. Residual circulation patterns in Ahuriri Estuary were ebb-dominated, indicating a likely net downstream movement in sediment. Flow was highly channelised within the middle - lower estuary, with a low energy regime in the upper estuary. This suggested that sediment introduced into the estuary from the Taipo Stream is likely to be flushed from the estuary if it reached the middle estuary. However, flow velocities and lack of residual currents in the upper estuary resulted in a large proportion of sediment introduced during storm runoff settling out of suspension, resulting in net deposition in close proximity to the source.

Sediment grain-size and consequently the settling velocity were found to be the main contributing factor to sediment dispersal. Fine silts were found to be transported the furthest downstream with a large proportion being transported from the estuary mouth and the model domain, respectively. A large proportion of coarser silts and fine sands were found to settle out of suspension in close

proximity to the sediment source. An increased settling velocity resulted in an increased influence of the simulation conditions at the time of sediment release, as it was the initial transport of coarser grain-sizes which determined their ultimate depositional location. Sediment deposition was greatest in close proximity to the source and in upper intertidal regions, which are a major sink for suspended sediments due to their sheltered nature. This was correlated with greater organic carbon content and finer grain-sizes in these areas, suggesting a depositional environment. A general trend of fining of grain-size from high energy to low energy environments was identified. In these areas, sediment reworking due to tidal action and wave-related processes was limited.

ACKNOWLEDGEMENTS

My primary thanks go to my supervisor, Dr. Karin Bryan. Her enthusiasm and support throughout the course of this project has been greatly appreciated. I also wish to thank Dr. Malcolm Green for the initiation of this project, guidance in the early days and support, despite his busy schedule.

Thank you to Dirk Immenga for help with field work, and to my field assistants, Mum and Dad for coming out into the mud to take sediment samples.

Thanks are expressed to the Hawke's Bay Regional Council for the funding of this project. The technical support received by various council staff has also been greatly appreciated. In particular I would like to thank Anna Madarasz-Smith for the initiation of this project and for the support throughout the course of the research. I would also like to thank Craig Goodier for providing the bathymetry for this study and his support in the early days of modelling.

Thanks are expressed to DHI for the use of the software. I would also like to thank Glen Reeve for his help in the model basics.

The University of Waikato and the Broad Memorial Fund provided financial assistance for which I am extremely grateful.

Thanks to all the Earth & Ocean Sciences students and staff for your support and laughs over the last 18 months. In particular, thanks to the crew for the brightening up the dungeon. Thanks go to Woodsy for being my sounding board for ideas and Matlab questions. Thanks also to Bradley Hopcroft and Brendan Roddy for GIS help.

Thank you to all my family and friends for your support and encouragement. Special thanks go to Mum and Dad for the love, support and encouragement over the last two years and for encouraging me to go to Germany. I couldn't have done it without you. Thank you also for the enthusiasm towards my research and help in the field. Thanks also to Bradley Hopcroft for his support throughout the last 18 months and for all the technical support.

TABLE OF CONTENTS

LIST OF FIGURES

LIST OF TABLES

CHAPTER ONE

INTRODUCTION

1.1 OVERVIEW

New Zealand's estuaries have been infilling with sediments since their formation approximately 15,000 years ago (Dyer 1994; Green & McDonald 2001). Anthropogenic influences have accelerated estuarine sedimentation through processes such as deforestation and urban and industrial development (Sheffield et al. 1995; Ogden et al. 2006). This increased sedimentation may lead to a change in channel geometry and tidal prism, increased flooding risk, and impacts on the ecological environment (Pimentel et al. 1995; Lal 1998; Owens et al. 2005). The rate of infilling is dependent on the sediment influx from the catchment, marine sources and the estuarine physical processes that determine the extent of sediment flushing or retention (Thrush et al. 2004).

Since the mid-1800's, Ahuriri Estuary has undergone many significant changes. Catchment changes have resulted in increased drainage and anthropogenic discharge (Chagué-Goff et al. 1998). This is consistent with estuarine evolution throughout New Zealand (Table 1.1) and reports that sedimentation has increased in other estuaries by a factor of 10 (Swales et al. 2002 as cited in Green 2008).

Table 1.1. Sedimentation rates for various stages of settlement in New Zealand estuaries ($mm.yr^{-1}$).

Location	Pre-settlement	Polynesian settlement	European settlement	Source
Whangapoua	0.03 – 0.08	0.12 – 0.13	0.9 – 1.5	Hume & Dahm 1992
Gt. Barrier Island estuary	0.39	0.93	1.23	Ogden et al. 2006
Whangamata	0.1	0.3	11	Sheffield et al. 1995

Contaminants entering the estuary such as heavy metals and nutrients bind to fine sediments, which can result in an accumulation of contaminants in estuarine

environments such as intertidal areas where fine sediments accumulate (Owens et al. 2005; Walling 2005). Understanding sediment reworking is imperative for determining the fate of fine sediments and contaminants entering the estuary. Sediments may be reworked under tidal currents (Bass et al. 2007; Manning & Dyer 2007) and wave-driven oscillatory currents (Dolphin 2004; Green & Coco 2007). Therefore, characterising the sediment dynamics of an estuary and the dominant physical forcing is important in predicting and mitigating sediment and contaminant accumulation.

Increasing contaminant loading is a concern for the future health of Ahuriri Estuary as it is flanked by agricultural, urban and industrial development. An investigation into the recent anthropogenic impact on the estuary was carried out by Chagué-Goff et al. (1998) to identify potential contaminant loading concerns. Increases in zinc, chromium, lead and copper were identified in recent sediments (since 1950) and was attributed to increased industrialisation in Napier City. Increased copper concentrations were identified in recent sediments in a core taken in a part of the estuary flanked by agricultural land. This increase in copper was attributed to agricultural runoff. Due to the nature of the landuse of the catchment, the estuary may be susceptible to contaminant build up. In order to understand the processes which lead to contaminant build up and mitigate adverse effects, the sediment dynamics must be further understood.

In order to understand the sediment dynamics of a system using field observations a high spatial and temporal resolution dataset is required, which can be costly and labour intensive (Winter 2004). Numerical modelling is cost-effective tool in estuarine management. It can be used to design and assess proposed management processes aimed at preserving the ecological and cultural amenity of the system and in the mitigation of engineering works and development impacts (Lumborg & Windelin 2003; Bass et al. 2007; Hu et al. 2009). In this study a combination of hydrodynamic modelling, sediment transport modelling and surficial sediment analysis will be used to characterise the sediment dynamics of Ahuriri Estuary. This may then be used in future modelling applications in the prediction of contaminant build up and the development of management plans.

1.2 RESEARCH AIM AND OBJECTIVES

The primary aim of this research is to characterise the sediment dynamics of Ahuriri Estuary and to determine how the estuary acts as a processor of sediments. This was achieved by the following specific objectives:

i. Characterise the hydrodynamic processes of the estuary over a spring-neap tidal cycle using measured data in the calibration of the MIKE 21 Flow model.

ii. Predict sediment transport pathways, areas of potential accretion and erosion using the calibrated hydrodynamic model in the forcing of the MIKE 21 Mud Transport model.

iii. Infer sediment dynamics, transport pathways and areas of potential erosion and accretion from surficial sediment characteristics.

iv. Combine findings of the previous objectives into a conceptual model of the sediment dynamics of Ahuriri Estuary.

The main findings of this research were presented at the Coasts & Ports 2009 Conference, Wellington, New Zealand. The conference proceedings paper is included in Appendix V.

1.3 THESIS OUTLINE

Following this introductory chapter, a description of the study site and its physical setting is given in **Chapter Two.** It summarises the extensive changes the estuary has undergone in recent history and the implications of these on the sedimentation regime.

In **Chapter Three,** the topic of hydrodynamic modelling is introduced. The set-up and calibration of the MIKE 21 Flow model is discussed, and the results of the hydrodynamic modelling presented. The calibrated model is used in the MIKE 21 Mud Transport model.

An overview of the set-up of the sediment transport model, including prediction of freshwater inflows and a sensitivity analysis is given in **Chapter Four**. The model is applied to a large number of simulations to predict the sediment dynamics of Ahuriri Estuary.

In **Chapter Five,** the spatial variation in sediment grain-size parameters and organic carbon content in Ahuriri Estuary are described and are used in the inference of sediment dynamics of the estuary.

Chapter Six provides a summary of sediment reworking in the estuary as a result of wave-related processes, and combines the approaches to characterising the sediment dynamics into a conceptual model.

A summary of the key findings of this research is given in **Chapter Seven**. Included in this chapter are some suggestions for future research to enhance the findings of this study and to progress further in the prediction and mitigation of the health of the estuary.

CHAPTER TWO

PHYSICAL SETTING AND RECENT HISTORY

2.1 INTRODUCTION

Ahuriri Estuary has a unique recent history as a consequence of its geological history and recent anthropogenic alteration. Maori and European settlement in the Napier region lead to small scale land reclamation, followed by dramatic uplift induced by the 1931 Napier earthquake and subsequent engineering works.

In this chapter the study site is introduced, along with a summary of the geological and physical setting. The changes the estuary has undergone in recent history are described, from early subsidence to the dramatic uplift of the 1931 Napier earthquake, followed by the recent anthropogenic changes to the estuary. The implications of these on the sedimentation regime of the estuary are also considered.

2.2 STUDY SITE DESCRIPTION

Ahuriri Estuary (39º30S, 176º52E) is a microtidal, well-mixed lagoon situated in southern Hawke Bay, New Zealand (Figure 2.1). The estuary is flanked by the urban and industrial development of Napier City and agricultural areas along the margins of the upper estuary. The present day estuary covers an area of 4.7 km^2, and is shallow with extensive intertidal areas and a maximum depth of 2.6 metres in the main tidal channel.

The estuary is divided into three sub-estuaries. The boat harbour is closest to the coast, where the tidal inlet is located. The Pandora Bridge delineates the western boundary of the boat harbour (Figure 2.1). For the purposes of this study, the boat harbour is termed the lower estuary. A number of dredging operations have been carried out in this area, including maintenance dredging of the inlet and adjacent to Pandora Bridge. This area is flanked on both sides by urban developments. Adjoining the lower estuary is the middle estuary, which is delineated by the Pandora Bridge to the east and the Highway Bridge to the west.

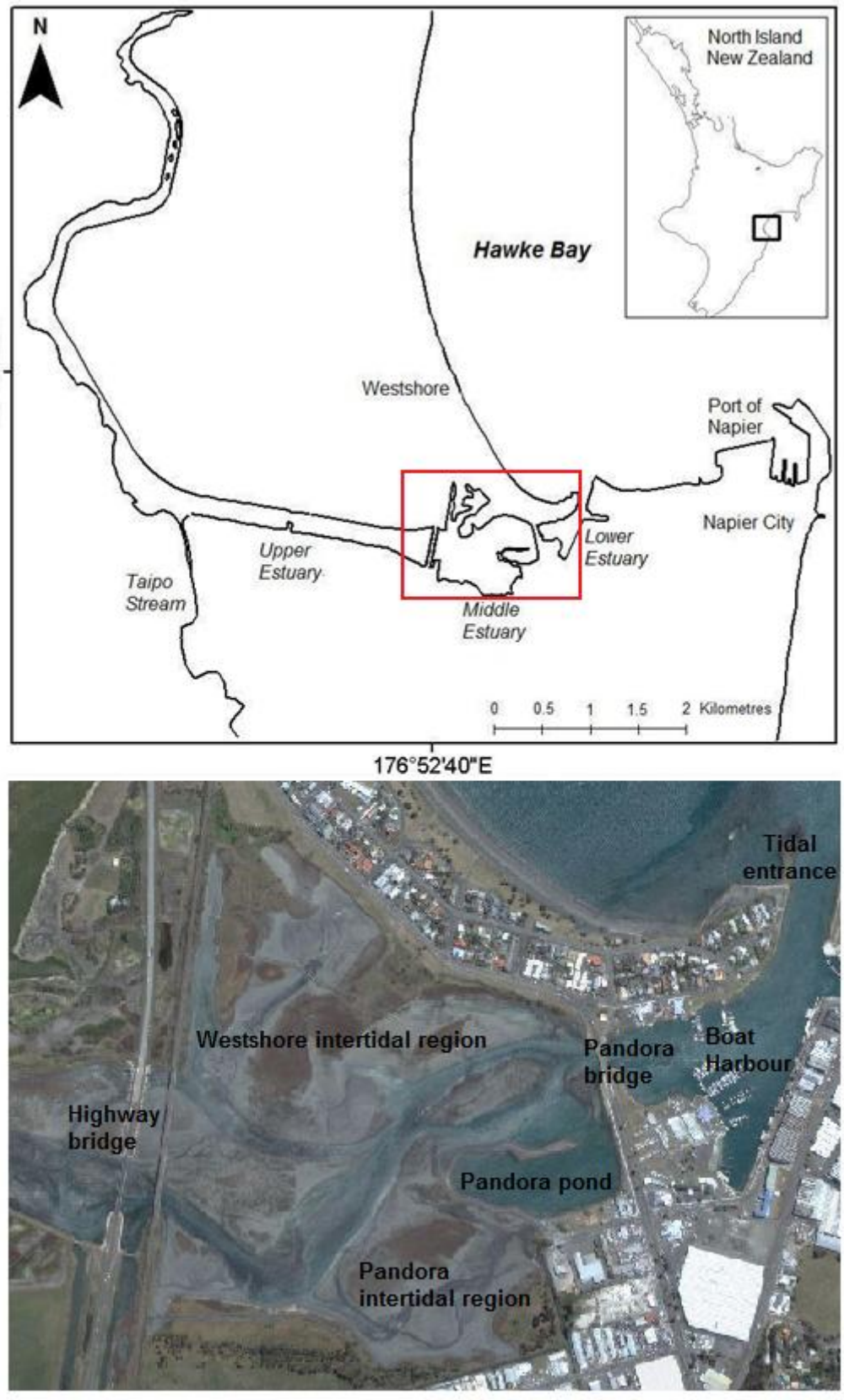

Figure 2.1. Site map of Ahuriri Estuary. The upper, middle and lower estuaries are shown. The bridges delineate the sub-estuary boundaries. Inset: North Island of New Zealand and locality of Hawke Bay. Aerial photograph illustrates the main channel geometry and important features of the middle and lower estuaries. Image from Google Earth.

The middle estuary encompasses most of the intertidal flat regions in the estuary. There are several islands in the middle estuary covered in salt-marsh vegetation. The intertidal flats on the northern side of the main tidal channel are collectively termed the Westshore intertidal region. On the southern side of the main tidal channel, there is also a large intertidal area, termed the Pandora intertidal region. This area is flanked by the Pandora industrial area. A purpose-built recreational walkway meanders across the northern reaches of the Westshore intertidal area. The middle estuary is subject to recreational pressures, namely kayaking, windsurfing and sailing. The Pandora Pond (Figure 2.1) is a popular swimming area.

For the purposes of this study, the remainder of the estuary upstream of the Highway Bridge is termed the upper estuary. This encompasses the main outfall channel, which is flanked by man-made stopbanks. The agricultural land behind these stopbanks lies below mean sea level. The Westshore Lagoon and Southern Marsh lie behind the stopbanks near the Highway Bridge. The Westshore Lagoon is connected to the main outfall channel by a culvert. Throughout the surrounding area a number of drains were constructed following exposure of the area as a result of the uplift of the 1931 Napier earthquake. These discharge into the estuary, some controlled by pumping stations and floodgates. Upstream of the main outfall channel, the remainder of the upper estuary is shallow and has low flow velocities. However, the area rises and falls significantly with the tide. At the western end of the main outfall channel in the upper estuary, the Taipo Stream enters the estuary (Figure 2.1). The Taipo Stream is the only freshwater input other than the intermittently pumped drains. Taipo Stream arises in the Poraiti Hills, draining a small catchment of 15.5 km^2. The stream flows through urbanised and agricultural areas with very low velocities. These low velocities are attributable to the low lying nature and low slope of the catchment. Therefore, considerable flows occur during storm conditions only.

Ahuriri sediments are derived from marine sources and the weathering of catchment soil and rock. Gravel-sized sediments are common in the estuary, derived from erosion of the estuary margins, transported to the estuary prior to 1931 by the Tutaekuri River and from washover deposits due to storm

overtopping of the gravel barrier spit. These are evident in the form of buried gravel beds (Komar 2007).

2.2.1 Hydrodynamics

Ahuriri Estuary is a shallow, microtidal, well-mixed lagoon. Hume et al. (1990) calculated a tidal prism volume of 196,330 m^3. Due to its shallow nature, (maximum depth of 2.6 metres), the estuary is still well-mixed despite the relatively small tidal prism. Tides are semi-diurnal and are the dominant hydrodynamic forcing of the estuary. Napier has a mean tidal range of 1.4 metres and a spring tidal range of 1.9 metres (Hull 1987). In this study, the measured spring tidal range at a location just landward of the Pandora Bridge was 1.5 metres. Frictional losses result in a reduction of the height of the tidal wave as it enters the estuary and travels through the boat harbour. Further reduction through the middle and upper estuaries is evident. Hume et al. (1990) measured a tidal range in the main outfall channel of 0.48 metres, whereas the tidal range was 1.39 metres at the Port of Napier.

The estuary is sheltered by the Poraiti Hills which are located to the southwest. The sheltered nature of the estuary combined with small fetches imposed by large complex intertidal areas and islands limits local wave generation. Freshwater inflows into the estuary are minimal, with the Taipo Stream being the only significant freshwater source. The stream is low flowing and therefore has a minor influence on the hydrodynamics of the estuary, with the exception of large rainfall events.

2.2.2 Climate

Climate data for this study were collected by the Napier Aero Aws climate station located at the Napier airport (39º46S, 176º86E). These data were obtained from the National Institute of Water and Atmospheric Research (NIWA) CliFlo database. Rainfall recorded at the Napier airport site, located in close proximity to the estuary, ranges from 700 – 1100 $mm.yr^{-1}$. A more detailed description of precipitation events and the subsequent predicted discharge of freshwater into the estuary are discussed in Chapter Four. A mild mean annual temperature of 14.0

°C is recorded for the area. Figure 2.2 illustrates wind directions and velocities for wind data collected at the Napier airport site. The prevailing wind direction is from the south-west, but westerlies, easterlies and north-easterlies are also common. Recorded maximum gusts are mainly from westerlies.

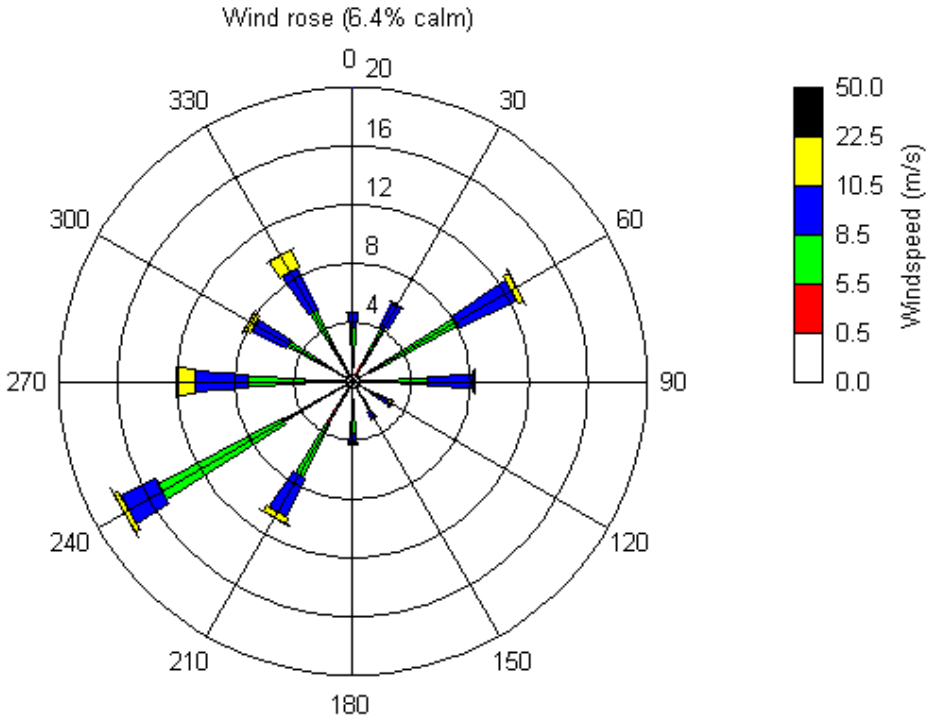

Figure 2.2. Wind directions and speeds from the Napier Aero Aws climate station. Data from CliFlo (2009).

2.3 REGIONAL SETTING

2.3.1 Geological and tectonic setting

The unique history of Ahuriri Estuary is attributable to its geological and tectonic setting. Hawke Bay is part of the accretionary prism, located on the Australian plate approximately 160 km west of the Hikurangi Trough (Figure 2.3). The Hikurangi Trough is a shallow marine trench which has formed as a result of the Pacific plate subducting under the Australian plate at a rate of approximately 50 $mm.yr^{-1}$ (Hull 1987). As a result of this convergence, the basement rock was uplifted and exposed to form the North Island axial ranges (Figure 2.4). This basement rock is comprised of Triassic to early cretaceous undurated sandstone and mudstone (greywacke and argillite) (Field et al. 1997). During the period of uplift of this basement rock, large volumes of gravel-sized sediments were eroded

and transported to the coast by the Hawke's Bay rivers which arise in the ranges. This large volume of sediment delivered to the coast allowed for the formation of a Holocene sand and gravel barrier, deposited approximately 4500 years ago at the time of a sea level low stand (Hull 1986). The Ahuriri Lagoon formed behind this barrier and slowly infilled with sediment transported by the Esk and Tutaekuri Rivers.

An exposed stratigraphic sequence located in the Poraiti region south-west of the estuary proper allowed for the identification of distinct phases in the development of the estuary. Waimihia lapilli deposits, dated at 3500 years B.P., were overlain by thick peat deposits, said to be primarily accumulated between 3500 and 1750 years B.P. during a period of rapid sea level rise (Hull 1986). Relative sea level rise in the area as a result of tectonic subsidence later resulted in the breach of the barrier. This inundated the area creating the Ahuriri Lagoon. This tectonic subsidence has been identified throughout the Hawke Bay region (Ota et al. 1989). The tectonic subsidence in the Hawke Bay area is dated as beginning approximately 500 years B.P., identified by the burial of human bones below undisturbed estuarine sediments (Hull 1986). These estuarine conditions persisted until the 1931 Napier earthquake which uplifted the area, creating the present day estuary.

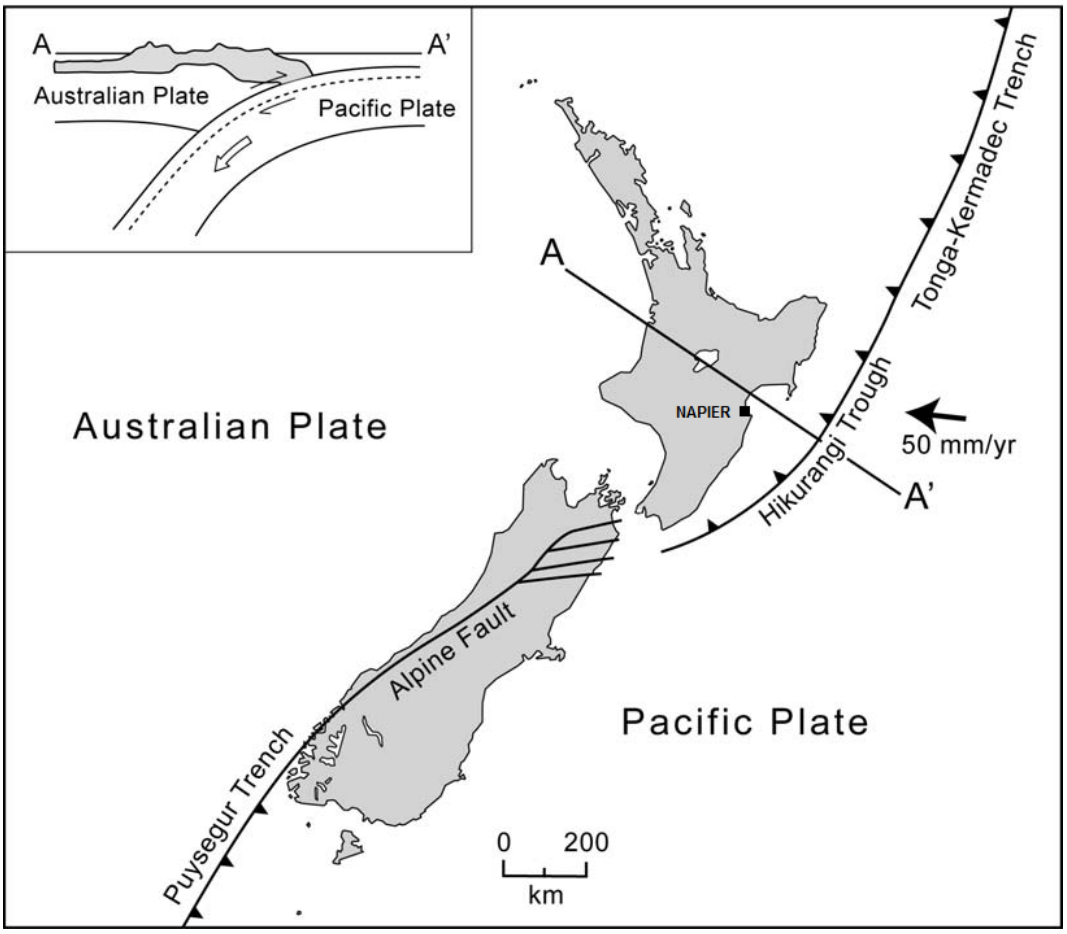

Figure 2.3. Tectonic setting of New Zealand. Napier lies approximately 160km west of the Hikurangi Trough. Inset: Cross-section from A – A' across the Hawke Bay depicting the trough, axial ranges and accretionary wedge. From Komar (2007).

The estuary catchment drains the coastal Poraiti Hills, which are part of the accretionary wedge created by the convergence of the Australian and Pacific plates. The coastal hills are comprised of Pliocene - Pleistocene marine sediments and limestone. The Ahuriri catchment is generally relatively stable, formed on siltstones, sandstones and limestones. The area was classified by the Hawke's Bay Catchment Board as having slight to moderate erosion severity. However, intense rainstorms are likely to result in significant erosion, providing an influx of freshwater, sediment and debris into the estuary.

Figure 2.4. Greywacke and argillite basement rock was uplifted and exposed to form the North Island axial ranges. The Ruahine Ranges are the source of the large volume of greywacke gravel eroded and transported to form the Holocene gravel barrier of the Ahuriri Lagoon. From Bland (2001).

2.3.2 Wave climate

Studies of waves were undertaken by Smith (1968 and 1984) based on long term observations (cited in Mead et al. 2001). It was concluded from these studies that the majority of waves approach from the east – south east direction, followed by waves from the east – north east direction. The Port of Napier has a wave buoy deployed in 15 metres water depth located offshore of the port breakwater. Average significant wave height in July and August was in the order of 1.2 metres. Storm waves during the months June – September had an average significant wave height of 2.5 – 3.5 metres.

The southern Westshore coast is protected from ocean waves by the sheltering of Bluff Hill and the port breakwater, and the complex tidal inlet prohibits the propagation of swell into the estuary (Mead et al. 2001). Gibb (1962) also illustrated that the entrance to Ahuriri Estuary is relatively sheltered from waves from the dominant approach angle (Figure 2.5).

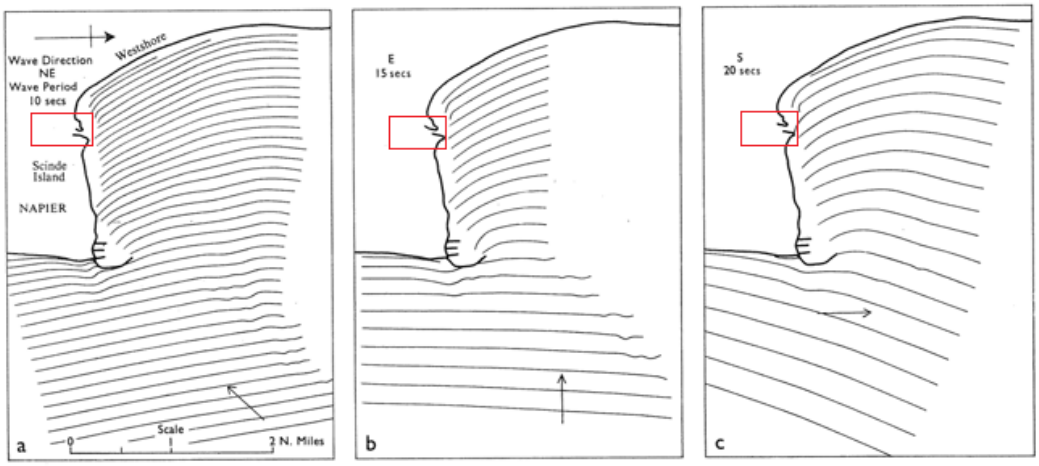

Figure 2.5. Wave refraction patterns from the dominant approach angles for the southern Hawke Bay region. The entrance to Ahuriri Estuary is sheltered by the headland and Port of Napier breakwater. From Gibb (1962). Red boxes indicate location of Ahuriri Estuary.

2.4 RECENT HISTORY

The estuary has undergone many changes in recent history. The most dramatic change was the uplift of 1-2 metres of the 1931 Napier earthquake. However, there have been a number of anthropogenic changes to the estuary, both prior to and following the uplift of the earthquake. All of these changes have had a significant impact on the hydrodynamics and sedimentation of the estuary.

2.4.1 Maori colonisation

Maori colonisation of the Ahuriri Lagoon region is dated at approximately 1100 AD. By the early 1700's there were numerous settlements near the lagoon (Chagué-Goff et al. 2000). The estuary holds cultural and spiritual values for the Maori people and was a significant source of food in the 19th century. Prior to European settlement the lagoon discharged to the coast at an outlet to the northern reaches of the lagoon at Keteketerau. This outlet was blocked during a storm, leading the Maori people to dig another outlet near Scinde Island in the general vicinity of the existing outlet (Chagué-Goff et al. 1998). The lagoon was reported to be a primarily freshwater lagoon prior to the opening to the coast which was dug out at the southern reaches of the spit. The change from a freshwater lagoon to one with tidal influence is evident from the shellfish record (Chagué-Goff et al. 1998).

2.4.2 European colonisation

European settlement began in the mid-1800's and has had an important influence on the development of the estuary and its catchment. Following the sale of the land to the crown by the Maori people, the beginning of the drainage of swamp land for development ensued. Vast areas were cleared of native bush for agricultural development and for building materials for infrastructure. This deforestation of the area would have had a significant effect on the influx of fine sediment into the estuary at this time.

Engineering development of the estuary began with the construction of the Ahuriri breakwaters on either side of the inlet in the late 1870's to stabilise the entrance. The construction of the port breakwater extending from the headland began in the late 1880's to early 1890's. This effectively increased the headland effect, protecting the southern Westshore coast from wave activity. As a result, waves reaching Westshore were approximately half the size of waves reaching the Westshore barrier beach pre-construction of the port breakwater (Komar 2007).

2.4.3 1931 Napier earthquake

The 1931 Napier earthquake, measuring 7.8 on the Richter scale, induced uplift of the Ahuriri Lagoon ranging from 1 – 2 metres (Chagué-Goff et al. 2000). The uplift exposed approximately 13 km^2, more than one third of the previously inundated area of the lagoon of 38.4 km^2. Figure 2.6 depicts the dramatic changes to the lagoon as a result of the uplift. Figure 2.6 A shows the lagoon prior to 1931, and Figure 2.6 B shows the estuary following uplift. The Tutaekuri River, which previously flowed into the lagoon, was diverted south to discharge directly to the coast as a consequence of the uplift. This sudden uplift resulted in rapid emptying of the lagoon (Hull 1990). It was reported at the time (cited in Komar 2007) that the tide had just begun to ebb at the time of the earthquake. The ebb flow continued at normal ebb velocities, but soon gathered force and within a few minutes flowed with an estimated velocity of 24 $km.hr^{-1}$. These high current velocities were said to be maintained until after the following high tide. This catastrophic emptying of the lagoon was supported by eye-witness accounts, a

number of which mention the vast numbers of fish left exposed on the previously inundated bed (McConnochie 2004).

Figure 2.6. A. Aerial photograph of the lagoon prior to uplift **B.** Ahuriri Estuary after the uplift of the 1931 Napier earthquake. Photos: Hawke's Bay Museum.

The influence of the earthquake was highlighted in a study carried out by Chagué-Goff et al. (2000). A change in grain-size in the middle estuary reflected the change in depositional environment at this site. The basin where the core had been taken was 1.5 metres deeper than the present day. This area had a lower energy environment allowing for greater deposition of fine sediments. The uplift induced by the earthquake lead to channelisation, higher flow velocities and subsequently a higher energy environment, favouring the deposition of sandy sediment. A lack of ^{210}Pb in sediments supports the winnowing of fine sediment, as the preservation of lead is inextricably related to fine sediment accumulation. The core taken near

the mouth of the Taipo Stream suggests that the sedimentary environment in the upper estuary was not considerably altered by the uplift (Chagué-Goff et al. 2000).

2.4.4 Land claim and development

Following the uplift of the 1931 Napier earthquake the previously inundated region was drained and developed for agricultural and industrial use. An extensive drainage channel network was constructed to allow for the region to be developed (Figure 2.7). Many of these drains currently discharge directly into the estuary. Much of this land and nearby development lies below sea level. Common in most cases of land claim, the need to protect this newly claimed land required flood protection measures and further engineering works. These flood defences are hard protection structures, which often have implications for estuarine hydraulics, sedimentation, habitat adjustment and various other implications for the ecosystem (French 1997).

Figure 2.7. Image of the estuary illustrating the construction of the main outfall channel and the extent of the drainage network channels required to make previously inundated land viable for agricultural development. Source: Hawke's Bay Museum.

2.4.5 Evolving estuarine morphology and sedimentation

Historical surveys carried out by the Hawke's Bay Catchment Board in 1963 and 1978 were used to investigate mean bed level changes in the estuary. There were changes identified in the sedimentation of the lagoon between the two surveys. Net accretion was evident in the middle estuary and up to the centre of the main outfall channel. Decreased bed levels of the upper reaches of the main outfall channel and upstream past the Taipo Stream were evident. There was also evidence of accretion in the northern reaches of the upper estuary. The present day main inflow of freshwater and sediment into Ahuriri Estuary is from the Taipo Stream. However, the channel is excavated to reduce sedimentation and flooding risk, effectively reducing the sediment available for influx into the estuary.

The estuary is located within the Bay View littoral cell, bound to the north and south by headlands. This littoral cell has shown to be in equilibrium, suggesting little net diabathic or parabathic movement of sediment (Komar 2007). This suggests that there is a low input of marine sediment into the estuary.

2.5 CONCLUSIONS

The present day Ahuriri Estuary owes its unique history primarily to its tectonic setting and geological history. This has contributed to the sedimentological regime of the estuary. The main influences are as follows:

- The lagoon was formed behind a Holocene sand and gravel barrier during a period of sea level low stand. During the time of uplift of the North Island axial ranges, large volumes of greywacke gravel were eroded and transported to the coast by the Esk and Tutaekuri Rivers. The lagoon underwent continued tectonic subsidence until the dramatic uplift of the 1931 Napier earthquake.
- The 1931 Napier earthquake changed the sedimentation regime of the estuary. The lower region of the estuary became highly channelised, inducing higher tidal current velocities. The upper estuary energy regime was not significantly changed and is still a muddy depositional environment. Sediment supply was greatly reduced due to the diversion of the Tutaekuri River as a result of the uplifted terrain.
- Extensive engineering works were carried out in the estuary, ensuring the protection of the land behind the stopbanks. This altered the hydrodynamics and consequently the sediment dynamics of the estuary.
- The port breakwater was constructed in the late 1800's, effectively extending the effect of sheltering by the headland and reducing the wave height and energy in the lower region of the Westshore coast.

The sedimentation regime of the estuary has continued to evolve since the uplift of the earthquake and extensive engineering works in the estuary. There has been net accretion in the upper estuary and various intertidal regions, but also decreased bed levels were recorded in the landward reaches of the main outfall channel. This study aims to further develop an understanding of the present day sedimentation regime of the estuary.

CHAPTER THREE
HYDRODYNAMICS OF AHURIRI ESTUARY

3.1 INTRODUCTION

In recent history, the hydrodynamics of Ahuriri Estuary have undergone many changes due to both natural and anthropogenic influences. The uplift of the 1931 Napier earthquake and the subsequent engineering works changed the hydrodynamic regime of the estuary significantly over the last century. The present day hydrodynamics of the estuary are primarily tidally-driven. There is little freshwater inflow, as the uplift diverted the previous inflow from the Tutaekuri River south to flow directly out to the coast.

In this chapter a background of estuarine hydrodynamics and hydrodynamic modelling is given. The flow model initialisation for Ahuriri Estuary is discussed, along with the calibration and validation of the model using measured data from field deployments. The hydrodynamics of the estuary will be characterised based on the modelling results, which will have implications for the sediment transport discussed in the following chapters.

3.2 ESTUARINE HYDRODYNAMICS AND NUMERICAL MODELLING

3.2.1 Estuarine hydrodynamics

Estuarine hydrodynamics are a function of site specific interactions between tides, salinity, bathymetry and climatic conditions such as wind stress. It is necessary to characterise circulation processes in estuaries due to their importance for the sediment dynamics of the estuary and for ecological environment. Classification schemes have been devised based on topography and circulation (e.g. Dyer 1973; Pritchard 1952). Estuarine circulation patterns result from stratification due to density differences and mixing processes within the estuary. The circulation of currents in the estuary bring dissolved oxygen and nutrient rich waters into the system, and flush waste, excess nutrients, and heavy metal runoff from the system. Classification of estuaries based on circulation is predominantly governed

by the relative influences of tidal currents and freshwater inflow, and the degree to which freshwater inflow mixes with the high salinity tidal currents. However, other factors such wind stress, waves, physical structures and bedforms also promote mixing. Morphology is also a governing factor in circulation, where sharp changes can induce intense turbulent mixing events (Gardner & Smith 1978). All these parameters must be taken into account when characterising the hydrodynamics of an estuary.

Non-uniform bathymetry can also create tidal asymmetry, which causes a residual current. Residual currents are the currents remaining after tidal currents have been averaged, illustrating circulation patterns. They are calculated by averaging the tidal currents over a given time period. Residual currents are caused by the non-linear interactions within the estuary, along with wind and freshwater (van de Kreeke 1988). It is also possible to determine residual currents by separating the non-linear currents into the first order equation (oscillatory tidal current) and second order equation (residual current) (Tee 1988). Density-driven residual currents exist in estuaries where stratification is evident, such as salt-wedge conditions. Density-driven residual flows are often found in areas with low tidal ranges (e.g. Murphy & Valle-Levinson 2008). However, residual currents are generally a combination of both baroclinic and barotropic flows. Residual circulation due to non-density related processes results from the deformation of the tidal wave as it propagates into the estuary by frictional forces, causing barotropic non-linearities (Jay & Smith 1988). The constriction of tidal flows through tidal channels and inlets also will result in residual currents (Stommel & Farmer 1952). Barotropic residual currents may also arise from current shear inducing vorticity, giving rise to eddies. Such eddies are associated with sediment deposition (Ferentinos & Collins 1979). Hamilton (1990) found that tidal range and varied freshwater inflow induced widely variable residual flow in the Columbia River estuary. Tidal processes dominated residual mean flow, but with greater freshwater inflow into the estuary, the stratification and intrusion length of the salt-wedge were less influenced by tidal propagation. Therefore, it is a combination of physical forcing parameters which cause a mean residual current.

3.2.2 Hydrodynamic modelling of estuaries

Present day development in coastal areas and landuse change in recent history have resulted in the requirement for robust numerical modelling packages to enable the calculation of flood risk, impact of engineering works, the impact on ecological environments, and more. Due to the wide variation in physical forcing, geometry, hydrodynamics and circulation of estuarine systems, a wide range of numerical models have been developed, specialised for differing purposes. In environments where there is vertical heterogeneity due to stratification, the need to resolve baroclinic flow requires the use of a three-dimensional model. If baroclinic flow and stratification are of interest only, or the system is laterally homogenous, a laterally-averaged model may be desirable (Liu et al. 2002). In shallow, well-mixed environments such as in this study, vertically-integrated models are often preferable to three-dimensional models, as there is no need to resolve the vertical dimension due to a homogenous water column. However, two-dimensional modelling does introduce some loss of performance. Residual currents may be underestimated (Tee 1988), as currents are depth averaged, and vertical eddy viscosity and the viscous boundary layer are not resolved.

Estuarine models must include flooding and drying, to allow for the emergence of the intertidal flat on the ebb tide. The inclusion of flooding and drying capabilities in estuarine modelling allows for a more accurate prediction of tidal exchange and flushing of the intertidal environment, and enables the model to solve for complex geometries and bathymetries. Chen et al (2008) carried out a particle trajectory study using two numerical models, one with flooding and drying capabilities. Without flooding and drying, tidal flow did not follow channel geometry, and did not produce reliable results. However, accurately resolving moving boundaries associated with flooding and drying processes poses a challenge. High grid resolution is required to ensure stability when attempting to model shallow areas of complex geometry where wetting and drying occurs, such as fine creek networks in intertidal areas (Bates & Hervouet 1999; Defina 2000). Nested bathymetric grids allow for this, with higher resolution in intertidal areas.

Relatively recent studies have highlighted the need to couple tidal currents and the wave orbital currents induced by wind waves (e.g. Green et al 1997). Local wind-wave generation in estuaries with complex geometries and intertidal flats is

influenced by tidal level, with exposed areas limiting fetch. Wave height is found to vary over the intertidal flat with respect to tidal level due to the dissipation of energy at the leading edge of the water body due to friction as it moves across the intertidal flat (Green et al 1997; Green & Coco 2007).

3.2.3 MIKE 21 Flow model (FM)

The two-dimensional MIKE 21 Flow model (FM) is used in this study to simulate the tidal hydraulics of Ahuriri Estuary. The MIKE 21 FM solves the vertically integrated Saint-Venant equations for mass continuity and momentum in the horizontal dimensions. The equations are solved using finite differencing to determine water depth and velocities within each cell (DHI 2004). The model is forced at the boundaries by tides and freshwater inflows, and may include outflow pathways. Frictional losses are parameterised in the model by the bed roughness and eddy viscosity, which account for turbulent energy loss on a scale smaller than that which can be resolved with the existing grid size. The two-dimensional model is used in this study as stratification and vertical heterogeneity are negligible and are therefore not of interest for this study.

3.3 HYDRODYNAMIC DATA COLLECTION

In order for the MIKE 21 FM to accurately predict the hydrodynamics of Ahuriri Estuary, the model must be calibrated and verified using measured data. Current direction and velocity data were measured during discrete spring and neap tide deployments using 3 Sontek Triton ADV current meters. Spring deployment was for the period 20/10/2008 17:00 – 22/10/2008 9:00, and neap deployment for the period 20/01/2009 17:00 – 22/01/2009 09:00, each for a duration of 3 full tidal cycles. The current meters were deployed at 3 sites (Figure 3.1) throughout the lower estuary for model calibration purposes. Locations were taken with a handheld global positioning system (GPS), which is accurate to 4-5 m at the site (Table 3.1). The instruments at sites 1 and 3 (termed ENT and BRI respectively) were mounted on a frame, with the probe approximately 1 m from the bed, therefore measuring free stream current parameters. The instrument at site 2 was buried in the sediment to ensure immersion at high tide, measuring the current

parameters approximately 30 cm from the bed (See Figure 3.2 for deployment configurations).

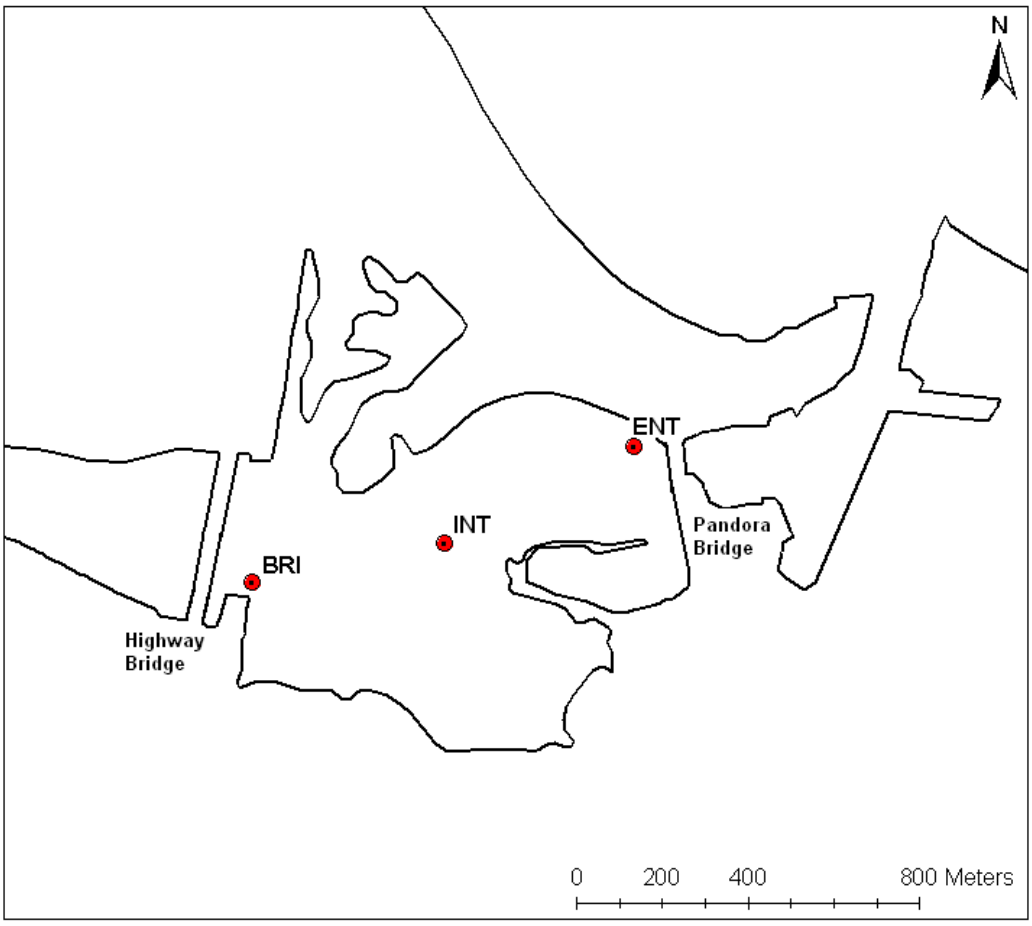

Figure 3.1. Locations of instrument deployment in the Ahuriri Estuary. ADV current meters were located near the entrance (ENT), intertidal channel edge (INT) and near the Highway Bridge (BRI).

Table 3.1. ADV Instrument deployment locations. Locations are given in New Zealand Transverse Mercator (NZTM), with an accuracy of 4-5 m.

Site	Easting	Northing	Site description
ENT	1,933,516.703	5,622,453.616	Near middle estuary entrance in main channel
INT	1,933,965.927	5,622,226.202	Buried in intertidal area on main channel edge
BRI	1,933,516.703	5,622,136.195	Near main outfall channel, by Highway Bridge in main channel

Figure 3.2. Sontek Triton-ADV current meters used in field deployment. **A**. Steel frame used for deployment in the channel at sites ENT and BRI. **B**. Steel frame used to stabilise buried instrument.

An acoustic doppler current meter measures the different directional velocities using the doppler effect. The probe consists of an acoustic transmitter, and 3 acoustic receivers (Figure 3.3). The acoustic transmitter emits sound waves of a known frequency, which travels through the water at a known speed, and may be reflected by particles or bubbles in the water column. The reflection of the sound waves results in a change in frequency of the sound waves, termed the doppler shift. It is the reflected sound waves which are recorded by the acoustic receivers, and the three-dimensional configuration of the receivers allows for the output of cartesian (xyz) velocities. These cartesian velocities are then used for the calculation of current speed and direction.

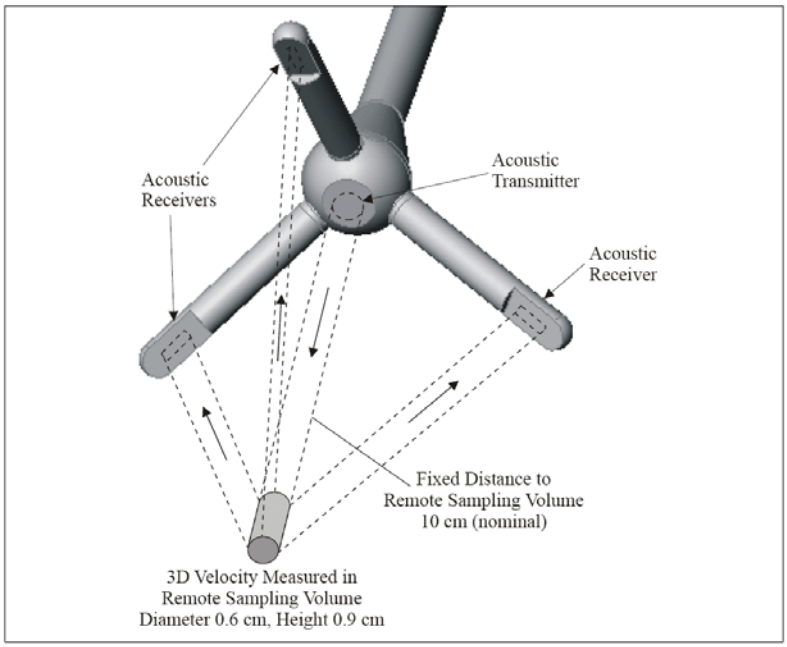

Figure 3.3. Sontek Triton-ADV current meter measurement principle. From Sontek Triton ADV Operation Principles Manual (2001).

Data collected were averaged to give a sampling interval of 15 minutes. A higher resolution was not required as the instruments were measuring tidal velocities only. The instruments were not programmed to measure waves, as at the time of duration the weather was calm with no waves evident within the estuary. The instrument also recorded pressure, which was assumed to be due to hydrostatic pressure only.

3.4 MODEL INITIALISATION

3.4.1 Bathymetry

An existing bathymetric grid was used in this study, previously created by HBRC using light detection and ranging (LiDAR) data for exposed areas at low tide and survey measurements for inundated areas (Figure 3.4). The datum for the bathymetric data was the HBRC datum, which specifies a mean sea level of 10.3 m. Upon analysis of aerial photographs of the study area, it was concluded that there have been no significant changes to the bathymetry and channel geometry since the creation of the bathymetric grid in 2003, and use of the existing grid was feasible for the current study. The highly channelised flow in the estuary, and the narrow nature of the channels required a high resolution grid of 10 m x 10 m. Such a resolution was viable in this study, as computational time was low due to the small size of the study area.

3.4.2 Boundary conditions

The only entrance to Ahuriri Estuary is through the small boat harbour adjoining the coast. The model boundary was placed offshore to enable a more accurate simulation of the constriction of tidal flow through the entrance. Initial surface elevation was set to MSL according to HBRC datum. The model was forced at the open coast boundary using a timeseries derived from tidal information from the NIWA free tide prediction service (www.niwa.co.nz/our-services/online-services/tides). The tides were splined to provide continuous data at 15 minute intervals, and converted to HBRC datum, with a mean sea level of 10.3 m. Due to the presence of stopbanks in the upper estuary with much of the land behind the stopbanks below sea level, initialising the model grid with a surface elevation equivalent to MSL resulted in land area being inundated. Therefore an initial

surface elevation of 9 metres was assigned to the model grid. A warm-up period of 5 days was run to allow the model surface elevation to equilibrate to MSL. A test was carried out on extracted model data to ensure mean water level had reached equilibrium by the conclusion of the warm-up period.

Freshwater inflows into the estuary are minimal and were therefore not included in the forcing for the calibration stage of the tidal flow modelling.

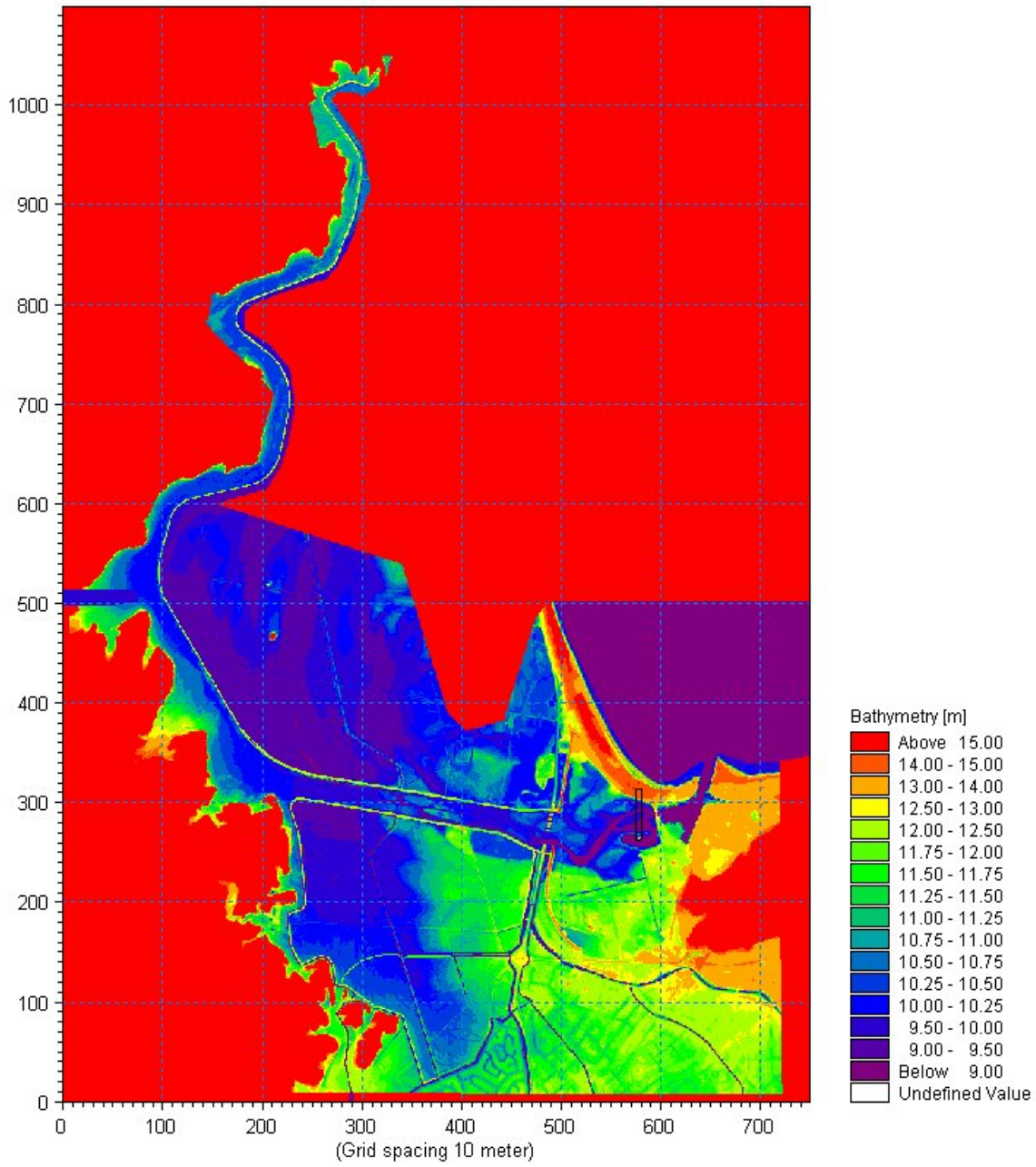

Figure 3.4. Bathymetric grid created in 2003 using LiDAR data and manual channel measurements. Datum is Hawke's Bay Regional Council datum, MSL = 10.3 m. From Hawke's Bay Regional Council.

3.4.3 Remaining parameters

To account for exposure and inundation of intertidal areas, flooding and drying depths were specified, of 0.07 m and 0.05 m respectively. Coriolis was ignored in this study, as the small dimensions of the estuary would mean the effects would be negligible.

3.5 MODEL CALIBRATION

In order to accurately simulate the hydrodynamics of Ahuriri Estuary, the hydrodynamic model must be calibrated with site specific measured data. This section the MIKE 21 Flow model calibration and validation using measured data is discussed.

3.5.1 Directional analysis

In order to determine the model grid location for the extraction of data to compare with ADV data, the model bathymetry was given a geographical reference. The bathymetry was georeferenced in ArcGIS using coastline and bridge location data (given in NZTM) as reference points. The geographical co-ordinates of ADV deployment location were overlain onto this georeferenced image. From this the corresponding grid cell was determined.

In determining the location for model data extraction to compare with measured data, the positional accuracy of the model and GPS must be considered. The positional accuracy of the model can only be as accurate as half the cell width (5 m), and the positional accuracy of the handheld GPS is 4-5 m at the study site. Therefore, with a minimum positional accuracy error of 10 m, the grid cell corresponding to deployment location may be one of the adjacent cells to the calculated location of the cell for data extraction. Therefore, a grid of 9 cells was extracted for analysis to determine which model cell data calibrate best with measured data (Figure 3.5).

For each of the grid cell locations, ADV current meter data and model data were compared for water depth and current direction. U velocity represents current velocity in the east – west direction, and V velocity in the north – south direction.

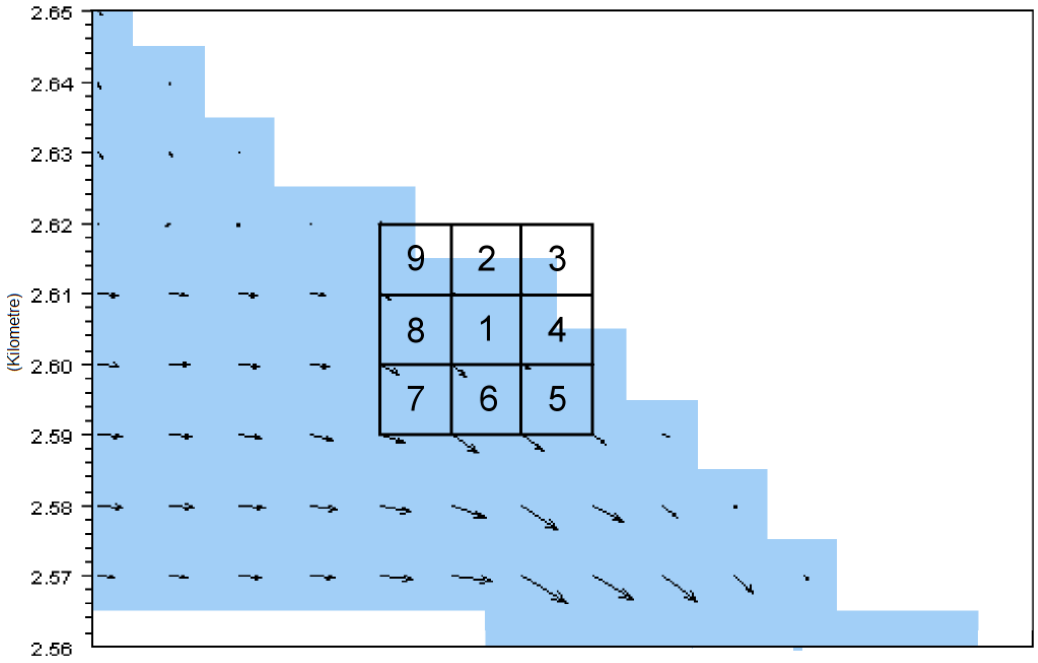

Figure 3.5. Schematic illustrating grid cell location, 1, and adjacent cells for which model data is extracted for directional calibration. Note the variability in current vectors between cell locations.

In order to determine the correct cell for model data extraction, an analysis of flow direction was undertaken. As current speeds were modified by bottom roughness and eddy viscosity, and the flow was highly channelised, current direction was the primary parameter in determining which grid cell data should be extracted for calibration. However, only cells in which predicted water depths were comparable to measured water depth were considered for directional analysis. Modelled water depths were calculated by subtracting the depth of the grid cell of data extraction from surface elevation data, which is relative to HBRC datum. Measured water depths were calculated from pressure data from the ADV current meters (dBar), where 1 bar is equal to 1 m water depth, according to the hydrostatic assumption. A good initial calibration was shown between measured and modelled water depth, which was surprising given the complexity of the channel geometry and size relative to the grid resolution. Root mean square error (RMSE) was also calculated for current direction. However, due to the high variability and noise of the dataset, the root mean square error was not considered the best indicator. Speed was not used as an indicator, as it is later altered with an investigation into bed roughness and eddy viscosity.

Table 3.2 indicates the grid cell location and cell number in the extracted grid for each of the three deployment locations, based on the directional calibration shown in Figures 3.6, 3.7 and 3.8 for ENT, INT and BRI locations respectively. Concurrent results were shown for both spring and neap deployment, therefore the same grid cell was used for data extraction for both spring and neap simulations.

Table 3.2. Cell number in extracted 9x9 grid of best directional simulation and the ordinates of the cell in the bathymetric grid.

Site	Cell number in extracted grid	Grid cell ordinates
ENT	7	586,291
INT	5	538,292
BRI	7	497,259

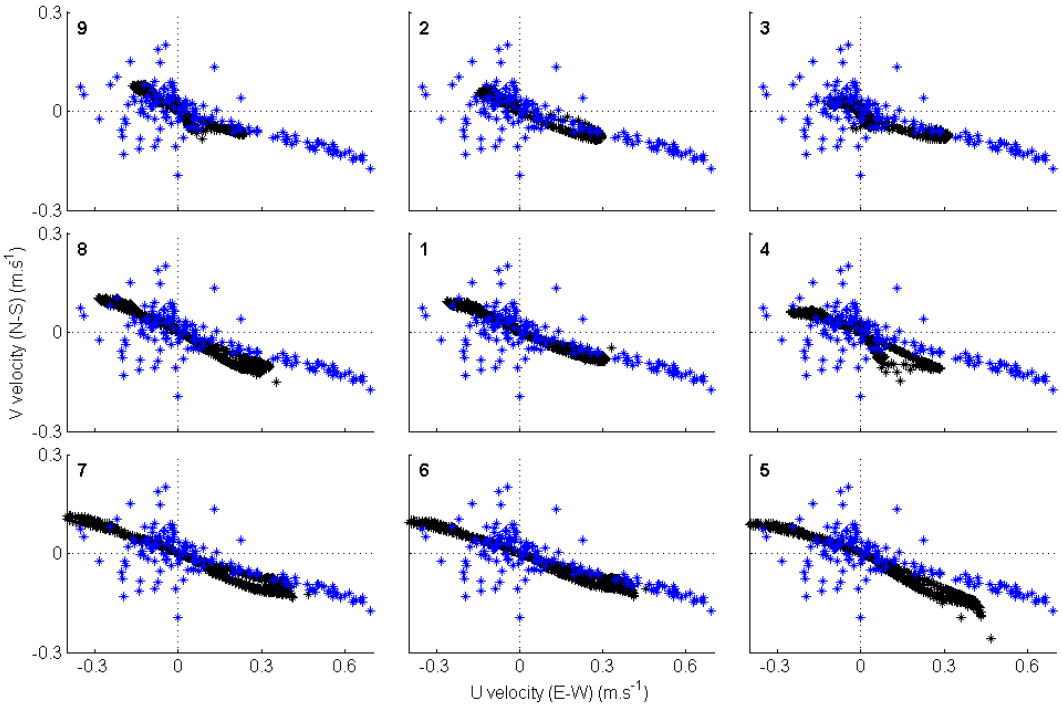

Figure 3.6. Comparison of model and ADV current direction at entrance site, ENT. Black markers indicate model data and blue markers indicate measured data. Panels are numbered from 1-9 corresponding to grid cell number of 3x3 extracted grid. See Figure 3.5 for grid configuration.

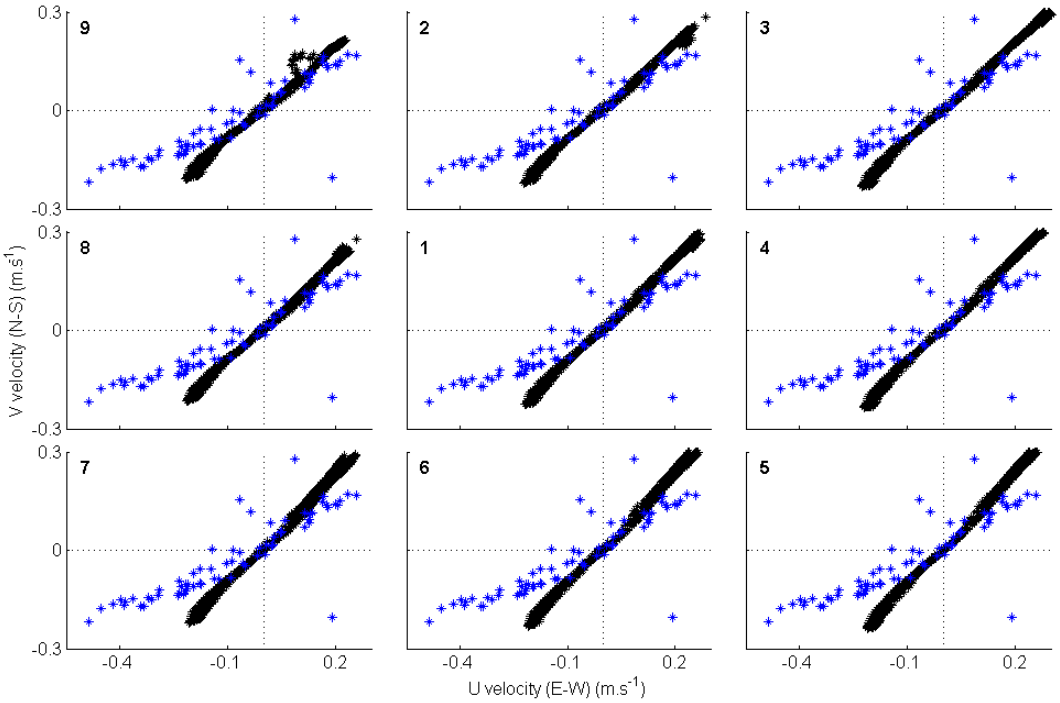

Figure 3.7. Comparison of model and ADV current direction at channel edge site, INT. Black markers indicate model data and blue markers indicate measured data. Panels are numbered from 1-9 corresponding to grid cell number of 3x3 extracted grid. See Figure 3.5 for grid configuration

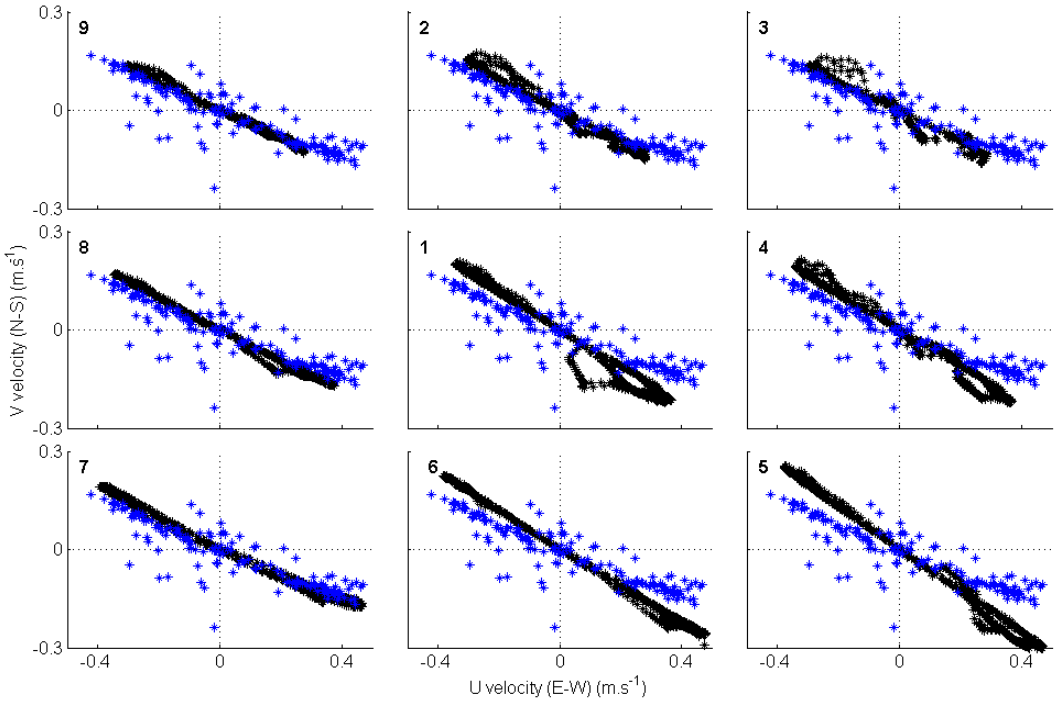

Figure 3.8. Comparison of model and ADV current direction at bridge site, BRI. Black markers indicate model data and blue markers indicate measured data. Panels are numbered from 1-9 corresponding to grid cell number of 3x3 extracted grid. See Figure 3.5 for grid configuration

3.5.2 Calibration parameters

3.5.2.1 Bed Roughness

Bed roughness influences current speed and therefore timing of tide reversal in estuaries. Current speed and timing are important in the simulation of estuarine hydrodynamics and consequently will have an important implication for sedimentation within the estuary. A bed roughness calibration was carried out using the Manning number (Equation 3.1).

$$M = \frac{25.4}{k_s^{1/6}} \qquad \text{(Equation 3.1)}$$

Where k_s is the Nikuradse bed roughness, which is proportional to grain-size. DHI recommend a default value of 32 $m^{1/3}.s^{-1}$ for a median grain-size of 0.1 mm. However, for calibration purposes, the Manning number was chosen based on the best simulation of current velocities. Model simulations were run using a Manning number varying between 10 and 100. It was found that the ideal bed roughness varied between calibration sites. A variable bed roughness file was desirable, however a mean value of M = 38 $m^{1/3}.s^{-1}$ was used as the variable bed roughness grid could not be implemented in the DHI installation used here.

3.5.2.2 Eddy viscosity

The eddy viscosity in the model was varied to determine the effect on the timing of the tide. At all sites, the tide turns slightly early relative to measured data, within in the order of 10 minutes. The tide predictions are modelled based on a network of tide recorders located around New Zealand. The data are accurate to within 0.1 m in height, and 5-10 minutes in time. There are no recorders situated in the vicinity of Hawke Bay, with the closest recorders located at Moturiki Island and Riversdale. Therefore, the assumption can be made that error in the timing of the tide may be up to 10 minutes.

Different values trialled for eddy viscosity included 0.025, 1 and 2 $m^2.s^{-1}$. A high value dampened current velocities, whereas a very low value allowed the tide to

move through the estuary too quickly, with the modelled tide at the ENT site earlier than in the measured data. Taking into account both of these effects of the eddy viscosity on results, a value of 1 $m^2.s^{-1}$ was found to be appropriate.

3.5.3 Calibration results and model validation

The measured tidal data from the spring tide deployment for 3 tidal cycles were used to calibrate the model, for the period 20/10/2008 17:30 to 22/10/2008 7:30. Data for calibration are ideally measured for a longer time period, however due to logistical constraints current meter deployments were limited to two days. Data measured during neap tide deployment were used to verify the model.

Overall the model simulated tidal height, current velocities and direction well. The calibration and validation results are presented in such a way that a direct comparison can be made between all variables of modelled and measured data at each site for spring and neap deployments.

3.5.3.1 Entrance site (ENT)

At the entrance site, water depth is accurately predicted by the model, with an accuracy of ± 0.07 m (Figure 3.10 A). The model predicted current velocity relatively accurately with an error of ± 0.18 $m.s^{-1}$, although the current velocity was slightly under-predicted during the outgoing tide (Figure 3.10 B). It is a shortcoming of the model at this site that the asymmetry in the current speeds of the measured data was not predicted to the same extent by the model as is measured at the entrance site. However, there was a degree of tidal asymmetry evident, particularly during neap tide conditions (Figure 3.16 B). Direction and the timing of tide reversal were accurately predicted by the model at the entrance site, with an error of ± 88.6 degrees. This error is attributed to the large amount of noise in the data. However, it is evident that the timing of reversal and mean direction of the incoming and outgoing tide is well predicted by the model (Figure 3.16 C). Timing of the tide reversal calibrated to within the accuracy of the NIWA tide prediction model of 5-10 minutes.

The model is validated by the neap tide simulations. At the entrance site, the model predicts water depth with an accuracy of ± 0.05 m (Figure 3.16 A). There is

a slight offset evident between spring and neap data, which is addressed in section 3.5.3.4. Direction is slightly better predicted by the model during neap conditions at the entrance site with an error of ± 72.7 degrees.

3.5.3.2 Intertidal site (INT)

Measured data from the intertidal site have been displayed only at high tide, as at low tide the probe emerged from the water, thus recording noise only for pressure, velocity and direction. Water elevation, current speed and direction calibrated well at this site (Figure 3.12). Water depth at the intertidal site was well-calibrated, with an error of ± 0.05 m (Figure 3.12 A). The model validation with neap data confirms the water depth was accurately predicted for this site, with an error ± 0.06 m (Figure 3.18 A). Current speed at the intertidal site calibrated well, with an accuracy of ± 0.05 $m.s^{-1}$ (Figure 3.12 B). This was supported by the model validation at this site, where current speeds were predicted with an accuracy of ± 0.06 $m.s^{-1}$ (Figure 3.18 B). Direction also calibrated well at this site, with an error of ± 31.7 degrees (Figure 3.12 C), and an error of ± 55.2 degrees in the model validation (Figure 3.18 C).

3.5.3.3 Bridge site (BRI)

Water elevation at the bridge site calibrated well, with an accuracy of ± 0.07 m. The model accurately predicted the asymmetrical tidal flow seen in the measured data (Figure 3.14 A). The shape of the tidal curve is also reflected in the modelled current speed at this site, where model accurately simulated the ebb tidal asymmetry, to within ± 0.15 $m.s^{-1}$ (Figure 3.14 B). Current velocity in the validation of the model at this site was predicted with an accuracy of ± 0.16 $m.s^{-1}$ (Figure 3.20 B). The modelled and measured current direction at this site calibrated well, with an error of ± 106.2 degrees. Again, this relatively large error is attributed to the amount of noise in the direction data, but is evident in Figure 3.14 C that the timing of the tide and direction during the incoming and outgoing tide that the modelled direction is a good fit with measured data. The noise in the directional data is evident at low tide, and therefore the probe was likely to have been emergent at low water. The well-calibrated direction at this site is also

reflected in the u and v velocities. Modelled and measured data both show evidence of differing incoming and outgoing tidal direction (Figure 3.15 C & D). This is attributable to channel morphology, which bends both seaward and landward of the measurement site. A small discrepancy in the timing of reversal is evident between measured and modelled data. However, the timing of reversal from ebb to flood tide is difficult to decipher as there is noise in the measured data where the probe was emergent at low tide. For the neap deployment, the modelled water depth shows some discrepancy with measured data, with an error of ± 0.14 (Figure 3.20 A). This offset is further explained in section 3.5.3.4 below.

3.5.3.4 Spring – Neap offset

It is evident from comparison between the calibration of the model with spring tide data and the validation of the model using neap tide data that there is a discrepancy between the two simulations. Data were extracted from the model near the open ocean forced boundary to determine whether an offset existed between spring and neap model forcing. As Figure 3.9 illustrates, there was an offset of 0.07 m between the MSL of the spring and neap simulations. However, this discrepancy between spring and neap data is exaggerated at the entrance (ENT) and bridge (BRI) sites in Figures 3.16 and 3.20, respectively. As water depths at the intertidal site calibrated well, this is thought to be an artefact of the resolution of the grid. The depth given in the bathymetry gives an average representation of the 10 x 10 m area. However, it is highly possible that the point location where the ADV current meter was deployed may have a slight difference in elevation than the elevation assigned to the entire grid cell. It is also possible that the location of deployment during the neap tide may differ from that of the spring deployment. The spring data for the bridge site calibrate well, and the positional accuracy of the GPS when re-deploying instruments for the neap tide was in the order of 4-5 m at the site.

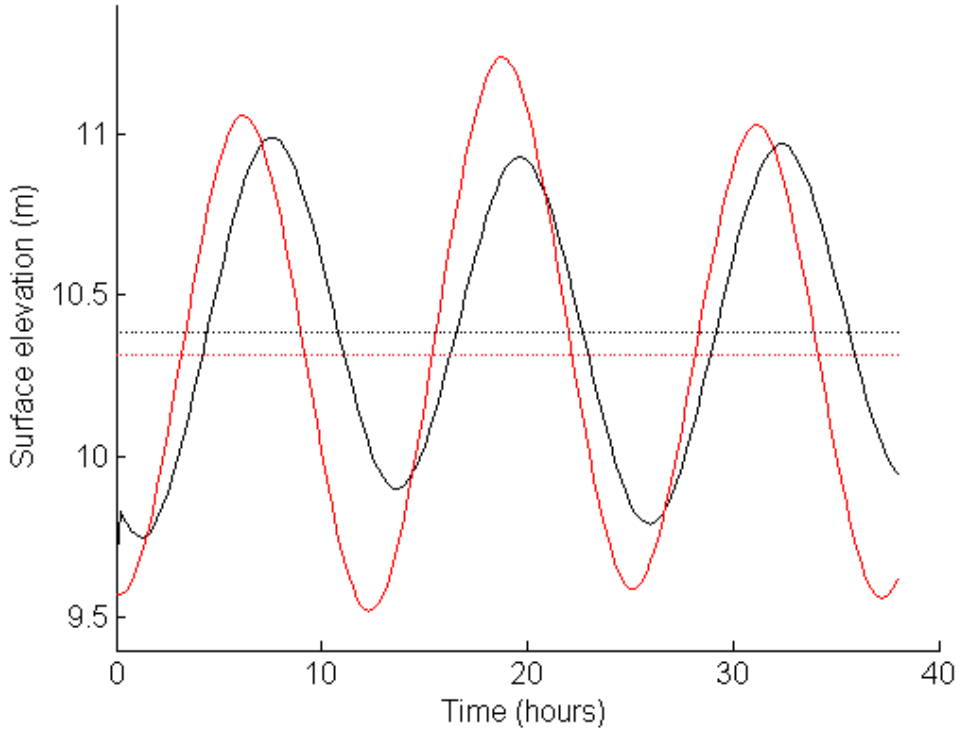

Figure 3.9. Spring data (red) and neap data (black) were extracted from the model near the open ocean boundary. MSL is also given. An offset between spring MSL and neap MSL of 0.07 m was calculated.

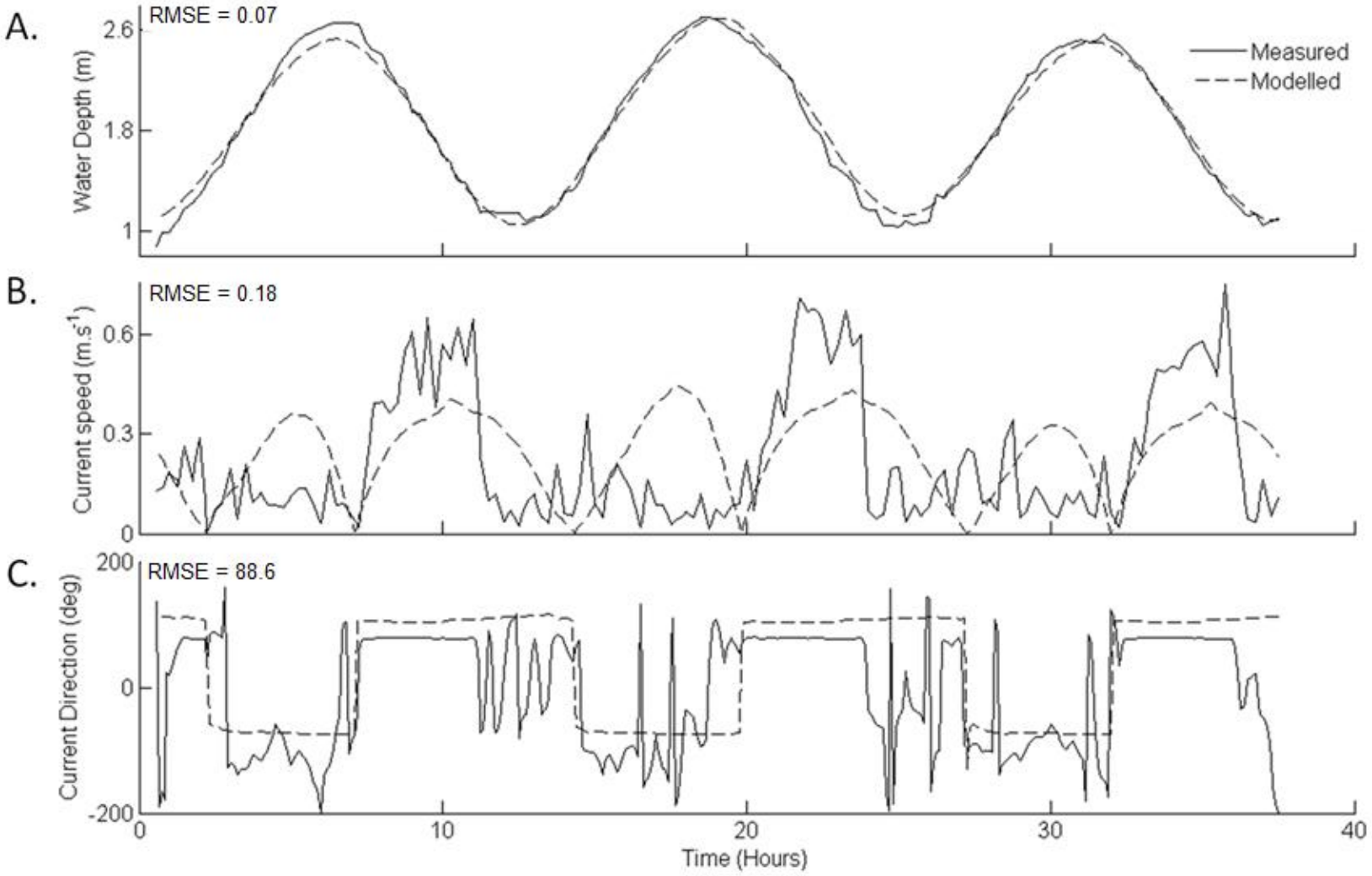

Figure 3.10. Calibration parameters for entrance site (ENT) under spring tide conditions. Measured and modelled data are given for **A.** water depth **B.** current speed and **C.** current direction. Direction is given in degrees relative to true north.

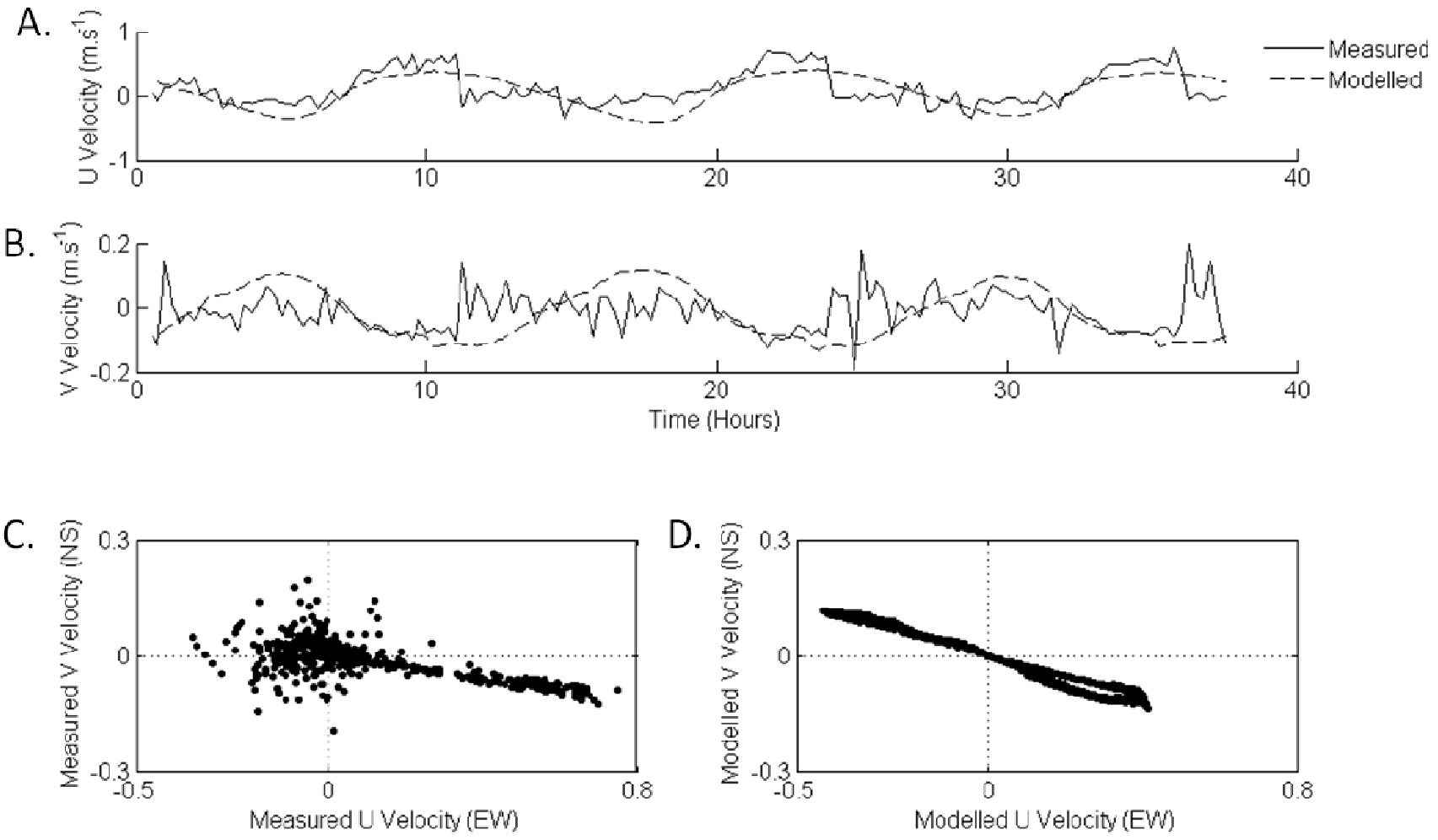

Figure 3.11. Calibration parameters for entrance site (ENT) under spring tide conditions. **A.** U velocities and **B.** V velocities are shown for measured data (solid line) and modelled data (dashed line). **C.** Measured U velocity vs. measured V velocity and **D.** Modelled U velocity vs. modelled V velocity.

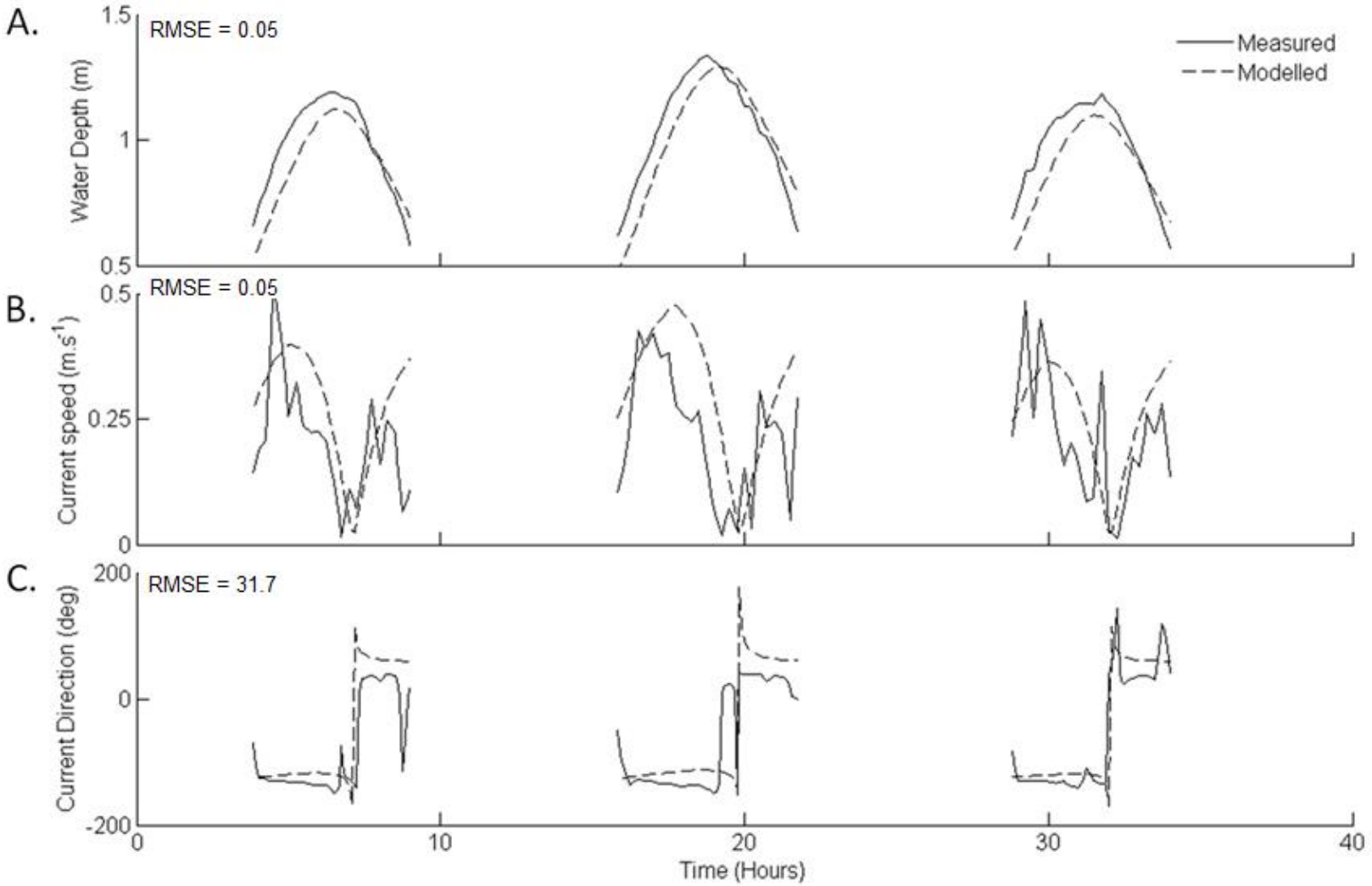

Figure 3.12. Calibration parameters for intertidal site (INT) under spring tide conditions. Measured and modelled data are given for **A.** water depth **B.** current speed and **C.** current direction. Direction is given in degrees relative to true north.

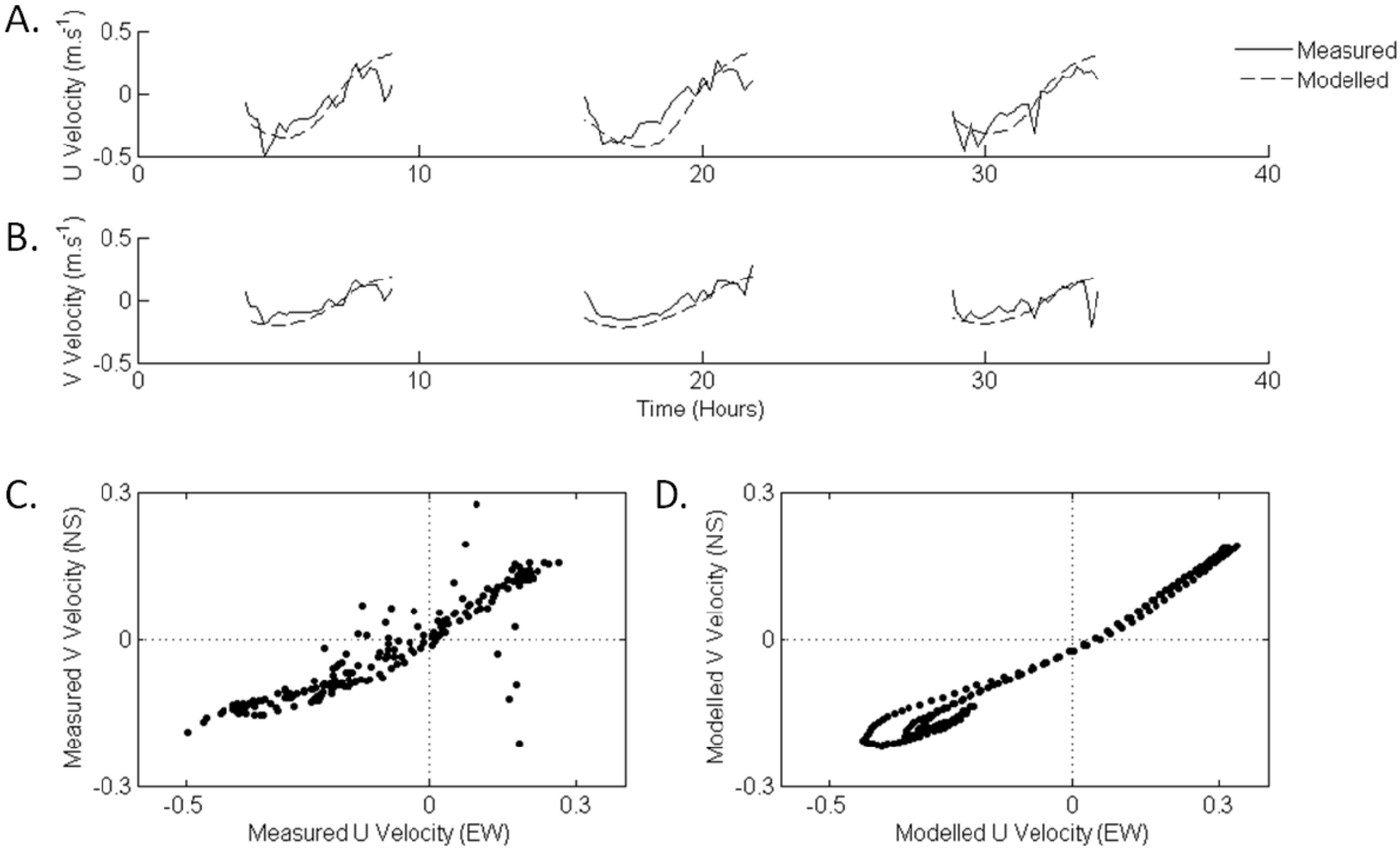

Figure 3.13. Calibration parameters for intertidal site (INT) under spring tide conditions. **A.** U velocities and **B.** V velocities are shown for measured data (solid line) and modelled data (dashed line). **C.** Measured U velocity vs. measured V velocity and **D.** Modelled U velocity vs. modelled V velocity.

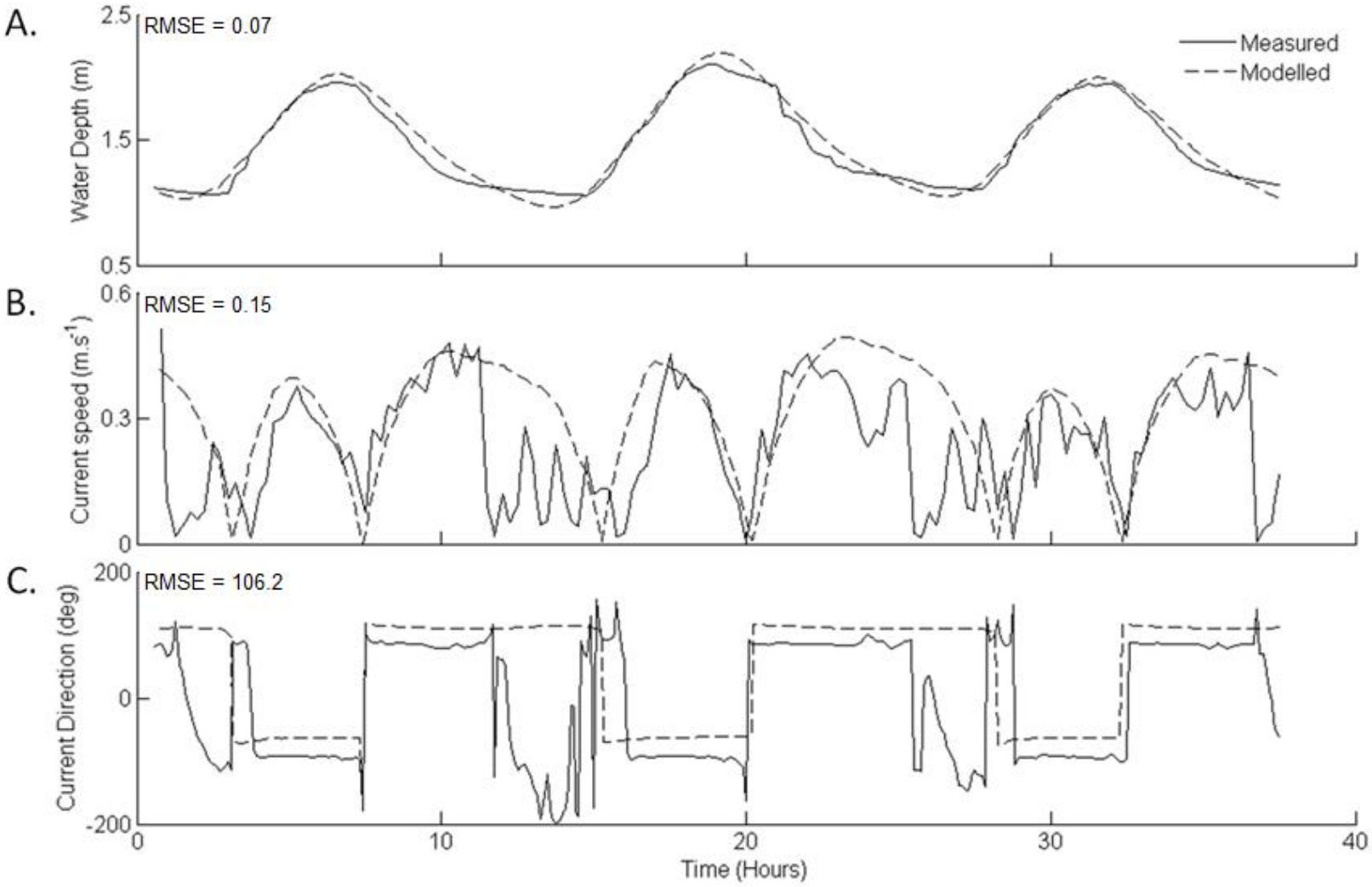

Figure 3.14. Calibration parameters for bridge site (BRI) under spring tide conditions. Measured and modelled data are given for **A.** water depth **B.** current speed and **C.** current direction. Direction is given in degrees relative to true north.

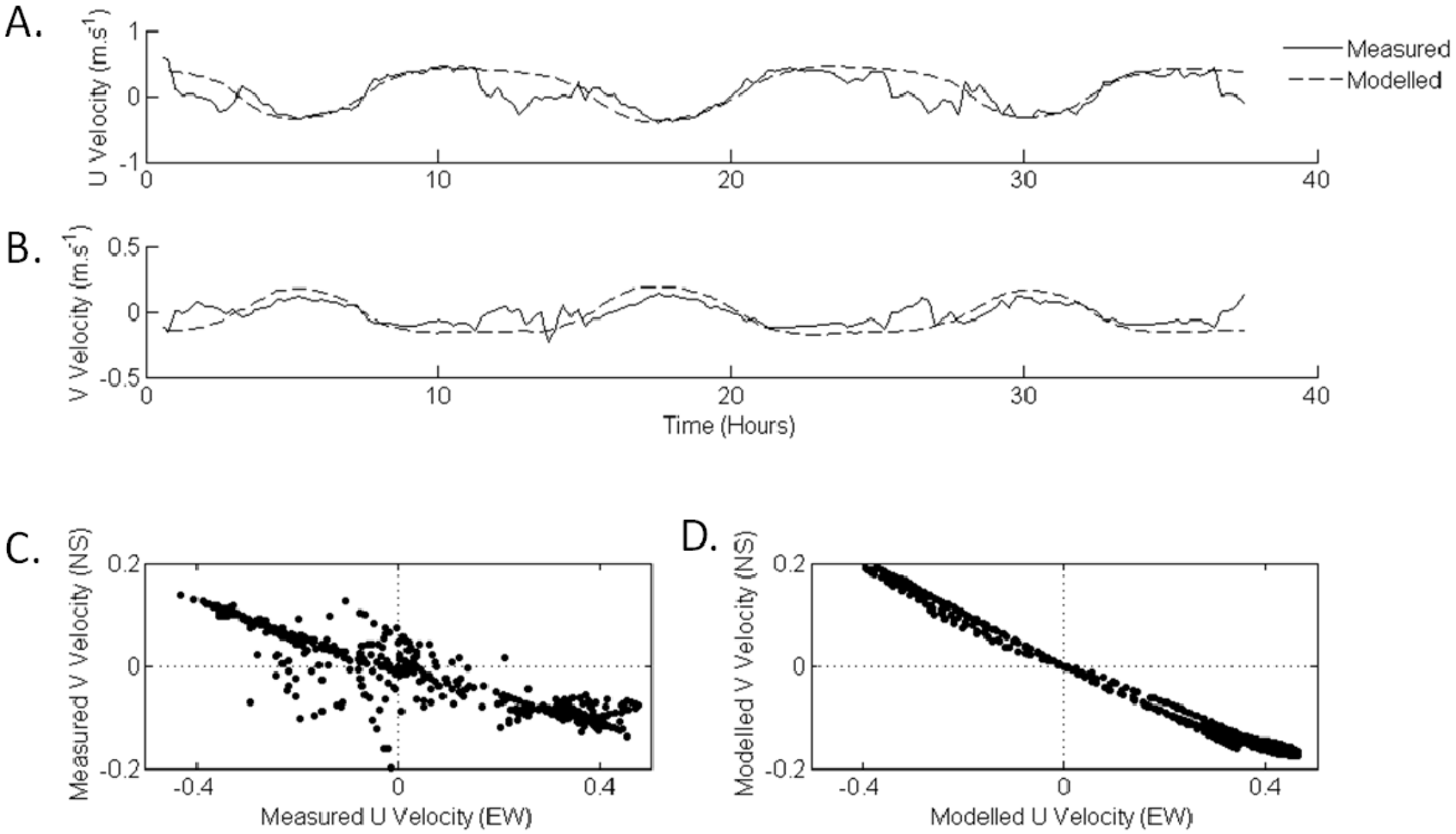

Figure 3.15. Calibration parameters for bridge site (BRI) under spring tide conditions. **A.** U velocities and **B.** V velocities are shown for measured data (solid line) and modelled data (dashed line). **C.** Measured U velocity vs. measured V velocity and **D.** Modelled U velocity vs. modelled V velocity.

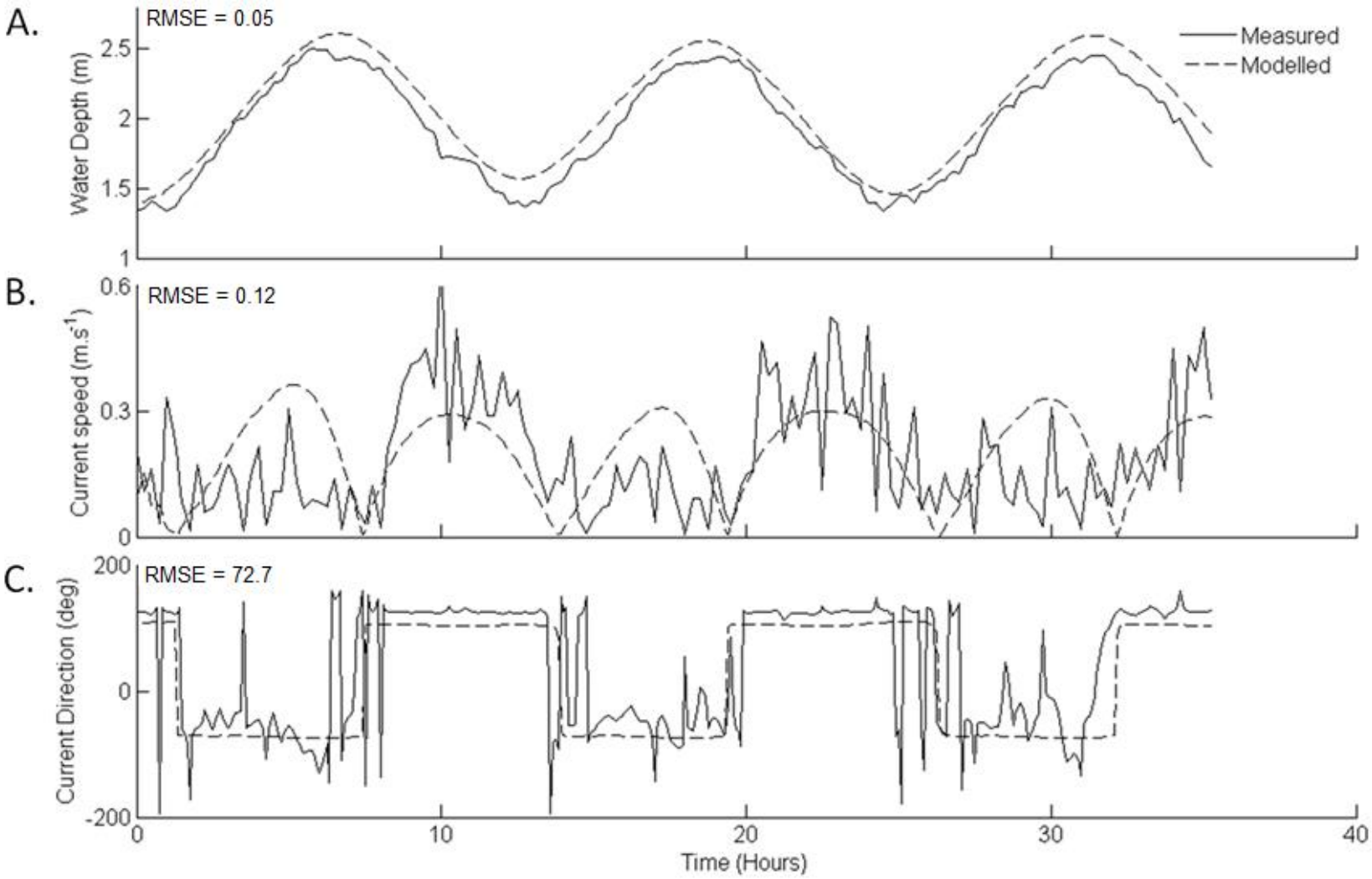

Figure 3.16. Calibration parameters for entrance site (ENT) under neap tide conditions. Measured and modelled data are given for **A.** water depth **B.** current speed and **C.** current direction. Direction is given in degrees relative to true north.

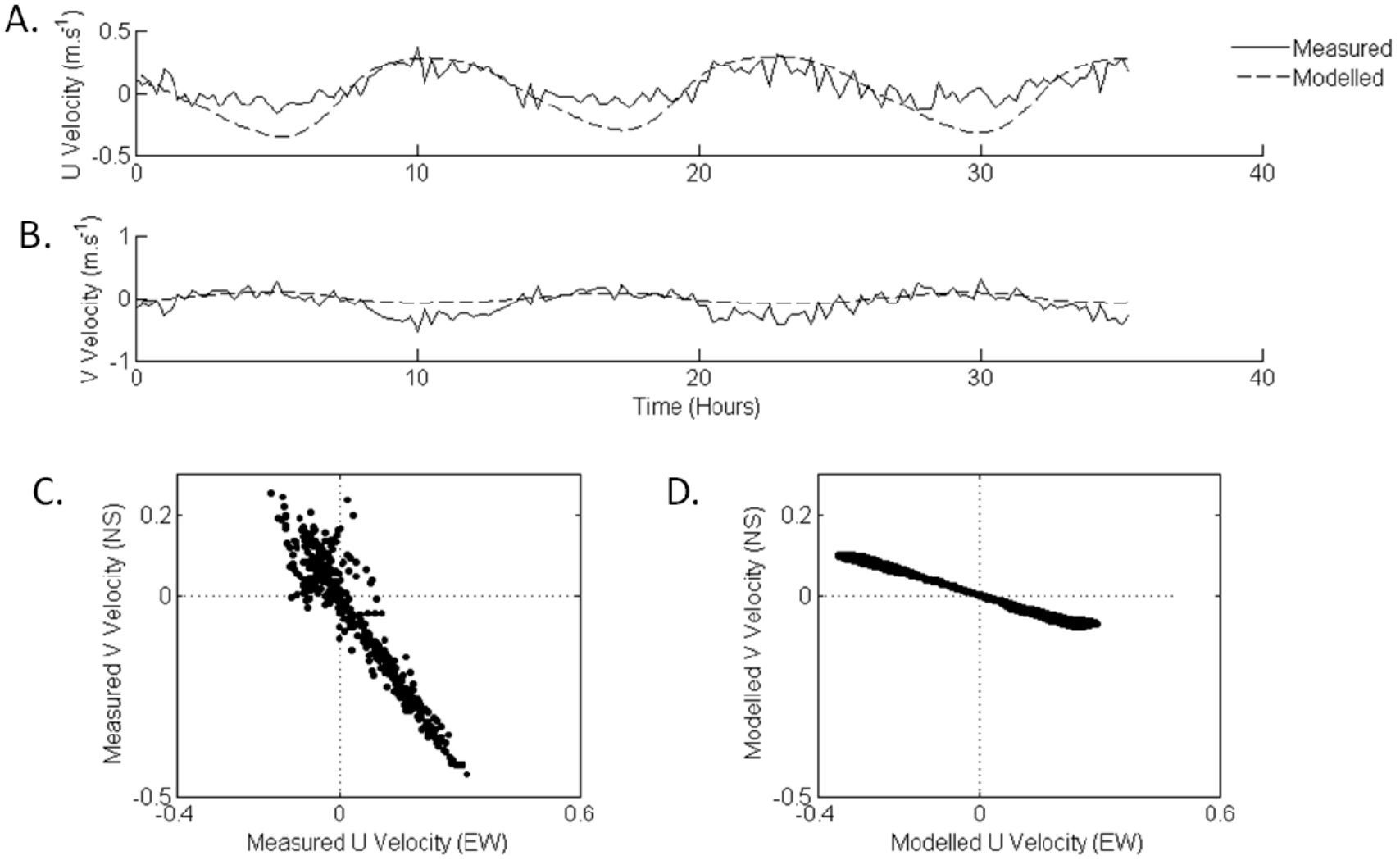

Figure 3.17. Calibration parameters for entrance site (ENT) under neap tide conditions. **A.** U velocities and **B.** V velocities are shown for measured data (solid line) and modelled data (dashed line). **C.** Measured U velocity vs. measured V velocity and **D.** Modelled U velocity vs. modelled V velocity.

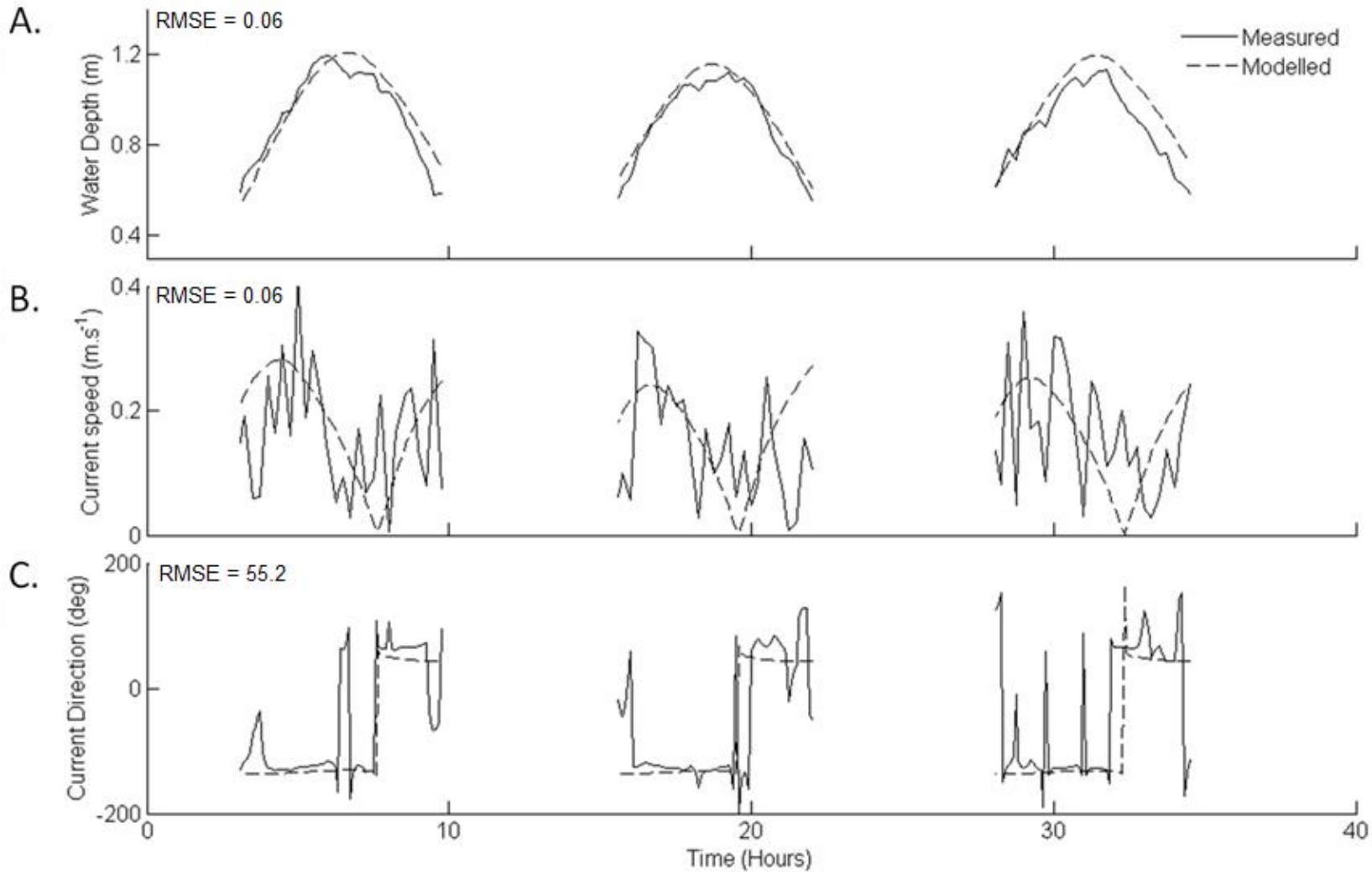

Figure 3.18. Calibration parameters for intertidal site (INT) under neap tide conditions. Measured and modelled data are given for **A.** water depth **B.** current speed and **C.** current direction. Direction is given in degrees relative to true north.

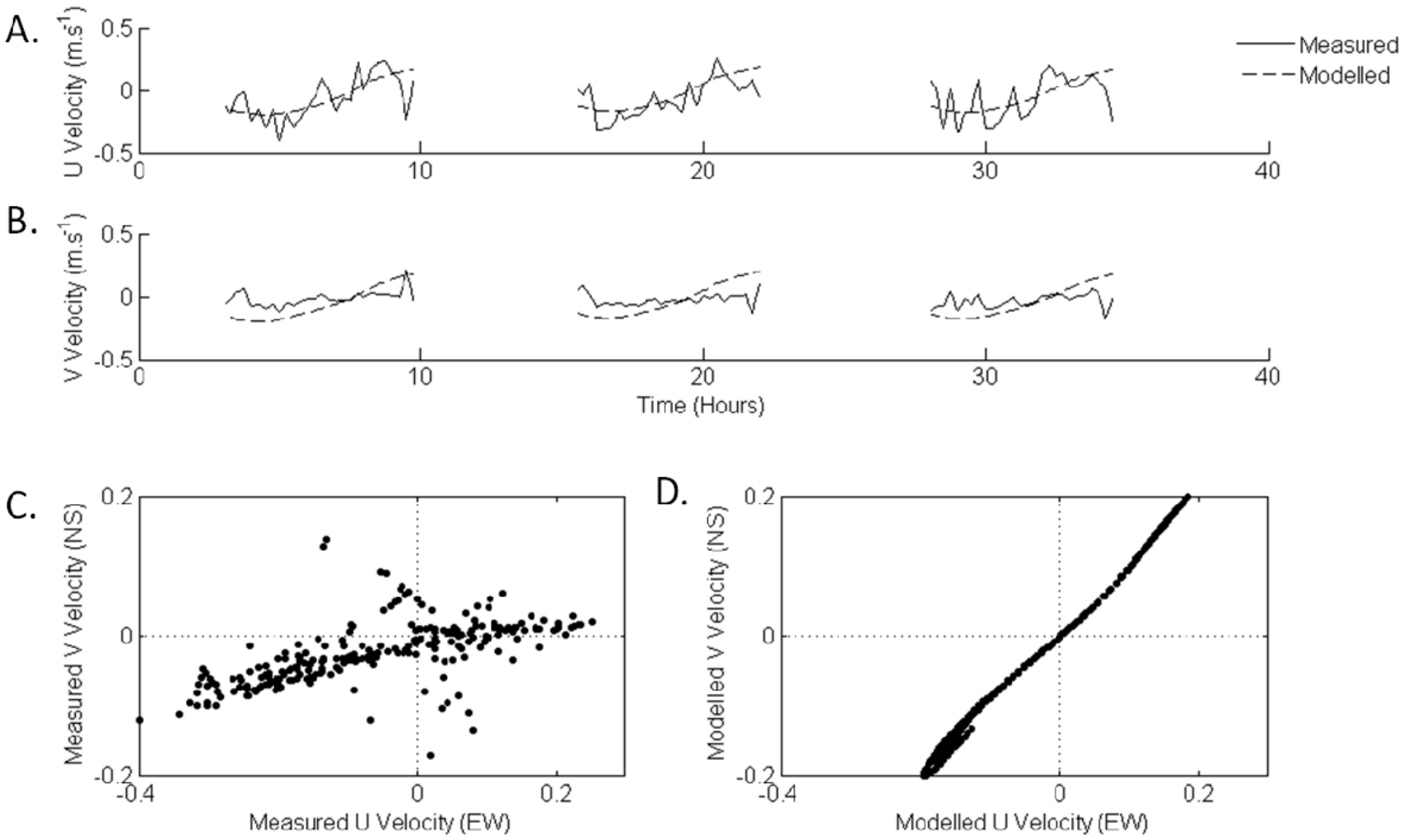

Figure 3.19. Calibration parameters for intertidal site (INT) under neap tide conditions. **A.** U velocities and **B.** V velocities are shown for measured data (solid line) and modelled data (dashed line). **C.** Measured U velocity vs. measured V velocity and **D.** Modelled U velocity vs. modelled V velocity.

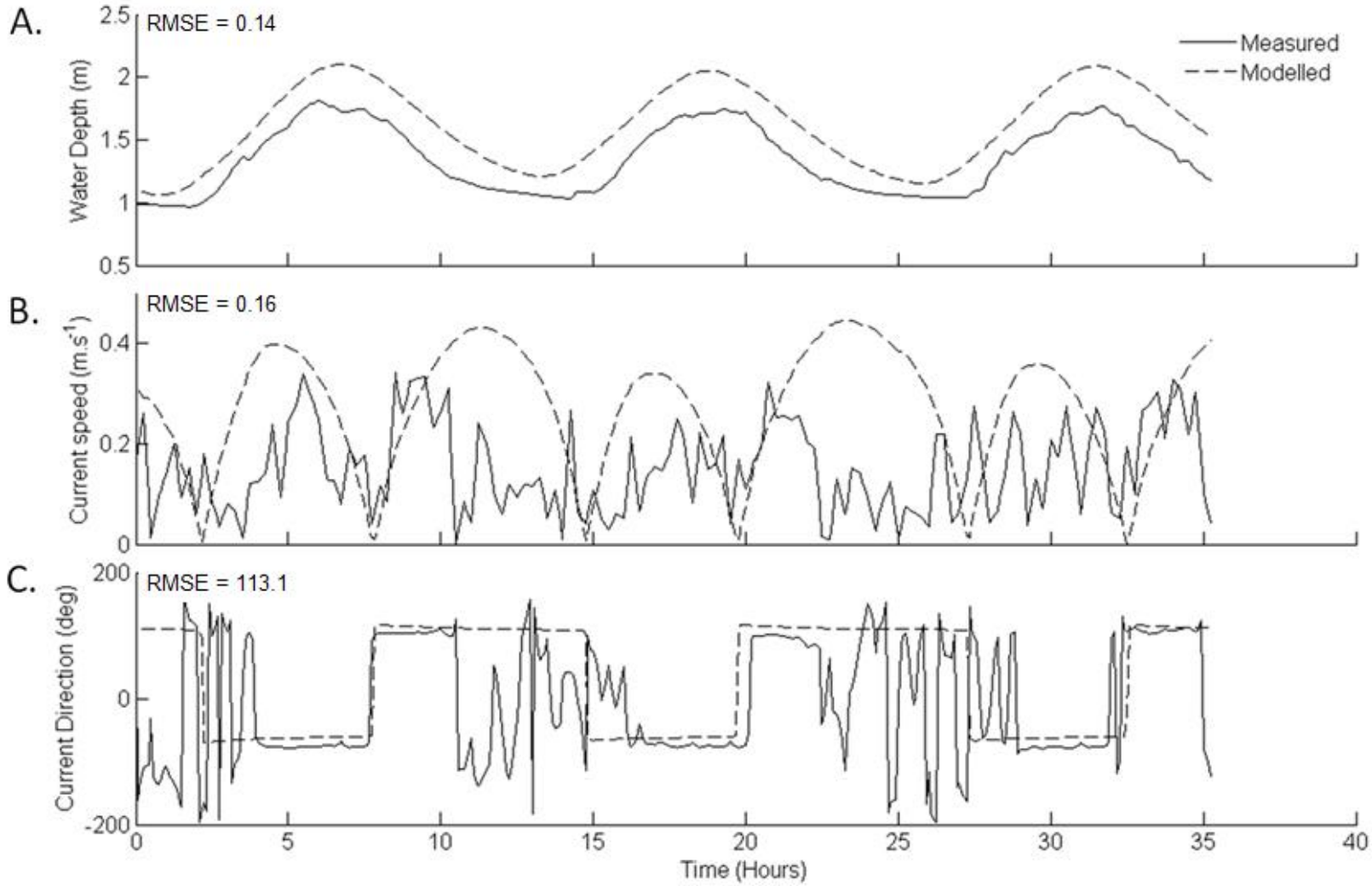

Figure 3.20. Calibration parameters for bridge site (BRI) under neap tide conditions. Measured and modelled data are given for **A.** water depth **B.** current speed and **C.** current direction. Direction is given in degrees relative to true north.

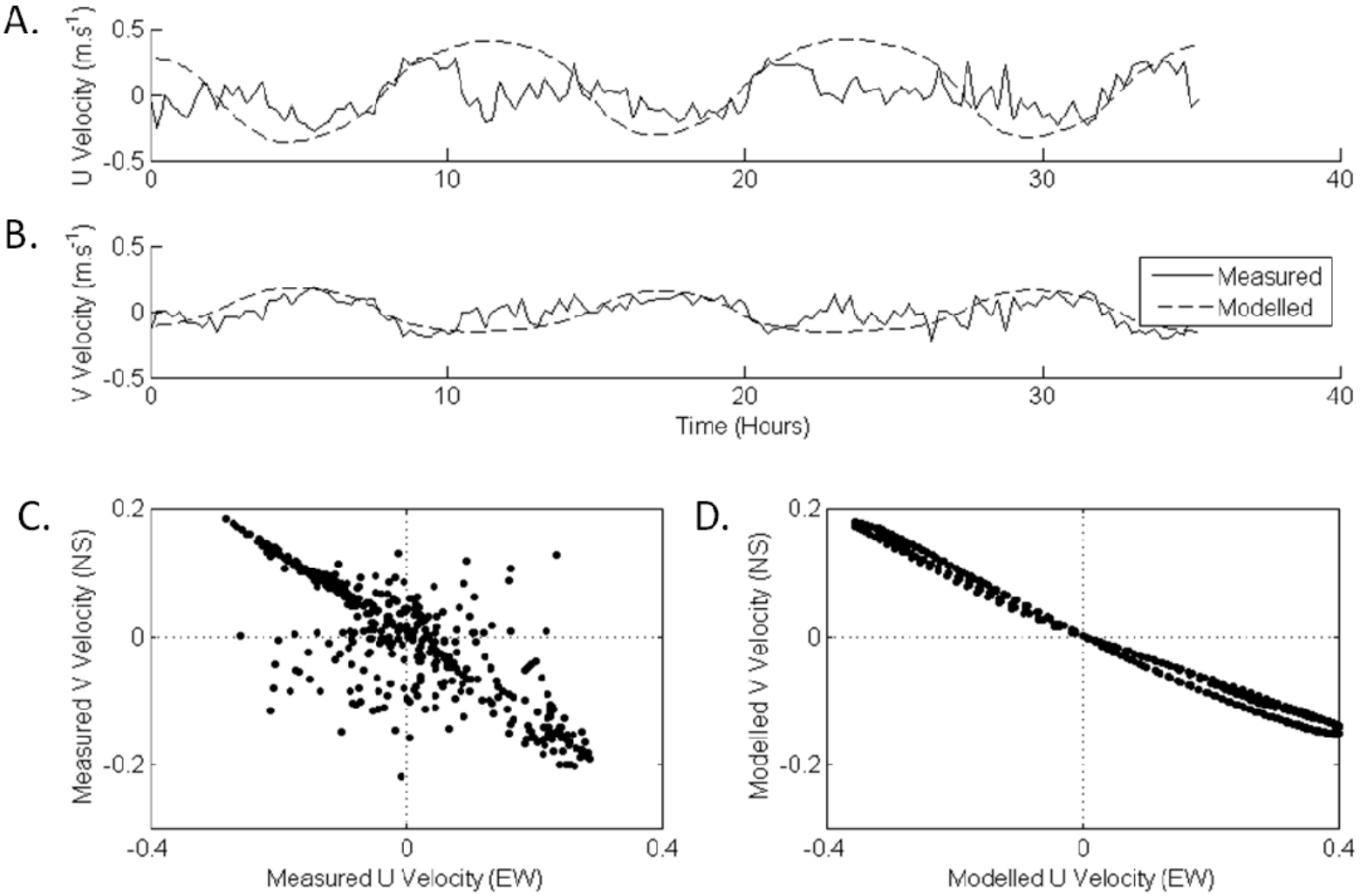

Figure 3.21. Calibration parameters for bridge site (BRI) under neap tide conditions. **A.** U velocities and **B.** V velocities are shown for measured data (solid line) and modelled data (dashed line). **C.** Measured U velocity vs. measured V velocity and **D.** Modelled U velocity vs. modelled V velocity.

3.6 HYDRODYNAMICS RESULTS

3.6.1 Hydrodynamic observations

Ahuriri Estuary is a small, microtidal estuary with a very shallow and complex bathymetry. As a result of this shallow complex morphology, frictional losses are evident over small spatial scales. Peak flow velocities recorded during field deployments are relatively low (Table 3.3). The greatest velocities were recorded by the ADV deployed at the entrance site (ENT). At this site the tidal flow is constricted through the narrow opening of the passage between the middle and lower estuary under the Pandora Bridge (referred to herein as the Pandora Passageway), increasing tidal velocities. This is particularly evident on the outgoing tide as the instrument is located in the main channel draining the entire estuary. The maximum free-stream velocity recorded at this site was 0.76 $m.s^{-1}$.

Table 3.3. Peak current velocities in $m.s^{-1}$ measured by ADV current meters during spring and neap deployments.

Location	**Peak velocity incoming tide**		**Peak velocity outgoing tide**	
	Spring	**Neap**	**Spring**	**Neap**
ENT	0.36	0.31	0.76	0.64
INT	0.53	0.42	0.35	0.31
BRI	0.45	0.34	0.48	0.34

The measured current velocities are generally smaller than 0.5 $m.s^{-1}$, with the exception of peak outgoing velocities at the entrance site. A spring - neap variation in peak velocities is also notable, with considerably lower velocities for the incoming and outgoing tide at all sites during neap tide conditions.

3.6.2 Hydrodynamic model results

Peak flows in the main channel reached velocities of up to 0.5 $m.s^{-1}$ under spring tide conditions and slightly lower velocities under neap tide conditions. See Appendix VII for hydrodynamic model videos for which the following results and discussion are based upon.

Figures 3.22 to 3.25 show the evolution of the tidal currents over both the incoming and outgoing tides during spring and neap simulations. Areas where tidal flow was constricted into increasingly narrow pathways must be balanced by an increase in velocity according to the law of mass conservation. This resulted in the greatest velocities in the estuary, evident through the Pandora Passageway, the very narrow channels in the upper estuary and the tidal inlet. Velocities were also amplified through the Pandora Passageway by the convergence of the two main channels in the middle estuary from either side of the bank. During spring low tide the current velocities were also higher than during neap low tide, as flows were further restricted in the channel during a spring low tide (Figure 3.24) and there was a greater tidal prism due to the greater tidal range. Current velocities in the main channel in the middle estuary during the outgoing tide reached a maximum of 0.6 $m.s^{-1}$ during spring tide conditions, compared to a maximum of 0.4 $m.s^{-1}$ during neap tide conditions.

Tidal flow penetrated furthest into the upper estuary during spring tide conditions. Flow velocities in the upper reaches were relatively low. However, a maximum of 0.6 $m.s^{-1}$ was reached where the channel narrows. The Taipo Stream was highly influenced by the tide, rising and falling considerably. In the main outfall channel, located in the upper estuary, there is an area of complex morphology with a number of emergent islands. At mid to low tide, the flow was constricted through a complex network of small tidal channels through this area. Tidal velocities here were increased in order to conserve mass.

Pandora Pond is an area of the estuary where there is seen to be currents entering the area but negligible return currents. Early in the incoming tide the flows refracted around the southern edge of the Pandora Passageway to enter the Pandora Pond area (Figure 3.22). This process only occurred in the early stages of the incoming tide. As the currents increased in velocity through the Pandora Passageway with time in the tidal cycle, there was less refraction and the currents were instead propelled further into the middle estuary.

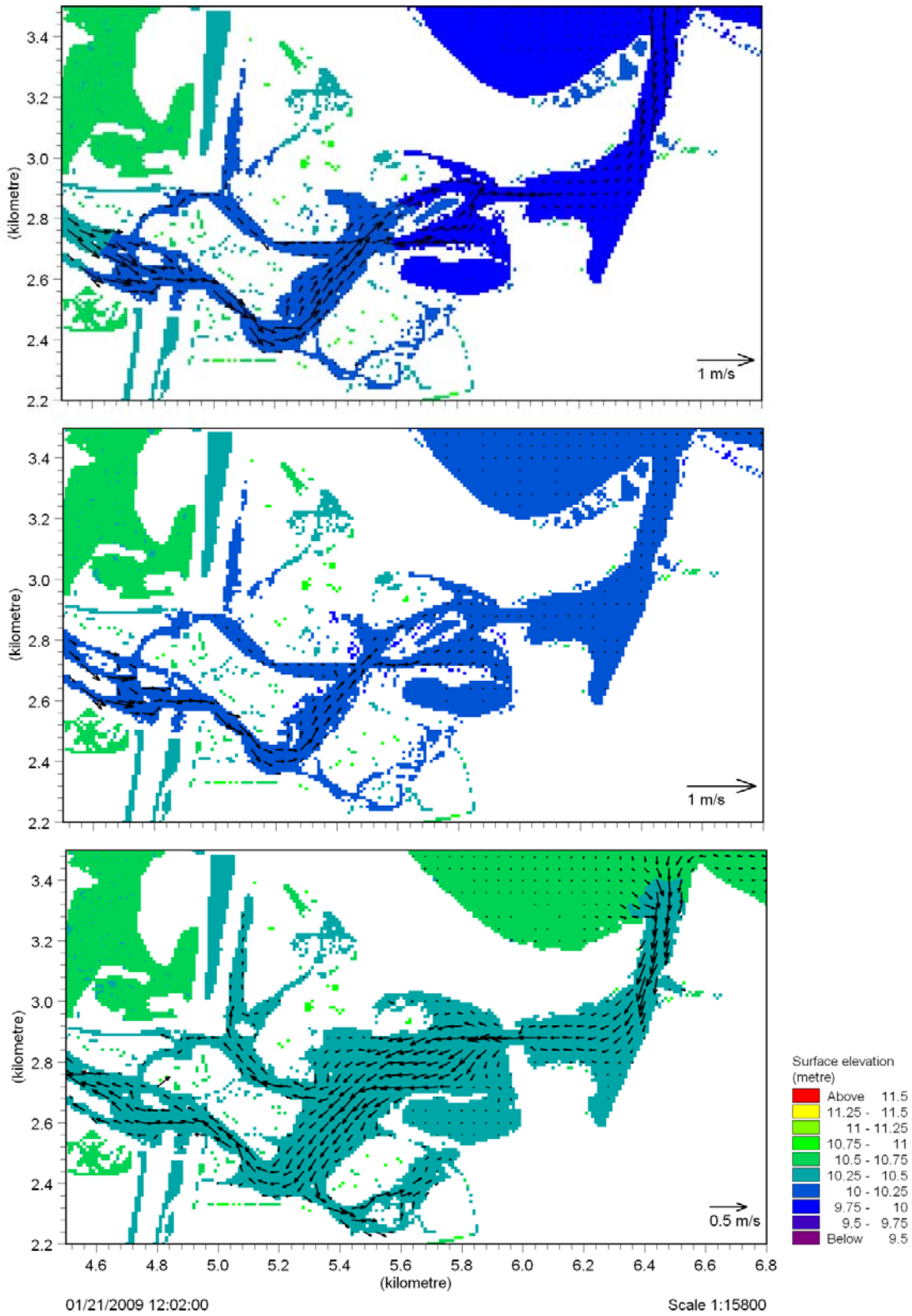

Figure 3.22. Tidal current and direction vectors and surface elevation over a full neap tidal cycle – 1 of 2. Snapshots are taken at 2 hour intervals. Note the varying reference vector for scale. White areas indicate dry land.

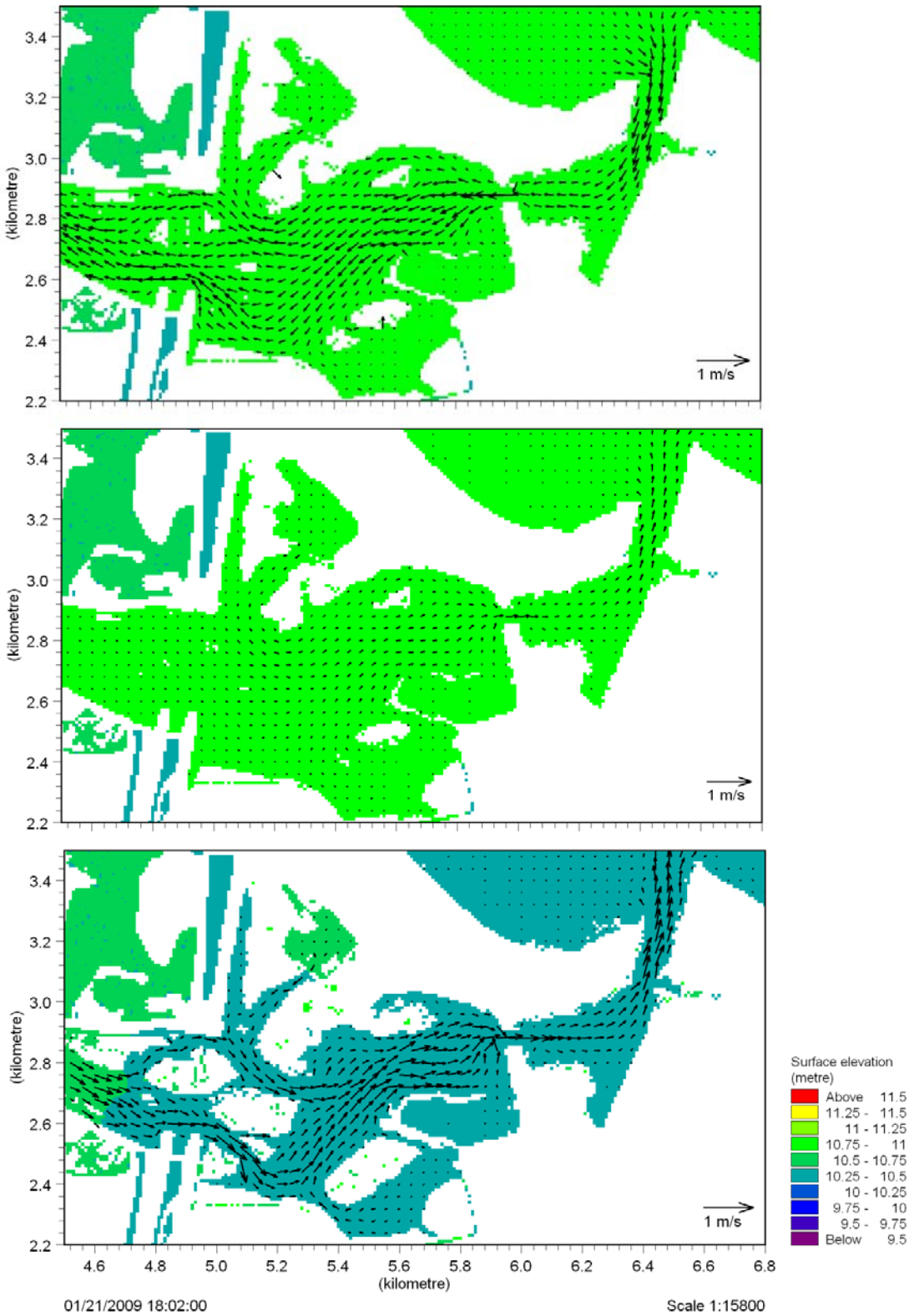

Figure 3.23. Tidal current and direction vectors and surface elevation over a full neap tidal cycle – 2 of 2. Snapshots are taken at 2 hour intervals. Note the varying reference vector for scale. White areas indicate dry land.

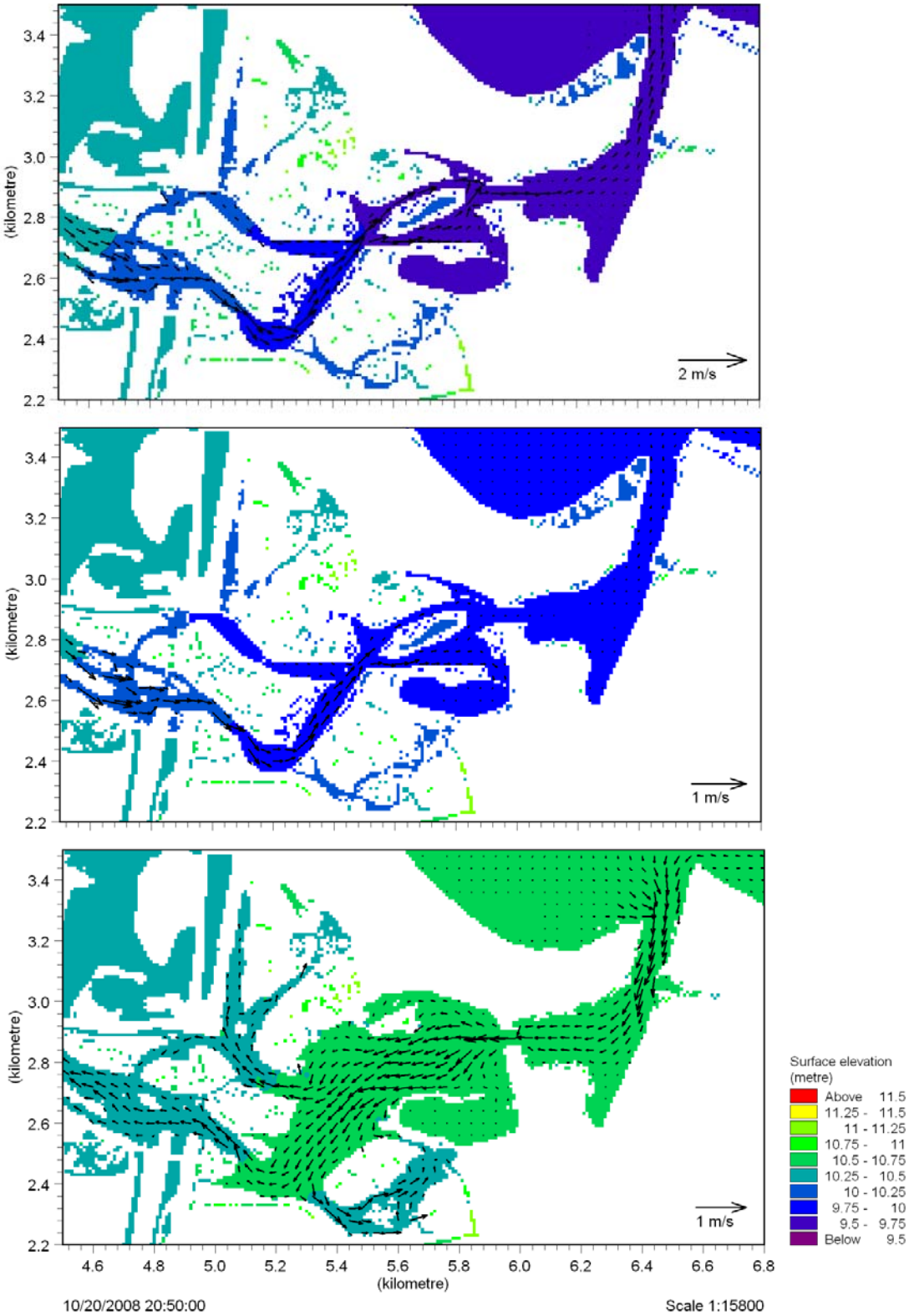

Figure 3.24. Tidal current and direction vectors and surface elevation over a full spring tidal cycle – 1 of 2. Snapshots are taken at 2 hour intervals. Note the varying reference vector for scale. White areas indicate dry land.

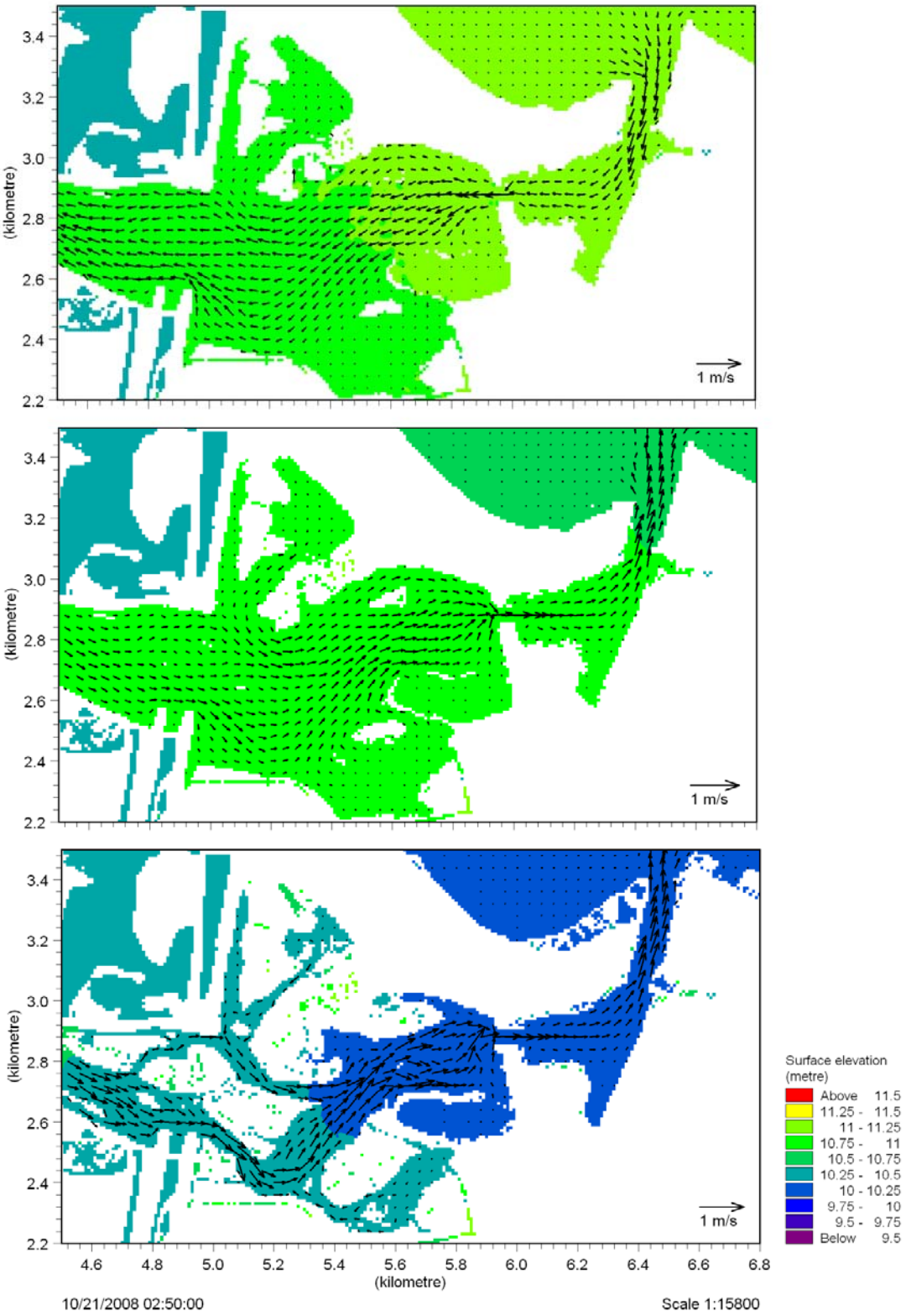

Figure 3.25. Tidal current and direction vectors and surface elevation over a full spring tidal cycle – 2 of 2. Snapshots are taken at 2 hour intervals. Note the varying reference vector for scale. White areas indicate dry land.

Although tidal flows are primarily restricted to the channels in Ahuriri Estuary, there are noteworthy currents into intertidal areas both north and south of the main channel in the middle estuary (Figure 3.26). These flows are restricted to the intertidal shallow channels, with negligible flows outside of these channels.

Some initial transients occurred in the neap model, but quickly dissipated (See Appendix VII).

3.6.3 Residual circulation

Modelled tidal currents were averaged over a two tidal cycles during a spring tide simulation, commencing and concluding at low tide. Mean residual circulation in Ahuriri Estuary was ebb-dominated (Figure 3.27), induced by the asymmetry in the tidal current velocities observed in the measured and modelled data. The residual current velocities were relatively low throughout the entire estuary, generally less than 0.25 $m.s^{-1}$, with the greatest velocities in the channels. In the upper estuary residual circulation was minimal with the exception of areas where tidal flow is constricted by morphology (Figure 3.27). In the middle estuary residual currents are greatest in the channels and are ebb-dominated. However, the intertidal channel regions show flood-dominated flows. This is expected as during the flood tide velocities are greatest in the intertidal areas. During the outgoing tide, tidal flow was less directional with lower velocities in intertidal areas. This is reflected in the data measured by the ADV at the intertidal site. The ADV was situated near the channel edge, and it is evident that flood tidal currents had higher velocities than ebb tidal currents (Figure. 3.12). In the far reaches of the intertidal regions there was little discernible residual flow.

Relatively strong residual currents in the seaward direction were evident through the Pandora Passageway with an apparent eddy formation in the central area of the boat harbour (Figure 3.28). There were also strong residual current velocities through the main tidal inlet channel, with the ebb tidal jet current shear producing apparent eddies on both sides of the exit plume.

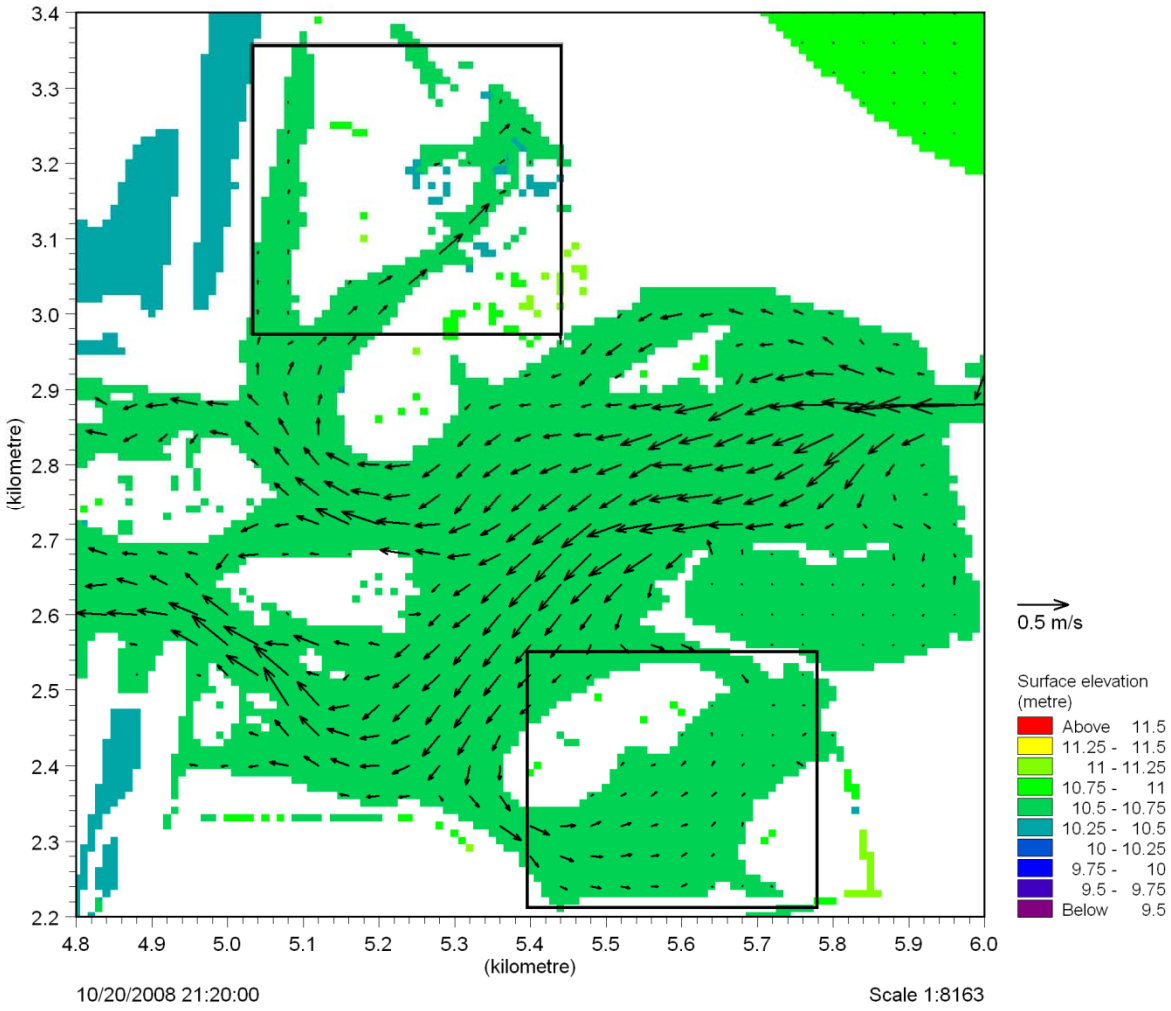

Figure 3.26. Tidal current and direction vectors and surface elevation on an incoming tide under spring tide conditions. Black boxes indicate intertidal regions where measurable current velocities are observed to feed intertidal areas during the incoming tide. Low velocities are evident in the intertidal flat region. Note reference vector for scale. White areas indicate dry land.

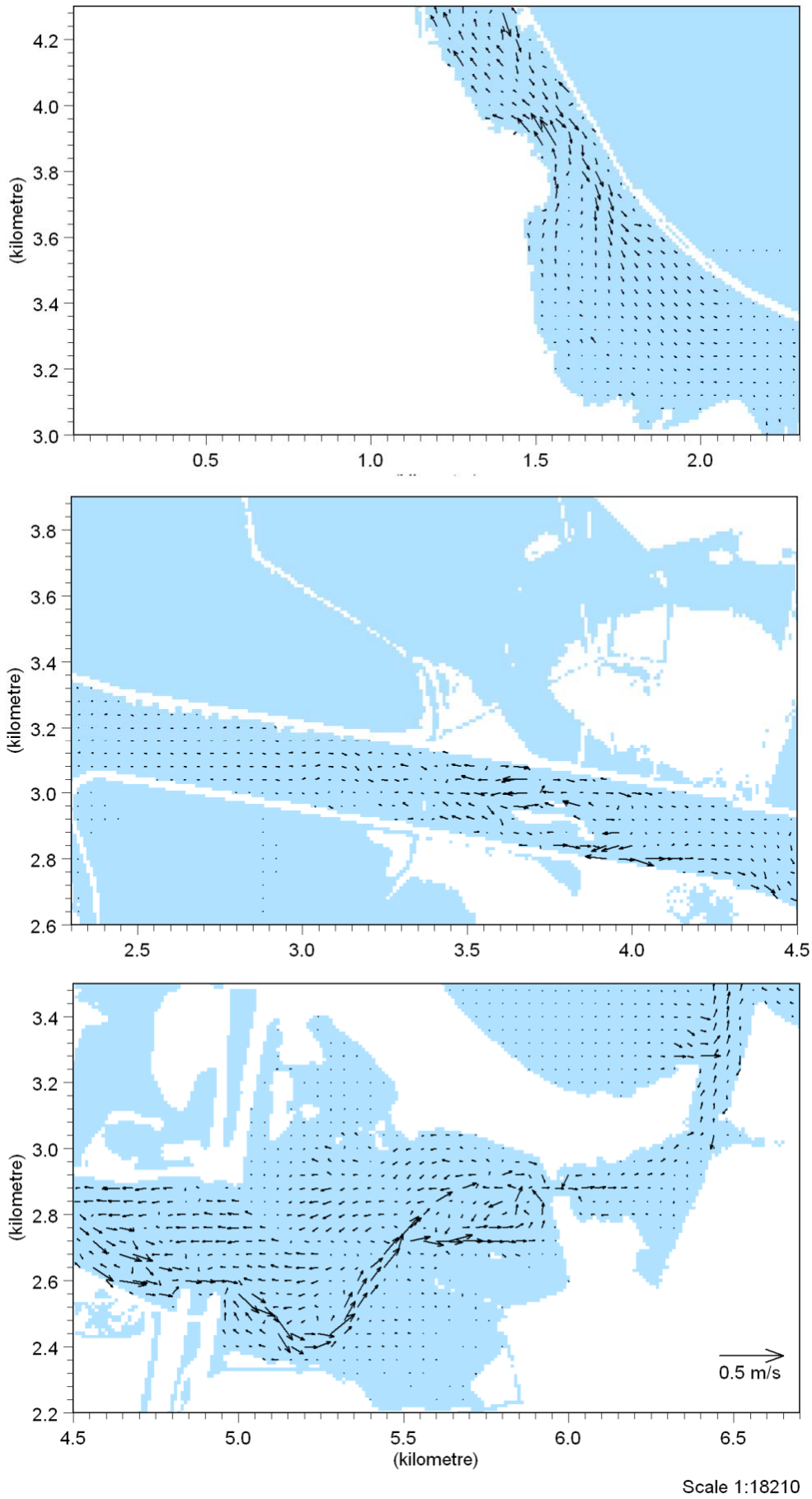

Figure 3.27. Residual current speed and direction averaged over two full tidal cycles during spring tide conditions. Vectors indicate residual current speed and direction. Note reference vector for scale. White areas indicate dry land.

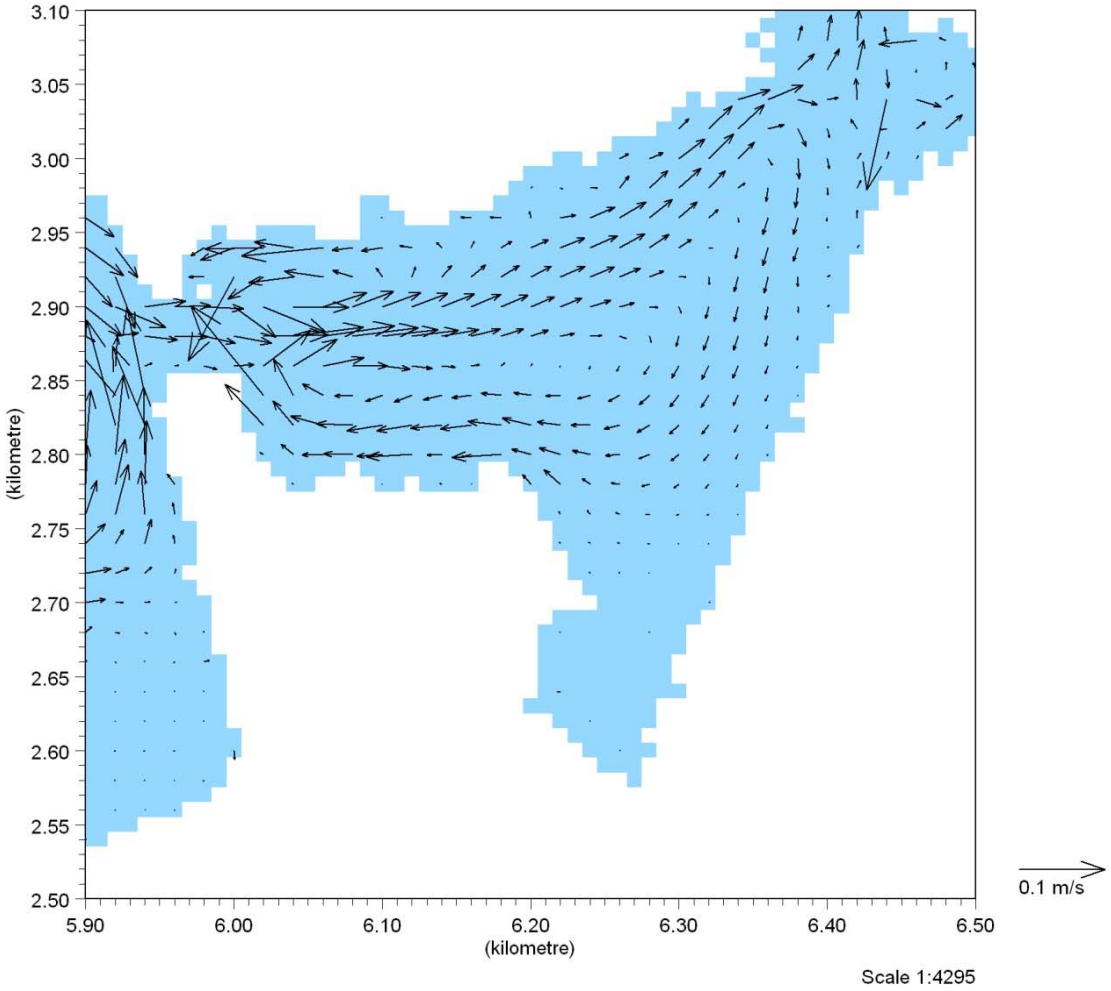

Figure 3.28. Residual current speed and direction averaged over two full tidal cycles during spring tide conditions in the lower estuary (boat harbour). Vectors indicate residual current speed and direction. Note reference vector for scale. White areas indicate dry land.

3.7 DISCUSSION

The hydrodynamic model calibration and validation illustrate the model is capable of accurately predicting the hydrodynamics of Ahuriri Estuary, although outgoing current speeds were slightly under-predicted at the entrance site. This is thought to be due to the difficulty in adequately representing the complex morphology in the model grid. The model has been shown to accurately predict relative current speeds, tidal asymmetry and residual currents, which govern sediment transport processes.

Current speeds within the Ahuriri Estuary were relatively low, particularly in intertidal areas. The maximum measured current speed occurred at the entrance measurement site, where flows were constricted by the Pandora Passageway. Remaining current velocity measurements at other sites in the estuary were generally below 0.5 $m.s^{-1}$. Modelled current velocities were generally concurrent with the measured data, and modelled current velocities in the intertidal areas were negligible. For the major part of the estuary, it is unlikely that the magnitude of currents found in the estuary possess the ability to entrain sediments from the bed into suspension.

The critical Shields parameter provides an estimation of the initiation of sediment movement, and is a function of bed shear stress and grain size (Reeve et al. 2004). The critical Shields parameter for tidal flows is calculated using the mean current velocity 1 metre from the bed, $\overline{u_{100}}$, the free stream velocity (Equation 3.2).

$$\theta_c = \frac{\bar{\tau}}{(\rho_s - \rho) g d} \qquad \text{(Equation 3.2)}$$

Where ρ_s is the density of sediment (assumed to be quartz sand) ($kg.m^{-2}$), ρ is the density of seawater ($kg.m^{-3}$), g is gravitational acceleration ($m.s^{-2}$), d is grain-size (m) and $\bar{\tau}$ is time-averaged bed shear stress, defined for tidal flows by Nielsen (1992) using Equation 3.3.

$$\bar{\tau} = {}^{1}/_{2}\, \rho\, 0.003\, \overline{u_{100}}^{2} \qquad \text{(Equation 3.3)}$$

For a sand grain 105 µm in diameter (the dominant sand sized grain diameter in Ahuriri sediments) and a mean current velocity of 0.5 $m.s^{-1}$, a critical Shields parameter of 0.02 is given. The maximum current velocity measured in the estuary (excluding the Pandora Passageway) is used in this calculation, as for the major part of the estuary current velocities are low and unlikely to induce incipient sediment motion. The Shields curve (Figure 3.29) suggests that sand grains are likely to move should the Shields parameter be greater than 0.03. The Shields parameter calculated for a 105 µm diameter sand grain suggests that the strongest measured currents in Ahuriri Estuary (excluding the Pandora Passageway) will not meet the incipient motion criterion and sand-sized particles will not be transported as bed load or be entrained into the water column.

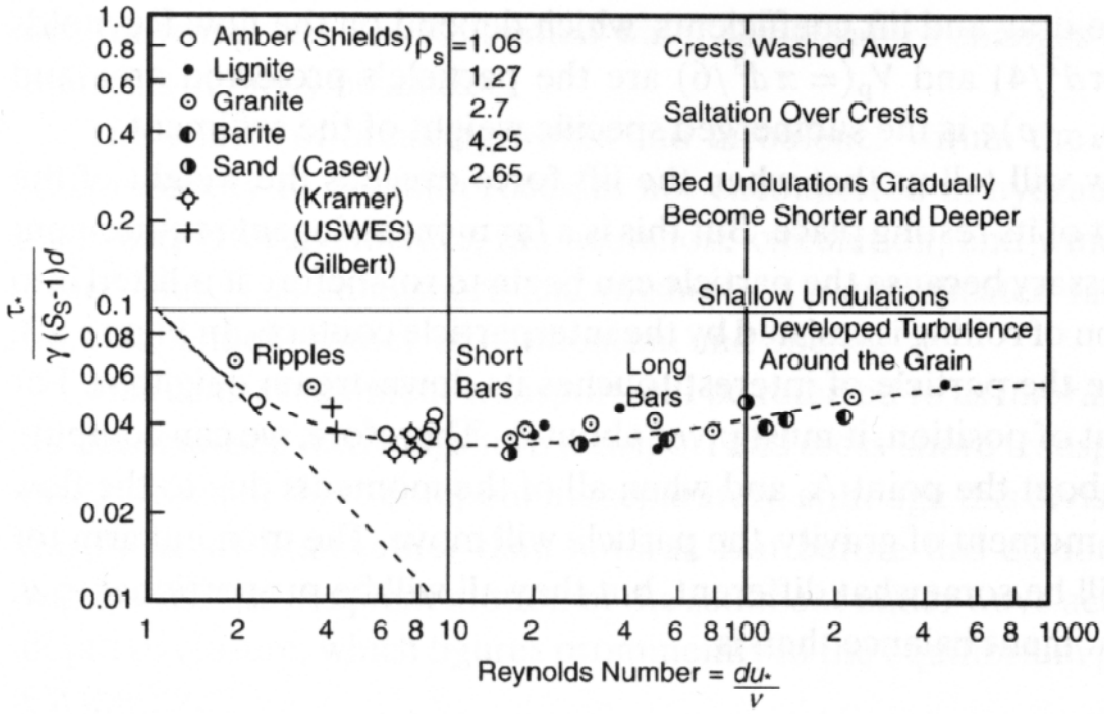

Figure 3.29. Shields parameter for the initiation of motion for steady flow. This relationship is able to be applied to flow under tidal currents, as critical shear stress is time-averaged. From Dean & Dalrymple (2002).

Current speeds in intertidal areas were relatively low. However, results indicated the incidence of considerable currents in low intertidal channels, which feed the intertidal flats on the incoming tide (Figure 3.26). The low intertidal currents identify these intertidal areas as a potential area of sediment accretion. Intertidal flats are a major sink for suspended sediments, with sediment cores taken in intertidal areas in other studies illustrating lamination consistent with regular sedimentation (Dyer 1994). This is consistent with cores taken in intertidal areas of Ahuriri Estuary (Chagué-Goff et al. 2000). Should the settling velocity be such that the sediment transported into these areas allows the sediment to settle out of the water column, it is likely to remain on the bed. For a grain size of 60 μm, with a calculated Stokes settling velocity of 0.00032 $m.s^{-1}$ in an intertidal area with negligible currents and an approximate depth of 0.5 m, it would take approximately 26 minutes to settle out of suspension. The upper intertidal flats are inundated for periods in excess of 26 minutes, indicating that these areas are a likely area of accretion. Tidal currents are low to negligible in these areas, and the limited fetch and sheltered nature of the estuary indicate that it is unlikely sediment will be resuspended once deposited in these areas.

Residual circulation patterns in Ahuriri Estuary were ebb-dominated with highly channelised residual currents in the middle estuary. The residual circulation is set up by the tidal asymmetry seen in the measured and modelled data. Tidal asymmetry is a fundamental governing factor in the net transport of sediments (Eisma 1998), and is therefore an important aspect in the hydrodynamic modelling of this study.

The time-averaged tidal currents gave rise to a number of residual eddies. Residual eddies are caused by the transfer of vorticity from the first order current (tidal current) to the second order current (residual current) (Zimmerman 1981). In the case of the residual eddies observed in Ahuriri Estuary, the cause of the transfer of vorticity is velocity shear. Residual eddies are observed on either side of the ebb tidal jet and in the lower estuary. The velocity shear induces vorticity, creating a rotational flow moving away from the ebb tidal jet. The velocity shear also decreases velocity, which ultimately results in the settling of suspended sediments.

The residual eddy in the lower estuary is due to the geometry of the estuary, where on the outgoing tide the currents had a much higher velocity in the direct vicinity of the exit plume through Pandora Passageway than in the southern area. This causes a shear velocity and sets up a clockwise rotational circulation. It was stated that a major component of sediment reaching the middle estuary is likely to be transported seaward due to the seaward directed and highly channelised residual currents in the middle estuary. The presence of this residual eddy suggests that this may act as a trap for sediments entering the lower estuary, preventing sediments from exiting the system, as tidally induced eddies are often inextricably linked with sediment deposits (Ferentinos & Collins 1979). The currents in the southern lower estuary are low, therefore increasing the likelihood sediments will settle out of suspension at this site. The potential of accretion for this area is confirmed by observed dredging operations during field work and previous dredging operations at the Napier Sailing Club site (Appendix I), which is located in the vicinity of the residual eddy.

3.8 CONCLUSIONS

The MIKE 21 FM predicted the hydrodynamics of Ahuriri Estuary well, despite the difficulty of adequately representing the complex morphology in the model grid. The main findings for the hydrodynamics of Ahuriri Estuary are as follows:

- The hydrodynamic model calibrated well with a maximum error of 0.07 m for water depth, 0.18 $m.s^{-1}$ for current speed and 113.1 degrees for current direction. The large directional error was attributed to noise.
- The residual circulation and tidal asymmetry were well-predicted by the model. These are the main governing physical processes in net sediment transport direction, which is important for the objectives of this thesis.
- High current velocities in the order of 0.6 $m.s^{-1}$ are limited to the channelised areas of the estuary, with negligible currents in the intertidal areas. The low current speeds predicted are unlikely to initiate incipient sediment movement or bring sediments into suspension.
- Suspended sediment on the incoming tide which is flushed into the intertidal domain is likely to settle out in the low-flowing upper intertidal areas during inundation periods.
- The well mixed nature of the estuary and low freshwater inflow limits stratification and baroclinic flow due to density differences. The residual circulation pattern of Ahuriri is forced by barotropic flow. A number of residual eddy formations are highlighted in the residual circulation pattern, caused primarily by velocity shear on the outgoing tide following the constriction of tidal flow through the Pandora Passageway and the tidal inlet.
- The residual eddy in the lower estuary traps sediment in this location. The currents in the southern part of the estuary are negligible and therefore sediment will settle out of suspension, and is unlikely to be subsequently resuspended. Dredging operations in the approximate location of this eddy confirm this.

The MIKE 21 Flow model discussed in this chapter is the basis for the sediment transport model in the following chapter, and therefore must have the ability to accurately simulate the hydrodynamics of the Ahuriri Estuary. Based on model calibration, validation and results it is evident the model is capable of adequately

reproducing the observed hydrodynamics of the estuary and may therefore be applied in the sediment transport investigation.

CHAPTER FOUR
SEDIMENT TRANSPORT MODELLING

4.1 INTRODUCTION

In order to accurately predict sediment transport within the estuary using numerical modelling techniques, a well-calibrated hydrodynamic model is required. The bed shear stresses used in the calculation of sediment transport are derived from the hydrodynamic model presented in Chapter Three.

Hydrodynamic processes are the primary governing factor of sediment transport in estuarine systems, although physical, biological and chemical processes all interact to determine the direction, magnitude and mechanisms of sediment transport in estuaries. As discussed in Chapter Three, tidal forcing was the main hydrodynamic forcing in Ahuriri Estuary, as local wave generation is limited by small fetch distances and the sheltered nature of the estuary due to the presence of the Poraiti hills to the west to south-west. The strongest currents are limited to the channels, with low flow velocities in the upper estuary and intertidal areas. It is these characteristics of the estuary which make it susceptible to adverse effects from a large sedimentation event. Although residual currents show ebb-tidal dominance suggesting net sediment transport will be seaward (refer Chapter 3, Section 3.6.3), the phase of the tide at time of release of the sediment, the extent of freshwater flow and the grain-size are likely to affect whether the sediments are exported by the highly channelised flow or retained in the estuary.

In this chapter the topics of sedimentation in estuaries and the numerical modelling of sediment dynamics are discussed. The initialisation of the MIKE 21 Mud Transport model is described, including a sensitivity analysis of the governing model parameters. Scenarios of different magnitudes of rainfall events and subsequent sediment injection into the estuary, timing of the spring-neap cycle, timing of the tidal cycle and grain-sizes are then used to characterise the sediment dynamics of the estuary.

4.2 SEDIMENT TRANSPORT AND NUMERICAL MODELLING BACKGROUND

4.2.1 Sediment transport background

Sediment transport is a function of the shear stress at the bed, τ_0, which is proportional to the flow speed. In this study, where the local generation of waves is largely prohibited by limited fetch, τ_0 is proportional to current speed, and is given by Equation 4.1.

$$\tau_0 = \rho C_D \overline{U}^2 \qquad \text{(Equation 4.1)}$$

Where $\overline{U}$ is the depth-averaged velocity (m.s^{-1}), ρ is the sediment density (kg.m^{-3}) and C_D is the drag coefficient. In natural environments, however, the drag coefficient is highly variable and therefore difficult to approximate (Green & McCave 1995).

The movement of sediment and the mode by which sediment will be transported (i.e. as bedload or suspended load) is a function of shear stress, grain-size and density. The critical Shields parameter, τ_c, can be used to determine whether sediment will move and the mode by which it will be transported (Nielsen 1992). It is defined under steady flow by Equation 4.2.

$$\theta_c = \frac{\tau_c}{(\rho_s - \rho) g D} \qquad \text{(Equation 4.2)}$$

Where τ_c is the critical shear stress for erosion of sediment from the bed, ρ_s is the density of the sediment (kg.m^{-3}), ρ is the density of seawater (kg.m^{-3}), g is gravitational acceleration (m.s^{-2}) and D is the median grain-size (m).

Dean and Dalrymple (2002) suggest that sediment will move when the critical shields parameter is greater than 0.03, dependent slightly on the Reynolds number, which is a function of the bed roughness and consequently flow turbulence. If the value is greater than 0.1, bedload transport is likely to occur and

a variety of different bedforms may result, depending on the sediment composition and size and the current velocity.

Whether sediment will be transported as suspended load is also highly dependent on the sediment settling velocity, ω_s. The settling velocity of sediment less than 0.1mm is commonly calculated using the Stokes calculation given by Equation 4.3.

$$\omega_s = \frac{gD^2(\rho_s - \rho)}{18\mu} \qquad \text{(Equation 4.3)}$$

Where g is gravitational acceleration (m.s^{-2}), D is the median grain-size (m), ρ_s is the density of the sediment (kg.m^{-3}), ρ is the density of seawater (kg.m^{-3}) and μ is the viscosity of the medium. If the shear velocity is less than the particle settling velocity, sediment will not be transported in suspension. If the shear velocity is greater than the settling speed, suspended sediment transport will occur (Reeve et al. 2004).

The settling velocity is difficult to calculate for fine estuarine sediments due to their cohesive nature once clay content exceeds 5 – 10 % of sediment composition (Bearman 1989). The fine clay particles flocculate upon the convergence of fresh and saline water, increasing the particle settling velocity to a point of maximum floc size, which is limited by fluid shear (Dyer 1988). The result is a settling velocity which exceeds that of the constituent grains (Kranck 1984), ultimately resulting in greater deposition. Once cohesive sediment has settled, the critical shear stress for erosion increases with time as the deposit consolidates (Winterwerp 2007). The rate of erosion of fine sediments is largely due to bulk density, which increases with time allowed for consolidation (Lick et al. 2007). A greater shear stress is required to erode material from the bed for cohesive sediments than cohesionless sediments, and erosion tends to occur in flocs.

Flocculation and deflocculation processes also contribute to the turbidity maximum, a zone of deposition and high suspended sediment concentration (SSC) in estuaries with a heterogeneous salinity profile. Suspended sediment in the upper water column which is transported in the seaward direction sinks to the lower water column, and is directed landward due to the residual landward current

direction of high density seawater. Due to this process, the turbidity maximum is located near the head of the salt intrusion (Dyer 1988). This high turbidity zone varies both spatially and temporally, due to freshwater and sediment influx and tidal range. Increased flocculation occurs when sediment is mixed with saline water, resulting in increased settling velocity and consequently higher deposition rates. Deflocculation may occur upon mixing into the surface layers and with increased influx of freshwater (Dyer 1988).

4.2.2 Numerical modelling background

There are many processes in the numerical modelling of sediment transport which are difficult to parameterise. The accurate parameterisation of settling velocity is important as it governs sediment deposition (Manning & Dyer 2007). It is often parameterised by a single value, however is often highly variable spatially and temporally due to flocculation processes (Winterwerp et al. 2002). Cohesive sediment modelling must allow for the processes of flocculation and deflocculation and therefore must include salinity. These processes are included in numerical models with the settling velocity, which may be used as a calibration parameter (Cheviet et al. 2002; Violeau et al. 2002).

The main calibration parameters for the numerical modelling of mud transport are the critical erosion stress for erosion and deposition. These parameters determine whether erosion or deposition will occur given the calculated bed shear stresses from the hydrodynamic model. Model initialisation should allow for the spatial heterogeneity in erosional and depositional characteristics, which are primarily due to grain-size and cohesiveness (Lumborg & Windelin 2003; Hu et al. 2009). A high resolution dataset of sediment characteristics is desirable for the accurate initialisation and calibration of the model. However, this is often unavailable due to cost constraints. Additionally, vertical heterogeneity exists with depth into the sediment profile, therefore the specification of layers with differing properties such as bulk density allows for an accurate simulation of the morphological evolution of the bed.

4.3 METHODS

4.3.1 MIKE 21 Mud Transport (MT) model

The MIKE 21 Mud Transport (MT) module calculates sediment transport based upon the advection-dispersion equation, which is vertically integrated in the MIKE 21 two-dimensional model (Lumborg & Windelin 2003), given by Equation 4.4.

$$\frac{\overline{\partial c}}{\partial t} + V_x \frac{\partial c}{dx} + V_y \frac{\overline{\partial c}}{\partial y} = \frac{1}{h}\frac{\partial}{\partial x}\left(h\, D_x\, \frac{\overline{\partial c}}{\partial x}\right) + \frac{1}{h}\frac{\partial}{\partial y}\left(h\, D_y\, \frac{\overline{\partial c}}{\partial y}\right) + \sum_{i=1}^{n} \frac{S_i}{h}$$

(Equation 4.4)

Where c is the depth-averaged concentration (g.m^{-3}), V_x and V_y are depth-averaged flow velocities derived from the MIKE 21 FM (m.s^{-1}), D_x and D_y are the dispersion coefficients (m^2.s^{-1}), h is depth (m) and S_i is the source and sink term (g.m^2.s^{-1}). This source and sink term parameterises the deposition and erosion of sediment in the advection-dispersion equation. Sediment transport, erosion and deposition are dependent on the bed shear stress, calculated from current data from the underlying hydrodynamic module. Whether sediment is eroded or deposited depends on the relationship between the critical shear stress for erosion, τ_{ce}, the critical shear stress for deposition, τ_{cd}, and the bed shear stress, τ_b. These values are parameterised in the model and are used as calibration parameters. Bed shear stress, τ_b, is calculated using Equation 4.5.

$$\tau_b = 0.5\rho_w f_c V^2 \qquad \text{(Equation 4.5)}$$

Where τ_b is the bottom shear stress, ρ_w is the density of seawater (kg.m^{-3}), f_c is the current friction factor, and V is the current velocity (m.s^{-1}). The current friction factor and the current velocities are derived from the MIKE 21 FM.

Erosion in the MIKE 21 MT model is calculated by Equation 4.6, as first described by Parchure and Mehta (1985), and detailed in Lumborg and Windelin (2003).

$$S_E = E_e^{\left(\propto \sqrt{\tau_b - \tau_{ce}}\right)} \qquad \text{(Equation 4.6)}$$

Where S_E is the erosion rate ($g.m^{-2}$), E is erodibility of the bed ($g.m^{-2}.s^{-1}$), τ_{ce} is the critical shear stress for erosion ($N.m^{-2}$) and α is the erosion coefficient ($m.N^{-0.5}$).

Deposition is calculated in the MIKE 21 MT model using the formula originally proposed by Krone (1962) and is given by Equation 4.7.

$$S_D = W_s C_b P_d \qquad \text{(Equation 4.7)}$$

Where S_D is the deposition rate ($g.m^{-2}$), ω_s is the settling velocity, parameterised in the model by the Stokes model (Equation 4.3), C_b is the near bottom concentration ($g.m^{-3}$) and P_d is the probability of deposition, which is dependent on τ_b and τ_{cd} (Lumborg & Windelin 2003).

Many of the parameters discussed above have a user-specified parameter which enables the calibration of the model to individual sites. The critical shear stresses for erosion and deposition, the erosion coefficient, settling velocity are all parameterised in the model and can be used as calibration parameters. In this study the model is not calibrated, but these parameters are adjusted to provide results within realistic ranges.

4.3.2 Initialisation of the MIKE 21 MT model for Ahuriri Estuary

In order to accurately simulate the sediment dynamics of Ahuriri Estuary, the MIKE 21 MT model is initialised using a compilation of parameters from other studies. The critical shear stress for erosion is investigated in an erosion coefficient sensitivity analysis. Some of the other initial parameters are given in Table 4.1.

Table 4.1. MIKE 21 MT model initial conditions.

Parameter	Initial Conditions
Initial concentration	0 $mg.l^{-1}$
Initial bed thickness	0 metres
Dispersion coefficient	1 $m^2.s^{-1}$
Boundary concentration	0 $mg.l^{-1}$
Source concentration	100 $mg.l^{-1}$
Erosion description	Soft mud
Erosion coefficient factor	6.5
Erosion coefficient	0.00005 $kg.m^2.s^{-1}$
Density of the bed	150 - 2000 $kg.m^{-2}$

Sediment erosion, deposition and transport are dependent on bed shear stress, which is calculated from the tidal currents extracted from the underlying hydrodynamic model. Whether sediment is eroded or deposited under the predicted hydrodynamic regime is governed by the critical shear stress for erosion, τ_{ce}, and deposition, τ_{cd}. The calculation of the critical shear stress for erosion is difficult to calculate mathematically (McCave 1984). Therefore, the model was initialised with parameters derived primarily from the literature (Table 4.2). These findings were then used as a guideline for a sensitivity analysis of τ_{ce}.

Table 4.2. MIKE 21 MT model parameters used in previous studies. Note τ_{cd} and τ_{ce} are dependent on the grain-size used in the study, and are therefore given as a range for each study.

Critical shear stress for deposition, τ_{cd} ($N.m^{-2}$)	**Critical shear stress for erosion, τ_{ce} ($N.m^{-2}$)**	**Erosion coefficient, α ($m.N^{-0.5}$)**	**Source**
0.05 – 0.3	0.19 – 0.8	6.5	Lumborg & Pejrup 2005
0.002 – 1.0	0.1 – 0.7	10-20	Lumborg & Windelin 2003
0.18 – 1.1	---	---	Mehta & Partheniades 1975
0.05	1.04	---	de Villiers & Basson 2007
0.02 – 0.8	0.02 – 0.8	---	Hu et al. 2009
---	---	10-20	van Rijn 1989
---	0.04-0.62	4.2-25.6	Parchure & Mehta 1985
$0.21 < \tau_{cd} < 0.37$	---	---	Haralampides et al. 2003

The critical shear stresses for erosion and deposition and the settling velocity are dependent on the grain-size used in the simulation. Three grain-sizes, 10, 60 and 105 μm were chosen for the simulations in Ahuriri Estuary based upon modal peaks observed in the grain-size distributions (See Appendix VI) and to cover a range of simulation conditions. These grain-sizes correspond to fine silt, coarse silt and fine sand, respectively. Grain-size dependent model input variables are shown in Table 4.3.

Table 4.3. Grain-size dependent MIKE 21 MT model input variables.

Grain-size (μm)	**W_s ($m.s^{-1}$)**	**τ_{ce} ($N.m^{-2}$)**	**τ_{cd} ($N.m^{-2}$)**
10	0.000009	0.35	0.05
60	0.00032	0.3	0.21
105	0.001	0.5	0.1

Sediment was injected into the estuary at the junction where the Taipo Stream meets the estuary with a source concentration of 100 $mg.l^{-1}$. This concentration was used to simulate storm "flushing" of the stream bed in a conservative approach to sediment generation from the catchment.

Settling velocity was calculated for each of the constituent grain-sizes as a constant velocity according to the Stokes model (Equation 4.3). Flocculation is not included in this study due to the difficulty in simulating salinity based upon the synthetic hydrograph input data.

Morphological calculations were not of interest in this preliminary study, therefore were not included in the simulation. The bed level was set to zero to allow for the tracking of sediment input from the source. The transport and ultimate fate of the sediments injected into the estuary at a point source was of primary interest. In order to understand the dynamics of this injected sediment, instantaneous concentration flux ($kg.s^{-1}$) and cumulative mass (kg) were recorded at locations A, B and C, which span across the entire estuary width (Figure 4.1).

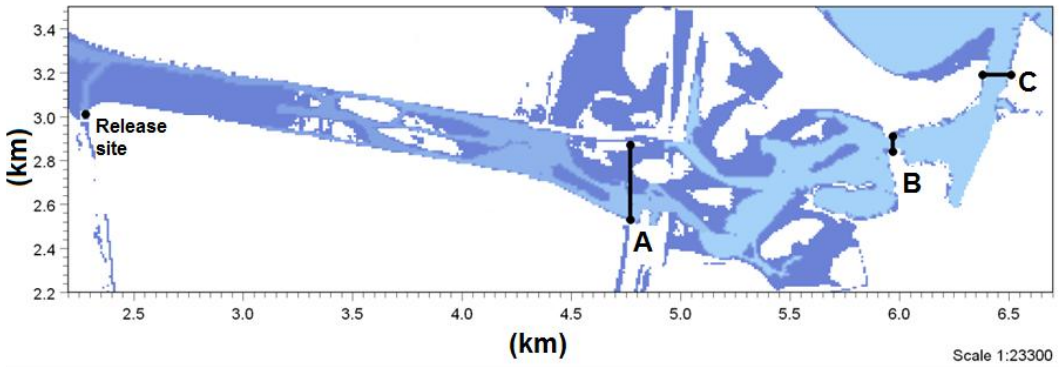

Figure 4.1. Lines A, B and C indicate recording sites for instantaneous and cumulative sediment flow. Lines also delineate the upper, middle and lower estuaries. The sediment release site is located at the junction where the Taipo Stream discharges into the upper estuary.

The lines delineate the boundaries between the upper, middle and lower estuaries. Line A records the flux of sediment from the upper to the middle estuary, line B records the flux from the middle estuary to the lower estuary, and line C records the flux from the lower estuary to the coast.

4.3.3 Design hydrograph for freshwater input

In order to simulate scenarios of storm discharge and subsequent sediment injection into the estuary, stream flow is required at a high resolution timescale. Such factors as the timing of the peak discharge in the timing of the tide are of interest. Therefore a storm hydrograph is required rather than just a singular value for flow rate. The Taipo Stream is the only freshwater discharge into the estuary of significance, arising in hill country to the south-west of the estuary. The stream flows through urbanised and rural areas of the catchment, with a low gradient slope and subsequently low flow. There is an observed difference in flow from rural to urbanised sub-catchments with very low flow in parts of the stream (Figure 4.2) (Cooke 2006). During calm weather conditions (not raining) the discharge is very low with flows recorded as low as 4 $l.s^{-1}$. A sparse record of individual measurements of discharge for the Taipo Stream was available, however a hydrograph was required for the purposes of freshwater input for this study.

Figure 4.2. Taipo Stream in an urbanised area of the catchment. There is noticeable algal growth and little discernible flow. From Cooke (2006).

As the Taipo Stream drains a primarily ungauged catchment a modelled "design hydrograph" was required for freshwater model input. Storm runoff was estimated from rainfall data using the empirical model outlined in the U.S. Soil Conservation Service handbook (SCS 1972) which has been adapted to specific catchments in the Auckland region (Beca Carter Hollings & Ferner Ltd 1999).

Daily rainfall data measured by the Napier Aero Aws climate station were acquired for the area for a period of one year. The data were available from The National Climate Database (CliFlo 2009). A histogram of rainfall events is shown in Figure 4.3. Table 4.4 lists the probability of occurrence, p, which is determined from the percentage of occurrence of the rainfall band in one year. The recurrence interval, T, for each rainfall band was then calculated using Equation 4.8.

$$T = \frac{1}{p} \times 100 \qquad \text{(Equation 4.8)}$$

Table 4.4. Rainfall bands, probability of rainfall event and the recurrence interval.

Rainfall (mm)	**% of rainfall events**	**Probability, p**	**Recurrence Interval, T (years)**
>10mm	83.8	0.84	1.19
10-20	9.1	0.091	11
20-40	5.2	0.052	19.2
40-60	1.1	0.011	91
60-100	0.7	0.007	143
100+	0.1	0.001	1000

A minimal rainfall event of 10 mm was required to generate any discernible stream flow from catchment runoff using the SCS rainfall-runoff model. Therefore, a minimal rainfall event of 20 mm was chosen, as although catchment runoff and subsequent stream flow were calculated with rainfall events smaller than 20 mm, a sufficient discharge and flow velocity would be required to flush sediment from the stream bed into the estuary. In order to characterise the influence of freshwater discharge on the transport and dispersal of sediment, a range of stream discharges were calculated for model input. Rainfall events of 20, 40, 60 and 100 mm were chosen for the calculation of storm hydrographs for the input of freshwater in the sediment transport model.

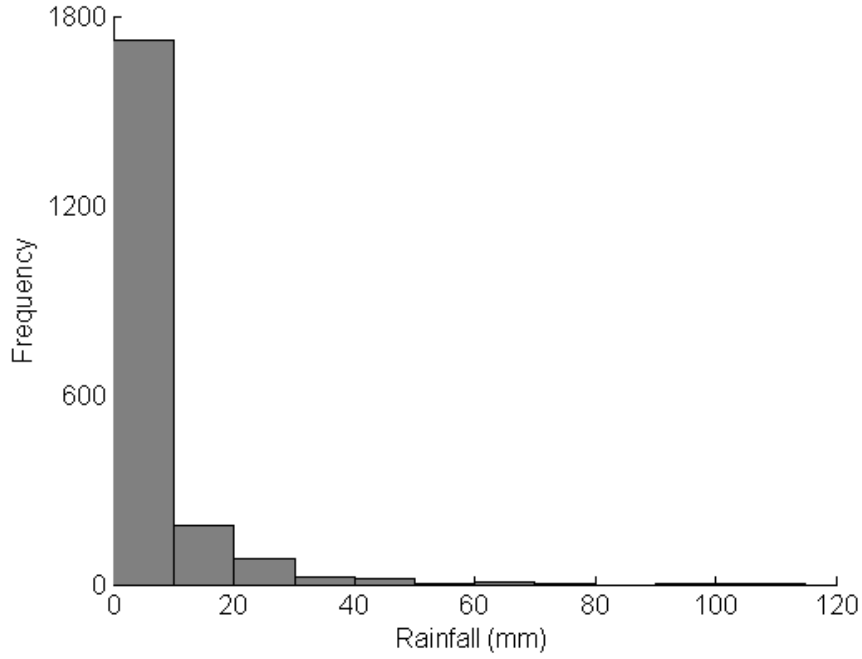

Figure 4.3. Histogram of the frequency of rainfall events (mm) measured at the Napier Aws Aero site downloaded from the NIWA CliFlo database (http://cliflo.niwa.co.nz/). Recurrence intervals were calculated from frequency data.

In order to determine discharge from the catchment after losses to storage and infiltration, catchment properties such as landuse and soil type were evaluated. Figure 4.4 depicts the Taipo Stream catchment and the environments through which the stream flows.

Soil properties were classified according to the New Zealand soil classification (NZSC) scheme (Figure 4.5) and subsequently assigned a SCS hydrologic soil group class according to drainage and storage properties (Table 4.5). The SCS hydrological soil groups as defined in the SCS national engineering handbook (SCS 1972) are;

A. Low runoff potential. Soils have high infiltration rates, even when thoroughly wetted and consist primarily of deep, well to excessively drained sands and gravels. High rate of water transmission.
B. Soils have moderate infiltration rates when thoroughly wetted and consist primarily of moderately deep to deep, moderately coarse textures. Moderate rate of water transmission.
C. Soils have slow infiltration rates when thoroughly wetted and consist primarily of soils with a layer that impedes downward movement of water,

or soils with moderately fine to fine texture. Slow rate of water transmission

D. High runoff potential. Soils have very slow infiltration rates when thoroughly wetted and consist primarily of clay soils with a high swelling potential, soils with a permanent high water table, soils with a claypan or clay layer at or near the surface, and shallow soils over impervious material. The soils have a very slow rate of water transmission.

Table 4.5. Taipo catchment soil classification (NZSC), predominant soil characteristics and the assigned SCS hydrologic soil group class.

Soil Name	**NZSC**	**Characteristics**	**SCS hydrological soil group**
Light sandy loam	PPU	Perch gley pallic soil with duripan	C
Complex	PIT	Immature pallic soil	C
Fine sandy loam	RFT	Fluvial recent soil	B
Stony sandy loam	PIT	Immature pallic soil	C
Sandy loam	PPU	Perch gley pallic soil with duripan	C
Sandy loam	PIT	Immature pallic soil	C
Ahuriri silt loam and clay	WGFU	Raw gley soil	D

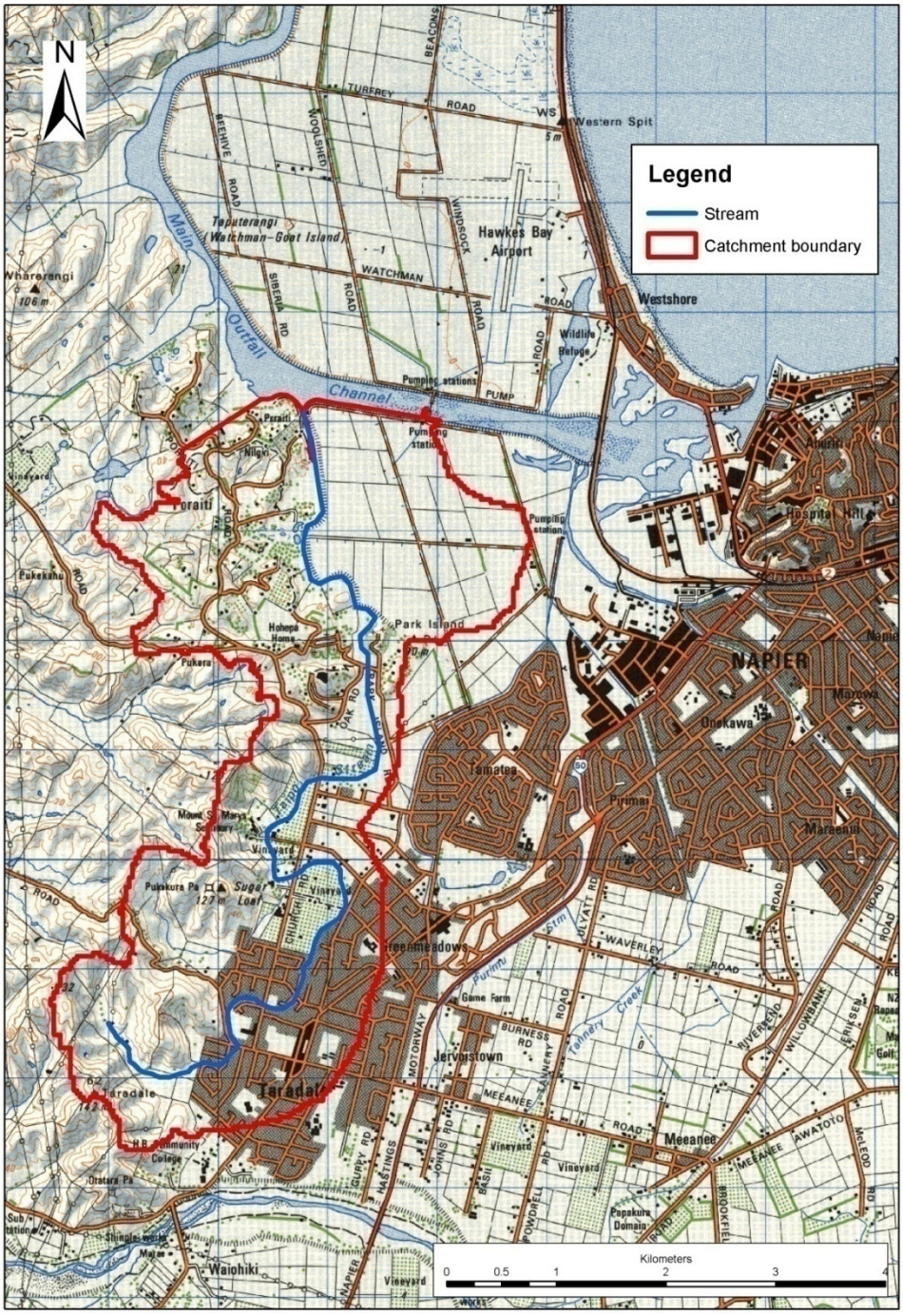

Figure 4.4. Taipo Stream catchment. The Taipo Stream is the only significant freshwater inflow into the estuary. Map created from Land Information NZ 1:50,000 Topographic database using ESRI ArcGIS.

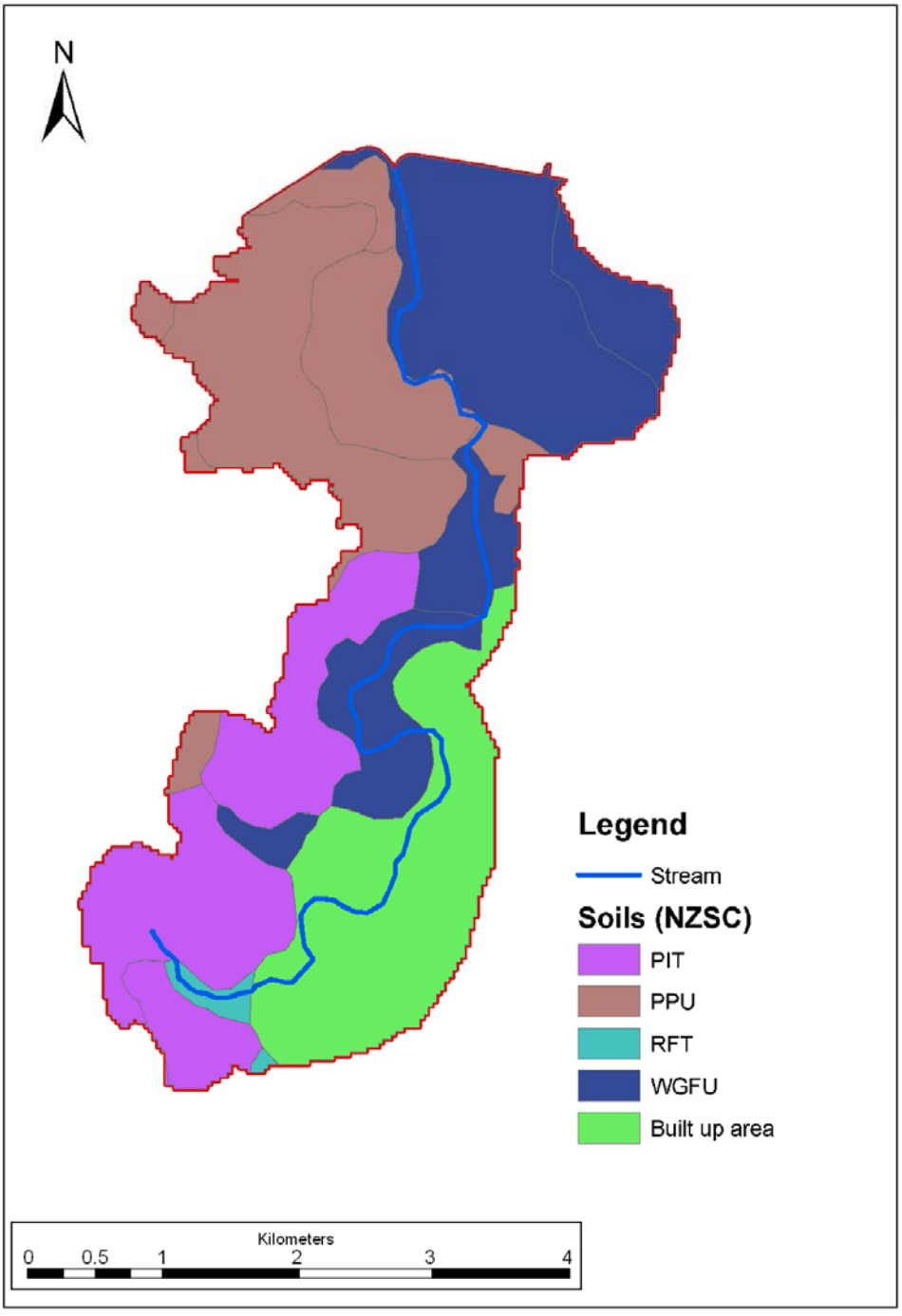

Figure 4.5. Taipo catchment soil classification (New Zealand Soil Classification) and the areal extent of each unit. Data obtained from Newsome et al. (2000).

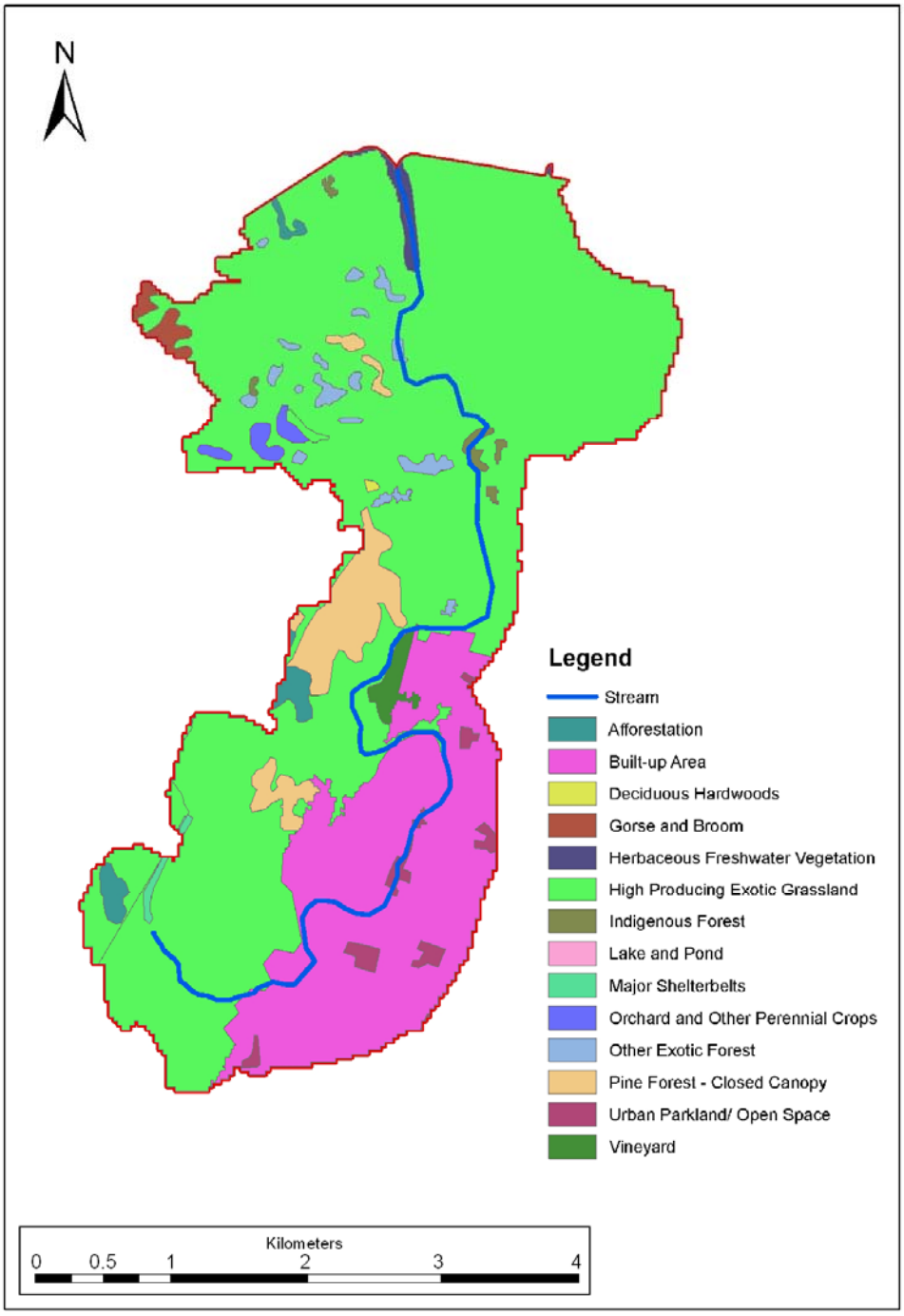

Figure 4.6. Taipo catchment landuse classification and the areal extent of each unit. Data obtained from Newsome et al. (2000).

The areal extent of each of the soil units and landuse classes were calculated. The landuse classification (Figure 4.6) and hydrologic soil group were used to determine a curve number for each unit. The U.S. Soil Conservation Service empirically derived rainfall-runoff curves to define the relationship between the two variables. The curves range from 0 (no runoff) to 100 (total runoff) percent and are based upon the properties of the catchment which define storage and infiltration (SCS 1972). See Appendix II for table of known curve numbers and Table 4.6 for curve numbers assigned to units of the Taipo catchment.

Table 4.6. Landuse and soil characteristics for each sub-unit of the Taipo Stream catchment and the associated curve numbers. Curve numbers are derived from SCS (1972).

Land-use	**Hydrologic Soil Group**	**Curve Number**
Orchard and other perennials	C	66
Vineyard	D	66
Major shelterbelt	C	86
Pine and Forest-closed canopy	C	70
Gorse and broom	C	60
Indigenous forest	C	70
Afforestation	C	77
Urban parkland/Open space	-	74
Built up area	-	86
Other exotic forest	C	70
High producing exotic grassland	B C D	79 86 89

The curve numbers and areal extent for each sub-unit of the catchment were then combined in a weighted curve number for the entire catchment. This weight-averaged curve number represents the soil and landuse properties for the catchment as a whole and was used in the calculation of storage for the catchment. A series of calculations using catchment storage determine the time of

concentration, which is the time taken for the rainfall in the catchment to be concentrated into the Taipo Stream to produce a measurable discharge. The time of concentration is then used in the calculation of the peak discharge flow rate. The values for time of concentration and peak flow rate are applied to a set of given ordinates which predetermine the percentage of flow per unit time to give an idealised synthetic hydrograph (Figure 4.7). See Appendix II for a full record of calculations and synthetic hydrograph ordinates. The synthetic hydrograph calculations were repeated for each of the storm rainfall depths required for model simulation. Hydrographs for each of the storm rainfall events are also given in Appendix II.

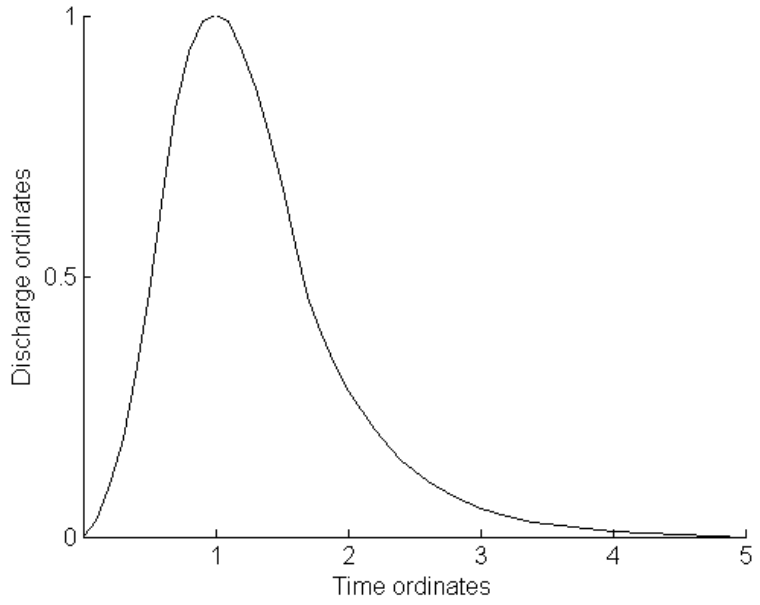

Figure 4.7. Schematic of an idealised design hydrograph. The values of peak discharge and time of concentration are applied to a given set of ordinates (from SCS 1972) which predetermine percentage of flow per unit time to give the idealised hydrograph curve.

4.3.4 Erosion coefficient sensitivity analysis

In order to accurately simulate the sediment dynamics of Ahuriri Estuary, a sensitivity analysis was carried out to ensure the parameterisation of the critical shear stress for erosion will result in realistic findings. As there was insufficient data for a full calibration of the MIKE 21 MT model, the sensitivity analysis provides some assurance that the model results are viable. As the sediment dynamics and patterns of dispersal, accumulation and erosion were of importance,

rather than absolute values of accretion and erosion, this was deemed sufficient for the purposes of this study.

The values used in other studies, summarised in Table 4.2, are applied in the following erosion coefficient sensitivity analysis and are critical in the dependability of model results. This parameter influences the magnitude of sediment transport and erosion in the estuary. The values for critical shear stress for erosion were derived from Table 4.7.

Table 4.7. Values chosen for the parameterisation of the MIKE 21 MT model for this study ($N.m^{-2}$)

Grain-size (μm)	**Critical shear stress for erosion, τ_{ce}**	**Values used in other studies**	**Source**
10	0.35	0.35; 0.02-0.8; 0.1-0.7	Liu et al. 2009; Hu et al. 2009; Lumborg & Windelin 2009
60	0.3	0.3; 0.35	Lumborg 2005; Liu et al. 2009
105	0.5	0.5	Lumborg 2005

A series of models were run under neap tide conditions. Under these conditions, it is expected that the fine fraction will be resuspended by tidal currents in small concentrations, as demonstrated in field observations with no waves evident at time of measurement (e.g. Green & Coco 2007). The models included a source input of sediment suspended in freshwater discharge from the Taipo Stream. Stream flow was constant for the duration of the model at a rate of 5 $m^{-3}.s^{-1}$ with a suspended sediment concentration of 0.025 $kg.m^{-3}$. An initial bed thickness of 0.1 metres was included to allow for sediment resuspension from the bed by tidal currents. A series of models with different values for critical erosion stress were run for three grain-sizes, 10, 60 and 105 μm, which correspond to fine silt, coarse silt and fine sand, respectively. A low value for τ_{ce} will result in sediment resuspension from the bed occurring at lower current velocities. The models were initialised with existing sediment on the bed to allow for the examination of resuspension of each of the simulated grain-sizes.

Suspended sediment concentrations (SSC) were extracted at four sites within the estuary (Figure 4.8), located in the channel in areas of differing energy environments in an attempt to provide a wide overview of processes within the estuary.

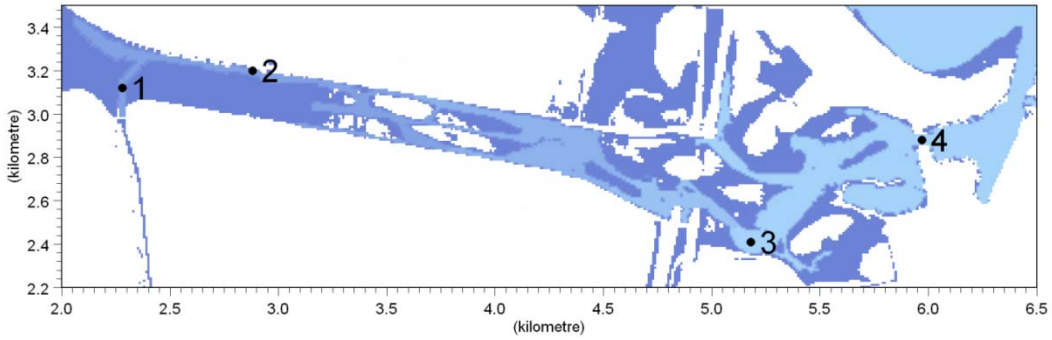

Figure 4.8. Sites of data extraction of SSC for the tuning of the critical shear stress for erosion. Sediment source is from the Taipo Stream, located directly south of site 1.

4.3.5 Timescale for model runs

An analysis was undertaken of preliminary model runs to determine the timescale needed to characterise processes which govern the sediment export from the estuary or deposition within the system. Models were run for a period of approximately 4.5 days with a moderate discharge. A mean grain-size of 60 μm was used, in order to simulate "average" conditions. A storm hydrograph was calculated for discharge following a 40 mm rainfall event, and was released into the estuary at the junction where the Taipo Stream joins the estuary with a sediment concentration of 0.025 $kg.m^{-3}$. This sediment concentration was chosen as it represents an average concentration of sediment influx with an average storm rainfall-runoff event. Simulations were carried out under mean tidal conditions. Following analysis of mean tidal conditions, a further analysis under spring tidal conditions was undertaken to determine whether the tidal regime had an important effect on the timescale of export of sediment from the estuary.

4.3.6 Timing in the tidal cycle of sediment release

The timing in the tidal cycle of sediment release and the subsequent dispersal, deposition and export of the sediment was investigated. A mean grain-size of 60 μm was used with a corresponding Stokes settling velocity of 0.00032 $m.s^{-1}$ and mean-tide simulation conditions were used. A storm event with a storm rainfall magnitude of 40 mm was used to calculate storm hydrograph data. The storm hydrograph simulated a source of freshwater discharge into the estuary with a SSC of 100 $mg.l^{-1}$.

Twelve scenarios were modelled with peak sediment release coinciding with low water slack and every subsequent hour to encompass one entire tidal cycle. The peak discharge of the hydrograph occurs approximately 1.8 hours after discharge commences following a storm event. Each model scenario was run for 36 hours following model the commencement of the storm hydrograph discharge.

In order to define sediment retention and export, the percentage of total sediment crossing lines A, B and C (see Figure 4.1 for locations) were calculated.

4.3.7 Sediment transport and deposition modelling

In order to determine the dominant sediment transport pathways in Ahuriri Estuary and the main areas of potential accretion, a series of simulations encompassing a wide range of conditions (Table 4.8) were evaluated. A total of 96 model scenarios were modelled.

Table 4.8. Sediment transport and deposition model simulation conditions.

Rainfall event (mm)	Tide	Grain-size (μm)	Timing of sediment release
20	Spring	10	High water
40	Neap	60	Low water
60		105	Mid-ebb
100			Mid-flood

For these sediment transport and deposition scenarios, the initial and boundary sediment concentrations were set to zero. This allowed for the calculation of the percentage of total sediment influx which was discharged from the estuary or settled in distinct sub-estuaries. The initial thickness of the bed was set to zero and the density of the bed was set at an artificially high value to prevent erosion. This enabled the calculation of the deposition of the sediment which was injected into the estuary by the Taipo Stream in the upper estuary only. Sediment fluxes across discharge lines A, B and C (locations given in Figure 4.1) were recorded for each model run for comparison of the percentage of sediment influx being transported through the estuary. Sediment was released with the peak in the discharge hydrograph coinciding with the timing of the tide in Table 4.7. The sediment fluxes and model results are interpreted and used in the characterisation of sediment transport pathways within the estuary.

In order to identify areas of potential accretion, the estuary was divided up into 8 sub-estuaries (Figure 4.9), and the volume of sediment deposited in each sub-estuary was calculated from the total bed mass change ($kg.m^{-3}$).

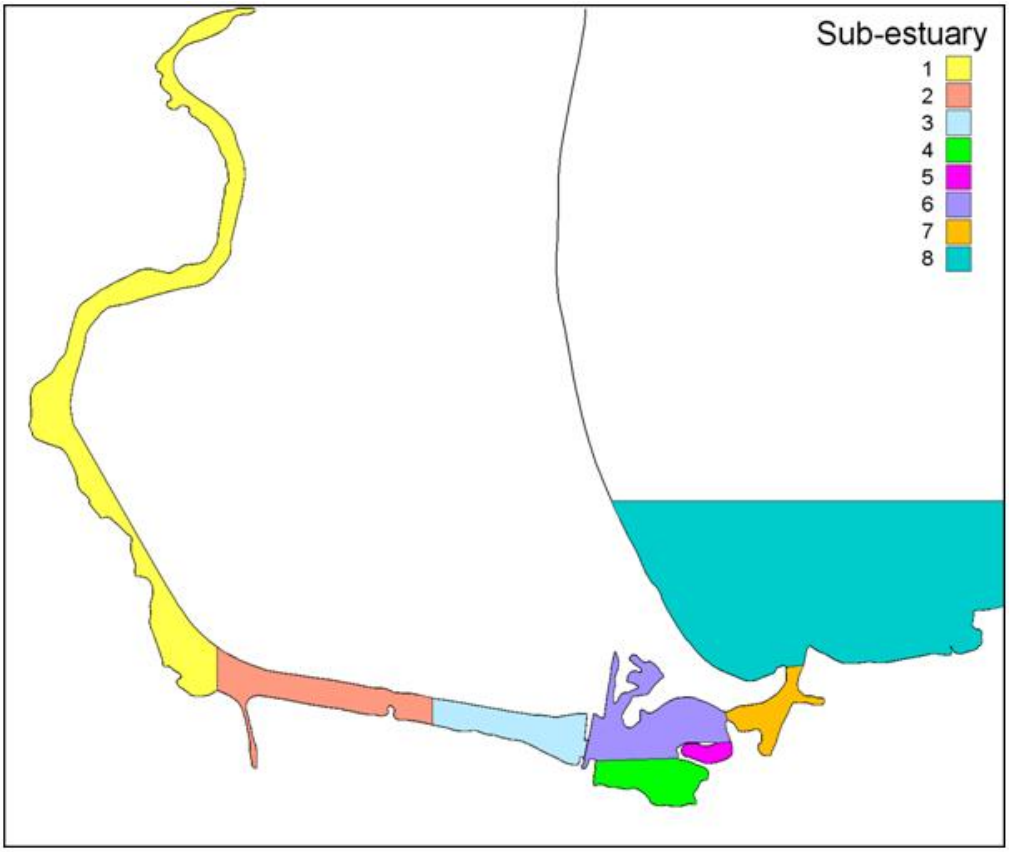

Figure 4.9. Locations of sub-estuaries within Ahuriri Estuary used in the evaluation of sediment deposition and areas of potential accretion.

The total bed mass change was extracted for the entire model grid at the conclusion of the model simulation. In order to evaluate the amount of sediment in each sub-estuary the bed mass change given for each grid cell was multiplied by 100, as there were 100 m^2 in each 10 m x 10 m grid cell. The total sediment mass deposition (kg) was then calculated for each sub-estuary.

4.3.8 Erosion scenario modelling

A series of models were run to characterise the erosion patterns for different grain-sizes within Ahuriri Estuary. For each grain-size, a spring and neap tide simulation was carried out to determine areas of potential erosion and the fate of the eroded sediment within the estuary. The models were initialised with existing bed sediment which had not been acted upon by tidal currents. Vertical heterogeneity in sediment density exists with depth into the bed. Therefore, the specification of layers with differing bulk density allows for an accurate

simulation of the morphological evolution of the bed. This is included in the modelling of erosion. Emphasis is placed on patterns of erosion and accretion, rather than actual values of bed volume changes, as the characteristics of the underlying bed layers were approximated based upon the sensitivity analysis for the critical shear stress for erosion. There was no input of freshwater or sediment in these simulations. This was to allow for the identification of areas of potential erosion, the redistribution of existing bed sediment and to determine whether the eroded sediment is deposited within the estuary. Each simulation was for a period greater than 4 days to allow the bed sediment to reach equilibrium.

4.4 RESULTS

4.4.1 Erosion coefficient sensitivity analysis

4.4.1.1 Fine silt (10 µm)

An ambient SSC of 0.025 kg.m^{-3} was evident at sites 1 (Figure 4.10 B) and 2 (Figure 4.10 C) as they were close to the site of the source. At site 1, a τ_{ce} greater than 0.1 did not induce sediment resuspension and only the ambient source concentration was present. Very low current speeds at this site resulted in very little sediment resuspension.

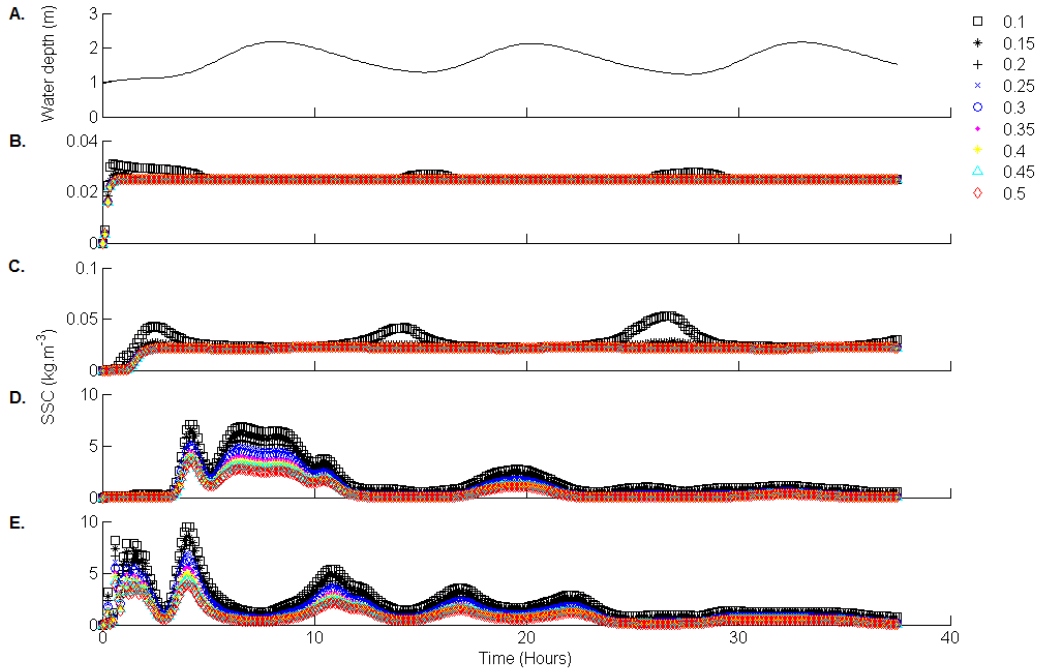

Figure 4.10. Suspended sediment concentrations at the erosion-tuning data extraction sites for a grain-size of 10 µm. **A.** Water depth at site 1 is given as an indicator of the tide. SSC are given for **B.** Site 1 **C.** Site 2 **D.** Site 3 and **E.** Site 4. Legend indicates the value of critical erosion stress, $\tau_{ce.}$, used in model simulation.

At site 2 (Figure 4.10 C) a greater concentration was evident for a τ_{ce} value of 0.1 than other values of τ_{ce}, indicating erosion from the bed upstream at site 1. Under peak outgoing tidal currents however, there was a greater concentration at site 2 than site 1 for τ_{ce} values of 0.1 and 0.15, indicating in-situ resuspension from the bed. The peaks in SSC also arrived earlier in the outgoing tide at site 2 than at site 1, confirming that this sediment was not advected from further upstream. High concentrations of suspended sediment were evident at sites 3 (Figure 4.10 D) and 4 (Figure 4.10 E). This sediment was not locally suspended but was advected to

the site of measurement by tidal currents from the tidal inlet and Pandora Passageway. Sediment was scoured at these sites due to the high current velocities through these constricted pathways. There were also peaks evident at site 3 for the lower values of τ_{ce} during mid-tide currents. These peaks were attributed to high current velocities in the narrow tidal channel landward of the Highway Bridge on the outgoing tide, which induced resuspension from the bed and advected the sediment to site 3.

4.4.1.2 Coarse silt (60 µm)

Simulations for a grain-size of 60 µm did not show an ambient concentration analogous to that of the source concentration, other than at site 1 (Figure 4.11 B). For τ_{ce} values of 0.02 and 0.05, suspended sediment was continually detected at all sites.

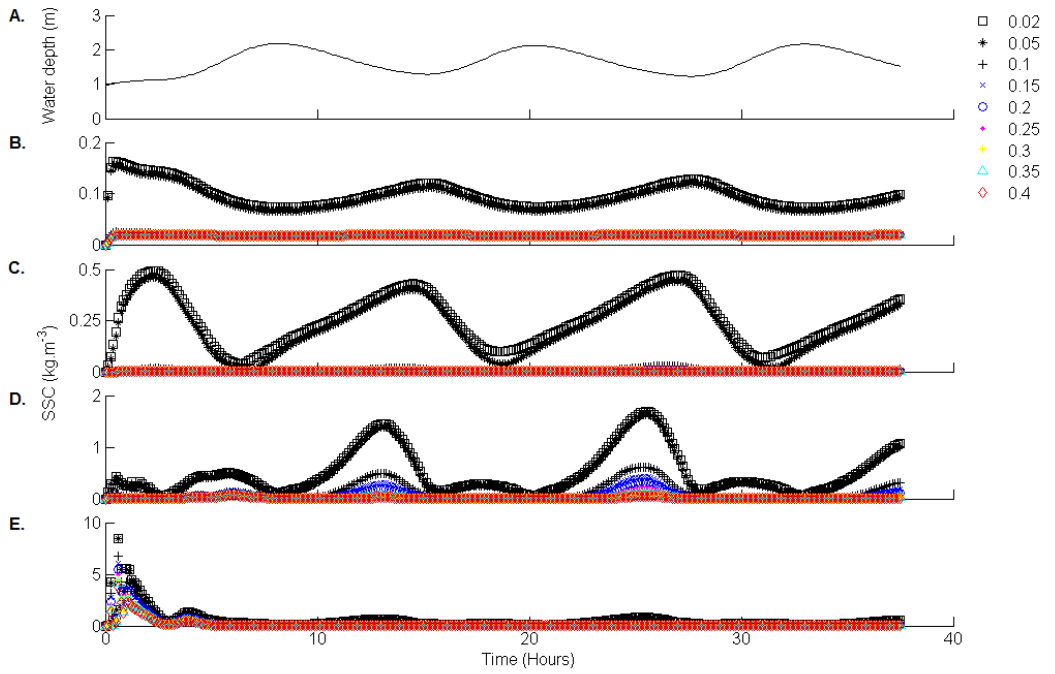

Figure 4.11. Suspended sediment concentrations at the erosion-tuning data extraction sites for a grain-size of 60 µm. **A.** Water depth at site 1 is given as an indicator of the tide. SSC are given for **B.** Site 1 **C.** Site 2 **D.** Site 3 and **E.** Site 4. Legend indicates the value of critical erosion stress, $\tau_{ce.}$, used in model simulation.

At site 1 (Figure 4.11 B), a τ_{ce} of 0.02 and 0.05 had sediment concentrations constantly greater than that of the ambient source concentration. This is due to the freshwater discharge scouring sediment from the bed and the advection of the sediment past site 1. At site 2 (Figure 4.11 C), a τ_{ce} of 0.02 and 0.05 show much greater SSC than other values. Close inspection reveals that under peak tidal currents there was increased SSC for all τ_{ce} values at site 3 (Figure 4.11 D). The sediment measured at site 3 on the outgoing tide is resuspended from the bed in the narrow tidal channels in the upper estuary just landward of the Highway Bridge and advected to the site. Here peak tidal current velocities are high as a result of the narrow tidal channels. Therefore, there is a much greater concentration of sediment measured at site 3 on the outgoing tide than on the incoming tide. At site 4 (Figure 4.11 E) there is a high SSC measured for all values of τ_{ce}, which is attributable to the scour of sediment through the Pandora Passageway.

4.4.1.3 Fine sand (105 µm)

Figure 4.12 indicates that fine sand was resuspended in very small concentrations under peak current velocities only. Sediment concentrations at site 1 (Figure 4.12 B) were lower than the source concentration, suggesting sediment settled out of suspension in close proximity to the source. SSC did not change with varying τ_{ce}, suggesting that the SSC measured at these sites was not a result of erosion, either local or advected, but rather an ambient concentration which was advected to the site from the source by tidal currents. The higher concentration on the outgoing tide was likely a result of tidal currents carrying sediment from the source which is located at the far reaches of tidal flow penetration.

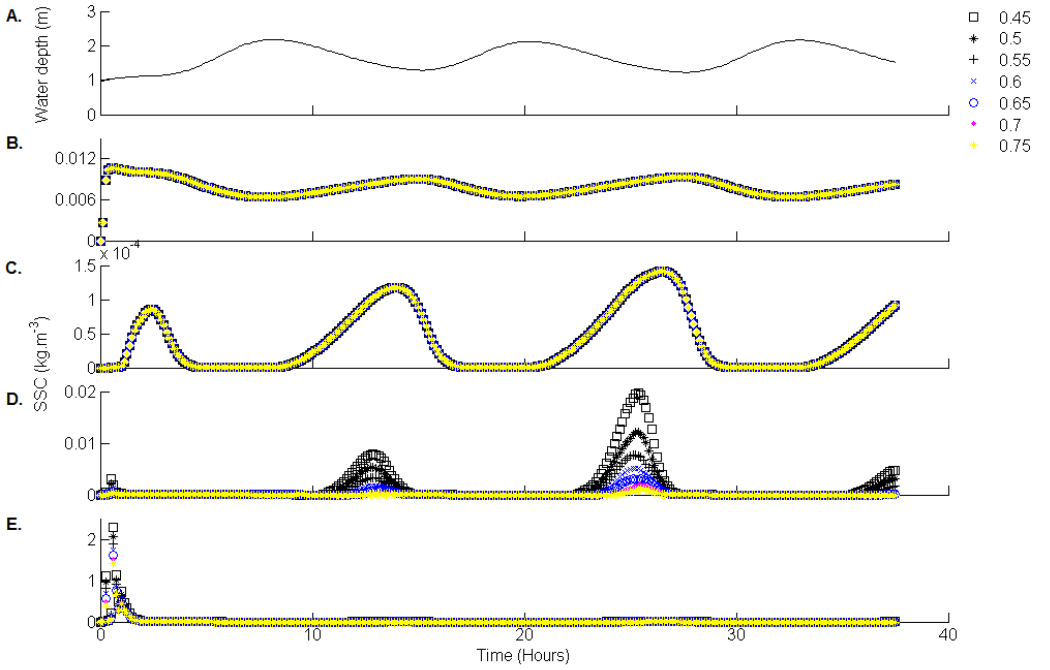

Figure 4.12. Suspended sediment concentrations at the erosion-tuning data extraction sites for a grain-size of 105 µm. **A.** Water depth at site 1 is given as an indicator of the tide. SSC are given for **B.** Site 1 **C.** Site 2 **D.** Site 3 and **E.** Site 4. Legend indicates the value of critical erosion stress, $\tau_{ce.}$, used in model simulation.

There was evidence of sediment resuspension by the tidal currents at site 3 (Figure 4.12 D) only. Tidal flow was constricted in the narrow channel landward of the Highway Bridge and peak velocities on the outgoing tide entrained sediment from the bed into suspension. The sediment was advected through the main channel, where it is detected at site 3. All values of τ_{ce} show a measurement of SSC on the outgoing tide at this site, with no discernible value of SSC at other times in the tide. This indicates that the SSC can be attributed to resuspension. At site 4 (Figure 4.12 E), evidence of scour through the tidal inlet and the Pandora Passageway was clear from sediment concentrations. The sediment is advected to site 4 with all values of τ_{ce} indicating erosion. At all other times in the tide, concentrations were zero, suggesting an initial scour of the existing bed sediment, and advection away from the site.

4.4.2 Timescale for model runs

Figure 4.13 illustrates the cumulative sediment flux across the estuary mouth. For mean tide conditions a large proportion of the sediment input is retained in the

estuary. After the initial flux of sediment from the estuary mouth 24 hours after sediment release, the percentage of sediment exported from the estuary remains relatively constant. The simulation was carried out under high tide release and low tide release to ensure the chosen timescale for subsequent model runs will encompass processes under the different scenarios modelled. As Figure 4.13 illustrates, under spring and mean tide conditions, and low and high tide release, sediment transport across the estuary entrance stabilises at approximately 30 hours after release. A greater flux of sediment into the lower estuary from release at high tide results in sufficient sediment to be transported across the estuary mouth with each subsequent tidal cycle. Sediment released at high tide during mean-tide conditions has a slight flux of sediment back into the estuary, which decreases with each tidal cycle. This is likely due to a loss of sediment from the model domain. A timescale for all subsequent model runs of 36 hours was chosen to ensure sediment dynamics has stabilised at the conclusion of the model run, illustrated by the red line in Figure 4.13.

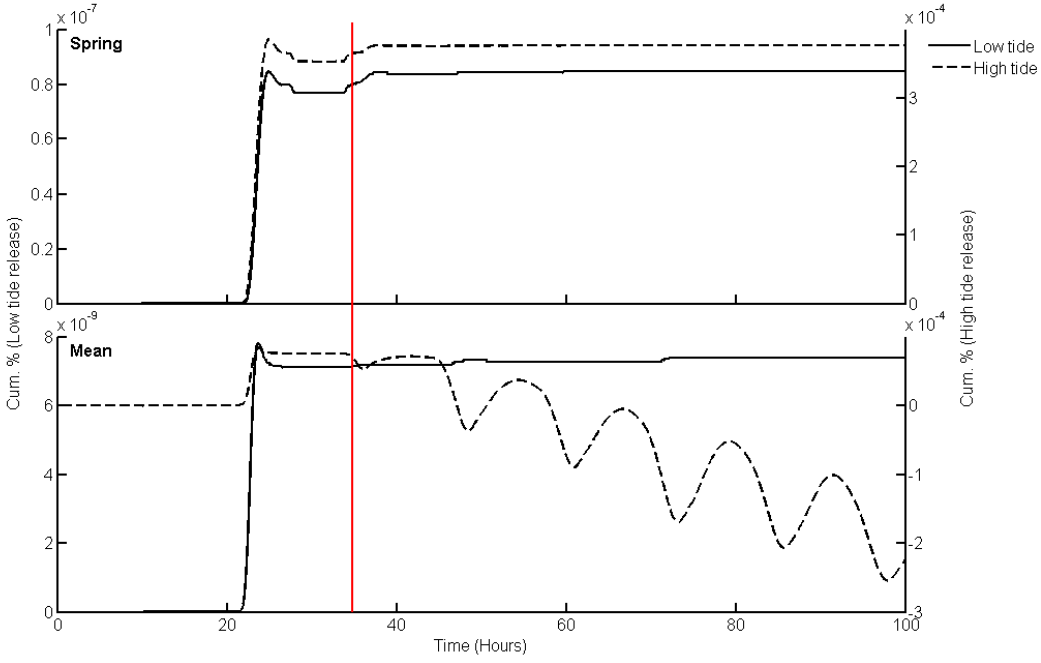

Figure 4.13. Cumulative percentage of total sediment input to exit the mouth of the estuary under mean tide and spring tide conditions. Solid line represents sediment release at low tide (Left-hand y-axis) and dashed line represents sediment release at high tide (Right-hand y-axis). Red line indicates the cut-off point in time after which relatively little sediment is exported from the estuary.

4.4.3 Timing in the tidal cycle of sediment release

Timing of sediment release in the tidal cycle was defined by the timing in the tide at the offshore boundary where the model is forced with modelled tide data. There was a considerable lag in the reversal of the tide between the tidal inlet and in the upper estuary where the sediment source site is located, in the order of 3 hours. This time lag must be considered when interpreting the results of the timing of sediment release in the tidal cycle.

Sediment released at high water resulted in greater sediment discharge from each sub-estuary than sediment release at low water (Figure 4.14). This is expected, as sediment released at high-water slack is likely to be transported downstream with the outgoing tide. However, there were lower volumes of downstream transport of sediment at high-water slack than during the outgoing tide. This is attributable to the lag in the tide in the upper estuary. At the time of sediment release, landward currents are evident at the mouth of the Taipo Stream due to the lag. A proportion of the sediment released is transported upstream prior to tide reversal.

Sediment release at low-water slack is likely to settle out of suspension faster due to the shallow water depth and the transport downstream being limited by the incoming tide. Figure 4.14 illustrates that sediment release at low-water slack behaved somewhat differently to all other times of release in the tidal cycle. At the time of the release of sediment from the mouth of the Taipo Stream, downstream tidal currents were still evident in the upper estuary, resulting in the transport of sediment downstream. However, upon reaching the middle and lower sub-estuaries, the flow of the tidal direction had reversed and sediment transport downstream was limited by the incoming tide. The sediment remaining in suspension was flushed into intertidal areas where subsequent deposition was evident.

Scenarios of sediment released upon the incoming tide all displayed a similar behaviour. The sediment was mainly flushed back upstream into the Taipo Stream by the incoming tide. A large proportion settled out of suspension in close proximity to the mouth of the Taipo Stream in the upper estuary, which resulted in a uniform net deposition of 0.1 – 0.2 $kg.m^{-3}$ near the release site. Deposited sediment was resuspended by the tidal currents upon the subsequent outgoing tide,

particularly evident in areas where the tidal channel narrows, and was transported across the measurement lines in relatively low volumes (Figure 4.14). The lowest percentage of sediment recorded at site A was following the release of sediment 1 and 2 hours after low-water slack on the incoming tide. A large proportion of the sediment was flushed upstream in the Taipo Stream. Low water depths in close proximity to the source site and low current velocities at the time of release resulted in very little transport of sediment considerable distances from the source. The volume of sediment transported downstream increases with increasing time after low water. This may be due to increased water depth near the source site with increasing time in the incoming tide. An increased water depth results in increased time required for sediment to settle out of suspension. Release of sediment closer to high tide also results in a greater likelihood of downstream transport on the outgoing tide.

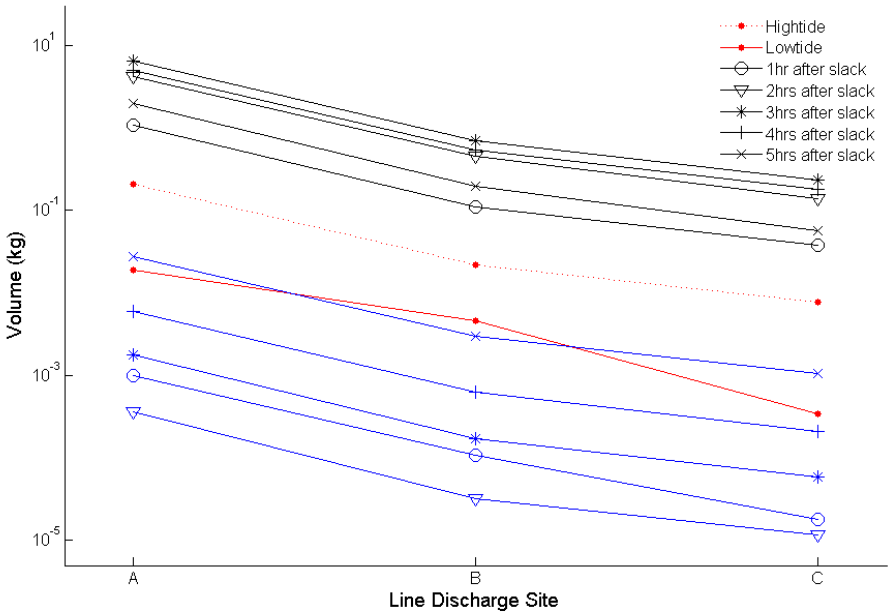

Figure 4.14. Volume of total sediment input discharged across lines A, B and C. Symbols depicted in legend indicate hours after high and low water slack. Black lines indicate sediment release upon outgoing tide, blue lines indicate sediment release upon incoming tide.

Sediment released on the outgoing tide had the greatest volume of sediment discharge. Sediment released 1 hour after high water had the lowest volumes of sediment transported downstream on the outgoing tide. This was due to the lag in the reversal of the tide, with incoming tidal currents evident in the upper estuary

at the time of release. Sediment was initially flushed further upstream of the release site in the estuary and a large proportion was flushed back into the Taipo Stream with the rising tide. Sediment predominantly settled out of suspension in close proximity to the site of the source. Sediment released 5 hours after high-water slack also had a relatively low volume of sediment transported downstream in comparison to the remaining outgoing tide simulations. This was a result of the reduced water level at the sediment source site which allowed for sediment to settle out of suspension in a short period of time.

The reversal of the tide in the upper estuary occurred at approximately the same time as sediment release 3 hours after high-water slack. As a consequence, sediment release at this time resulted in the greatest volumes of downstream sediment transport. Sediment was initially transported downstream, with sufficient water depth that sediment did not settle out of suspension immediately following release. Similar volumes of sediment transported downstream across lines A, B and C were measured for simulations of sediment release 2 and 4 hours after high-water slack for the same reasons.

For all simulations of sediment release on the outgoing tide, sediment deposition was evident in the area where complex morphology and emergent islands result in a network of tidal channels in the middle of the main outfall channel. Increased tidal current velocities when water is restricted through the narrow tidal channels during mid to low tide resulted in the resuspension of sediment upon subsequent incoming tides. This process was not evident in the simulations of release during the incoming tide, highlighting the importance of the initial transport of sediment.

It was evident from the discussed results of the 12 different scenarios of the timing in the tidal cycle that there are four general patterns of sediment dispersal. Although the results of sediment dispersal varied slightly for all of the release times on the incoming tide and the outgoing tide, the general patterns and volumes were similar. Therefore, these behaviours may be condensed into mid-outgoing tide and mid-incoming tide. High water and low water release vary considerably, therefore are maintained as individual scenarios. These four scenarios of timing of sediment release in the tidal cycle will be used in further scenario modelling.

4.4.4 Sediment transport pathways

The greatest influence on the transport of sediment in Ahuriri Estuary was grain-size. For model simulations of 10 μm grain-size, there was a considerable amount of sediment transported from the upper estuary to the lower estuary under most conditions, with a maximum of 65 % of sediment input leaving the upper estuary. For the 60 μm model runs, the percentages of sediment discharged from the upper, middle and lower estuaries were greatly reduced, with a maximum discharge from the upper estuary of 7 %. For a grain-size of 105 μm, a maximum discharge of 4.2 % was observed. Consequently, there were low sediment flux measurements leaving the middle and lower estuaries for a grain-size of 105 μm, other than sediment release following a 100 mm storm rainfall event.

The magnitude of the rainfall event had the greatest influence on sediment transport through the estuary within each grain-size investigation. An increase in the stream discharge was associated with a greater percentage of the total sediment influx transported downstream in the estuary. This was consistent for all grain-sizes. The general trend of decreasing sediment discharge percentages with increasing distance from the source was evident for each of the storm rainfall magnitudes. The cumulative flux of sediment decreased considerably from site A to site B. There is a further decrease, albeit much smaller, from site B to site C. Up to 8 % of fine sediment (10 μm) crossing line B was not measured crossing line C (Figure 4.15). This suggests that up to 8 % of the total sediment influx into Ahuriri Estuary is deposited in the boat harbour.

The timing of release also had an important influence on the sediment transport downstream. Timing of release at mid-flood and mid-ebb tide accounted for a maximum difference of 47 % of total sediment input transport from the upper estuary for the 10 μm grain-size simulations. For each of the grain-sizes, a pattern due to timing of release was evident. As the sediment discharge percentage measured at each of the sites is a function of the discharge percentage at site A, the pattern generally follows through from site A to site C. Figure 4.15 shows that for a grain-size of 10 μm, sediment released at high-water slack and mid-ebb tide had the greatest percentage of downstream transport. The lowest percentage of sediment transport downstream resulted from release at low-water slack. For the 60 μm grain-size simulations, sediment transport through the estuary was greatest

following release during high-water slack and mid-ebb tide (Figure 4.16). This is to be expected, as the release of sediment just prior or during the outgoing tide is likely to be transported with the tidal currents and result in the seaward transport of sediment. However, the pattern of sediment transport changed with an increase in freshwater influx following a 20 mm storm rainfall event to a 40, 60 or 100 mm event. Following a 20 mm storm rainfall event, the percentage of sediment transported from the upper estuary was similar for release at low-water slack and mid-flood tide. Freshwater influx was low, therefore sediment was not transported very far from the source. Sediment settled out of suspension in the upper reaches of the upper estuary where tidal current velocities are low. For greater freshwater influxes, the sediment was initially flushed further downstream following release at low-water slack, aided by the lag in tide reversal in the upper estuary. This resulted in a greater percentage of sediment which settled in the lower reaches of the upper estuary. Tidal currents on subsequent outgoing tides were able to entrain this sediment into suspension, due to the greater velocities in the region as a result of the narrow constricted channels. The transport of sediment downstream upon release during mid-flood tide was halted by the incoming tide progressing through the upper estuary, flushing the sediment back into the upper reaches of the upper estuary. Sediment settled out of suspension in these upper reaches where tidal current velocities were low and there was no secondary resuspension. Therefore, the percentage of total sediment influx transported through the estuary was lowest following the release during mid-flood tide conditions.

The transport of coarser sediment was generally limited to within the upper and middle estuary as sediment discharge from the estuary mouth is negligible (Figure 4.17). The general decrease in percentage of total sediment influx crossing each line occurred at each of the simulated grain-sizes. The finer grain-sizes follow a similar pattern of discharge downstream. However, the 105 μm grain-size transport from the upper estuary recorded at site A did not follow through to site C (Figure 4.17). Sediment release at low-water slack resulted in a small volume of sediment transported downstream from the upper estuary. However, none of this sediment was discharged from the estuary mouth. Release of sediment during mid-ebb tide produced the greatest percentage of total sediment influx transported from the upper estuary. This is to be expected as sediment released upon the

outgoing tide is more likely to be transported further downstream. The total flux from the upper estuary reduces considerably between measurement sites A and B, and again between B and C, resulting in a low volume of sediment exported across the estuary mouth.

Sediment transport during spring and neap simulations resulted in considerably different volumes of transport downstream (e.g. Figure 4.15). A difference in the percentage of total sediment transport downstream of up to 44 % resulted from the differing hydrodynamic regime imposed by spring and neap tidal conditions for a grain-size of 10 µm. The greatest differences in sediment transport during spring and neap conditions resulted from sediment release at high-water slack. The least difference in spring and neap simulation conditions resulted from sediment release at mid-ebb tide. This general pattern was also evident for the 60 µm and 105 µm simulations.

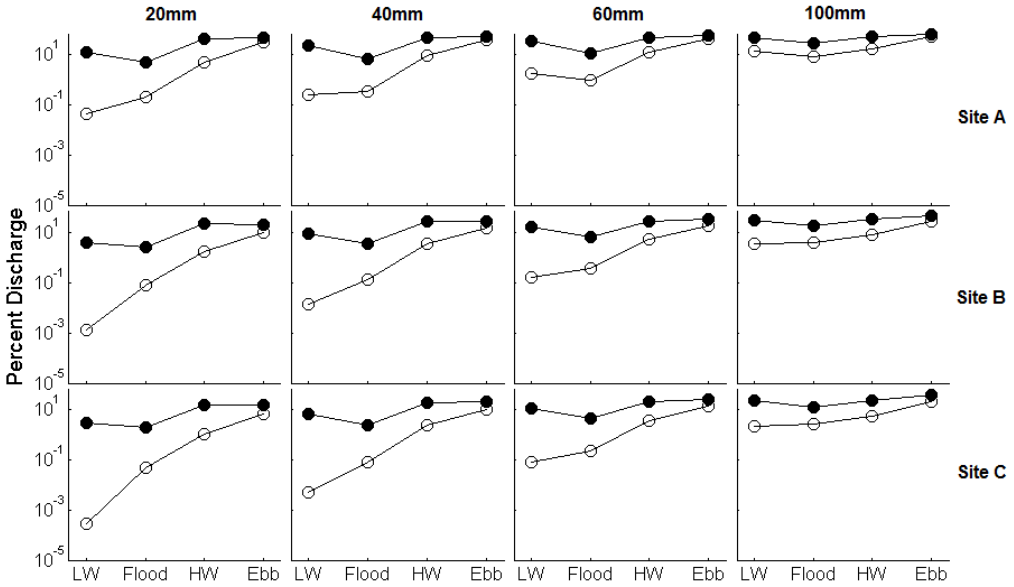

Figure 4.15. Percentage of total sediment input discharged across line sites A, B and C following a storm rainfall event for a grain-size of 10 µm. Solid circles represent results from spring tide simulations, hollow circles represent results from neap tide simulations.

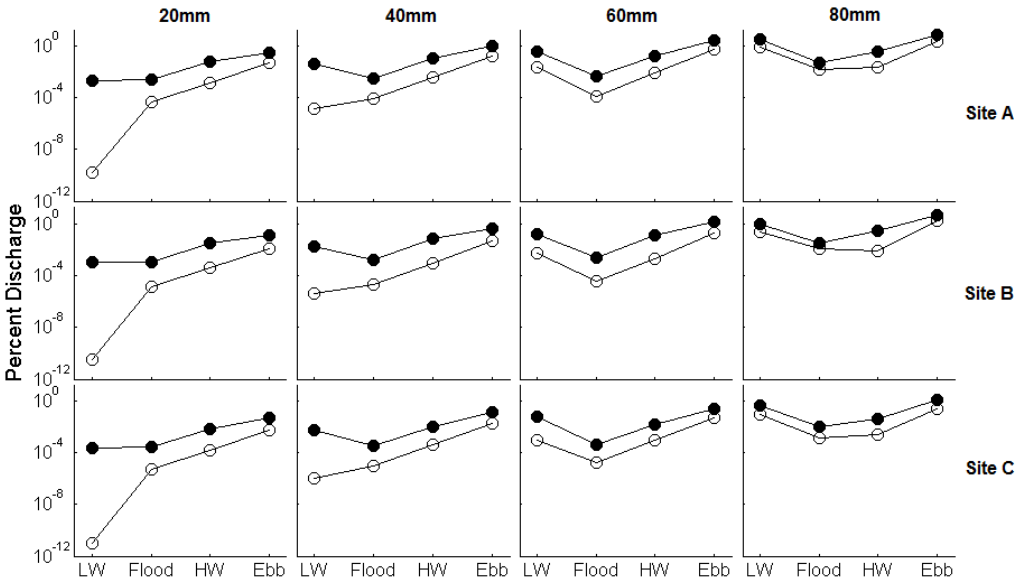

Figure 4.16. Percentage of total sediment input discharged across line sites A, B and C following a storm rainfall event for a grain-size of 60 µm. Solid circles represent results from spring tide simulations, hollow circles represent results from neap tide simulations.

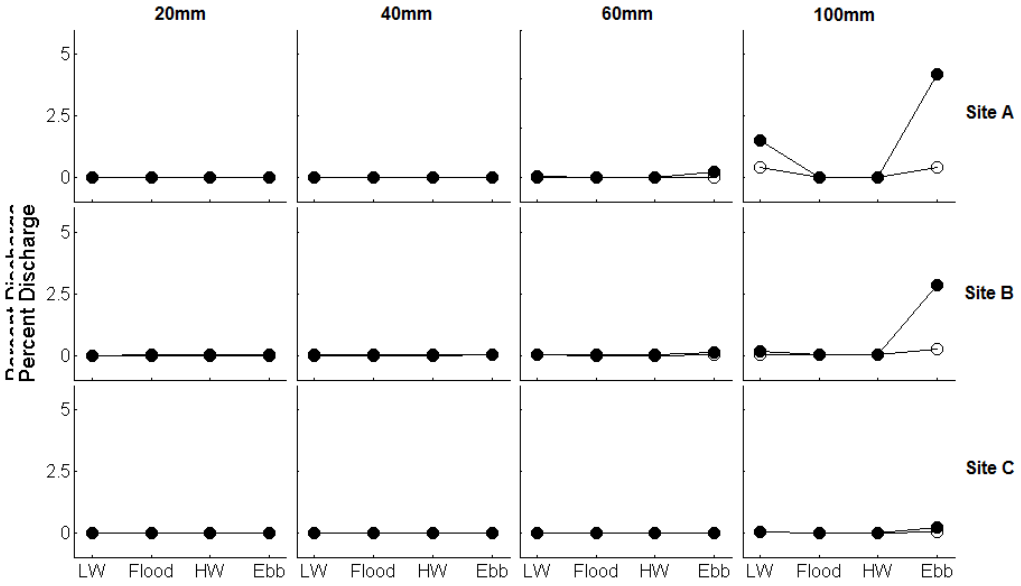

Figure 4.17. Percentage of total sediment input discharged across line sites A, B and C following a storm rainfall event for a grain-size of 105 µm. Solid circles represent results from spring tide simulations, hollow circles represent results from neap tide simulations.

4.4.5 Sediment deposition

The sediment fluxes used to infer sediment transport through the estuary also give some insight into the proportion of total sediment influx remaining in the upper, middle and lower estuaries. In order to determine in more detail where in the upper, middle and lower estuaries the sediment is deposited, an analysis of bed-level change in each sub-estuary (as defined in Figure 4.9) was undertaken.

It was found that for all grain-size simulations, the predominant area of accretion was in sub-estuary 2 (e.g. Figure 4.19). The shallow nature of the upper estuary and low current speeds resulted in a large percentage of sediment injected into the estuary settling out of suspension in the sub-estuary where the sediment source is located under all simulation conditions. For the coarser grain-size simulations (60 and 105 μm), very small volumes sediment were deposited in sub-estuaries downstream of the upper estuary (which encompasses sub-estuaries 1, 2 and 3) (Figures 4.19 and 4.20). Increasing distance downstream from the sediment source resulted in a decrease in sediment deposition, but increases again in sub-estuaries 6, 7 and 8. Sediment released just prior to tide reversal and transported downstream on the ebb tide was flushed into intertidal areas with the incoming tide and the inundation of intertidal areas which are largely encompassed by sub-estuary 6. This was illustrated in Chapter 3, Section 3.6.3. It was in this area where sediment deposition is greatest in the lower reaches of the estuary (e.g. Figure 4.18). A large proportion of sediment was deposited in sub-estuary 7 despite its small area. There was also a large volume fine sediment flushed from the estuary and deposited offshore in sub-estuary 8 (Figure 4.18). High freshwater influx led to a large proportion of sediment to be lost from the system across the open offshore boundary. These findings are summarised in Table 4.9 below.

Table 4.9. Percentage of total sediment influx lost from the model domain across the open offshore boundary. Results are given for spring tide conditions as this resulted in the greatest loss from the model domain.

Simulation conditions	20 mm	40 mm	60 mm	100 mm
10 µm	53%	53%	55%	59%
60 µm	11%	6.1%	4.1%	2.8%
105 µm	2.8%	1.8%	1.5%	1%

The amount of sediment lost from the model domain increased with increasing rainfall intensity for the 10 µm simulations. For the 60 and 105 µm simulations, there was a decrease in the amount of sediment which is unaccounted for in the model domain with increased flushing. This is likely to be an artefact of the Taipo Stream not being included in the sub-estuary depositional calculations. Low rainfall intensity allowed for greater flushing of sediment back upstream into the Taipo Stream with the incoming tide, as sediment was not initially transported away from the source. With increased flushing associated with increased rainfall intensity, the sediment was initially flushed a distance away from the source, reducing the volume of sediment flushed back into the Taipo Stream.

The greatest sources of variation in the sites of sediment deposition and proportion of sediment retained in the estuary within each grain-size investigation were the magnitude of the storm rainfall event and the sediment size (Figure 4.18). Finer sediments reached further downstream and showed the highest values of deposition in sub-estuaries 7 and 8 and export from the system. Further, increasing sediment volumes are deposited in these lower estuaries at greater storm rainfall discharges. At these greater freshwater discharge volumes, there is a considerable loss of sediment from the system, particularly of the fine sediment (10 µm). Over half of the total sediment influx is lost across the open boundary. This value decreases with decreasing freshwater influx to 53 % exported from the estuary at the lowest freshwater influx.

In general, sub-estuary 2 retains the greatest proportion of the sediment influx, with the exception of the fine sediment during neap-tide conditions, where a slightly higher percentage is retained in sub-estuary 3. During neap tide

conditions, greater volumes of sediment are deposited in sub-estuaries 1 and 2 than during spring-tide conditions. Greater tidal velocities during spring-tide conditions result in increased flushing downstream. Due to the greater retention of sediment in the upper sub-estuaries, there were lower volumes deposited downstream during neap tide conditions.

At low freshwater influxes, sediment was largely retained in sub-estuary 2. Freshwater influx momentum was not sufficient to transport sediment downstream of the source sub-estuary and sediment settled out of suspension in close proximity to the source. Tidal currents in the vicinity of the main depositional area are weak (See Chapter 3, Section 3.6.3) and are generally unable to penetrate the upper estuary with appreciable velocities.

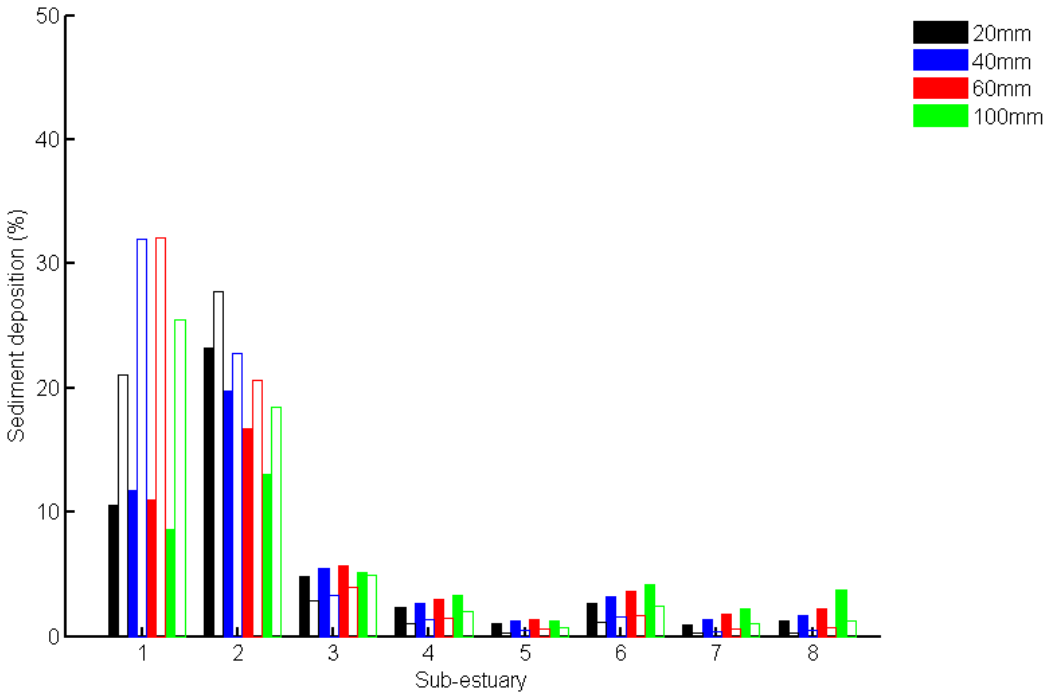

Figure 4.18. Percentage of total sediment input deposited in each sub-estuary for a grain-size of 10 µm. Solid bars indicate spring tide simulation results, hollow bars indicate neap tide simulation results. Storm rainfall magnitudes indicated by legend.

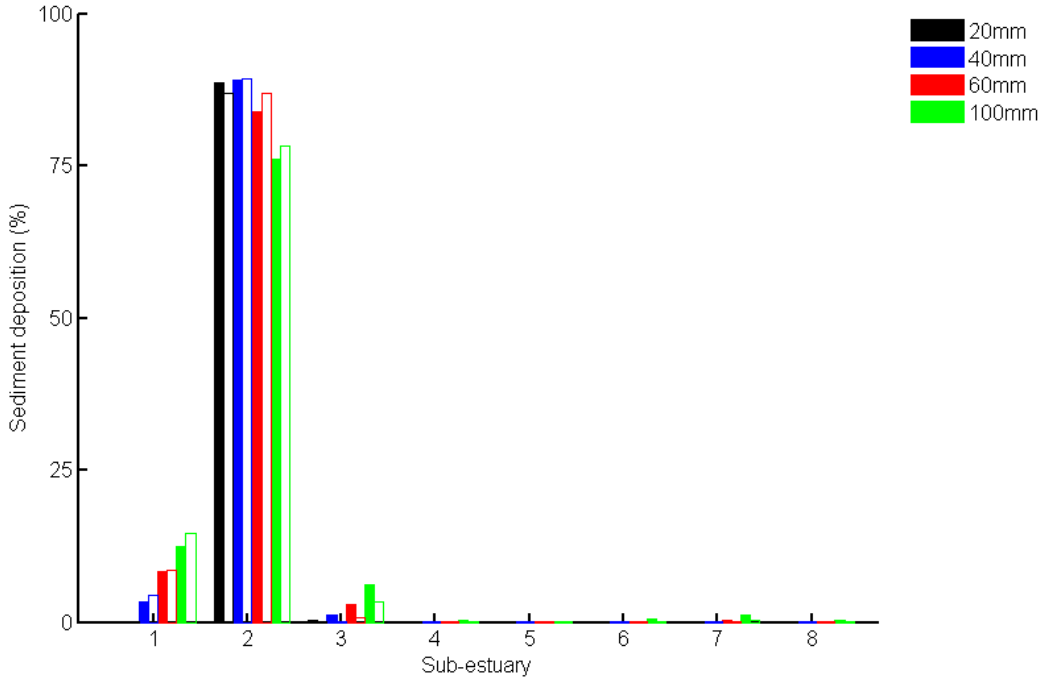

Figure 4.19. Percentage of total sediment input deposited in each sub-estuary for a grain-size of 60 µm. Solid bars indicate spring tide simulation results, hollow bars indicate neap tide simulation results. Storm rainfall magnitudes indicated by legend.

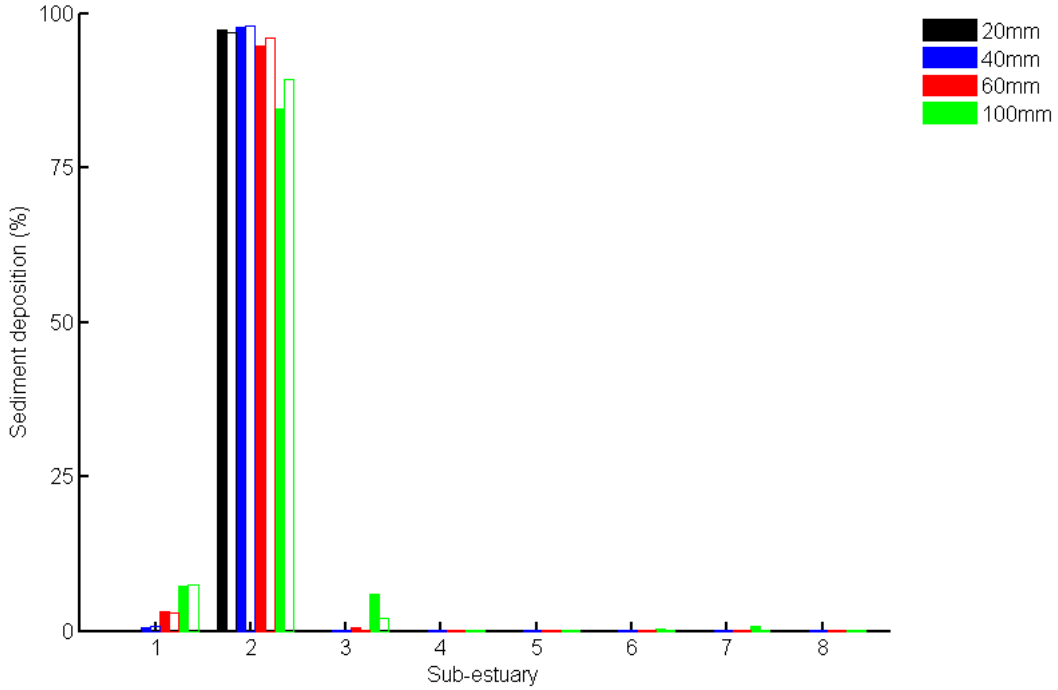

Figure 4.20. Percentage of total sediment input deposited in each sub-estuary for a grain-size of 105 µm. Solid bars indicate spring tide simulation results, hollow bars indicate neap tide simulation results. Storm rainfall magnitudes indicated by legend.

The timing in the tidal cycle of sediment release also had a notable influence on the sites of sediment deposition. Figure 4.21 illustrates the significance of the timing of sediment release in the tidal cycle for a simulation of 10 µm grain-size following a 40 mm storm rainfall event during spring tide and neap tide conditions. The percentage of total sediment retained in the estuary varied as a result of the timing of sediment release, ranging from 38 – 59 %. There was also a considerable difference in the final locations of sediment deposition. Sediment transport from the upper estuary was greatest when sediment release coincides with mid-ebb tide, with a large proportion deposited in sub-estuary 6. Sediment released on the ebb-tide showed similar behaviour to that of high-water release. Upon analysis of the suspended sediment concentration, it was evident that a plume of suspended sediment was transported downstream, reaching the middle estuary just prior to tide reversal. The incoming tide flushed the suspended sediment back into the intertidal regions of the middle estuary, particularly sub-estuary 6 (Figure 4.22). Sediment released during low-water slack and flood-tide conditions had a greater retention in the source sub-estuary and subsequently a lower proportion of deposition in the downstream sub-estuaries. Release during mid-flood conditions resulted in the greatest transport upstream, with a large volume of deposition in sub-estuary 1, located upstream of the sediment source site. There was also a considerable variation according to spring – neap conditions. As aforementioned, spring tidal currents induced greater downstream flushing due to greater velocities and consequently a greater ability to transport sediment.

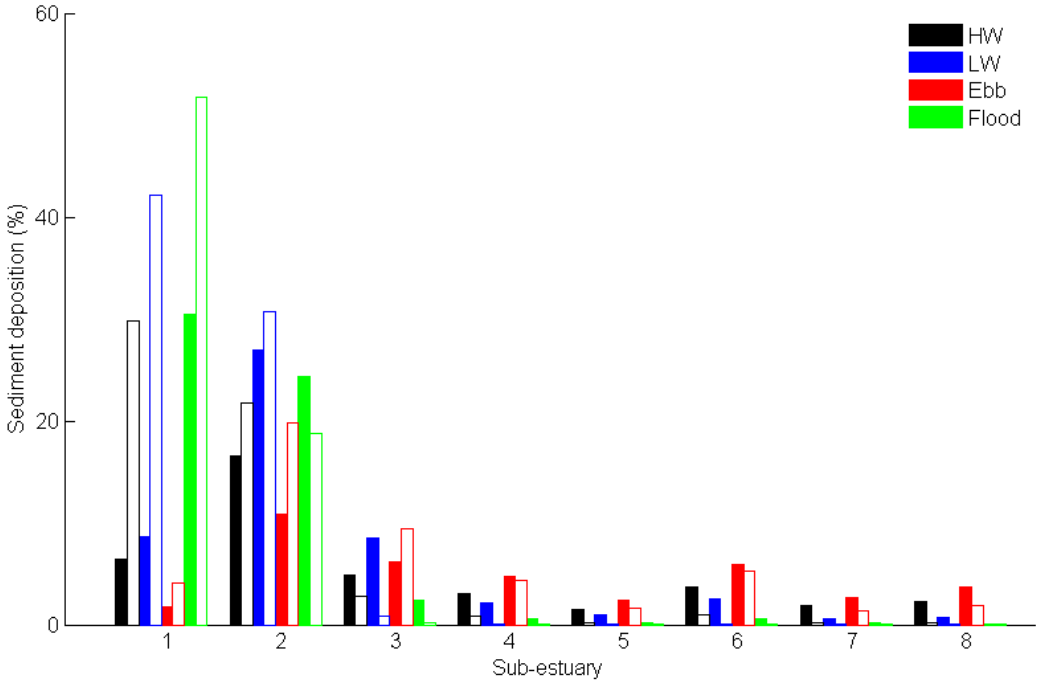

Figure 4.21. Percentage of total sediment input deposited in each sub-estuary for a grain-size of 10 µm and a storm rainfall magnitude of 40 mm. Solid bars indicate spring tide simulation results, hollow bars indicate neap tide simulation results. Timing of sediment release in the tidal cycle is indicated by legend.

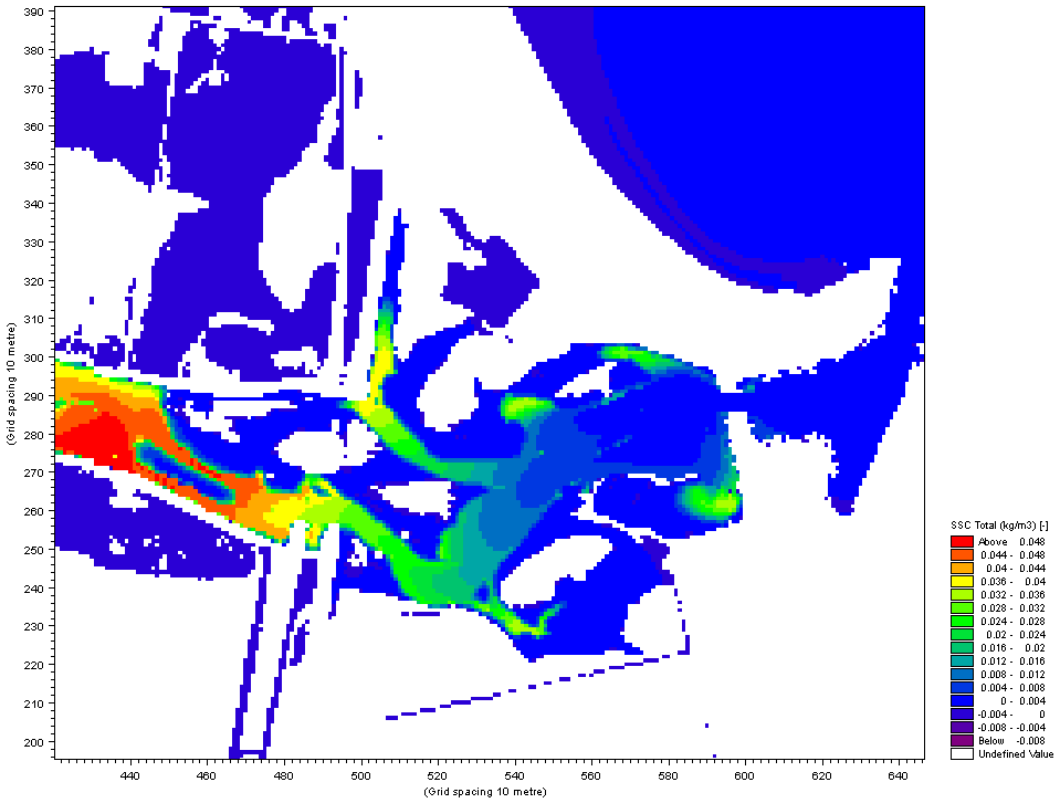

Figure 4.22. Fine suspended sediment (10 µm) released at low-water slack is flushed into intertidal areas and back into the upper estuary by the incoming tide.

4.4.6 Erosion

As the model runs were initialised with an existing layer of sediment in the bed upon which tidal currents had not yet acted upon, the main areas of erosion were in the tidal channels, particularly the main channel in the middle estuary. There were large amounts of erosion evident in all areas where a constriction of the tidal flow through narrow channels was evident. This process was apparent from the erosion evident in the narrow tidal inlet, through the narrow Pandora Passageway and in the emergent island/complex channel network in the upper estuary. For all simulations there were small volumes of sediment eroded from the bed in intertidal regions, primarily confined to the intertidal channels.

Figure 4.23 A illustrates the total bed level change for a grain-size of 10 μm at the conclusion of the model run. Negative bed level changes were generally restricted to the tidal channels. The extent of erosion generally lies in the range of -60 – 40 $kg.m^{-2}$. Figure 4.23 B illustrates the total bed level change for a grain-size of 60 μm at the conclusion of the model run, which lies within the range of -50 – 0 $kg.m^{-2}$. The erosion of sediment was slightly greater for a grain-size of 60 μm than for 10 μm due to the cohesion of the finer sediments. The cohesion induces a slightly greater critical shear stress for erosion of 0.35 $N.m^{-2}$ for 10 μm sized sediment, and a value of 0.3 $N.m^{-2}$ for 60 μm sized sediment. However, the patterns of erosion and potential areas of erosion remained the same. Figure 4.23 C illustrates the total bed level change for a grain-size of 105 μm at the conclusion of the model run, which lies within the range of -80 – 0 $kg.m^{-2}$. Large changes in the total bed volume are evident in the channels, with very high values. This is attributed to the constant bed density, as this was not variable with each bed layer as it is with the finer grain-sizes. The 10 and 60 μm grain-size simulations are assigned a variable bed density, as fine sediments de-water and increase in bulk density with depth into the bed.

Deposition of the eroded sediment in the estuary was evident for all grain-size simulations. All positive bed volume changes were attributable to sediment eroded from the bed as no sediment source was included in these simulations. For all simulations there was apparent sediment deposition on the main tidal channel margins in the middle estuary (Figure 4.23). Sediment deposition on the channel flanks was greatest for the fine sand simulations (105 μm). This is attributable to a

greater settling velocity. For all grain-sizes sediment deposition was evident in the lower estuary (boat harbour). The greatest volumes of deposition in the boat harbour resulted from the 105 μm simulations. The higher settling velocity resulting in sediment settling out of suspension as the current slows in the lee of passing through the Pandora Passageway on the outgoing tide.

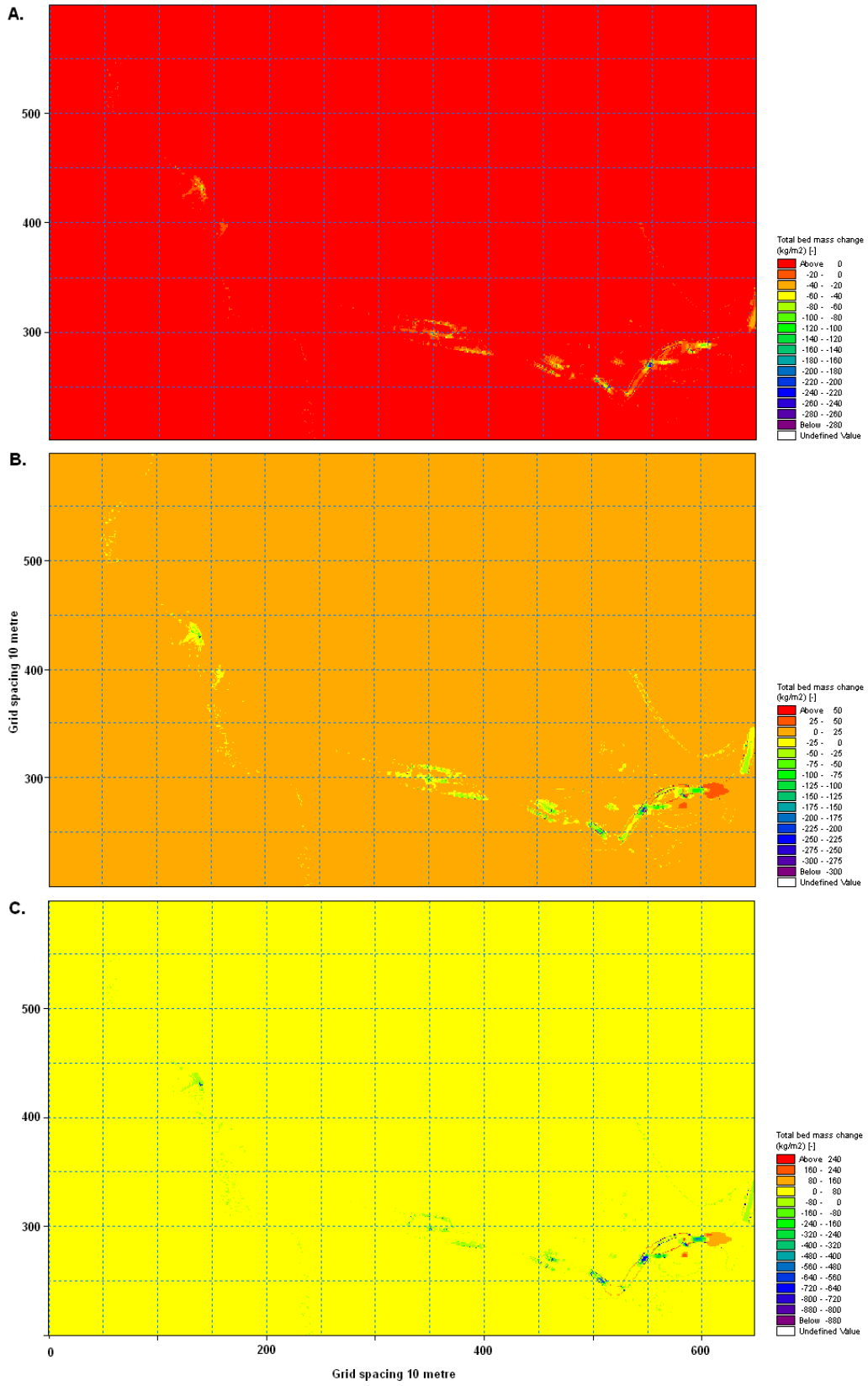

Figure 4.23. Total bed level change for grain-size simulations of **A.** 10 µm **B.** 60 µm and **C.** 105 µm. A negative bed level change indicates erosion and a positive bed level change indicates accretion.

4.5 DISCUSSION

4.5.1 Erosion coefficient sensitivity analysis

Values of SSC under varying τ_{ce} were investigated and compared with those measured in previous modelling studies and field observations found in the literature with comparable grain-size and current velocity fields. Such comparisons include:

- Hu et al. (2009) found that for a D_{50} of 10 μm, modelled and measured SSC calibrated well using a spatially varying critical erosion stress of 0.02-0.8 $N.m^{-2}$ under tidal currents ranging from 0-2 $m.s^{-1}$. This spatially varying critical erosion stress was based predominantly on inundation times.
- Green et al. (1997) observe a SSC in the range of 30-40 $mg.l^{-1}$ (D_{50} of 200 μm) on an intertidal flat in Manukau Harbour, where currents ranged from 0-0.5 $m.s^{-1}$. However, they found that tidal currents alone were incapable of resuspending sediment on the intertidal flat.
- Talke and Stacey (2008) measured tidally averaged sediment concentrations of approximately 20 $mg.l^{-1}$ during calm conditions. For a critical erosion stress of 0.35 $N.m^{-2}$, similar concentrations are observed at site 3 under peak incoming tidal currents of similar current velocities (0.1 $m.s^{-1}$).
- Brennan et al. (2000) observe SSC in the range of 0 – 50 $mg.l^{-1}$ under current speeds of approximately 0.2 – 0.5 $m.s^{-1}$ in a channel environment similar to that of site 4. At peak current velocity, the SSC reaches 200 $mg.l^{-1}$. The suspended sediment collected revealed it was predominantly silt and clay, analogous to the smaller sediment sizes being modelled in this study.

Based on these comparisons with field observations and modelling scenarios, the values for critical shear stress for erosion used in this study were demonstrated to produce reliable results.

4.5.2 Sediment transport pathways and timing of release

The transport of sediment in Ahuriri Estuary was primarily a function of the grain-size. There was a large difference in the amount of sediment exported from the model domain between grain-size simulations. The settling of a large proportion of the sediment influx in close proximity of the site was evident for the larger grain-size simulations, primarily a function of the settling velocity. In the model, the grain-size was parameterised by the value assigned for the settling velocity, calculated using the Stokes model. Flocculation processes may occur for the finer grain-size (10 μm) upon the convergence of the freshwater influx with the saline estuarine water body, resulting in an increased settling velocity (Winterwerp et al. 2002). However, flocculation processes were not included in the simulation. Should flocculation occur, it is likely to take place in the upper estuary, resulting in increased deposition. A similar study carried out in the Central Waitemata Harbour (CWH), Auckland, New Zealand showed similar results. For all grain-sizes, there were large fractions of total sediment deposited in sub-estuaries in the immediate vicinity of the source sub-estuary (Green 2008). In the CWH study there was also large proportions of sediment evident in the deep channels. This was not evident in the simulations in this study, as sediment was either deposited in the destination sub-estuaries, or lost from the model domain by the end of simulation. The shallow and narrow nature of the main tidal channel and consequently, the relatively high current velocities, ensure the main tidal channel is a transport pathway only. The CWH study also investigated the transport pathways of sediment by concreting all sub-estuaries apart from the one in question. Ahuriri Estuary is rather linear in shape, with one main tidal channel. As a consequence, the sediment transport pathways are relatively predictable, highlighted by the hydrodynamics of the estuary.

The water depth in the upper estuary, which is a function of the timing in the tidal cycle, was important in the downstream transport of sediment. The transport of sediment from the upper estuary was generally low when released at low-water slack. Due to a shallow water depth, sediment settled out of suspension in a shorter time period, simply because there is less distance to the bed. This resulted in a greater proportion of sediment being deposited in close proximity to the source. At shallow water depths, the connectivity between the upper reaches of

the upper estuary with the rest of the estuary is greatly reduced due to a complex area of emergent islands and very narrow tidal channels. Therefore, sediment was trapped in the upper estuary and settled out of suspension in this upper region. Current velocities in this area were low, therefore unable to induce a shear stress at the bed capable of resuspending sediments in this region.

The downstream transport of sediment introduced into the estuary from the Taipo Stream downstream was highly attributable to secondary resuspension, with the exception of very fine sediments. As tidal currents did not penetrate into the upper reaches of the upper estuary with considerable velocities, any sediment settling out of suspension in these upper reaches is likely to remain in place. The transport of sediment from the upper estuary was highly dependent on initial transport to the lower reaches of the upper estuary before settling out of suspension. Here, tidal currents have the ability to resuspend sediment on subsequent tides.

The timing in the tidal cycle of the release determined whether sediment remained in close proximity to the site, or was transported further downstream where tidal currents have the ability to rework the sediment once deposited. From this location, stronger tidal currents were able to either directly transport the sediment downstream upon the first tidal cycle, or were capable of secondary resuspension during subsequent tidal cycles. For very fine sediment, the low settling velocity meant the timing of sediment release was not as important as for coarser grain-sizes. The increasing water depth with time in the flood tide also allowed for the dispersal of sediments from the source and sufficient connectivity of flow between the upper and middle estuaries.

The magnitude of freshwater input had an influence on the effect of the timing in the tidal cycle of sediment release, particularly for the coarser grain-sizes. The greater the freshwater inflow, the greater the initial transport of sediment downstream. As previously discussed, it was this initial downstream transport of sediment which was most important for medium to coarse grain-sizes.

The variation in sediment transport attributable to spring tide and neap tide simulations was small in comparison to grain-size and freshwater input. However, there were important differences, with the timing in the spring-neap cycle accounting for a large difference in the downstream transport of sediment. The

lower current velocities during neap-tide conditions resulted in less flushing from the upper estuary, and lower volumes of initial deposition in the emergent island area, where sediments were later reworked by subsequent tides.

4.5.3 Areas of potential accretion

Dividing the estuary into 8 sub-estuaries allowed for the establishment of areas of potential accretion. The bed volume changes confirmed that the complex morphology of emergent areas and narrow tidal channel network in the upper estuary restricts the transport of sediment downstream from the Taipo Stream. In the majority of scenarios, this area restricted the downstream transport of sediment, resulting in maximum bed volume changes in sub-estuary 2. A greater freshwater discharge allowed for greater flushing of the sediment downstream, as sediment was flushed downstream to where tidal currents have the ability to rework sediments on subsequent outgoing tides.

The general trend in bed volume change was a decrease in sediment accretion downstream of the sediment site, but an increase again in sub-estuaries 6, 7 and 8. Increased magnitude of freshwater inflow induced greater the bed volume changes in these sub-estuaries. Very fine sediments were able to remain in suspension for a large proportion to be transported across the open ocean boundary. The 10 μm grain-size simulations had the greatest percentage of total sediment input deposited in the middle and lower estuaries, with a large proportion exported from the model domain as it crossed the open ocean boundary. In the CWH study (Green 2008), much of the smallest grain-size (12 μm) remained in suspension at the end of one day and illustrated the greatest dispersal throughout the harbour. Similar results were indicated in Ahuriri Estuary, illustrated by the large proportion of the smallest grain-size lost from the model domain and greater deposition in the sub-estuaries in the middle and lower estuary. The coarser grain-sizes tended to settle out of suspension in close proximity to the source in sub-estuary 2. For a grain-size of 105 μm with a settling velocity as calculated by the Stokes model of 0.001 $m.s^{-1}$ (Equation 4.3). A time of only 16 minutes is required for the sediment to settle out of suspension. Therefore, sediment was not transported a considerable distance from the source.

A relatively large proportion of fine sediment was deposited in sub-estuary 6. This is attributable to suspended sediment flushed into the intertidal areas with the incoming tide and settling out of suspension where water depth and current velocities are low. Sub-estuary 7 also experienced a considerable amount of deposition, relative to the area it encompasses. It is likely a result of the residual eddy formation which formed due to current velocity shear on the outgoing tide. The current slowed after passing through the narrow Pandora Passageway, inducing vorticity as discussed in Chapter 3. Similar behaviour was evident in the CWH study, where a sub-estuary near the harbour mouth had deposition of sediment from all of the sub-estuaries in the harbour, aided by the eddy formation evident on the outgoing tide (Green 2007). In Ahuriri Estuary, the modelled sediment deposition in sub-estuary 7 is validated by the dredging operations carried out in this area. An approximated dredge volume of 10,900 m^3 was dredged from the boat harbour in 2008 and early 2009 (refer to Appendix I for site location). There were four dredge sites, one of which lies in the direct vicinity of the boat harbour residual eddy. Residual eddies are often found to be associated with depositional centres (e.g. Ferentinos & Collins 1979; Wang et al. 2009).

The direction of tidal flow at the time of release of sediment into the estuary greatly influenced the initial transport direction and location of deposition. Tidal currents do not induce bed shear stresses sufficient to rework sediments in the majority of the upper estuary and on the intertidal flats. If the sediment is initially transported downstream to an area where tidal currents are able to resuspend the sediment, there will be greater transport downstream and discharge from the estuary. The secondary reworking of sediments by tidal currents was restricted to certain areas, mainly the main tidal channels and the area located in the upper estuary where emergent islands restrict tidal flow to a narrow network of channels. At this site current speeds were predicted in Chapter Three to reach up to 0.6 $m.s^{-1}$. As indicated by Figure 4.24, all of the grain-sizes are subject to erosion and subsequent transport at given this current speed. It was this area where secondary sediment reworking occurred and was responsible for much of the downstream transport of the coarser sediments. The initial transport and depositional location was highly important in the overall transport and ultimate

depositional location of sediment introduced into the estuary from the Taipo Stream.

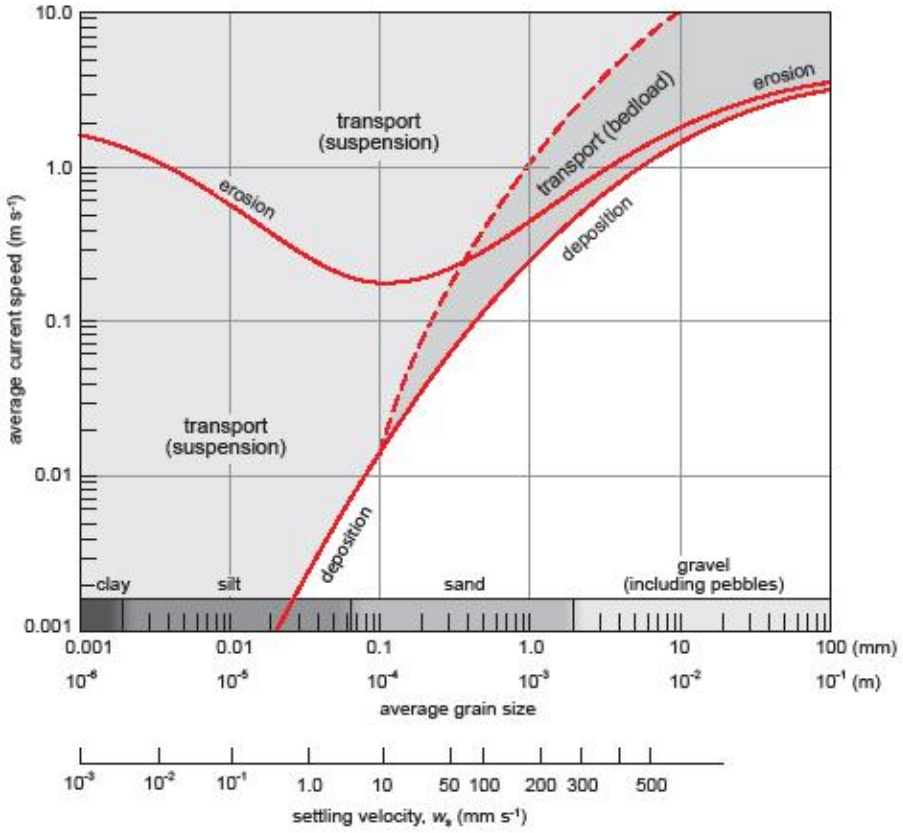

Figure 4.24. Schematic diagram showing the range of average current speeds at which sediment particles of different sizes are eroded. Diagram also shows the range of average current speeds at which sediment particles are transported, the mode of sediment transportation, and deposited. Adapted from Bearman (1989).

The CWH study included the radioisotopic dating of sediment cores and calculated sedimentation rates, used in the validation of the hindcast long-term model application. It was found that sedimentation rates predicted by the model (based on the event timescale MIKE 21 MT model simulations) were lower than the calculated sedimentation rates by approximately 25 %. However, the general patterns were well-predicted (Green 2008). The CWH study also illustrated that once sediment was deposited, it was generally stable under fair-weather conditions (i.e. no wind or local wave generation). Sediment was resuspended by wind storms which locally generated waves, which generally control sediment re-working in small, microtidal estuaries (Green 2008). Due to the relatively

sheltered nature of Ahuriri Estuary, this is likely to be the case in this study. However, this will be addressed further in Chapter 6.

4.5.4 Areas of potential erosion

The primary areas of erosion in Ahuriri Estuary were found to be restricted to the main tidal channels. Intertidal areas showed very little evidence of erosion from the bed, as tidal current velocities remain too low to entrain sediment from the bed in these areas. However, there was evidence of erosion in the intertidal channels. As the erosion discussed here is from initial bed sediment not at equilibrium, it must be noted that these areas of potential erosion are likely to be in equilibrium prior to a storm event. However, it suggests that any sediment influx into the estuary will not settle out in the main tidal channel, but rather be transported downstream by the tidal currents. There was considerable erosion from the bed in the upper estuary where tidal flow is constricted by emergent islands. Here the tidal current velocities were high, in the order of 0.6 $m.s^{-1}$, inducing high bed shear stress (refer to section 4.4.3). This high bed shear stress resulted in the entrainment of sediment from the bed in large volumes.

The volumes of eroded sediment for the 105 μm grain-size simulations were uncharacteristically high. This was attributed to the constant bed density, as this was not variable with sand bed layers as it is with the finer grain-sizes. The 10 μm and 60 μm grain-size simulations had bed layers with differing characteristics, including a variable bed density. The bed density increased with increasing depth. Following deposition of fine cohesive sediment, the density of the bed consolidates with time (Lick et al. 2007). With increasing time, and subsequently increasing bulk density, the critical shear stress for erosion also increases (Winterwerp 2007). However, the grain-size simulations of fine sand did not include variable bed characteristics with depth, and subsequently a constant rate of erosion resulted in greater volumes of erosion in the main tidal channels.

Sediment eroded from the bed was found to deposit on the intertidal margins of the main tidal channel and in the boat harbour in substantial volumes. The coarser grain-sizes were found to deposit in greater volumes, attributable to the sediment settling velocity. There was a large positive bed volume change, indicating

deposition, in the lee of the Pandora Passageway in the boat harbour. The predicted sediment accumulation here is confirmed by the relatively large volumes dredged from the area in 2008 and early 2009. Dredging sites 1, 2 and 3 (See Appendix I) correspond directly with the location of predicted sediment accumulation. Fine sediment was found to have lower deposition volumes, particularly in the aforementioned locations. A very low settling velocity prevented deposition in these areas despite the dramatic slowing of current velocities, as is the case in the boat harbour.

The model simulations in this study investigated constituent grain-sizes individually. However, in natural sediments there are a number of constituent grain-sizes. The presence of larger grain-sizes in the sediments results in armouring of the finer constituent grain-sizes. This may reduce the resuspension of the fine fraction, which may otherwise by highly erodible in the absence of larger grain-sizes. Dolphin (2004) found that silt-sized sediments had the same erosion threshold as sands, due to the armouring effect of sand. Therefore, the erosion of fine sediments discussed here may be an over-estimation of actual erosion rates. Erosion of sand is also reduced by the presence of silt and clay-sized particles (van Rijn 2007), which is not accounted for in these simulations of single grain-size constituents.

4.6 CONCLUSIONS

The MIKE 21 MT model was has been shown to predict the sediment dynamics of Ahuriri Estuary relatively well. From the scenario modelling discussed in this chapter, the following conclusions are drawn:

- The governing influence on the transport of sediment in Ahuriri Estuary was the grain-size and consequently the settling velocity. Coarser grain-sizes settled out of suspension in close proximity to the source, whereas fine silt-sized sediment was transported throughout the estuary. A large proportion of fine sediment was lost from the estuary mouth and the model domain, respectively.
- The magnitude of freshwater discharge and the timing of the release of sediment in the tidal cycle were also found to have an important influence in sediment transport and the location of deposition. These influences were increasingly evident with an increase in the grain-size used in the simulation, as the initial transport before settling out of suspension became increasingly important.
- Downstream of the upper estuary, the greatest volume of sediment deposited was evident in sub-estuary 6, which encompasses a large intertidal area. Sediment deposited here is likely to accumulate, due to the low current velocities and consequently the lack of secondary resuspension and transport.
- The sediment deposition in the boat harbour is attributable to the residual eddy formation on the outgoing and the slowing of tidal currents in the lee of the Pandora Passageway. The predicted sediment is confirmed by dredging locations.

The predicted sediment dynamics have been somewhat validated by the findings presented in this chapter. Inferred sediment dynamics from a surficial sediment analysis will provide further data for the validation of the predicted sediment dynamics. This will be further discussed in Chapter 6.

CHAPTER FIVE
SURFICIAL SEDIMENT ANALYSIS

5.1 INTRODUCTION

Analyses of surficial sediments in estuarine environments provide essential information of the sediment dynamics. Sedimentation rates may be inferred, along with present sediment transport pathways, areas of potential erosion and accretion, and possible sediment sources and sinks (McCave 1978; Gao et al. 1994). Such information is important for sedimentological and ecological studies, engineering applications and environmental investigations (le Roux 1994; Chang et al. 2001; Reeve et al. 2004).

In this chapter the estuarine sediments will be characterised, along with the inference of sediment transport pathways, areas of erosion and accretion, and sediment sources and sinks.

5.2 ESTUARINE SEDIMENTS

Estuaries are generally areas of active sedimentation. Sedimentation rates and the surficial sediment composition are a consequence of sediment supply and the hydrodynamic forcing of the system (Thrush et al. 2004). As discussed in Chapter Three, tidal currents are the dominant physical forcing in Ahuriri Estuary and are therefore likely to be the physical forcing governing the surficial sediment characteristics. Sedimentation events are hypothesised to be largely due to the influx of sediment during storm freshwater discharge, as the tidal inlet is relatively sheltered and narrow, likely preventing a significant influx of marine sediment (refer Chapter 2, Section 2.3.4).

Fine estuarine sediments are often cohesive in nature, which influences the processes of erosion and accretion within the estuary, as discussed in Chapter Four. The presence of bacteria and algae in intertidal environments often leads to increased cohesion due to the secretion of mucus by these organisms (Lelieveld 2003). The binding of the sediments by this mucus may result in an increased

critical shear stress for erosion. Conversely, macrofauna may lower the critical shear stress for erosion as a result of bioturbation (Le Hir et al. 2004).

Spatial distributions of grain-size parameters are a result of the sediment transport processes of the system (Mallet et al. 2000). Grain-size generally decreases from high energy environments to low energy environments, due to the winnowing of finer sediments by tidal currents and waves (de Boer 1998). The accumulation of fine sediments in low energy intertidal areas is associated with high nutrient, heavy metal and organic carbon concentrations due to their high capacity for adsorption (van Leussen and Dronkers 1988). The organic carbon content of surficial sediment may give insight into the physical regime of the estuary and recent sedimentological events (Sakamaki & Nishimura 2006). Organic matter provides a food source for macrobenthos. However, a high content leads to a high sediment biological oxygen demand (BOD) due to bacterial mineralisation and can lead to the build up of toxic by-products such as ammonia and sulphide (Hyland et al. 2005). Therefore, sediment organic carbon content is a useful indicator of the habitat quality for macrobenthos and the general health of the estuary (Sakamaki & Nishimura 2007). Organic material may increase the cohesion of the sediments (Nichols 1984), or decrease cohesion and subsequently shear strength at very high organic content (Marván et al. 2002), having implications for sediment deposition and resuspension.

5.2.1 Historical studies of sedimentation in Ahuriri Estuary

Chagué-Goff et al. (2000) found sediment accumulation rates in Ahuriri Estuary to be spatially variable. The highest sedimentation rates were found in the Westshore intertidal area (6.1 $mm.yr^{-1}$), and the lowest sedimentation rate was found at the western margin of the Taipo Stream (3.8 $mm.yr^{-1}$). They found isolated significant changes in the Cl and S concentrations associated with large floods. Large flood events inject catchment-derived sediments into the estuary. It is these large sedimentation events which are of importance as they provide a mechanism of burial of fine-grained contaminated sediments.

Sediment cores highlighted a change in sediment grain-size in the middle estuary, from silty to sandy sediments, as a result of the uplift induced by the 1931 Napier

Earthquake. This change in sedimentation marks a change in the depositional environment, particularly in the middle estuary. The uplift resulted in the channelised flows of the estuary at present, and subsequently an increase in depositional energy and stronger tidal flow for the majority of the estuary. This favours the deposition of sandy sediments. The uplift also diverted the Tutaekuri River which previously discharged into the estuary, providing a source of fine sediments. Cores taken in the intertidal and upper estuary regions do not show a significant change, with fine sediments prevalent in these cores. These areas remain low energy environments despite the uplift. This is a consequence of low tidal energy in these areas.

5.3 METHODS

Surficial sediment samples were collected from 46 sites within the middle estuary and lower reaches of the upper estuary (Figure 5.1). Sampling was undertaken as a series of transects spaced approximately 100 m apart. Several areas with discrete regions and were sampled as a group due to their geometry (e.g. group 1 and group 15 – See Figure 5.1). Within each transects, sediment samples were taken at a random spacing, ensuring all sub-environments included in the transect were sampled. The sampling was undertaken during the period 08/04/2009 – 09/04/2009. In order to ensure results were representative of the site, a replicate sample was taken from a random site approximately 1 m away from original sample. Surficial samples (approximately 0-2 cm) were collected using a hand trowel. Sub-samples were extracted for analysis for grain-size and organic carbon content. Sediment samples were grouped into sampling areas or transects (1 – 15). The samples were kept in refrigerated conditions for several weeks prior to analysis.

Figure 5.1. Locations of surficial sediment samples in Ahuriri Estuary. Replicate samples were taken approximately 1 m away from original sample location. Each number corresponds to individual sampling transects or groups. Transects were spaced approximately 100 m apart.

5.3.1 Sediment grain-size analysis

Each sediment sub-sample was wet-sieved to determine the weight percentage of gravel (> 2 mm). Sub-samples were analysed using the Malvern Mastersizer-S for sediment smaller than 2 mm in diameter. The Malvern Mastersizer-S calculates particle size using laser diffraction theory. Diffraction theory states that the diffraction angle is inversely proportional to grain-size. The diffracted laser pattern received by the detector is used to calculate the particle size. The grain-size is expressed in terms of equivalent spheres (Cooke 1990). Figure 5.2 illustrates the configuration and operational theory of the Malvern Mastersizer-S.

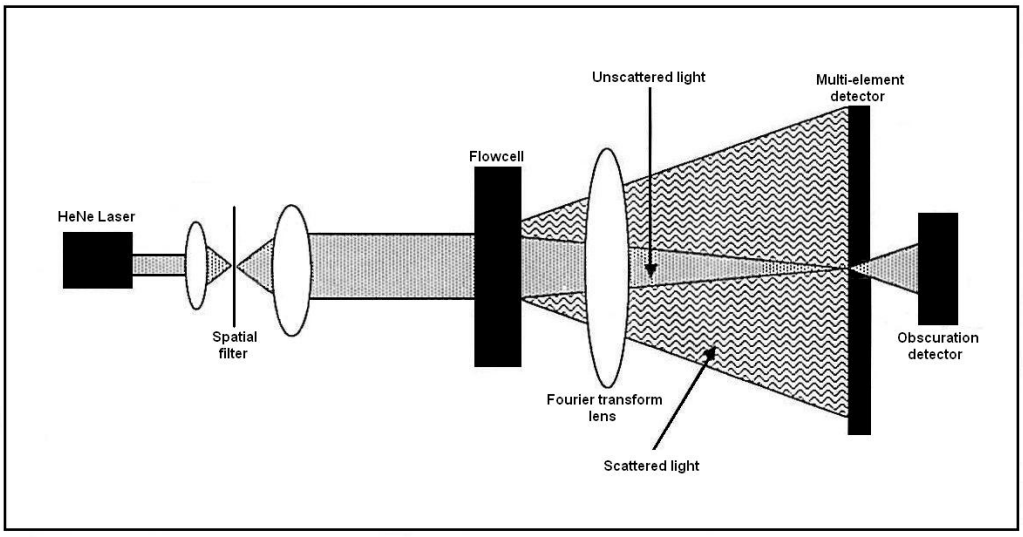

Figure 5.2. Schematic illustrating the configuration and operational theory of the Malvern Mastersizer-S using laser diffraction to determine particle size. Adapted from Cooke (1990).

Measurement of grain-size was carried out using standard operating procedure for marine sediment, ensuring sufficient ultrasonic vibration to break apart any flocs within the sample. Sub-samples were added directly to the suspension medium until an obscuration of approximately 17-20 % is reached, allowing for a sufficient signal to noise ratio. A full record of grain-size distributions as calculated by the Malvern Mastersizer-S are given in Appendix VI.

Grain-size statistical parameters were calculated using moment statistics. There is a large gravel fraction in many of the samples which was summarised as the weight of sediment greater than -1 phi (2 mm). Therefore the data are essentially open-ended. The Folk graphical method (1968) is recommended for open ended datasets, as moment statistics are based on the entire grain-size distribution. However, not all of the percentiles required in the calculation of graphical grain-size parameters were represented in the data due to the large gravel fraction. Therefore, grain-size parameters were calculated including and excluding the gravel content using moment statistics. The presence of gravel (and its associated weight percentage) greatly influenced the calculated moment statistics. Due to the relatively low current velocities in Ahuriri Estuary, the gravel was hypothesised to be derived in-situ from erosion of the estuary margins. Therefore, grain-size trends are skewed as a result of the presence of gravel and sediment transport

signals may be misrepresentative. See Appendix III for moment statistics calculations.

5.3.2 Organic carbon content

Loss-on-ignition (LOI) using the Stuart Muffle Furnace was undertaken to determine the proportion of organic carbon in each sediment sample. A sub-sample was oven dried at 50 °C. The sample was ground and weighed in a pre-weighted crucible to determine the dry weight of the sample. The sample was combusted in the Muffle furnace for 24 hours at 440 °C. An ignition temperature of 440 °C was chosen to minimise the overestimation of organic carbon content. LOI values may be overestimated due to losses of structural water from clay minerals, which may be significant at ignition temperatures above 450 °C, and the breakdown of carbonates, which may occur above temperatures of 500 °C (De Vos et al. 2005). Following combustion, the sample was re-weighed. Organic carbon content was calculated from the proportion the initial weight of the sample lost on ignition, given in Appendix IV.

5.4 RESULTS

5.4.1 Spatial distribution of surficial sediment characteristics

The grain-size distributions of the surficial sediments in Ahuriri Estuary were found to vary widely according to site. It was evident from the samples that there were combinations of clay, silt, sand and gravel modal peaks evident in the samples. Figure 5.3 illustrates the grain-size distribution for three sediment samples taken from very different energy environments. The grain-size distribution illustrated in Figure 5.3 A was taken in the upper Pandora intertidal region. As illustrated in Chapter Four, predicted current speeds in this area are low. This supports the deposition of silt, with the greatest modal peak evident for silt-sized sediment. Figure 5.3 B illustrates the grain-size distribution for a sample from the margin of the intertidal channel in the Westshore region. There are a number of modal peaks evident for clay, silt sand and gravel-sized sediments in this sample. This distribution was relatively unusual and was included here to illustrate the very fine clay-sized particles found in only 10 % of the samples.

Figure 5.3 C illustrates the grain-size distribution located directly adjacent to the Westshore barrier estuary margin. A relatively large proportion of the sediment was gravel and sand-sized sediment.

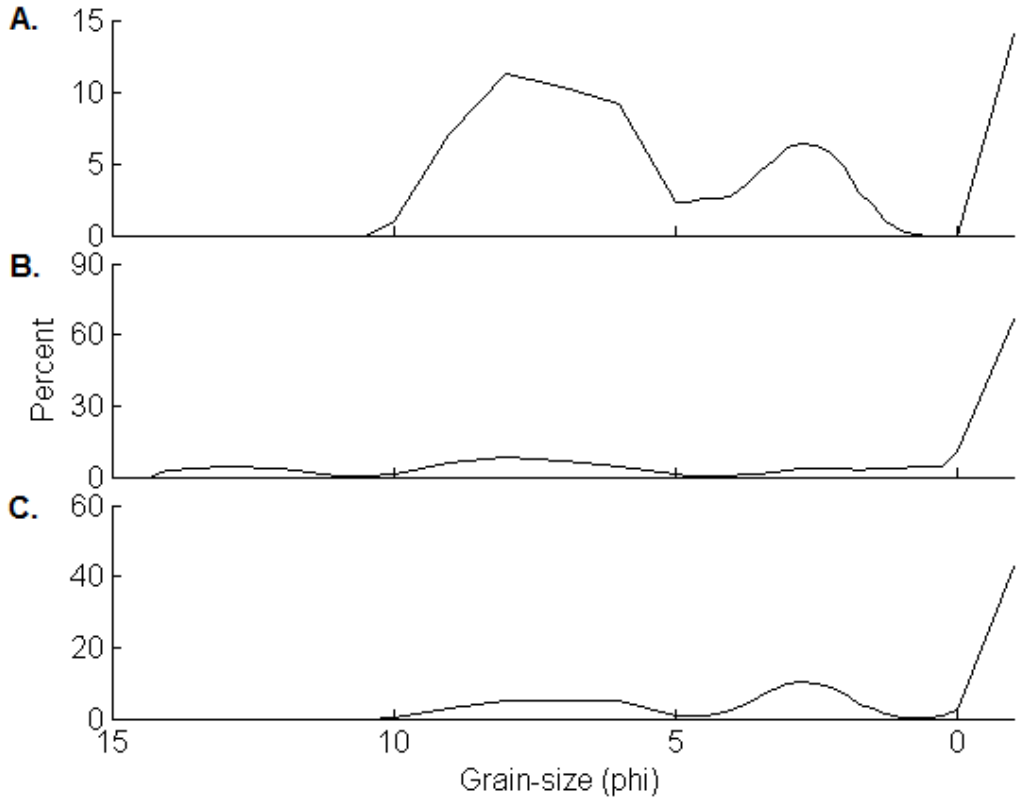

Figure 5.3 A. Grain-size distribution of sample taken from intertidal flat, sample 13C. **B.** Grain-size distribution of sample taken from intertidal channel, sample 3C. **C.** Grain-size distribution of sample taken adjacent to Westshore barrier, sample 1B.

5.4.1.1 Grain-size

The predominant grain-sizes present in the surficial sediment samples were classed according to the Wentworth size classification as gravel, fine to very fine sand, fine to very fine silt and clay. The presence of these size classes varied with spatial distribution throughout the middle sub-estuary. The mean grain-size was calculated for each of the samples including gravel content. It was evident that the largest grain sizes generally occurred in close proximity to the estuary margins. However, estuarine sediments often possess multiple modal distributions. Therefore, the mean grain size may be misrepresentative of the grain sizes contained in the sample. As the presence of gravel (and its associated weight percentage) greatly influences the mean grain size, gravel was excluded in mean grain-size distribution (Figure 5.4) and interpretation.

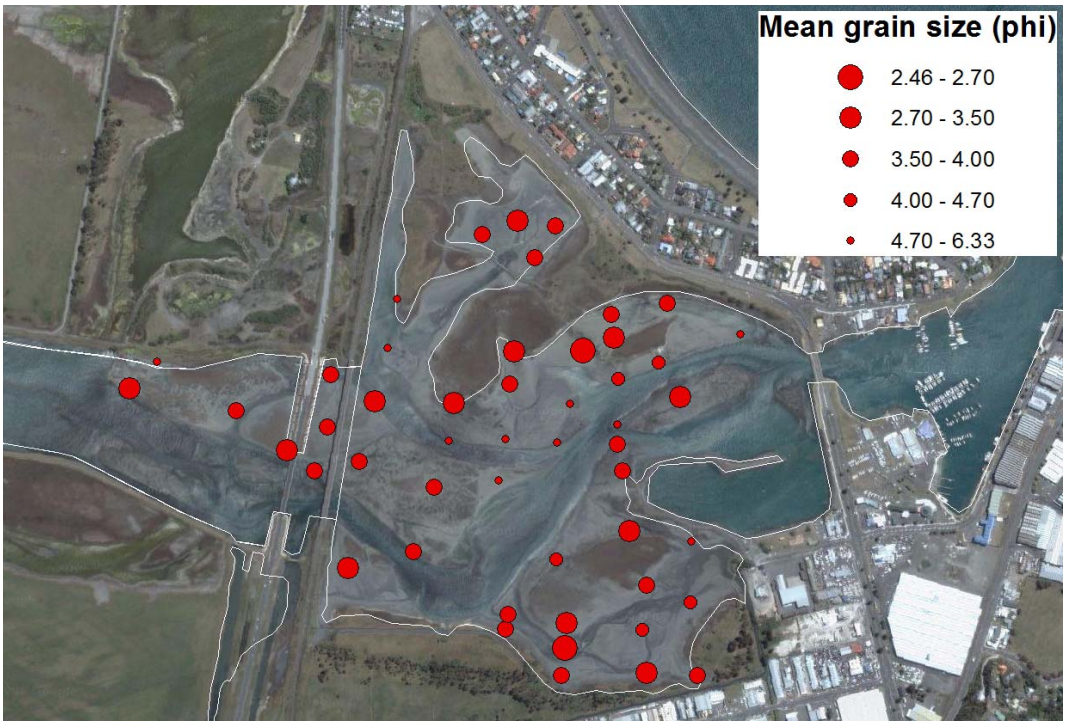

Figure 5.4. Mean grain-size (phi) of surficial sediment samples excluding the gravel content. Grain-size is indicated by the diameter of the marker as indicated in the legend.

The analysis of the spatial distribution of grain-size of surficial sediment in Ahuriri Estuary highlighted several large scale patterns. The most notable pattern was the largest mean grain-sizes were generally located in close proximity to the main tidal channel or intertidal channels. A closer inspection of the grain-sizes

represented at each of the sites identified a pattern in the distribution of sand and silt-sized particles. Silt-sized modal peaks were coarser in some regions in the Pandora intertidal region and sand-sized modal peaks were generally finest in the western-most reaches of the middle estuary and the lower reaches of the upper estuary. The sediment samples with the coarser modal peak in silt-sized sediments in the Pandora intertidal region were primarily located along the path of the main intertidal channel. Most of the surficial sediment samples contained clay-sized particles between 8 and 10 phi. Incidence of clay-sized particles finer than 10 phi were only evident in 10 of the 49 samples taken, all of which were located along an intertidal channel margin in the Westshore intertidal area and the adjacent main tidal channel. The presence of these fine clay-sized sediments greatly influenced the mean grain-size (Figure 5.4).

Sampling area 1 differed in grain-size distribution to the rest of the intertidal flat regions. The area was directly adjacent to the Westshore barrier, flanked on all sides by the estuary margin. Sand-sized sediments are also derived from the erosion of the estuary margin. Therefore, there was a large proportion of sand-sized sediments in these samples.

5.4.1.2 Sorting

The sorting of sediments sampled range from moderately sorted to extremely poorly sorted (Figure 5.5). This is a consequence of multiple modal peaks in the grain-size distributions. The spatial distribution of extremely poorly sorted sediments was generally inversely correlated with grain-size. A large mean grain-size generally resulted in better sorting. This is due to a large fraction of sand compared with silt and clay. Smaller mean grain-sizes were associated with modal peaks of silt and clay being present and were therefore relatively poorly sorted. The least poorly sorted sediments tend to be located adjacent to the main tidal channel or the intertidal channels. The presence of very fine clay-sized particles in samples along the margin of the main tidal channel resulted in the most poorly sorted sediments in Ahuriri Estuary.

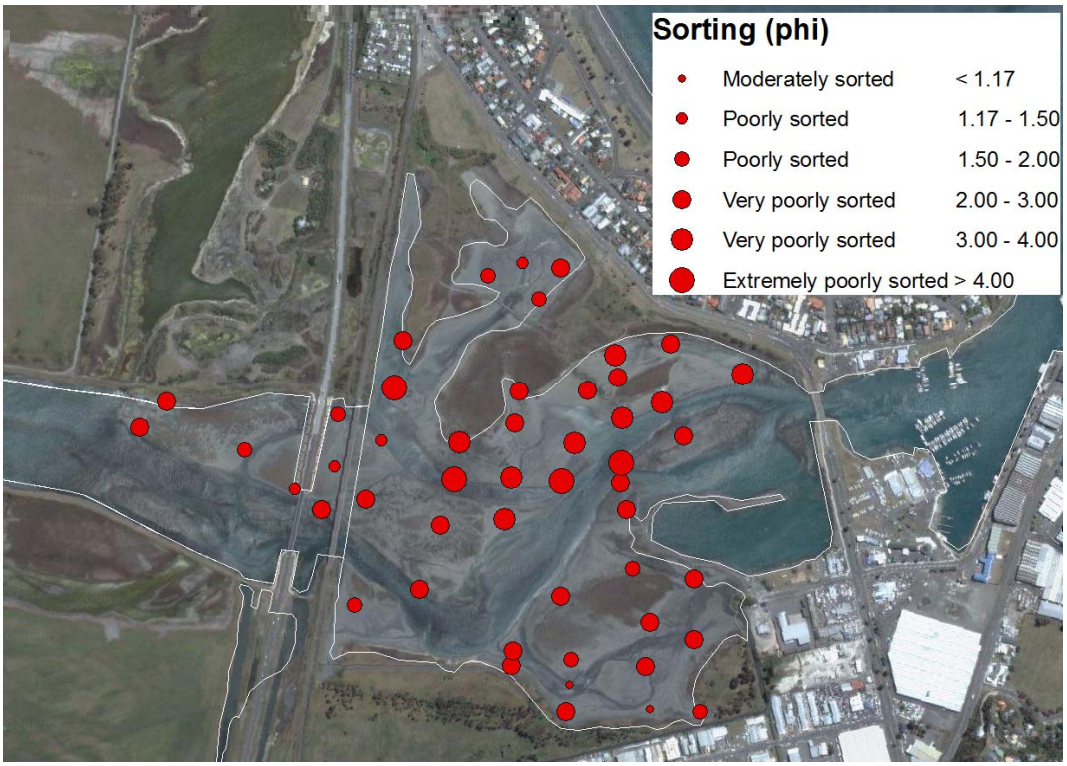

Figure 5.5. Sorting (phi) of surficial sediment grain-size distributions excluding gravel content. Degree of sorting is indicated by the diameter of the marker as indicated in the legend.

5.4.1.3 Skewness

The skewness of the sediment samples ranged from fine-skewed to strongly fine-skewed. It was evident in the spatial distribution that skewness was a function of grain-size. The presence of clay and silt-sized modal peaks influenced the skewness of the distribution. Increasingly coarse mean grain-sizes depicted in Figure 5.4 were shown in Figure 5.6 as increasingly fine-skewed. Conversely, increasingly fine mean grain-sizes were shown to be less fine-skewed.

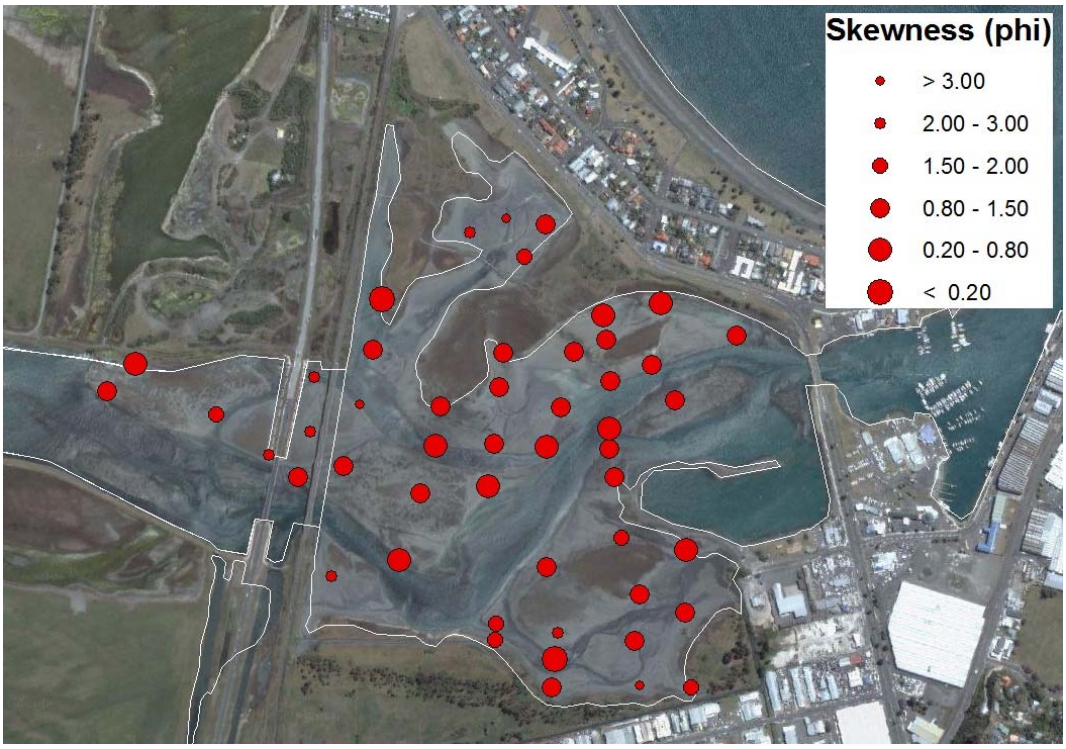

Figure 5.6. Skewness (phi) of surficial sediment grain-size distributions excluding the gravel content. Degree of sorting is indicated by the diameter of the marker as indicated in the legend.

5.4.2 Organic carbon content

Total organic carbon (TOC) content of the sediment samples ranged from 1.17 – 8.5 % of total dry weight. However, the majority of samples contained between 1.5 and 3.5 % organic carbon. The organic carbon content of the sediment was inversely proportional to mean grain size (Figure 5.7). A closer inspection of the grain-size distribution revealed that the TOC was correlated with the percentage of silt and clay.

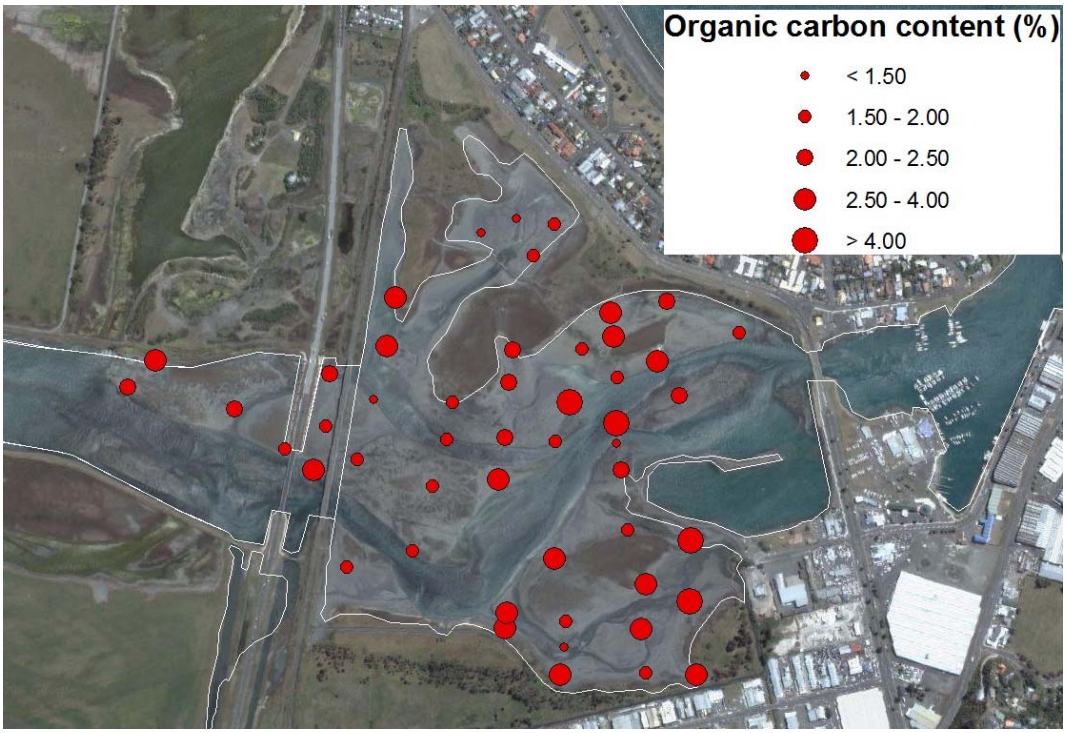

Figure 5.7. Organic carbon content (%) of surficial sediment samples. The percentage of organic carbon in sediment sample is indicated by the diameter of the marker as indicated in the legend.

Samples with low organic carbon content (i.e. less than 2 %) were generally located in relatively high energy environments, such as the main channel margins or adjacent to intertidal channels (Figure 5.7). These sediments had a lower proportion of silt and clay than sediments in low energy environments. However, sediment samples in the far northern reaches of the Westshore intertidal region showed low organic carbon content. This area is a relatively low energy environment. Sediment samples with relatively high organic carbon content (i.e. greater than 3 %) were located in relatively low energy environments, mainly close to the estuary margins and where there was no intertidal channel in close

proximity. The samples with the greatest percentages of organic carbon, samples 13B and 13C (See Figure 5.1), were located in the far reaches of the Pandora intertidal region, close to Pandora Pond. This is a very low energy environment, in the far reaches of tidal flow.

5.4.3 Temporal changes of surficial sediments

Monitoring sampling is undertaken annually by the HBRC at 3 sites which were chosen to best represent the estuary condition, as outlined in national assessment and monitoring protocol (Madarasz 2006). Sampling sites A, B and C are indicated in Figure 5.8. At each site, a grid of 60 m x 30 m was marked with 12 grid squares at each site. Within each grid square, a randomly located sample was taken. The geographical location of this randomly located sample was recorded for future sampling. However, the results for only 10 replicates were available for 2008, resulting in 10 replicates per site available for comparison between sampling years.

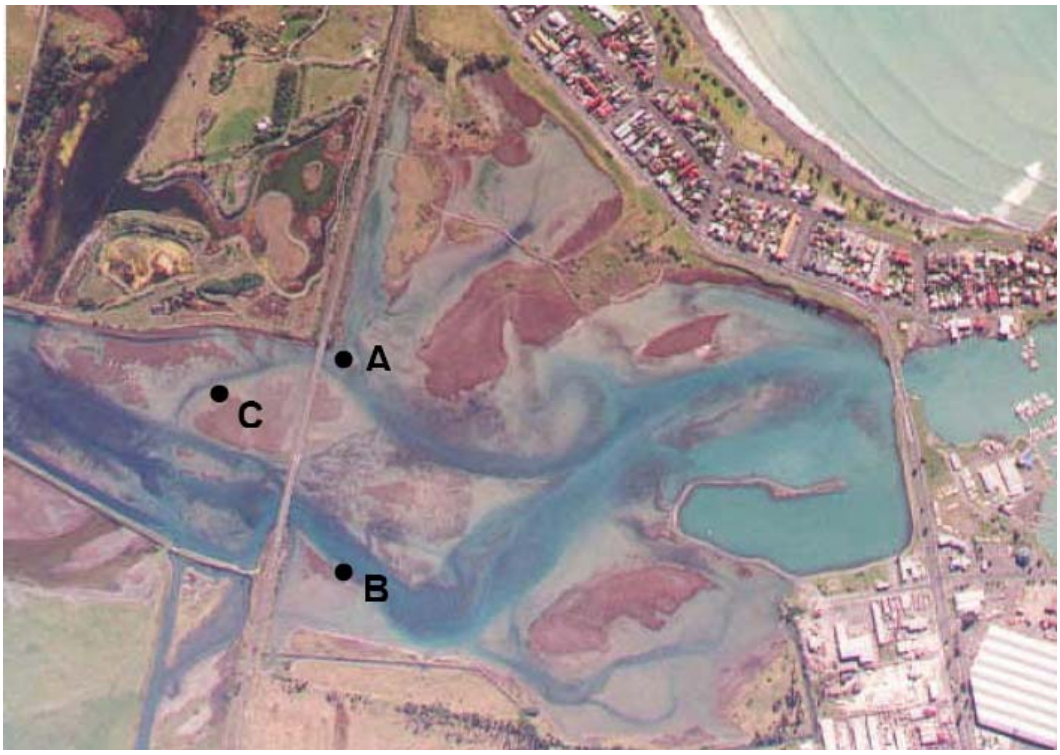

Figure 5.8. Hawke's Bay Regional Council (HBRC) monitoring sites. At each site, 12 replicate samples were taken from a grid cell 60 m x 30 m.

Historical data were compared to determine whether there has been a temporal change in the surficial sediment grain size distribution. Two years of data with corresponding sample locations were analysed in order to identify if there was a temporal change in the grain-size distribution. Figure 5.9 shows the percentage of sediment (wet weight) classed as gravel, sand and silt and clay for data collected during 2007 and 2008. Ideally a higher resolution dataset would be desirable for identifying trends in the temporal distribution of sediment, including a greater number of grain-size classes.

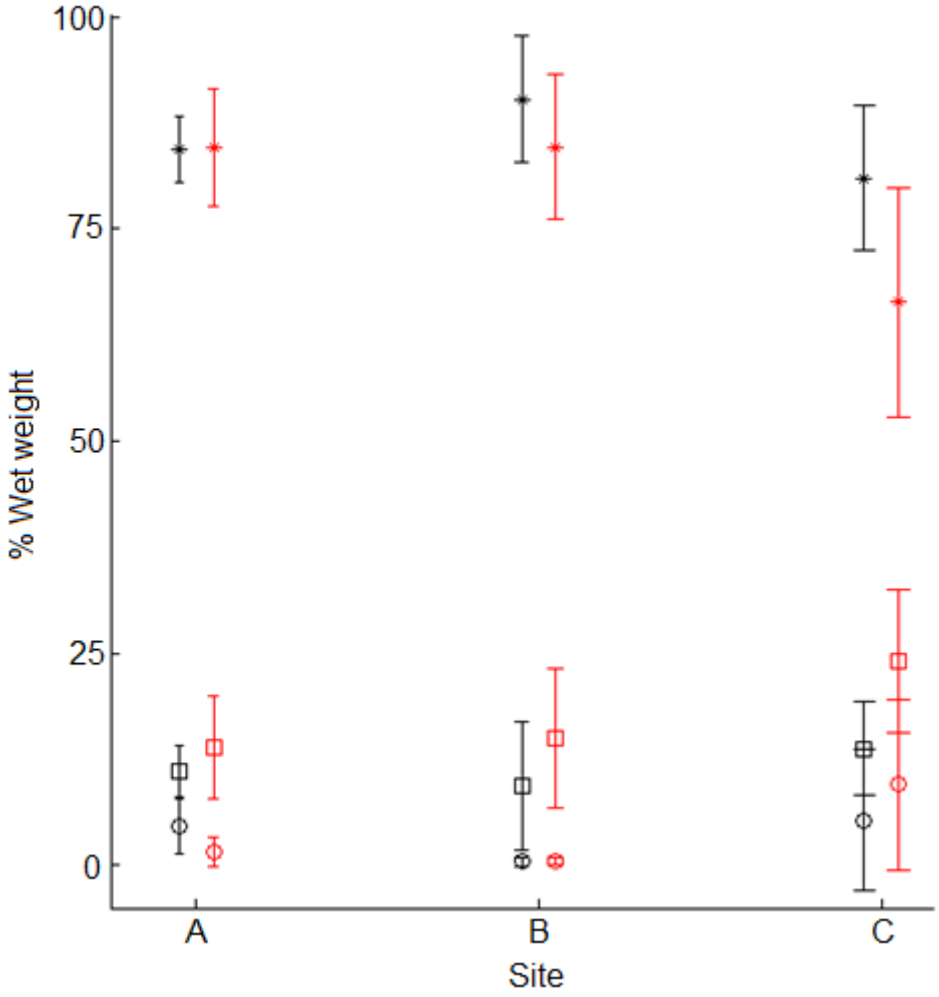

Figure 5.9. Grain-size classes for data collected during 2007 (red) and 2008 (black). Grain-size distributions have been condensed and classed as gravel (circles), sand (asterisks) and silt and clay (squares). Errorbars indicate one standard deviation.

There is the beginning of a trend evident in Figure 5.8. However, the variability within sampling years is greater than the variability between sampling years. There were differences in the mean percentage wet weight for each of the grain-size classes. As Figure 5.9 illustrates, there was an increase in silt and clay across all sites from 2007 to 2008. The greatest magnitude of change occurs at site C. The percentage of sand-sized sediment decreases from 2007 to 2008 at sites B and C, and remains relatively constant at site A. The percentage of gravel-sized sediment does not show considerable change at any of the sites and does not show a uniform behaviour across all sites. A longer dataset is required to make a conclusive assessment based on grain-size distributions of gravel, sand and silt.

5.5 DISCUSSION

5.5.1 Spatial distribution of surficial sediment characteristics

The grain-size distributions of samples in Ahuriri Estuary displayed numerous modal peaks of clay, silt, sand and gravel-sized sediment. A combination of 2-4 modal peaks was evident in the majority of the samples. This suggests that these sediments are derived from different sources and are locally derived. These sources are further discussed below.

Large percentages of gravel were evident in many of the samples taken from Ahuriri Estuary. The largest percentages of gravel were generally located in close proximity to the estuary margins or permanently exposed islands. This suggests gravel-sized sediments were locally generated from in-situ erosion of the Westshore shoreline, which was built by sand and gravel beach sediments and washover deposits (Komar 2007). Similar gravel-bearing deposits were identified in Raglan Harbour and were also attributed to shoreline erosion and lag and dump deposits from river inflow (Sherwood & Nelson 1979). Sand-sized sediments were also locally derived from the estuary margin. This was particularly evident in Sampling Area 1, where despite being a low energy environment the grain-size distributions were dominated by sand.

The spatial distribution of silt and clay-sized particles was correlated with the energy regime of the environment. Sediment samples with relatively low proportions of silt and clay were located adjacent to the main channel or main intertidal channels which "feed" the intertidal flats. At the channel edge, fine particles were winnowed away by the high energy tidal currents in the main channel. This leaves a greater proportion of the sediment as sand which was not transported from the site by tidal currents. The upper intertidal regions are shallow and consequently are much lower energy environments. This has allowed for the accumulation of fine sediment in these areas. In order to determine whether silt-sized particles are winnowed away in these intertidal channels, the shear velocity and subsequently Shields parameter are calculated based on the current velocities predicted in Chapter 3. Predicted tidal current velocities in these intertidal channels reached up to 0.5 $m.s^{-1}$ (refer Chapter 3, Section 3.6.2). Based on this

maximum current velocity, a shear velocity, u_*, was calculated according to Equation 5.1.

$$u_{*}=\sqrt{\frac{\tau_0}{\rho}} \qquad \text{Equation 5.1}$$

In order to calculate the shear velocity, the shear stress at the bed, τ_0, is required, calculated using Equation 5.2.

$$\tau_0 = \rho C_d \bar{u}^2 \qquad \text{Equation 5.2}$$

The maximum shear velocity induced by currents in these intertidal regions was calculated to be 0.015 $m.s^{-1}$ based upon a current speed of 0.5 $m.s^{-1}$ as modelled in Chapter Four. According to Figure 5.10, which was empirically derived, silt-sized particles will be eroded from these intertidal channel areas. Given the calculated shear velocity, the erosion threshold is exceeded, allowing for the winnowing of fine sediments from these areas. Whether sediment will move in these intertidal channels under tidal currents may be calculated by the Shields parameter for steady and quasi-steady flow (Equation 5.3).

$$\theta = \frac{\rho\, u_*^2}{(\rho_s-\rho)gD} \qquad \text{Equation 5.3}$$

Based grain-size for very fine silt of 3.9 μm, a Shields parameter of 1.8 was calculated. Dean and Dalrymple (2002) have illustrated that sediment is likely to move under steady flow if the Shields parameter is greater than 0.03. Therefore, the Shields parameter greatly exceeds the critical value for the entrainment of sediment into suspension. The samples with relatively high proportions of silt and clay were located in the centre of intertidal regions where the predicted tidal current velocities were low (i.e. 0.1 $m.s^{-1}$) to negligible. The shear velocities induced in these areas do not exceed the erosion threshold. For example, a current

speed of 0.1 $m.s^{-1}$ induces a shear velocity of 0.001 $m.s^{-1}$, which does not exceed the erosion threshold for any of the grain-sizes evident in Ahuriri Estuary (Figure 5.10). The Shields parameter given a current velocity of 0.1 $m.s^{-1}$ and a grain-size of 8 phi (3.9 μm) was calculated to be 0.01. Therefore, sediment deposited in these intertidal regions will not be eroded according to the criterion for incipient sediment motion (Dean & Dalrymple 2002) and are consequently areas of potential accretion. The Shields relationship and the relationship depicted in Figure 5.10 were derived for non-cohesive sediment, however. For very fine sediments, cohesion becomes important and the Shields relationship may no longer apply. Mehta and Lee (1994) suggest the calculation of critical shear stresses may only be applicable to sediments greater than 20 μm in diameter. There were sediments in the range of 0.05 – 20 μm in Ahuriri sediments which are likely to posses some cohesive properties. Fine silts (8 – 32 μm) were evident in considerable percentages of total grain-size distribution. However, these have been defined by van Rijn (2007) as weakly cohesive. Volumes of clay-sized sediment were generally less than 10 % in Ahuriri sediments, also weakly cohesive, and very fine clays were only evident in approximately 10 % of samples. Therefore, the use of the Shields relationship is generally applicable in Ahuriri Estuary.

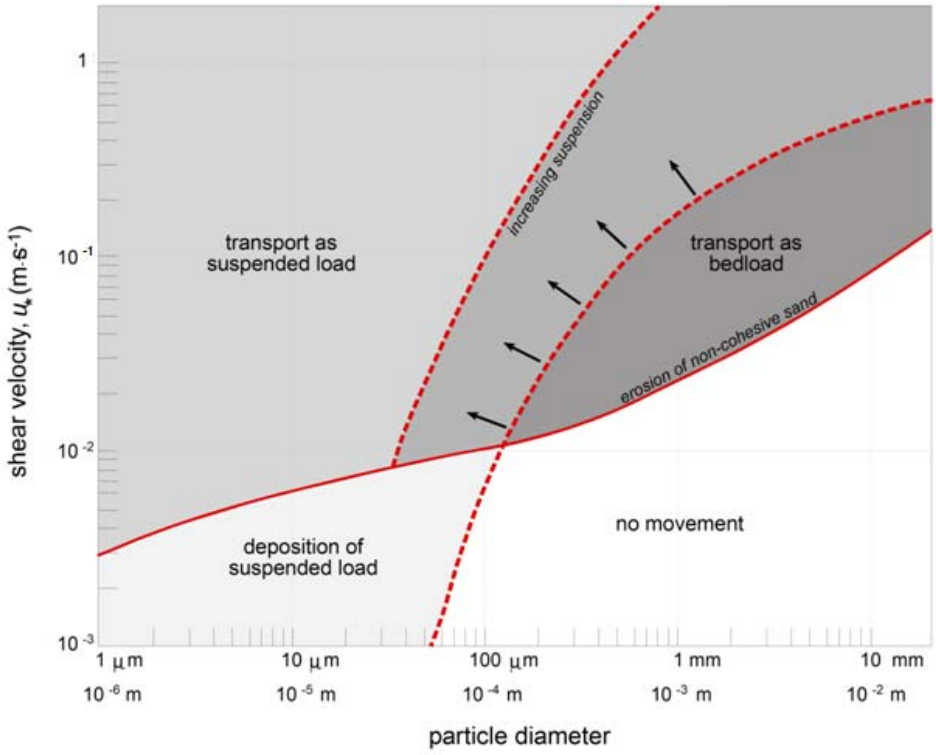

Figure 5.10. Empirically derived diagram showing the shear velocities at which non-cohesive sediment particles are eroded, transported and deposited. From Bearman (1989).

There were differences in the grain-size distributions between intertidal regions on the northern (Westshore) and southern (Pandora) sides of the main channel. The coarsest modal peak of the silt fraction was found in the sediment samples from the Pandora intertidal region, along the path of the main intertidal channel. This indicates that the coarser silt-sized sediment was transported by tidal currents in the intertidal channel, and finer silts were winnowed by the currents. The finest modal peak of the sand fraction was found in samples located in the western-most reaches of the middle estuary and the lower reaches of the upper estuary. This sand-sized sediment corresponds to the size of the sand in the numerical modelling investigations (Chapter Four). Fine sand introduced into the estuary at the mouth of the Taipo Stream was flushed downstream by the freshwater discharge and the outgoing tide. The numerical modelling of fine sand showed a large proportion was predicted to settle out of suspension before it is transported to the lower reaches of the upper estuary and the middle estuary. As discussed in Chapter Four, the initial transport of sand is highly influential in its ultimate depositional location. Sediment which is initially transported downstream from the source site and settles out of suspension is likely to be further transported on

the subsequent outgoing tide. It is expected that the finer sand will initially be transported further during the first tidal cycle following release into the estuary, perhaps to a location where secondary re-working of sediment is unlikely or sporadic. However, as indicated in Chapter Four, this process is likely to be highly influenced by the timing of sediment release in the tidal cycle. Coarser sands which settle out of suspension in the upper estuary and subsequently transported downstream on the following outgoing tide are likely to be transported further downstream, as they are resuspended early in the outgoing tide. This allows for a longer duration for downstream transport. Sediment reaching the middle estuary is likely to either be transported through the middle estuary with the tide through the main tidal channel, or be flushed into intertidal areas following the reversal of the tide. There is also increased incidence of winnowing of finer sediment the further downstream sediment is transported (McCave 1978). This results in a trend of increasing sand sizes in the samples along the Westshore intertidal area from upstream to downstream.

The sorting of sediments is a function of the grain-size distribution. Therefore, as the majority of samples taken from Ahuriri Estuary contained significant percentages of sand, silt and in some instances, clay, the sediments ranged from moderately sorted to extremely poorly sorted. The poorly sorted nature of the sediments suggests that the sediments are not transported significant distances, as transportation of sediments generally results in better sorting. In the instance where a significant proportion of clay was present in the grain-size distribution, mean grain-size and sorting were greatly influenced. The presence of a large proportion of clay-sized particles may often be attributable to high organic carbon content. The removal of organic material prior to particle size analysis was not undertaken. In order to achieve complete dispersion of the clay fraction in sediment samples, it is desirable to remove organic matter to prevent it from being included as part of the clay-sized particles of the sediment sample (Poppe et al. 2003). However, the sediment samples for which large proportions of clay-sized particles were present did not have particularly high organic carbon contents, ranging from less than 1.5 % to 4 %. The samples with very fine clay particles (i.e. 11 – 14 phi) which were all located along a particular flow path did not show particularly high organic carbon content. This suggested that the measurement of

clay in these particular samples is not an artefact of laboratory techniques but rather suggests a point source of very fine sediments entering the estuary. It is hypothesised that a point-source of freshwater containing fine clay-sized particles was discharged relatively recently prior to sediment sampling. The presence of this fine clay-sized sediment follows the path of the main Westshore intertidal channel and continues downstream along the margin of the main channel, limited to the Westshore side only. This follows a likely downstream pattern, which further supports the hypothesis of a point-source. A possible point-source is from the Westshore Lagoon, which is connected to the main outfall channel by a culvert. Flow from this culvert is likely to flow under the Highway Bridge and through the main intertidal channel, following the same path as the sediment samples which exhibit these fine clay-sized particles. Surficial sediments are reflective of recent sedimentological events. Another possible reason for the presence of clay in these samples may be from a recent depositional event. However, rainfall data prior to sampling does not indicate an event which would result in sediment influx into the estuary and the very clear path of samples with clay present does not support this. Temporal data would enable a more conclusive explanation.

The inference of sediment transport using a grain-size trend analysis is based upon trends as a result of sediment transportation. As previously mentioned, the local derivation of sediments and the short transport distances result in grain-size distributions, sorting and skewness which are not a function of sediment transport only. Therefore, the derivation of sediments from local sources does not support the application of a grain-size trend analysis in this study. However, a fining of sediments from high energy to low energy environments is evident. This suggests a net fining in the direction of transport often observed in other coastal environments (McCave 1978).

5.5.2 Organic carbon content

The organic carbon contents of surficial sediment samples taken from Ahuriri Estuary were relatively low. Most of the samples contained approximately 1.5 – 3.5 % total organic carbon. The maximum organic carbon percentages were found in the very far reaches of the Pandora intertidal region. Areas where the organic carbon content was relatively high in relation to other areas included the Pandora intertidal region (where the maximum organic carbon contents were located) and the central Westshore intertidal region. These areas are low energy environments where sediment is unlikely to be reworked following deposition. Samples taken from high energy environments such as the channel main channel margin tended to have low organic carbon contents (i.e. less than 2 %). These areas included samples taken in close proximity to intertidal channels. This indicates that the tidal currents rework the sediments, dispersing organic carbon from the sediment.

The spatial distribution of total organic carbon in estuarine sediments is usually correlated with the percentage of silt and clay sized sediment (Li et al. 2007), as was the case in this study. Although there was a general trend evident in the data which suggests organic carbon content is inversely proportional to the tidal energy of the environment, this general rule does not hold true for all of the sediment sample locations in Ahuriri Estuary. Sampling area 1 is a low energy environment with large proportions of fine sand. There was a large percentage of sand-sized sediment and a low content of organic carbon evident in these sediments. This low organic carbon content is attributable to the low proportions of silt and clay in the sediment at this site. High organic carbon content was evident in sediments with significantly higher percentages of silt and clay than sediments with low total organic carbon content. Similar correlations were evident in surficial sediment studies carried out by Li et al. (2007) in the Xiamen Bay, China and in Raglan Harbour, New Zealand (Sherwood & Nelson 1979). The spatial distribution in TOC was evidently a function of the percentage of the fine fractions (silt and clay) in the sediments. Duman et al. (2004) also identified the main depocentre in Izmir Bay, Turkey, inferred from surficial sediment analysis, had the greatest TOC content in the bay.

5.5.3 Temporal changes in surficial sediments

Analysis of historical data collected by HBRC for the years 2007 and 2008 identified a possible overall trend of a fining of the sediments at the three sampling locations. Site A in the HBRC study corresponded with samples 2B and 2C in this study. These samples contain very fine silts, in the range of the smallest silts found in the estuary, and a relatively high TOC content. Site B corresponded with sample 9A in this study, which contained no gravel and a low volume of clay-sized sediments. It has a bimodal distribution of fine to very fine sand and fine to very fine silt. Sand-sized sediments here were finer than the remainder of the Pandora intertidal area. Site C in the HBRC study corresponded with sample 15D in this study. This sample had slightly finer silts than the surrounding intertidal area and moderate organic carbon content. The findings from the past and present sedimentological studies suggest these three sites are likely depositional environments. The temporal changes in the sediment at these three sites also support the hypothesis that Ahuriri Estuary is primarily a depositional environment, according to the predicted sediment dynamics in Chapter Four. Chagué-Goff et al. (2000) calculated sedimentation rates at three sites in Ahuriri Estuary based on sediment core data. The highest sedimentation rate of 6.1 $mm.yr^{-1}$ was calculated from a core located in the Westshore intertidal area. Sediment samples taken in this region for this study displayed a high organic carbon content and incidence of fine sediment, suggesting sediment accumulation.

As discussed in Section 5.4.1, the surficial sediment characteristics are highly influenced by recent events. In Chapter Four, the transport pathways and ultimate depositional location of sediment released into the estuary following a storm were highly dependent on the timing in the tidal cycle, extent of freshwater inflow and the grain-size of the sediment. As the HBRC sampling regime aims to predict changes in the mean sediment characteristics, the sampling regime should include information regarding the conditions prior to and during the sampling period. This information should include recent storm activity, precipitation and possibly gauging of the Taipo Stream. Analysis would also benefit from a greater number of grain-size classes or divisions. The classification of percentage of sand, silt and clay only may conceal trends within each class.

5.5.4 Inference of sediment dynamics

Areas of potential accretion, erosion and winnowing are identified based on the grain-size distribution, organic carbon content and historical changes in sediment grain-size, as discussed in the previous sections. These areas were combined to produce a conceptual model of inferred sediment dynamics in the lower region of Ahuriri Estuary (Figure 5.11). The conceptual model indicates areas of potential erosion or winnowing of the fine sediments, areas of potential accretion, and the dominant sediment transport pathways. The boundaries between areas of transport, erosion and accretion were based upon depth contours.

Areas of winnowing or potential erosion were identified by low incidence of silt and clay proportions, along with low organic carbon content. In areas such as the main intertidal channel margins which "feed" the intertidal flats, current speeds of up to 0.5 $m.s^{-1}$ were modelled (refer Chapter 3, Section 3.6.2). Analysis of the Shields parameter for silt under such current velocities indicated that silt would be winnowed from these areas. Low energy environments, such as the intertidal flat regions, experienced very low to negligible current velocities. Predicted current speeds in such environments were 0.1 $m.s^{-1}$ or less. The Shields parameter calculated for silt in these environments did not exceed the critical value for suspension, indicating these environments were areas of potential accretion.

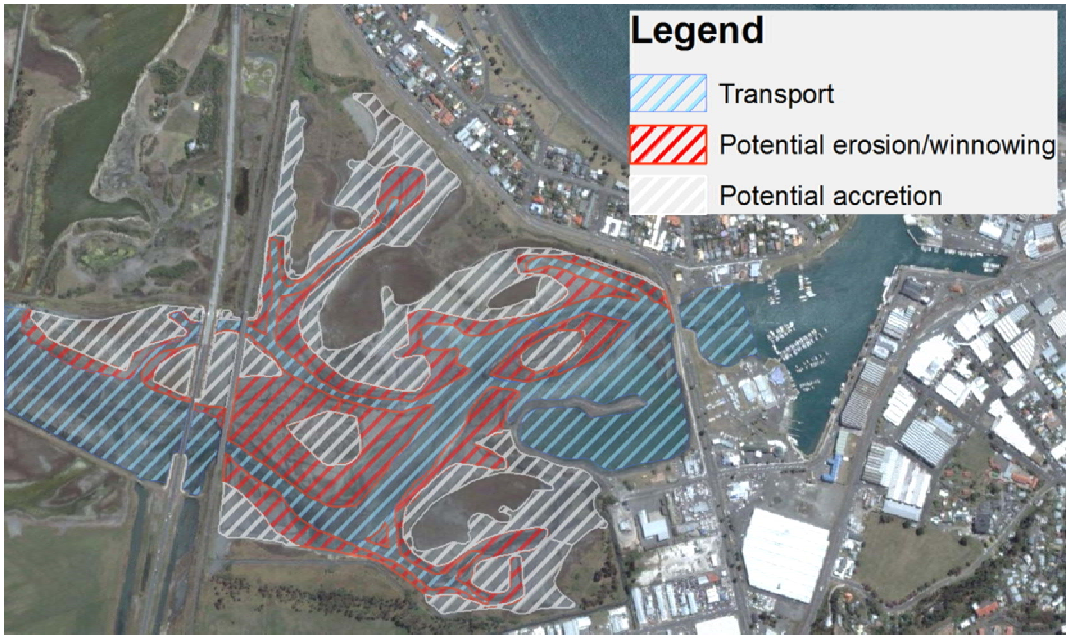

Figure 5.11. Conceptual model identifying areas of potential erosion, accretion and the dominant transport pathways, inferred from surficial sediment parameters.

TOC is a good indicator of potential erosion or accretion as it is inherently associated with fine sediments (Sherwood & Nelson 1979; Duman et al. 2004; Li et al. 2007). Areas of potential accretion were according to the same principles. A high TOC was associated with greater silt and clay proportion in the sediment. Greater TOC and proportions of fine sediments were located in low energy environments, mainly in the far reaches of intertidal areas, where the intertidal channels did not penetrate.

The exception to the aforementioned hypothesis was the incidence of very fine clay (in the range of 11 – 14 phi) in less than 10 % of the sediment samples taken from the middle sub-estuary. The locations of these samples followed a particular path, suggesting a point-source and recent downstream transport. Due to a low TOC content, it is unlikely that other influences such as biostabilisation have maintained the presence of clay in these samples.

Continued sediment sampling would allow for the identification of both spatial and temporal changes, and would help identify such point-sources of particularly fine clays and sediment grain-size distribution anomalies. Sampling of the Westshore Lagoon would allow for the confirmation of the supply of clay-sized sediment.

5.6 CONCLUSIONS

The surficial sediment analysis carried out in Ahuriri Estuary allowed for the inference of areas of potential erosion and accretion and the predominant sediment transport pathways in the middle estuary. From the spatial distribution of grain-size parameters and TOC the following conclusions were drawn:

- Sediments are derived from multiple sources, some of which are locally derived, such as gravel and sand from erosion of the Westshore barrier estuary margin.
- There were four different sedimentary regimes identified within the estuary;
    - Intertidal flat – low current velocities, high TOC, high abundance of silt-sized sediment.
    - Intertidal flat near Westshore barrier – low current velocities, low TOC and high abundance of locally derived sand and gravel from erosion of estuary margin.
    - Channel edge / Intertidal channel edge – high current velocities, low TOC, low abundance of silt-sized sediment.
    - Clay Anomaly – very fine clay-sized sediment located along a particular flow path suggesting a point-source.
- The HBRC sampling regime should include information such as precipitation prior to sampling period, as surficial sediment characteristics are highly variable dependent on conditions immediately prior to sampling (as discussed in Chapter Four). The resolution of the grain-size classes should also be increased to allow for the identification of trends within the main grain-size classes.
- Past and present sedimentological studies suggest Ahuriri Estuary is a depositional environment, mainly in intertidal regions in the middle and lower reaches of the upper estuary, supported by high TOC content and incidence of silt and clay.

A conceptual model was developed based on the above conclusions to identify areas of potential erosion and accretion and the main sediment transport pathways within the estuary. In Chapter Six, the conceptual model is compared with the modelled sediment dynamics as predicted in Chapter Four.

The comparison of the two techniques provides some validation of each of the models and a more comprehensive understanding of the sediment dynamics of Ahuriri Estuary.

CHAPTER SIX
WAVE-RELATED PROCESSES AND CONCEPTUAL MODEL

6.1 INTRODUCTION

The small, complex geometry of the estuary limits available fetch distances, thereby limiting local wave generation. However, despite these small fetch distances, small wind waves are often observed at times of high wind velocities. These small waves generate turbidity at the channel margins. Evidence of locally generated waves suggests the post-depositional redispersal of sediment may have an important role in the sediment dynamics of Ahuriri Estuary. Therefore, an investigation into locally generated waves was carried out to estimate the magnitude of sediment resuspension from oscillatory currents under waves.

The redispersal of sediments by wave-related processes will be combined with the findings of the numerical modelling of sediment transport and the inference of sediment dynamics from surficial sediment characteristics to produce a conceptual model. This conceptual model aims to characterise how the estuary behaves as a processor of sediments. Sediment transport patterns and areas of potential erosion and accretion are identified, which may be used in the development of management strategies for the estuary.

In this chapter the post-depositional processes due to locally generated waves and the subsequent bed shear stresses are predicted. A final discussion of the sediment dynamics is presented, incorporating the numerical modelling and surficial sediment analysis to produce a conceptual model.

6.2 SEDIMENT REMOBILISATION BY WAVES

6.2.1 Background

In environments where sufficient fetch allows for the generation of local waves, oscillatory currents are a major physical forcing of sediment transport, particularly in shallow environments with low tidal current velocities such as intertidal areas (Bell et al. 1997; Green et al. 1997; Dolphin 2004; French et al. 2008; Fagherazzi & Wiberg 2009). Green et al. (1997) found that turbidity in intertidal areas was controlled by the presence of waves and suspended sediment concentrations were well-predicted by a wave model alone. However, in estuarine environments the local generation of waves on tidal flats and intertidal areas is coupled with the tidal cycle. The rise and fall of the tide controls available fetch for wave generation, due to the submergence and emergence of intertidal areas. Wave-induced resuspension is not only due to the wave height and consequently the wave orbital velocity at the bed, but also the depth of the water. Sufficient water depth for the attenuation of wave orbitals limits wave resuspension. At high tide, increased fetch is modulated by the increase in water depth (Fagherazzi & Wiberg 2009). A maximum turbidity induced by waves is often present in the intermediate region between the progressive tidal edge and the tidal channel (Green et al. 1997). Here the wave orbital velocities are sufficient to penetrate to the bed but the water depth is not sufficient to attenuate these orbital currents. At the progressive edge of the tidal wave on an intertidal flat, friction prevents the formation of wave orbital velocities, but wave breaking may result in a "turbid fringe" of the water body (Green et al. 1997). In the tidal channel, small wind wave orbital velocities are likely to be attenuated and unable to penetrate to the bed.

6.2.2 Methods

Fetch distances were calculated for the prevailing wind directions of south-west and westerlies (refer Chapter Two). For a south-westerly wind, the greatest fetch distance crosses the middle estuary. For a westerly wind, the greatest fetch runs along the length of the upper estuary. Both fetches are limited to high-tide for a

period of approximately 4 hours due to the presence of intertidal areas (Figure 6.1).

Figure 6.1. Maximum fetch distances corresponding to the dominant wind directions. A westerly wind has a maximum fetch along the main outfall channel in the upper estuary. A south-westerly wind has a maximum fetch across the middle estuary. Both fetch distances are limited to high tide when intertidal regions are inundated.

Eastings and northings of the maximum distances of available fetch were calculated using Pythagoras Theorem to determine the distance between two points, marking the maximum distance of the water surface for which the wind may act upon. Wind speeds were obtained from the NIWA CliFlo database. Data were averaged over a period of one year to give a maximum gust speed of 15.8 $m.s^{-1}$ and a mean wind speed of 3.8 $m.s^{-1}$. Although the maximum gust speed is not generally maintained for a long period of time, it is used here in a conservative approach to local wave generation. Significant wave height and period for prevailing wind conditions were then able to be calculated given the fetch distance. Equation 6.1 was used to evaluate whether local wave generation in Ahuriri Estuary were duration or fetch limited.

$$D_{crit} = 1.167 \frac{F^{0.7}}{U^{0.4}} \qquad \text{(Equation 6.1)}$$

Where D_{crit} is the duration threshold (hr), F is the fetch length (km) and U is the wind velocity (m.s^{-1}). If the measured duration of wind conditions exceeds the critical duration, D_{crit}, the conditions are fetch-limited. As the measured duration has a maximum high tide period of 4 hours, according to D_{crit}, conditions in Ahuriri Estuary were fetch limited and a growing sea, determined by Equation 6.2.

$$F < 2.32U^2 \qquad \text{(Equation 6.2)}$$

If yes, the conditions are that of a growing sea. If not, the sea is fully developed. Given this information, a series of empirically derived equations are available for the calculation of significant wave height, H_s (Equation 6.3) and period, T_p (Equation 6.4), assuming a monochromatic wave field (Carter 1982).

$$H_s = 0.0163U\sqrt{F} \qquad \text{(Equation 6.3)}$$

$$T_p = 0.566U^{0.4}F^{0.3} \qquad \text{(Equation 6.4)}$$

In order to determine sediment resuspension from the bed by waves in the upper and middle estuaries, the bed shear stress induced by these locally generated waves is required. This is calculated for oscillatory flow by Equation 6.5.

$$\hat{\tau} = \frac{1}{2}\rho f_w(A\omega^2) \qquad \text{(Equation 6.5)}$$

Where $\hat{\tau}$ is the bed shear stress under oscillatory flow, ρ is the density of seawater, A is the orbital radius and ω is the radian frequency. The calculation of bed shear stress requires the wave friction factor, f_w, determined by Equation 6.6.

$$f_w = exp\left[5.213\left(\frac{r}{A}\right)^{0.194} - 5.977\right] \qquad \text{(Equation 6.6)}$$

Where A is the orbital amplitude above the boundary layer and r is the hydraulic roughness, which is approximated by $r = 30\ Z_0$, where Z_0 is the Nikuradse Bed Roughness (Equation 6.7) which characterises hydraulically rough flows.

$$Z_0 = \left(\frac{1}{30}\right) D \qquad \text{(Equation 6.7)}$$

Where D is the grain size (mm). Given these parameters, the Shields parameter may be calculated (Equation 6.8) to determine whether sediment will be entrained into suspension by the bed shear stress induced by the oscillatory currents under locally generated waves.

$$\theta = \frac{\hat{\tau}}{\rho(s-1)gD} \qquad \text{(Equation 6.8)}$$

Where s is the relative density of sediment ($s = \rho_s/\rho$), assuming a sediment density of quartz sand (2640 kg.m^{-3}) and density of seawater of 1520 kg.m^{-3}.

6.2.3 Results

The predictive equations for local wave generation (Carter 1982) were used to determine whether sediment will be resuspended by waves during storm conditions, based on the environmental conditions summarised in Table 6.1.

Table 6.1. Environmental conditions used in the equations for the prediction of H_s and T_p.

Sub-estuary	Fetch distance (m)	Average depth (m)
Upper estuary	3025	0.9
Middle estuary	1017	1

Significant wave height and period were calculated for both the mean wind speed and maximum gust speed given the fetch distance and average depth along the fetch distance for both of the estuarine environments. These values are given in Table 6.2. From these wave characteristics, the bed shear stress and subsequently the Shields parameter were calculated for each of the wave characteristics in Table 6.2. Figure 6.2 shows the Shields parameter values for each of the scenarios. In order to determine whether sediment will be resuspended under these particular wave characteristics, the critical Shields parameter, Θ_c, was calculated according to Equation 6.9 and Equation 6.10, derived by Soulsby and Whitehouse (1997).

Table 6.2. Significant wave height, H_s, and period T_p, for the upper and middle estuaries are given for both maximum gust and mean daily wind speeds.

	Upper estuary		Middle estuary	
Parameter	*U* (max gust)	*U* (mean daily)	*U* (max gust)	*U* (mean daily)
H_s (cm)	45	10	26	6
T_p (s)	2.4	1.3	1.7	0.97

$$\theta_c = \frac{0.3}{1+1.2\,D_*} + 0.055\left(1 - exp(-0.020 D_*)\right) \qquad \text{(Equation 6.9)}$$

$$D_* = \left[\frac{g(s-1)}{v^2}\right]^{1/3} d_s \qquad \text{(Equation 6.10)}$$

The three grain-sizes investigated in Chapter Four, 10 µm, 60 µm and 105 µm were used in this investigation. The critical Shields parameters were calculated to be 0.04, 0.055 and 0.056 respectively. These are shown in Figure 6.2 as $\Theta_{c,silt}$ for the 10 µm grain-size and $\Theta_{c,sand}$ for the 60 µm and 105 µm grain-sizes.

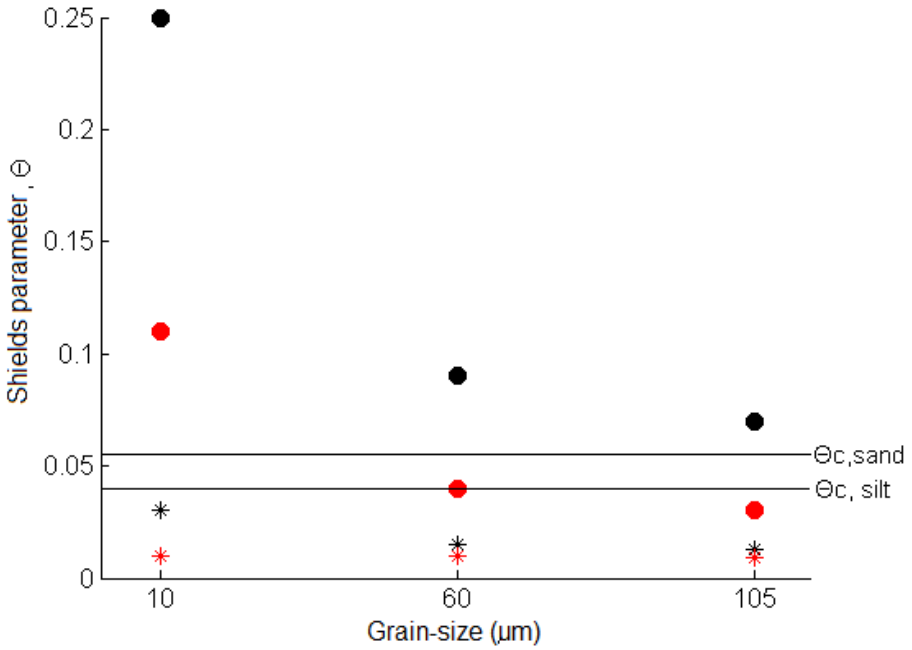

Figure 6.2. Shields parameter. Solid circles indicate waves generated by maximum wind gust velocity, asterisks indicate waves generated by mean daily wind velocity. Red symbols indicate waves generated in the middle estuary, and black symbols indicate waves generated in the upper estuary. $\Theta_{c,sand}$ delineates the critical Shields parameter for sand entrainment, $\Theta_{c,silt}$ for silt entrainment.

Figure 6.2 illustrates that waves generated by mean daily wind will not induce shear stress capable of resuspending both sand and silt-sized sediments, as the Shields parameter did not exceed the threshold for sediment entrainment. Maximum gust wind velocities induce shear stress capable of resuspending sediment of both sand and silt-sized sediments in the upper estuary. In the middle estuary, maximum gust wind velocities are capable of resuspending silt-sized sediment. Fine sand in the middle estuary will not be resuspended.

6.2.4 Discussion

The critical Shields parameter, calculated by the equations derived by Soulsby and Whitehouse (1997), determines whether sediment will be eroded by oscillatory currents under waves. The equation reportedly performs relatively well for both sand and silt-sized particles. However, Dolphin (2004) found that silt-sized particles were resuspended in considerable volumes during periods of wave activity when the Shields parameter exceeded the critical Shields parameter for sand. van Rijn (2007) also suggests that the erosion of sand particles is the

dominant mechanism, where silt and clay-sized particles are washed out together with sand particles. This indicates the armouring of the fine silts, producing a very similar critical entrainment threshold for silt and sand. However, this is likely dependent on recent sedimentological events. As illustrated in Chapter Four, silt deposition is evident in intertidal regions following sediment influx during a storm event. Following a depositional event of silt-sized sediment, insufficient time for reworking will result in the superposition of fine silts on underlying bed sediments. This sediment will not be armoured by larger sand-sized sediment. Therefore, the critical threshold for entrainment by waves will be lower directly following a depositional event. Sediment will be more easily mobilised due to low compaction and low incidence of sand, and consequently no armouring of the fine sediment.

Mean daily wind speeds did not produce waves with sufficient orbital currents to induce sediment resuspension in the middle estuary. This is primarily a function of the very limited fetch distance of 1017 m. Bell et al. (1997) found low wind speeds (i.e. <5 $m.s^{-1}$) produced wind waves sufficient to rework sediments to a depth of 2 cm. Fetch distances in this study were in the order of 20 km at high tide. Waves of this magnitude are not generated in Ahuriri Estuary under the prevailing wind conditions due to limited fetch. The maximum gust wind velocity did produce waves capable of sediment resuspension in the upper estuary and in the middle estuary for silt-sized sediments only. However, this is a conservative estimation of the maximum possible wave heights, using maximum gust winds. French et al. (2008) measured SSC of up to 600 $mg.l^{-1}$ during winds of 10–14 $m.s^{-1}$ which is considerably lower than the maximum gust speeds used in this study. However, fetch distance must be considered. Maximum gust wind is unlikely to be maintained at such a velocity or the duration of high water. However, Bell et al. (1997) also found that sediment was continually reworked by waves with a significant wave height in the order of 0.09 m. Mean winds in the upper estuary were shown to be capable of producing 0.10 m waves. As discussed in Chapter Two, historical surveys document a degradation of the bed in the upper half of the main outfall channel over time. As currents alone were incapable of resuspending sediment in the upper reaches of the main outfall channel, this must

be attributable to wave action. These surveys also identified net accretion in the middle estuary where wave generation is limited by small fetch distances.

Following the resuspension of sand and silt under oscillatory currents, the net transport of the resuspended sediment is a function of the tide (Green et al. 1997; Green & MacDonald 2001; Dolphin 2004). Just as timing of sediment release in the tidal cycle had a large influence on the transport and ultimate depositional location (refer Chapter Four, Section 4.4.3), the same principle applies to resuspended sediment by wave action. Sediment resuspended by waves prior to high tide is likely to be retained in the intertidal region. The sediment will be flushed further into the intertidal region with the incoming tide. This occurred with suspended sediment plumes upon tide reversal. At high-water slack, the sediment will likely settle out of suspension. For fine sand, sediment was calculated to settle out of suspension in only 16 minutes (refer Chapter Four, Section 4.4.3). Therefore, it is unlikely to be transported a considerable distance from the site of resuspension during high water. Wave-induced resuspension during the outgoing tide may be transported via intertidal channels into the main tidal channel. Tidal current velocities were in the order of 0.5 $m.s^{-1}$ in the main intertidal channels which drain the Westshore and Pandora intertidal regions. The Shields parameter for silt under this current velocity was calculated in Chapter 5 (refer Section 5.5.1) as 1.8. This greatly exceeds the threshold for movement of the bed, which is approximately 0.03, dependent slightly on the Reynolds number (Dean & Dalrymple 2004). Therefore, sediment will remain in suspension in these intertidal channels following the resuspension by wave oscillatory currents at mid-tide. Measured current velocities in the main tidal channel reached a velocity of 0.76 $m.s^{-1}$ during spring conditions. Current velocities of this magnitude will ensure turbulence maintains sediment in suspension, and may result in net transport of the sediment from the estuary. The presence of waves also prevents sediment from settling out of suspension, thereby aiding sediment transport (Green & Coco 2007). Sediment resuspension by waves in the upper intertidal region may not result in any net transport as predicted tidal currents were low in these regions.

The calculations used in this investigation into wave activity in Ahuriri Estuary assume a planar bed and non-cohesive sediments. Large-scale bedforms were not

prevalent in Ahuriri Estuary. As discussed in Chapter Four, cohesion in sediments with clay content greater than 5-10 % influences the erosion rate of the sediment. Clay content was low in sediment sampled in the estuary, generally less than 10% (refer Chapter 5, Section *5.4.1.1*). Therefore, the effect of cohesion is likely to be low (van Rijn 2007). The muddy sediments in Ahuriri Estuary are generally located where local wave generation would be prohibited by very small fetch distances (i.e. less than 400 metres). However, cohesion in Ahuriri Estuary may have been increased by biostabilisation and organic carbon content (Lelieveld 2003). Conversely, macrofaunal activity may have a destabilising effect, aiding the reworking of sediment by waves (Le Hir et al. 2007). It is difficult to include such effects in the calculations of erosion thresholds due to the temporal changes due to consolidation (Parchure & Mehta 1985).

6.3 CONCEPTUAL MODEL

In this section the main conclusions from the hydrodynamic and sediment modelling, surficial sediment characteristics and the reworking of sediments by wave action are combined to produce a conceptual model of the behaviour of the estuary as a processor of sediments. The sediment dynamics are a result of the sediment source, hydrodynamic forcing, particularly at the time of sediment input into the estuary, and the reworking and redispersal of sediment following deposition. The conceptual model provides an overview of the processes which distribute sediment and the areas of potential erosion and accretion. The model does not aim to produce actual rates of erosion and accretion but rather aims to characterise the estuary as a processor of sediments. This allows for the identification of the main transport pathways and areas of potential erosion and accretion. Validation of the numerical modelling of sediment dynamics in Ahuriri Estuary is discussed. The number of studies carried out in Ahuriri Estuary is relatively limited, concentrating on the influence of the 1931 Napier earthquake and anthropogenic changes. However, numerous documents and previous studies have provided observations that can be used to infer sedimentation regimes. These observations have provided support for the main findings of this research and will be discussed in this section.

Chapter Four identified the controlling factors of the transport, erosion and deposition of sediments in Ahuriri Estuary. The main influence was the grain-size and consequently the settling velocity. A large percentage of fine silt was exported from the model domain and had greater deposition in the downstream sub-estuaries as a consequence of a low settling velocity. The ebb-dominance in residual currents and the large tidal excursion resulted in a large proportion of sediment in suspension to be exported. The larger the grain-size used in model simulations, the greater the influence of other simulation conditions, such as the timing in the tidal cycle of sediment release and the magnitude of freshwater influx. There were also differences according to the timing in the spring-neap cycle, attributable to lower current velocities during neap simulation. However, the general patterns were the same.

Areas of potential accretion were identified as the upper reaches of the upper estuary, upper half of the main outfall channel, the Westshore intertidal region and

the boat harbour (Figures 6.3 and 6.4). Accretion in the upper half of the main outfall channel and upper reaches of the upper estuary is validated by findings of historical sedimentation surveys in Ahuriri Estuary. These surveys documented a positive bed level change in the upper estuary upstream of the Taipo Stream and the western half of the main outfall channel, upstream of the emergent islands region. Sediments in the upper reaches of the upper estuary are observed to be the muddiest sediments in Ahuriri Estuary. Low tidal current velocities and absence of wave reworking suggest that fine sediment deposited here is not further redispersed resulting net accretion. Due to the fine nature of the sediments and the runoff from agricultural soils, increased levels of contaminants have been measured in these areas and should continue to be monitored.

The intertidal regions were identified as areas of potential accretion. Sediment transport highlighted the flushing of sediments into intertidal areas in the lower estuary as the tide inundated the middle estuary. Low water depths, current velocities and an absence of wave reworking aid sediment deposition and subsequent accumulation in these areas. The areas of greatest potential accretion in intertidal areas were the upper reaches of the Pandora intertidal region and the western-most Westshore intertidal region. Accumulation in these areas is validated by calculated sedimentation rates of 4.3 $mm.yr^{-1}$ and 6.1 $mm.yr^{-1}$, respectively (Chagué-Goff et al. 2000). Surficial sediment analysis highlighted greater proportions of silt and clay in these intertidal regions and high TOC content, indicating a low energy, depositional environment. Sediment accumulation in these areas and the drains discharging into the estuary in the Pandora intertidal region mean that these areas are potential areas of contaminant accumulation.

Accretion of sediments was also identified in the lower estuary or boat harbour (Figure 6.4). Here there were two main mechanisms driving deposition, the slowing of currents in the lee of the Pandora Passageway and the residual eddy formation. Dredging operations were carried out in 4 locations in the boat harbour in 2007 and 2008 (refer Appendix I). Three of these sites are located directly in the lee of Pandora Passageway. The other dredge site location corresponds directly with the location of the residual eddy identified in Chapter Three. The model prediction of accumulation at these sites provides a validation of the model

performance. Similar results were seen in a similar modelling investigation in the Central Waitemata Harbour (Green 2008). Eddy formation on the outgoing tide resulted in a depocentre at the site of the residual eddy. Relative volumes of deposition differ according to the conditions at the time of sediment influx. Fine sediments also resulted in lower volumes of deposition as a large proportion remained in suspension to be transported from the estuary offshore and from the model domain. As sediment is dredged in this region and is relatively well flushed, risk of sediment contamination in this region is low.

Erosion and sediment reworking was generally restricted to the main tidal channel, the intertidal channels and areas where local generation of waves results in sediment reworking (Figures 6.3 and 6.4). The sediments on the margins of the interidal channels which "feed" these intertidal flats had relatively low silt and clay proportions and low TOC content. This suggested reworking of the sediment, flushing away the fines and organic carbon, leaving behind a greater proportion of sand-sized sediments. Erosion and sediment reworking as a result of wave action was illustrated in the upper estuary. Sufficient fetch in the upper estuary at high tide when the islands are generally submerged for the most part allowed for the local generation of waves under relatively high wind conditions. Tidal currents are also dramatically increased in this area as a result of the constriction of tidal flow through relatively narrow channels and transport large volumes of sediment as a consequence. The historical sedimentation surveys identified a degradation of the bed in this region. Sediment samples taken in the lower reaches of the main outfall channel also did not show high TOC content, suggesting sediments are reworked in this region. Therefore, risk of excessive contamination in this region is low.

The investigations carried out in this study suggest that Ahuriri Estuary is a depositional environment. Sediment accumulation in intertidal areas is predicted by sediment modelling, inferred by surficial sediment characteristics, and documented by historical sedimentation surveys. Chagué-Goff et al. (2000) calculated moderate sedimentation rates based upon core data in comparison with other New Zealand estuarine sedimentation rates (refer Chapter 1, Table 1.1).

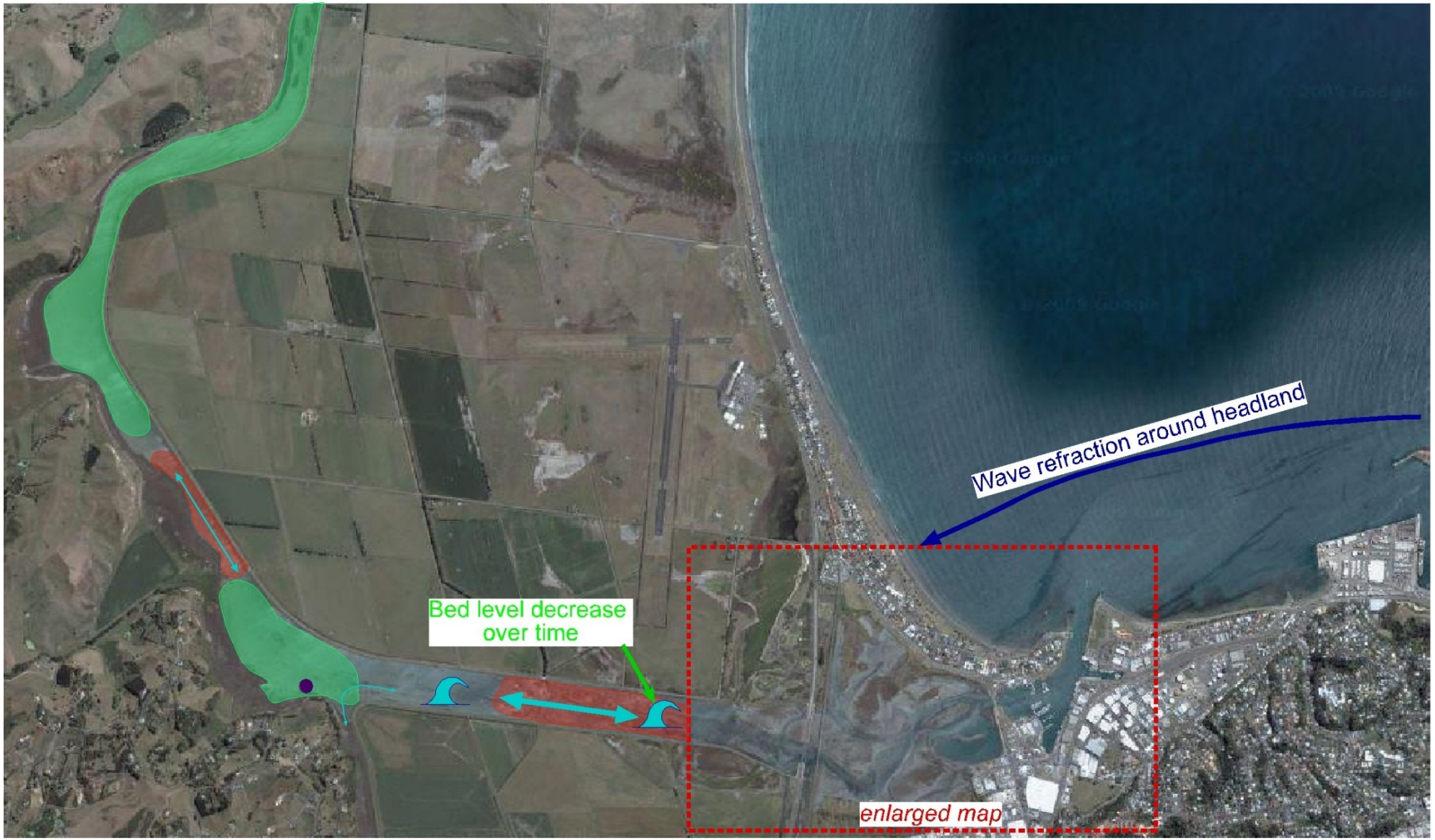

Figure 6.3. Conceptual model of the sediment dynamics of Ahuriri Estuary. Note: Enlarged map shown in Figure 6.4. Image from Google Earth.

Figure 6.4. Conceptual model of the sediment dynamics of Ahuriri Estuary. Image from Google Earth.

Although sedimentation rates are not as high as other estuaries, they are elevated from pre-European settlement.

The sediment dynamics and the behaviour of the estuary as a processor of sediments has been summarised in this chapter. In order to obtain quantitative sedimentation rates, the model must be fully calibrated and accurate measurements of sediment influx are required. Sediment influx rates of the Taipo Stream are relatively unknown and may therefore be an over-estimation of sediment volumes deposited in the estuary. However, the model has been validated by the findings in this chapter and has been shown to reproduce the sediment dynamics and patterns well. A similar study carried out in the Central Waitemata Harbour found that modelling reproduced the patterns well, but underestimated actual sedimentation rates by 25 % (Green 2008). The scale of the sediment dispersal and depositional patterns may be altered accordingly for future research into the volume of sediment transferred into the estuary by the Taipo Stream, and the relative importance of marine sediment influx. High current velocities through the tidal inlet suggest marine sediment may enter the estuary. However, this has not been quantified in this study and has been suggested to be relatively low, as the entrance is located within a stable littoral cell (Komar 2007). The quantification of these parameters would allow for an accurate simulation of actual volumes of sediment accumulation and erosion, which may be validated against sedimentation rates calculated in the core study by Chagué-Goff et al. (2000). Seasonality is also likely to influence the volumes of sediment influx into the estuary from storm rainfall events. For example, successive rainfall events will yield a lower sediment influx than a rainfall event following a dry period (Green 2008), which is ultimately a function of the seasonality at the time of sediment influx. This is likely to be an important consideration when accurately modelling sediment yield from the Taipo Stream.

The main findings of this research as summarised in the conceptual model are presented in Chapter 7.

CHAPTER SEVEN
SUMMARY AND RECOMMENDATIONS

7.1 SUMMARY

The key findings from this study are as follows:

- Ahuriri Estuary is ebb-dominated with a large tidal excursion and significant flushing. Therefore, sediment in suspension is likely to be transported from the estuary. Residual circulation in the boat harbour was shown to be associated with depositional centres.
- Initial transport of sediment prior to settling out of suspension had the greatest influence on the volume of sediment transported downstream and the ultimate depositional location. For fine-grained sediments with a low settling velocity a large volume was transported from the estuary. The larger the grain-size, the greater the importance of this initial transport.
- The timing of release of sediment into the estuary and the magnitude of freshwater influx influenced this initial transport of sediment and consequently the volume of downstream transport and location of deposition.
- A trend of fining of sediments and an increase in TOC in the middle estuary suggests transport from high energy to low energy environments.
- Upper intertidal flats in the middle estuary were found to be areas of accretion. Low current velocities and absence of local wave generation result in accretion as sediment deposited here is not reworked.
- Accretion was evident in the boat harbour, attributable to both current slowing in the lee of the narrow Pandora Passageway and the associated eddy formation resulting from velocity shear on the outgoing tide. This has been validated by dredging operations at these sites.
- Accretion was also evident in the upper reaches of the upper estuary. The muddiest sediments, absence of local wave generation, very low current velocities and positive bed level changes in historical sedimentation surveys suggests this to be a depositional environment.

- Erosion in Ahuriri Estuary is generally restricted to the lower main outfall channel, where local wave generation and increased tidal current velocities have resulted in degradation of the bed over time. Erosion was also evident in the intertidal channels. Tidal current velocities were capable of winnowing finer sediment, supported by a coarser grain-size and low TOC.
- Local wave generation is limited in Ahuriri Estuary due to limited fetches for prevailing wind conditions, but has been shown to have an important influence on the sediment dynamics.

7.2 RECOMMENDATIONS FOR FUTURE WORK

Sediment sampling is undertaken annually by the Hawke's Bay Regional Council as part of a monitoring programme. This sediment sampling regime should be extended to include data relating to sedimentation conditions such as recent storm events, any recent stream gauging, etc. This would aid in the validation of the findings of the sediment transport scenario modelling. The data should also include a higher resolution of grain-size classes in order to identify trends within the silt and sand grain-size classes.

The deployment of an ADV current meter during stormy conditions would allow for the direct measurement of locally generated waves in Ahuriri Estuary. This would allow for a more accurate characterisation of wave-induced sediment reworking and redispersal. The deployment of an optical backscatter sensor in both the estuary and the Taipo Stream would allow for the calibration of the model and an accurate sediment source concentration. Measured source concentrations would allow for a more quantitative approach to sedimentation volumes and rates.

Future large-scale modelling projects will likely include catchment modelling. This will also allow for a more accurate knowledge of sediment influx and quality of sediment entering the estuary. The results of this study may then be scaled accordingly to allow for increasingly accurate boundary conditions.

Continued sediment contaminant analysis, currently carried out by the HBRC, is recommended to ensure the health of the estuary is managed and maintained.

REFERENCES

Bass SJ, Manning AJ, Dyer KR 2007. Preliminary findings of a study of the upper reaches of the Tamar Estuary, UK, throughout a complete tidal cycle: Part 1: Linking hydrodynamic and sediment cycles. In: Maa JPY, Sanford LP, Schoellhamer DH ed. Estuarine and Coastal Fine Sediment Dynamics. Amsterdam, Elsevier. Pp. 1-14.

Bates PD, Hervouet JM 1999. A new method for moving-boundary hydrodynamic problems in shallow water. Proceedings of the Royal Society of London Series A. Mathematical Physical and Engineering Sciences 455(1988): 3107-3128.

Bearman G ed. 1989. Waves, tides and shallow-water processes. Oxford, Butterworth-Heinemann. 227 p.

Beca Carter Hollings & Ferner Ltd 1999. Guidelines for stormwater runoff modelling in the Auckland Region. TP 108. 26 p.

Bell RG, Hume TM, Dolphin TJ, Green MO, Walters RA 1997. Characterisation of physical environmental factors on an intertidal sand flat, Manukau Harbour, New Zealand. Journal of Experimental Marine Biology and Ecology 216: 11-31.

Bland KJ 2001. Analysis of the Pliocene forearc basin succession, Esk River Catchment, Hawke's Bay. Unpublished MSc Thesis thesis, University of Waikato, Hamilton.

Brennan ML, Schoellhamer DH, Burau JR, Monismith SG 2000. Tidal asymmetry and variability of bed shear stress and sediment bed flux at a site in San Francisco Bay, USA. In: Winterwerp JC, Kranenburg C ed. 6th International Conference on Cohesive Sediment Transport (INTERCOH 2000). Pp. 93-107.

Carter DJT 1982. Prediction of wave height and period for a constant wind velocity using the JONSWAP results. Ocean Engineering 9: 17-33.

Chagué-Goff C, Nichol SL, Ditchburn RJ, Trompetter W, Sutherland VT 1998. Earthquake and human impact on the sedimentology and geochemistry of Ahuriri Estuary, Hawke's Bay 98/23.

Chagué-Goff C, Nichol SL, Jenkinson AV, Heijnis H 2000. Signatures of natural catastrophic events and anthropogenic impact in an estuarine environment, New Zealand. Marine Geology 167: 285-301.

Chang YH, Scrimshaw MD, Lester JN 2001. A revised Grain-Size Trend Analysis program to define net sediment transport pathways. Computers and Geosciences 27: 109-114.

Chen CS, Qi JH, Li CY, Beardsley RC, Lin HC, Walker R, Gates K 2008.

Complexity of the flooding/drying process in an estuarine tidal-creek salt-marsh system: An application of FVCOM. Journal of Geophysical Research-Oceans 113(C7).

Cheviet C, Violeau D, Guesmia M 2002. Numerical simulation of cohesive sediment transport in the Loire estuary with a three-dimensional model including new parameterisations. In: Winterwerp JC, Kranenburg C ed. Fine Sediment Dynamics in the Marine Environment. Amsterdam, Elsevier. Pp. 529-544.

CliFlo 2009. The National Climate Database. National Institute of Water and Atmospheric Research. http://cliflo.niwa.co.nz/

Cooke J 2006. Recommendations on State of the Environment Monitoring for Hawke's Bay Urban Streams. 17 p.

Cooke S 1990. Laser diffraction particle size analysis – The Malvern Mastersizer-S. Internal Report. Hamilton, Department of Earth Sciences, University of Waikato.

Danish Hydrological Institute 2004. Mike 21 Coastal Hydraulics and Oceanography User Guide and Reference Manual. Hoersholm, DHI Software.

de Boer PL 1998. Intertidal Sediments: Composition and Structure. In: Eisma D ed. Intertidal Deposits: River Mouths, Tidal Flats and Coastal Lagoons. Florida, CRC Press. Pp. 525.

De Villiers JWL, Basson GR 2007. Modelling of long-term sedimentation at Welbedacht Reservoir, South Africa. Journal of the South African Institution of Civil Engineering 49(4): 10-18.

De Vos B, Vandecasteele B, Deckers J, Muys B 2005. Capability of Loss-on-Ignition as a Predictor of Total Organic Carbon in Non-Calcareous Forest Soils. Communications in Soil Science and Plant Analysis 36: 2899-2921.

Dean RG, Dalrymple RA 2002. Coastal Processes with Engineering Applications. Cambridge, Cambridge University Press. 475 p.

Defina A 2000. Two-dimensional shallow flow equations for partially dry areas. Water Resources Research 36(11): 3251-3264.

Dolphin TJ 2004. Wave-induced sediment transport on an estuarine intertidal flat. Unpublished thesis, University of Waikato, Hamilton. 154 p.

Duman M, Avci M, Duman S, Demirkurt E, Duzbastilar MK 2004. Surficial sediment distribution and net sediment transport patterns in Izmir Bay, western Turkey. Continental Shelf Research 24(9): 965-981.

Dyer KR 1973. Estuaries: A physical Introduction. Aberdeen, John Wiley and Sons. 140 p.

Dyer KR 1988. Fine sediment particle transport in estuaries. In: Dronkers J, van Leussen W ed. Physical Processes in Estuaries. Berlin, Springer-Verlag. Pp. 295-310.

Dyer KR 1994. Estuarine sediment transport and deposition. Sediment transport and depositional processes Oxford, Blackwell Scientific Publications. Pp. 193-218.

Eisma D 1998. Intertidal Deposits: River Mouths, Tidal Flats and Coastal Lagoons. Kennish M, Lutz P ed. Florida, CRC Press. 524 p.

Fagherazzi S, Wiberg PL 2009. Importance of wind conditions, fetch, and water levels on wave-generated shear stresses in shallow intertidal basins. Journal of Geophysical Research-Earth Surface 114: 12.

Ferentinos G, Collins M 1979. Tidally induced secondary circulation and their associated sedimentation processes. Journal of the Oceanographical Society of Japan 35: 65-74.

Field BD, Uruski CF, Beu AG, Browne GH, Crampton JS, Funnell RH, Killops SD, Laird M, Mazengarb C, Morgans HEG and others 1997. Cretaceous-Cenozoic geology and petroleum systems of the East Coast region, New Zealand. Institute of Geological and Nuclear Sciences Monograph 19. Lower Hutt.

Folk RL 1968. Petrology of Sedimentary Rocks. Austin, Texas, Hemphill Publishing Co. 166 p.

French PW 1997. Coastal and estuarine management. London, Routledge. 251 p.

French JR, Burningham H, Benson T 2008. Tidal and Meteorological Forcing of Suspended Sediment Flux in a Muddy Mesotidal Estuary. Estuaries and Coasts 31: 843-859.

Gao S, Collins MB, Lanckneus J, De Moor G, Van Lancker V 1994. Grain size trends associated with net sediment transport patterns: An example from the Belgian continental shelf. Marine Geology 121: 171-185.

Gardner GB, Smith DJ 1978. Turbulent mixing in a salt wedge estuary. In: Nihoul JCJ ed. Hydrodynamics of Estuaries and Fjords New York, Elsevier Scientific Publishing Company. Pp. 546.

Gibb JG 1962. Wave refraction patterns in Hawke Bay. New Zealand Journal of Geology and Geophysics 5:434-444.

Green MO, McCave IN 1995. Seabed drag coefficient under tidal currents in the Eastern Irish Sea. Journal of Geophysical Research-Oceans 100(C8): 16057-16069.

Green MO, Black KP, Amos CL 1997. Control of estuarine sediment dynamics by interactions between currents and waves at several scales. Marine Geology 144(1-3): 97-116.

Green MO, MacDonald IT 2001. Processes driving estuary infilling by marine sands on an embayed coast. Marine Geology 178(1-4): 11-37.

Green MO, Coco G 2007. Sediment transport on an estuarine intertidal flat: Measurements and conceptual model of waves, rainfall and exchanges with a tidal creek. Estuarine Coastal and Shelf Science 72(4): 553-569.

Green MO 2007. Central Waitemata Harbour Contaminant Study. USC-3 Model Description, Implementation and Calibration HAM2007-167.

Green MO 2008. Predicting decadal-scale estuarine sedimentation for planning catchment development. Sediment Dynamics in Changing Environments Conference. Pp. 8.

Green MO, Oldman J, Pritchard M 2008. Predicting long-term sedimentation and heavy-metal accumulation in estuaries. DHI Software Conference.

Hamilton P 1990. Modelling salinity and circulation for the Columbia River Estuary. Progress in Oceanography 25(1-4): 113-156.

Haralampides K, McCorquodale JA, Krishnappan BG 2003. Deposition properties of fine sediment. Journal of Hydraulic Engineering - ASCE 129(3): 230-234.

Hu KL, Ding PX, Wang ZH, Yang SL 2009. A 2D/3D hydrodynamic and sediment transport model for the Yangtze Estuary, China. Journal of Marine Systems 77(1-2): 114-136.

Hull AG 1986. Pre-A.D. 1931 tectonic subsidence of Ahuriri Lagoon, Napier, Hawke's Bay, New Zealand. New Zealand Journal of Geology and Geophysics 29: 75-82.

Hull AG 1987. A Late Holocene Marine Terrace on the Kidnappers Coast, North Island, New Zealand: Some Implications for Shore Platform Development Processes and Uplift Mechanism. Quaternary Research 28: 183-195.

Hull AG 1990. Tectonics of the 1931 Hawke's Bay Earthquake. New Zealand Journal of Geology and Geophysics 33: 309-320.

Hume TM, Roper DS, Cooke J, Langham N, Hay JR, Burke E 1990. Environmental impact assessment: Motorway alignment through Ahuriri Estuary, Napier. 8069/1.

Hume TM, Dahm J 1992. An Investigation of the Effects of Polynesian and European Land Use on Sedimentation in Coromandel Estuaries DSIR Consultancy Report No. 6104 for the Department of Conservation (Waikato Conservancy), Hamilton.

Hyland J, Balthis L, Karakassis I, Magni P, Petrov A, Shine J, Vestergaard O, Warwick R 2005. Organic carbon content of sediments as an indicator of stress in the marine benthos. Marine Ecology-Progress Series 295: 91-103.

Jay DA, Smith JD 1988. Residual circulation and classification of shallow, stratified estuaries. In: Dronkers J ed. Physical Processes in Estuaries. Berlin, Springer-Verlag. Pp. 21-41.

Komar PD 2007. The Coast of Hawke's Bay: Processes and Erosion Problems AM 07/02.

Kranck K 1984. The role of flocculation in the filtering of particulate matter in estuaries. In: Kennedy V ed. The Estuary as a Filter. New York, Academic Press. Pp. 159-175.

Krone RB 1962. Flume studies of the transport of sediment in estuarial shoaling processes. Berkeley, University of California.

Lal R 1998. Soil erosion impact on agronomic productivity and environment quality. Critical Reviews in Plant Sciences 17(4): 319-464.

Le Hir P, Monbet Y, Orvain F 2004. Sediment erodability in sediment transport modelling: Can we account for biota effects? 3rd Workshop on the Comparison of Laboratory and in situ Measuring Devices, and the Extrapolation of Flume and Erosion Device Data to the Field. Pp. 1116-1142.

le Roux JP 1994. An alternative approach to the identification of net sediment transport paths based on grain-size trends. Sedimentary Geology 94: 97-107.

Lelieveld SD, Pilditch CA, Green MO 2003. Variation in sediment stability and relation to indicators of microbial abundance in the Okura Estuary, New Zealand. Estuarine, Coastal and Shelf Science 57: 123-136.

Li G, Cao Z, Lan D, Xu J, Wang S, Yin W 2007. Spatial variations in grain size distribution and selection metal contents in the Xiamen Bay, China. Environmental Geology 52:1559-1567.

Lick W, Lick J, Jin L, Gailani J 2007. Approximate equations for sediment erosion rates. In: Maa JPY, Sanford LP, Schoellhamer DH ed. Estuarine and Coastal Fine Sediment Dynamics. Amsterdam, Elsevier. Pp. 109-128.

Liu WC, Hsu MH, Kuo AY 2002. Modelling of hydrodynamics and cohesive sediment transport in Tanshui River estuarine system, Taiwan. Marine Pollution Bulletin 44(10): 1076-1088.

Liu WC, Lee CH, Wu CH, Kimura N 2009. Modeling diagnosis of suspended sediment transport in tidal estuarine system. Environmental Geology 57(7): 1661-1673.

Lumborg U, Windelin A 2003. Hydrography and cohesive sediment modelling: application to the Romo Dyb tidal area. Journal of Marine Systems 38(3-4): 287-303.

Lumborg U, Pejrup M 2005. Modelling of cohesive sediment transport in a tidal lagoon - an annual budget. Marine Geology 218(1-4): 1-16.

Lumborg U 2005. Modelling the deposition, erosion, and flux of cohesive sediment through Oresund. Journal of Marine Systems 56(1-2): 179-193.

Madarasz AL 2006. Ahuriri Estuary Environmental Assessment and Monitoring.

Mallet C, Howa H, Garlan T, Sottolichio A, Le Hir P, Michel D 2000. Utilisation of numerical and statistical techniques to describe sedimentary circulation patterns in the mouth of the Gironde estuary. Comptes Rendus De L Academie Des Sciences Serie Ii Fascicule a-Sciences De La Terre Et Des Planetes 331(7): 491-497.

Manning AJ, Dyer KR 2007. Mass settling flux of fine sediments in Northern European estuaries: Measurements and predictions. Marine Geology 245(1-4): 107-122.

Marván FG, Wallis SG, Mehta AJ 2002. Episodic transport of organic-rich sediments in a microtidal estuarine system. In: Winterwerp JC, Kranenburg C ed. Fine Sediment Dynamics in the Marine Environment. The Netherlands, Elsevier. Pp. 713.

McCave IN 1978. Grain-size trends and transport along beaches: example from eastern England. Marine Geology 28: M43-M51.

McCave IN 1984. Erosion, transport and deposition of fine-grained marine sediments. Geological Society, London, Special Publications 15: 35-69.

McConnochie H 2004. After Works. Interviews and letters from survivors of the 1931 Hawke's Bay Earthquake. Napier, Brebner Print Digital.

Mead S, Black K, McComb P 2001. Westshore Coastal Process Investigation. A study to determine the coastal processes in the bay at Westshore and provide a long-term solution to erosion problems. Hamilton, ASR Marine and Freshwater Consultants.

Mehta AJ, Partheniades E 1975. An investigation of the depositional properties of flocculated fine sediments. Journal of Hydraulic Research 13(4): 361-381.

Mehta AJ, Lee SC 1994. Problems in Linking the Threshold Condition for the Transport of Cohesionless and Cohesive Sediment Grain. Journal of Coastal Research 10(1): 170-177.

Murphy PL, Valle-Levinson A 2008. Tidal and residual circulation in the St. Andrew Bay system, Florida. Continental Shelf Research 28(19): 2678-2688.

Newsome P, Wilde R, Willoughby E 2000. Volume 1: Label Formats, Land Resource Information System Spatial Data Layers. Palmerston North, Landcare Research New Zealand.

Nichols MM 1984. Effects of fine sediment resuspension in estuaries. In: Mehta AJ ed. Estuarine Cohesive Sediment Dynamics. Proceedings of a Workshop on Cohesive Sediment Dynamics. Berlin, Springer. Pp. 5-42.

Nielsen P 1992. Coastal bottom boundary layers and sediment transport. Liu PL ed. Singapore, World Scientific. 324 p.

Ogden J, Deng Y, Horrocks M, Nichol S, Anderson S 2006. Sequential impacts of Polynesian and European settlement on vegetation and environment processes recorded in sediments at Whangapoua Estuary, Great Barrier Island, New Zealand. Regional Environmental Change 6(1-2): 25-40.

Ota Y, Berryman KR, Brown LJ, Kashima K 1989. Holocene sediments and vertical tectonic downwarping near Wairoa, Northern Hawke's Bay, New Zealand. New Zealand Journal of Geology and Geophysics 32: 333-341.

Owens PN, Batalla RJ, Collins AJ, Gomez B, Hicks DM, Horowitz AJ, Kondolf GM, Marden M, Page MJ, Peacock DH and others 2005. Fine-grained sediment in river systems: environmental significance and management issues. River research and applications 21: 693-717.

Parchure TM, Mehta AJ 1985. Erosion of soft cohesive sediment deposits. Journal of Hydraulic Engineering - ASCE 111(10): 1308-1326.

Pimentel D, Harvey C, Resosudarmo P, Sinclair K, Kurz D, McNair M, Crist S, Shpritz L, Fitton L, Saffouri R and others 1995. Environmental and Economic Costs of Soil Erosion and Conservation Benefits. Science 267(5201): 1117-1123.

Poppe LJ, Eliason AH, Fredericks JJ, Rendigs RR, Blackwood D, Polloni CF 2003. Grain-size analysis of Marine Sediments: Methodology & Data processing. 00-358.

Pritchard DW 1952. Estuarine Hydrography. Advances in Geophysics 1: 243-280.

Reeve D, Chadwick A, Fleming C 2004. Coastal Engineering: Processes, Theory and Design Practice. New York, Spon Press. 461 p.

Sakamaki T, Nishimura O 2006. Dynamic equilibrium of sediment carbon content in an estuarine tidal flat: Characterisation and mechanisms. Marine Ecology: Progress Series 328: 29-40.

Sakamaki T, Nishimura O 2007. Physical control of sediment carbon content in an estuarine tidal flat system (Nanakita River, Japan): A mechanistic case study. Estuarine, Coastal and Shelf Science 73(3-4): 781-791.

Sheffield A, Healy T, McGlone M 1995. Infilling rates of a steepland catchment estuary, Whangamata, New Zealand. Journal of Coastal Research 11(4): 1294-1308.

Sherwood AM, Nelson CS 1979. Surficial Sediments of Raglan Harbour. New Zealand Journal of Marine and Freshwater Research 13(4): 475-496.

Soil Conservation Service 1972. SCS National Engineering Handbook: Hydrology. Washington U. S. Government Printing Office.

SonTek 2001. Triton Principles of Operation. San Diego, SonTek Inc.

Soulsby R, Whitehouse RJS 1997. Threshold of sediment motion in coastal environments. Pacific Coasts and Ports. Pp. 149-154.

Stommel H, Farmer HG 1952. Abrupt change in width in two-layer open channel flow. Journal of Marine Research 11: 205-214.

Swales A, Williamson RB, van Dam LF, Stroud MJ, McGlone MS 2002. Reconstruction of urban stormwater contamination of an estuary using catchment history and sediment profile dating. In: Green MO. 2008. Predicting decadal-scale estuarine sedimentation for planning catchment development. Sediment Dynamics in Changing Environments Conference.

Talke SA, Stacey MT 2008. Suspended sediment fluxes at an intertidal flat: The shifting influence of wave, wind, tidal, and freshwater forcing. Continental Shelf Research 28(6): 710-725.

Tee KT 1988. Modelling of tidally induced residual currents. In: Kjerfve B ed. Hydrodynamics of Estuaries. Volume 1: Estuarine Physics. Florida, CRC Press. Pp. 149-159.

Thrush SF, Hewitt JE, Cummings V, Ellis JI, Hatton C, Lohrer A, Norkko A 2004. Muddy waters: elevating sediment input to coastal and estuarine habitats. Frontiers in Ecology and the Environment 2(6): 299-306.

van de Kreeke J 1988. Dispersion in shallow estuaries. In: Kjerfve B ed. Hydrodynamics of estuaries. Volume 1: Estuarine Physics. Florida, CRC Press. Pp. 27-39.

Van Leussen W, Dronkers J 1988. Physical Processes in Estuaries: An introduction. In: Dronkers J, Van Leussen W ed. Physical Proccesses in Estuaries. Germany, Springer-Verlag. Pp. 560.

van Rijn LC 1989. Transport of cohesive materials. Delft Hydraulics H 461: 12.1-12.27.

van Rijn LC 2007. Unified View of Sediment Transport by Currents and Waves. 1: Initiation of Motion, Bed Roughness, and Bed-Load Transport. Journal of Hydraulic Engineering 133(6): 649-667.

Violeau D, Bourban S, Cheviet C, Markofsky MP, O., Roberts W, Spearman J, Toorman E, Vested HJ, Weilbeer H 2002. Numerical simulation of cohesive transport: intercomparison of several numerical models. In: Winterwerp JC, Kranenburg C ed. Fine Sediment Dynamics in the Marine Environment. Amsterdam, Elsevier. Pp. 75-90.

Walling DE 2005. Tracing suspended sediment sources in catchments and river systems. Science of the Total Environment 344(1-3): 159-184.

Wang Q, Zhang MM, Zhong SY, Du GY, Jin BF, Yang H, Song CG 2009. Dynamic sedimentation and geomorphologic evolution of the Laizhou shoal, Bohai sea, Northern China. Journal of Asian Earth Sciences 36(2-3): 196-208.

Winter C 2004. On the evaluation of sediment transport models in tidal environments. International Workshop on From Particle Size to Sediment Dynamics. Pp. 562-571.

Winterwerp JC, Bale AJ, Christie MC, Dyer KR, Jones S, Lintern DG, Manning AJ, Roberts W 2002. Flocculaton and settling velocity of fine sediment. In: Winterwerp JC, Kranenburg C ed. Fine Sediment Dynamics in the Marine Environment. Amsterdam, Elsevier. Pp. 25-40.

Winterwerp JC 2007. On the sedimentation rate of cohesive sediment. In: Maa JPY, Sanford LP, Schoellhamer DH ed. Estuarine and Coastal Fine Sediment Dynamics. Amsterdam, Elsevier. Pp. 209-226.

Zimmerman JTF 1981. Dynamics, diffusion and geomorphical significance of tidal residual eddies. Nature 290: 549-555.

APPENDIX I

DREDGING SITES

I-1. Dredging sites

Dredging was undertaken at the sites indicated in Figure A1-1 during 2008 and 2009.

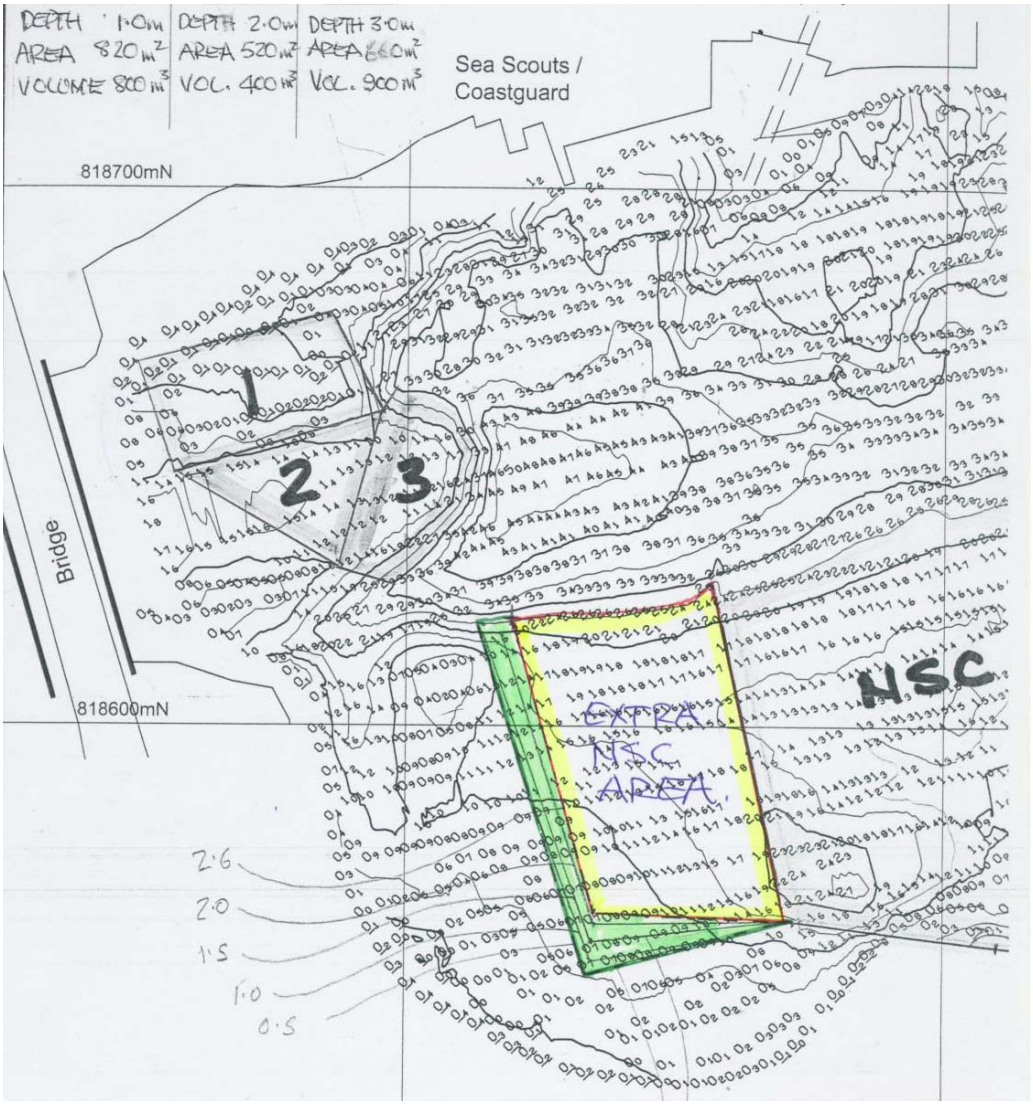

Figure A1-1. Dredging sites in the lower Ahuriri Estuary (Boat harbour). From Hawke's Bay Regional Council. Resource Consent, Coastal Permit. Consent No. CD070399Ea

APPENDIX II
SCS DESIGN HYDROGRAPH

II-1. Rainfall - runoff calculation

The SCS Rainfall to runoff curves were derived using Equation AII-1 and describe the relationship between rainfall and runoff.

$$Q = \frac{(P-Ia)^2}{(P-Ia)+S} \qquad \text{(Equation AII-1)}$$

Where Q is the runoff depth (mm), P is the rainfall depth (mm), Ia is the initial abstraction (mm) and S is the potential maximum retention after runoff begins (mm).

The initial abstraction is defined as the loss of rainfall before runoff occurs and is attributable to storage, evaporation, vegetation and infiltration. Based on empirical data the following initial abstraction values were derived by Beca Carter Hollings & Ferner Ltd (BCHF) (1999) as;

1. Pervious areas – 5
2. Impervious areas – 0

The runoff depth may then be used to calculate runoff volume and determine the design hydrograph for a given rainfall event.

II-2. Taipo Stream catchment soil properties

Table AII-1 describes the soil properties of the different sub-units of the Taipo Stream catchment.

Table AII-1. Soil type, classification and corresponding SCS hydrological soil classification for each of the sub-units of the Taipo Stream catchment.

Soil Type	Survey + Surcode	Domsoi	Series	NZSC	SCS hydrological soil group
Light sandy loam	Mid Hawke's Bay + MHKB	28A	Matapiro	PPU	C
Complex	Mid Hawke's Bay + MHKB	21C	Crownthorpe	PIT	C
Curtilage	Curtilage	-	-	-	-
Fine sandy loam	Heretaunga Plains + HERP	23	Farndon	RFT	B
Stony sandy loam	Mid Hawke's Bay + MHKB	21B	Crownthorpe	PIT	C
Sandy loam	Mid Hawke's Bay + MHKB	28	Matapiro	PPU	C
Sandy loam	Mid Hawke's Bay + MHKB	21	Crownthorpe	PIT	C
Ahuriri silt loam and clay	North Island Four Mile + NI4M	112	Ahuriri	WGFU	D

II-3. Taipo Stream catchment landuse properties

Table AII-2 describes the landuse properties of the different sub-units of the Taipo Stream catchment. Within each of the landuse sub-units, the soil was classified to give a curve number for each area. Within some landuse sub-units there were multiple soil units as illustrated in Table AII-2.

Table AII-2. Landuse classification, area, hydrological soil classification and associated curve numbers for each of the sub-units of the Taipo Stream catchment.

Landuse classification	**Area (sq.km)**	**Hydrologic soil group**	**Curve Number**
Orchard & other perennials	0.092	C	66
Vineyard	0.097	D	66
Major shelterbelt	0.032	C	86
Pine Forest-Closed canopy	0.62	C	70
Gorse & Broom	0.085	C	60
Indigenous forest	0.066	C	70
Afforestation	0.163	C	77
Urban parkland/Open space	0.17	-	74
Built-up area	3.32	-	86
Other exotic forest	0.26	C	70
High producing exotic grassland	10.6	B,C,D	79,86,89

II-4. Curve numbers

The curve number describes the relationship between rainfall and runoff. The curve number is dependent on soil type, landuse and hydrological condition (SCS 1986). Rainfall – Runoff curves using these initial abstraction values above are presented in Figure AII-1.

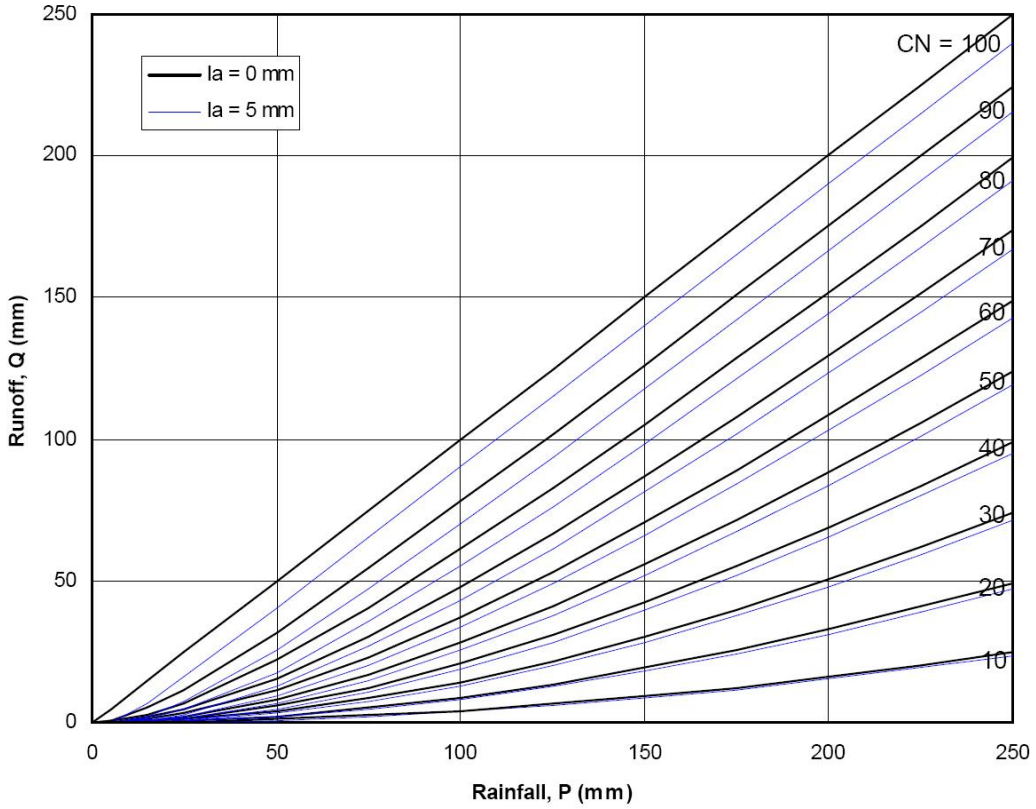

Figure AII-1. Rainfall – Runoff curves for initial abstraction depths of 0 and 5mm. From BCHF (1999).

Curve numbers for the Taipo Stream catchment were derived from the SCS National Engineering handbook (1986), given in Table AII-3.

Table AII-3. Runoff curve numbers for landuse and hydrologic soil group. Adapted from SCS (1975).

Cover type	**Hydrologic soil group**			
	A	B	C	D
Cultivated land				
- Without conservation treatment	72	81	88	91
- With conservation treatment	62	71	78	81
- Good condition				
Pasture				
- Poor condition	68	79	86	89
- Good condition	39	61	74	80
Meadow (good condition)	30	58	71	78
Wood or forest land	25	55	70	77
Open spaces, lawns, parks, golf courses etc.				
- Grass cover >75%	39	61	74	80
- Grass cover 50 – 75%	49	69	79	84
Commercial and business area	89	92	94	95
Industrial districts	81	88	91	93
Residential (1/8 acre average lot size)	77	85	90	92
Impervious area	98	98	98	98

However, as the Taipo Stream catchment was heterogeneous in catchment soil and landuse characteristics, a weight-averaged curve number was required, calculated by Equation AII-2.

$$CN = \frac{\sum CN_i A_i}{A_{tot}} \qquad \text{(Equation AII-2)}$$

The weighted curve number is calculated using the curve numbers and the associated areal coverage shown in Table AII-4.

Table AII-4. Weighted curve number calculation for the Taipo Stream catchment.

Curve number	Associated area (km)	CN(i)*A(i)	Weighted curve number
66	0.189	12.47	
86	10.30	885.97	
70	0.95	66.22	
60	0.085	5.10	
77	0.16	12.55	
74	0.17	12.58	
79	0.15	11.85	
89	3.5	311.50	
		1318.28	**85**

The weighted curve number may then be used to calculate the storage of the catchment using Equation AII-3.

$$S = \left(\frac{1000}{CN}\right) 25.4 \qquad \text{(Equation AII-3.)}$$

which was calculated to be 44.65 mm for the Taipo Stream catchment.

II-5. Time of concentration

The time of concentration, T_c, is used in the application of the design hydrograph ordinates. It is defined as the time it takes for runoff to travel from the hydraulically most distant part of the watershed to the point of reference (SCS 1975). T_c is calculated using the parameters outlined in Table AII-5.

Table AII-5. Parameters used in the calculation of the time of concentration.

Parameter	**Value**	
Channelisation factor, C	0.8	(BCHF 1999)
Catchment length, L (km)	10.82	(Derived using ArcGIS)
Catchment slope, S_c (m/m)	0.002	(Derived using ArcGIS)

The channelisation factor allows for the effects of urbanisation on runoff velocities (BCHF 1999). The time of concentration may then be calculated using Equation AII-5.

$$t_c = 0.14\ C\ L^{0.66} \left(\frac{CN}{200-CN}\right)^{-0.55} {S_c}^{-0.30} \qquad \text{(Equation AII-4)}$$

The time of peak concentration, T_p, is calculated by Equation AII-5.

$$t_p = \frac{2}{3} T_c \qquad \text{(Equation AII-5)}$$

II-6. Peak flow rate

The peak flow rate, q_p, is used in the application of the design hydrograph ordinates. It is calculated using catchment properties previously calculated, summarised in Table AII-6.

Table AII-6. Catchment properties used in the calculation of peak flow rate for the Taipo Stream.

Parameter	Value
Catchment Area, A (km^2)	15.5 (Derived using ArcGIS)
Runoff curve number, CN	85
Initial abstraction, Ia (mm)	5
Time of concentration, T_c (hrs)	2.4

In order to calculate the specific peak flow rate, the runoff index, c^*, must first be calculated by Equation AII-6.

$$c^* = \frac{P-2Ia}{P-2Ia+2S} \qquad \text{(Equation AII-6.)}$$

which was calculated to be 0.5 for the Taipo Stream catchment. This is used to determine the peak flow rate using Figure AII-2.

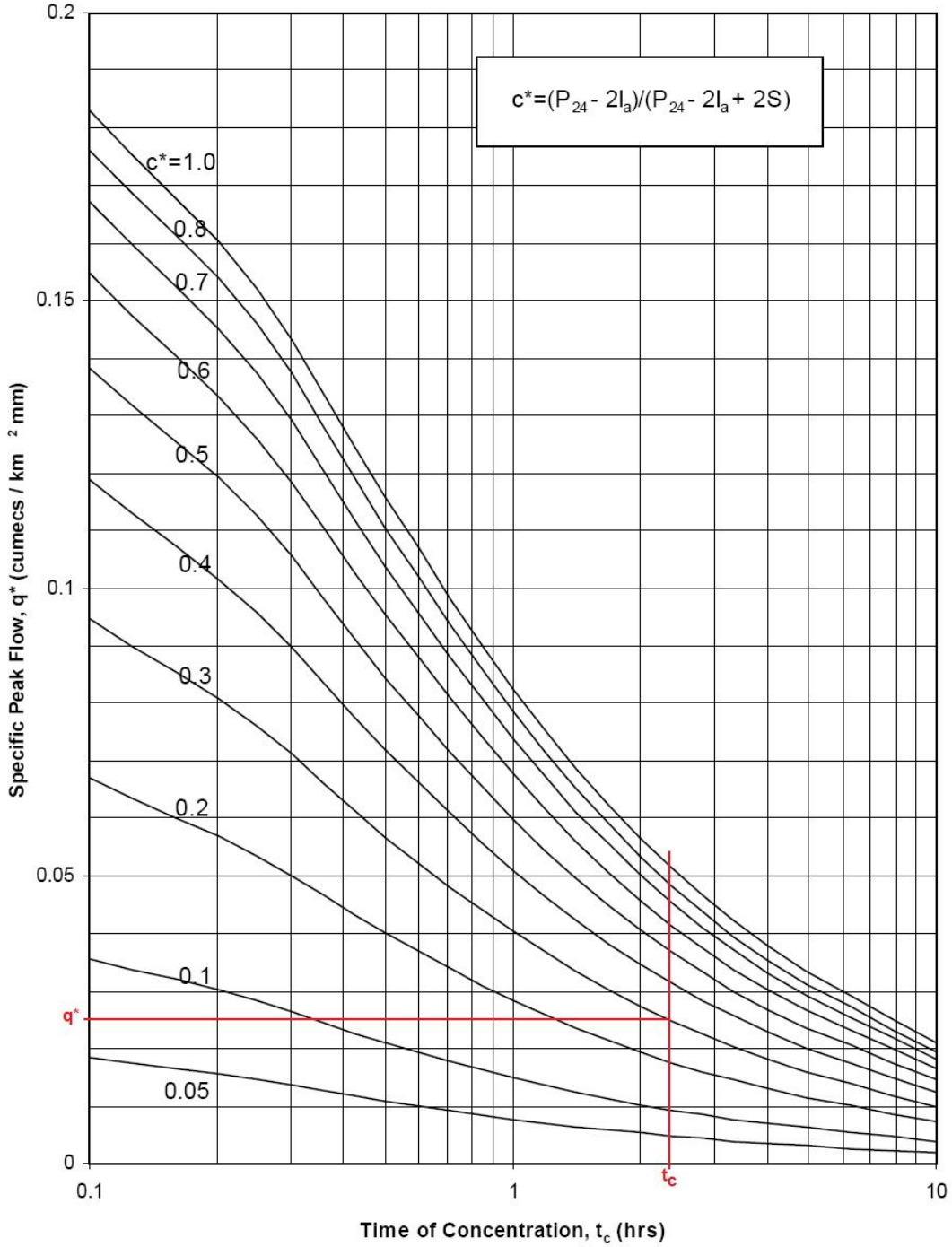

Figure AII-2. Specific peak flow rate for the Taipo Stream given the time of concentration and runoff index. Adapted from BCHF (1999). Red lines indicate example of a 40mm rainfall event.

The peak flow rate, q_p, is then able to be calculated using Equation AII-7.

$$q_p = q^* A\, P \qquad \text{(Equation AII-7.)}$$

II-7. Design hydrograph ordinates

The time of concentration and the peak discharge values are then able to be multiplied by the SCS design hydrograph ordinates, given in Table AII-7.

Table AII-7. Time and discharge ordinates to which the time of concentration and peak flow rate are applied to, respectively.

Time Ratios	Discharge ratios
0	0.000
0.1	0.030
0.2	0.100
0.3	0.190
0.4	0.310
0.5	0.470
0.6	0.660
0.7	0.820
0.8	0.930
0.9	0.990
1.0	1.000
1.1	0.990
1.2	0.930
1.3	0.860
1.4	0.780
1.5	0.680
1.6	0.560
1.7	0.460
1.8	0.390
1.9	0.330
2.0	0.280
2.2	0.207
2.4	0.147
2.6	0.107
2.8	0.077
3.0	0.055
3.2	0.040
3.4	0.029
3.6	0.021
3.8	0.015
4.0	0.011
4.5	0.005
5.0	0.000

II-8. Design hydrographs for storm rainfall events

20mm rainfall event

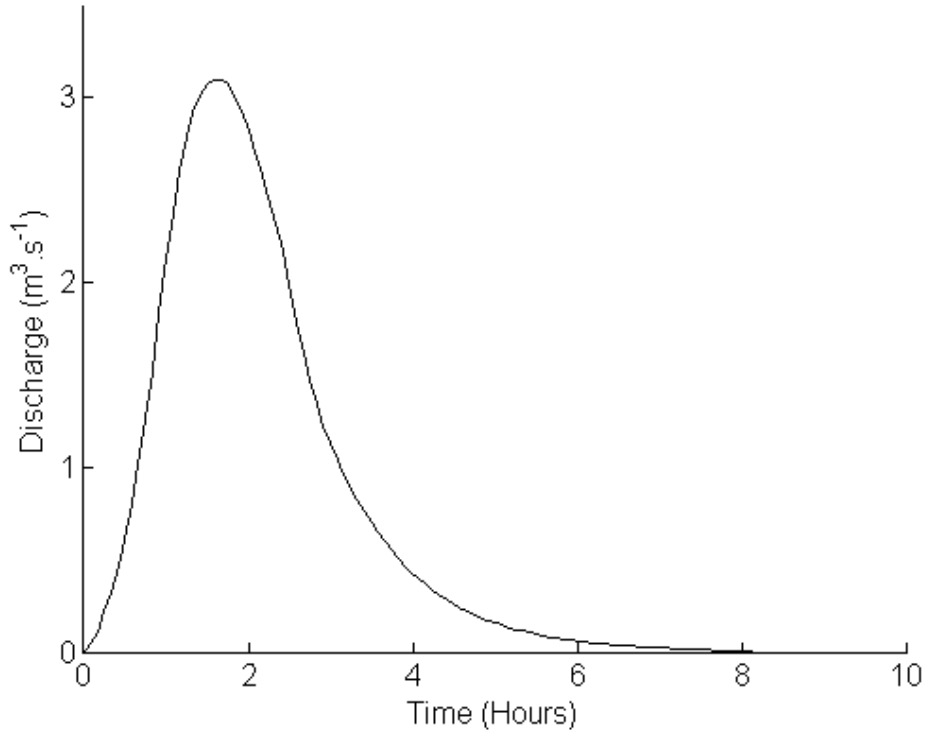

40mm rainfall event

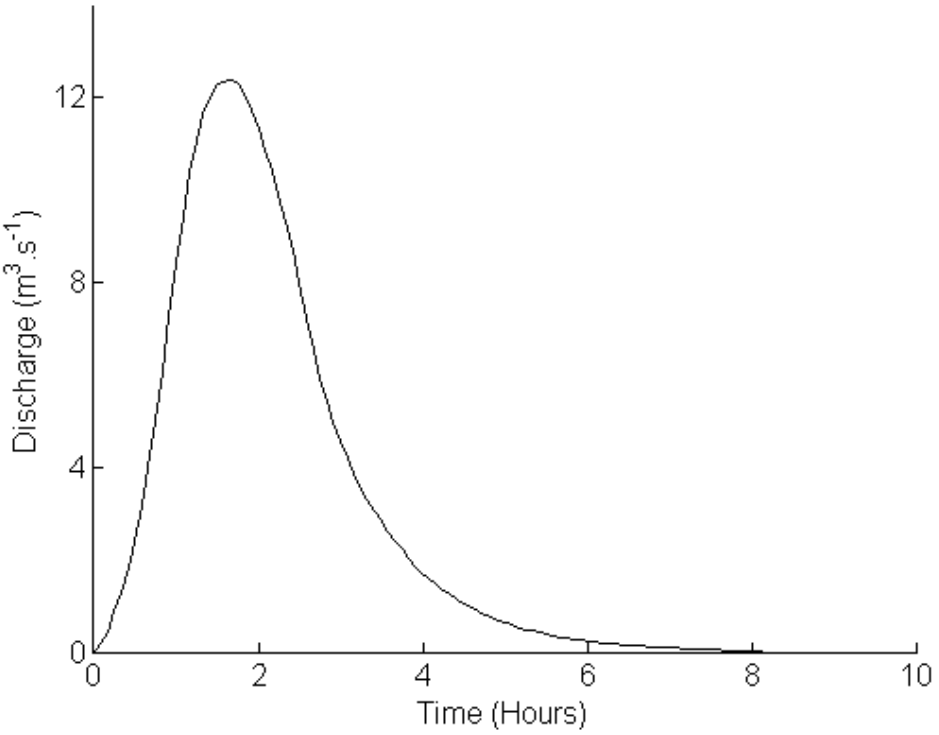

60mm rainfall event

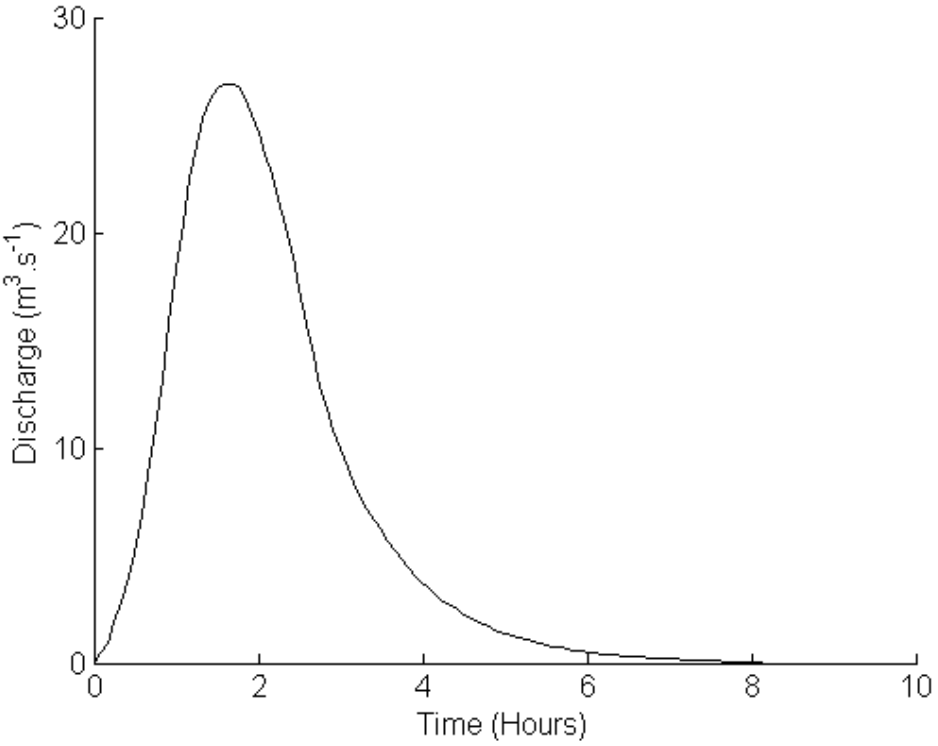

100mm rainfall event

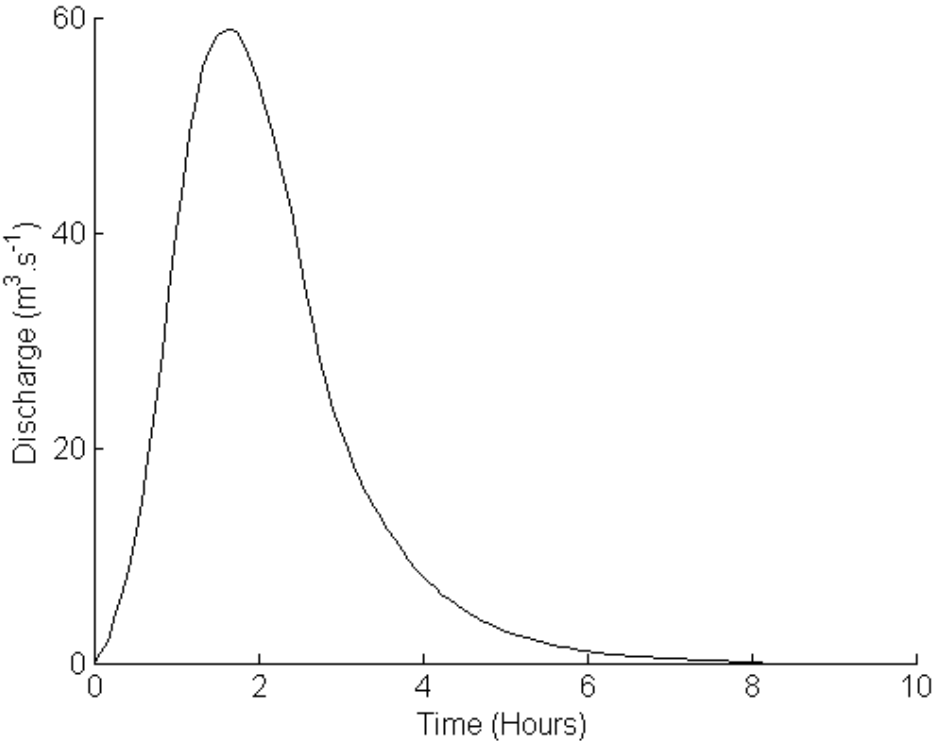

APPENDIX III

MOMENT STATISTICS FORMULA & SCALES

III-1. Moment statistics formula

First Moment (Mean):

$$\bar{x}_{\varphi} = \frac{\sum fm}{100}$$

Second Moment (Sorting):

$$\sigma_{\varphi} = \sqrt{\frac{\sum f(m-\bar{x})^2}{100}}$$

Third Moment (Skewness):

$$sk_{\varphi} = \frac{\sum f(m-\bar{x})^3}{100\sigma^3}$$

where *f* is the frequency in each grain-size grade present and *m* is the mid-point of each grain-size class interval (phi).

III-2. Grain-size parameter descriptions and scales

Udden-Wentworth Grain-size Classification

Table AIII-1. Udden-Wentworth grain-size classification. Divisions delineate boundaries between gravel, sand, silt and mud.

Grain-size (phi)	Grain-size (mm)	Classification
< -8.00	> 256.0	Boulder
-8.0 – -5.0	64.0 – 256.0	Cobble
-5.0 – -2.0	4.0 – 64.0	Pebble
-2.0 – -1.0	2.0 – 4.0	Granule
-1.0 – 0.0	1.0 – 2.0	Very coarse sand
0.0 – 1.0	0.5 – 1.0	Coarse sand
1.0 – 2.0	0.25 – 0.5	Medium sand
2.0 – 3.0	0.125 – 0.25	Fine sand
3.0 – 4.0	0.0625 – 0.125	Very fine sand
4.0 – 5.0	0.031 – 0.0625	Coarse silt
5.0 – 6.0	0.0156 – 0.031	Medium silt
6.0 – 7.0	0.0078 – 0.0156	Fine silt
7.0 – 8.0	0.0039 – 0.0078	Very fine silt
> 8.0	0.00006 – 0.0039	Clay

Sorting Classification

Table AIII-2. Sorting classification. From Folk (1968).

Sorting (phi)	Classification
< 0.35	Very well sorted
0.35 – 0.50	Well sorted
0.50 – 0.70	Moderately well sorted
0.70 – 1.0	Moderately sorted
1.0 – 2.0	Poorly sorted
2.0 – 4.0	Very poorly sorted
> 4.0	Extremely poorly sorted

Skewness Classification

Table AIII-3. Skewness classification. From Folk (1968).

Skewness (phi)	Classification
0.3 – 1.0	Strongly fine-skewed
0.1 – 0.3	Fine-skewed
-0.1 – 0.1	Near-symmetrical
-0.3 – -0.1	Coarse-skewed
-1.0 – -0.3	Strongly coarse-skewed

APPENDIX IV
SURFICIAL SEDIMENT ANALYSIS

IV-1. Surficial sediment grain-size parameters and organic carbon content

The moment statistics in Table AIV-1 were calculated excluding gravel content, and are based on the Mastersizer-S results presented in Appendix VI on the attached disc.

Table AIV-1. Surficial sediment grain-size parameters and organic carbon content used in the generation of spatial distribution maps in Chapter 5, Section 5.4.1

Sample	Mean grain-size (phi)	Sorting (phi)	Skewness (phi)	OC Content (%)
1A	3.635	1.977	1.668	1.595
1B	3.731	2.167	1.227	1.642
1C	3.124	1.314	3.198	1.398
1D	3.568	1.648	2.096	1.403
2A	5.783	2.878	-0.415	3.701
2B	5.544	4.061	0.812	2.727
2C	3.435	1.224	3.040	1.400
2D	3.637	2.496	0.989	1.808
3A	3.787	2.918	0.716	1.554
3B	3.866	2.063	1.123	1.587
3C	4.765	4.308	0.733	1.759
3D	3.004	3.009	0.942	1.872
4A	3.128	2.348	1.445	2.016
4B	3.668	2.638	1.105	2.074
4C	5.259	3.446	1.066	2.051
4D	6.326	3.838	0.768	3.320
5A	5.985	4.433	0.502	1.775
5B	5.412	3.700	0.811	4.249
5C	2.466	2.599	1.452	1.993
6A	3.880	3.038	0.534	3.611
6B	3.390	2.365	1.368	2.690
6C	4.306	3.594	1.177	1.800
7A	4.409	3.631	1.088	2.515
7B	3.689	2.876	0.793	2.404
8A	5.351	3.601	0.958	1.911
9A	3.387	1.514	2.225	1.985

Sample	Mean grain-size	Sorting	Skewness	OC Content

	(phi)	(phi)	(phi)	(%)
10A	3.525	2.070	1.831	2.574
10B	3.542	2.101	1.795	2.675
11A	3.836	2.105	1.432	2.694
11B	2.545	0.524	-0.034	1.200
11C	3.044	1.603	2.349	1.736
11D	4.474	2.296	1.036	3.365
12A	3.736	2.705	0.941	1.173
12B	3.625	2.644	0.996	2.105
12C	3.465	1.973	1.872	1.899
12D	3.887	2.355	1.080	3.100
12E	4.270	2.036	1.192	3.198
12F	2.979	1.157	3.471	1.619
13A	3.767	1.939	1.504	3.166
13B	4.075	2.108	1.213	8.450
13C	5.034	2.566	0.418	7.735
14A	5.570	4.280	0.759	4.278
14B	3.493	2.358	1.394	2.384
15A	3.541	1.774	2.033	2.415
15B	3.557	1.440	2.467	1.673
15C	3.684	2.287	1.244	2.550
15D	3.459	1.378	2.532	1.768
15E	3.915	1.976	1.586	2.444
15F	3.380	2.190	1.455	2.218
15G	4.835	2.691	0.550	3.443

APPENDIX V

COASTS & PORTS 2009 CONFERENCE PROCEEDINGS PAPER

Sediment dynamics of Ahuriri Estuary, Napier,

New Zealand

Tracey M. Eyre[1], Karin R. Bryan[1] and Malcolm O. Green[2]
[1]University of Waikato, Hamilton, New Zealand
[2]NIWA, Hamilton, New Zealand

Abstract

The Ahuriri Estuary is located on the east coast of the North Island, New Zealand. The aim of this study is to characterise sediment transport pathways and areas of potential erosion and accretion to provide the data necessary to enhance the understanding of the fate of contaminants entering the estuary and to provide a basis for future large-scale modeling applications. A Mike 21 Flow model was calibrated using field data from two field deployments conducted during a spring and neap tide. Residual circulation patterns in the Ahuriri Estuary were ebb-dominated which ultimately indicates a downstream movement in sediment is likely. Flow was highly channelised within the lower estuary, with a low energy regime in the upper estuary suggesting that sediment introduced into the estuary from the Taipo Stream is likely to be flushed from the estuary if it reaches the middle estuary. Preliminary sediment transport modelling results confirm that a large proportion of sediment reaching the middle estuary is further transported downstream. Fine sand was found to settle out of suspension in the upper estuary in close proximity to the source site, whereas mud and silt sized sediments were flushed into the middle and lower estuary. Sediment in suspension in the middle estuary during the incoming tide migrated into intertidal areas, which were a major sink for suspended sediments due to their sheltered nature. The timing of the release of sediment in the tidal cycle was also illustrated to have a significant influence on the transport and ultimate depositional location of sediments introduced into the estuary. Ahuriri Estuary experiences sedimentation events under a range of conditions, with deposition varying in location and severity, and is therefore vulnerable to sedimentation.

1.0 Introduction

New Zealand's estuaries have been infilling with sediments since their formation commencing approximately 15,000 years ago (Dyer 1994). Anthropogenic influences have accelerated estuarine sedimentation through processes such as deforestation, and urban and industrial development (Sheffield et al. 1995; Hume 2003). Increased sedimentation leads to a change in channel geometry and tidal prism, increases flooding risk, navigation and impacts the ecological environment (Pimentel et al. 1995; Lal 1998). The rate of infilling is dependent on the sediment influx from the catchment, marine sources and the estuarine physical processes that determine extent of sediment flushing or retention (Thrush et al. 2004). Heavy metals and nutrients bind to fine sediments, which can result in an accumulation of contaminants in estuarine environments such as intertidal areas where fine sediments are deposited (Walling 2005). Understanding sediment reworking is also imperative for determining the fate of fine sediments and contaminants entering the estuary. Sediments may be reworked under tidal currents (Bass et al. 2007; Manning et al. 2007) and wave-driven oscillatory

currents (Dolphin 2004; Green & Coco 2007). Therefore, characterising the sediment dynamics of an estuary and the dominant physical forcing is important in predicting and mitigating sediment and contaminant accumulation.

Numerical modelling of sediment accumulation and erosion provides a vital tool in estuarine management. It can be used to design and assess proposed management processes aimed at preserving the ecological and cultural amenity of the system and mitigating impacts on the system by engineering works and development (Lumborg & Windelin 2003; Hu et al. 2009; Bass et al. 2007).

In this paper the hydrodynamics of Ahuriri Estuary are discussed along with a preliminary investigation the transport pathways and fate of sediments of differing grain-sizes. The emphasis is on sediment transport patterns and understanding Ahuriri estuary as a processor of sediments, as opposed to predicting specific sediment dynamics.

2.0 Study Area

Ahuriri Estuary (39º30S, 176º52E) is a microtidal, well-mixed lagoon situated near Napier in Hawke Bay, New Zealand (Fig. 1). The estuary formed behind a Holocene sand and gravel barrier, undergoing repeated subsidence, which was reversed by the uplift of the 1931 Napier earthquake (Chagué-Goff et al. 2000). The present-day estuary covers an area of 4.7 square kilometres, being a remnant of the lagoon prior to uplift which covered an area of 38.4 square kilometres. The estuary is shallow with extensive intertidal areas, with a maximum depth of 2.6 m in the channels. The estuary has a measured spring tidal range of 1.5 m at the entrance. In this study, the estuary is divided into the lower estuary (commonly known as the boat harbour), the middle estuary and the upper estuary. The area is sheltered by the Poraiti hills which are located to the southwest (not shown in Fig. 1). This combined with small fetches imposed by large complex intertidal areas and islands in the estuary limits local wave generation. The estuary is also sheltered from ocean swell as the complex inlet and coastline orientation prohibit propagation of swell into the estuary. Freshwater inflows into the estuary are minimal. The Taipo stream (Fig. 1) is the only freshwater input other than intermittently pumped drains. Taipo stream arises in the Poraiti hills, draining a small catchment. Significant flow occurs only during storm conditions. Ahuriri sediments are derived from marine sources, biogenic sources and the weathering of catchment soil and rock of volcanic origin. Remnant blocks of volcanic rock can be found in the estuary, with gravel clasts analogous to those of the gravel banks found in the intertidal region.

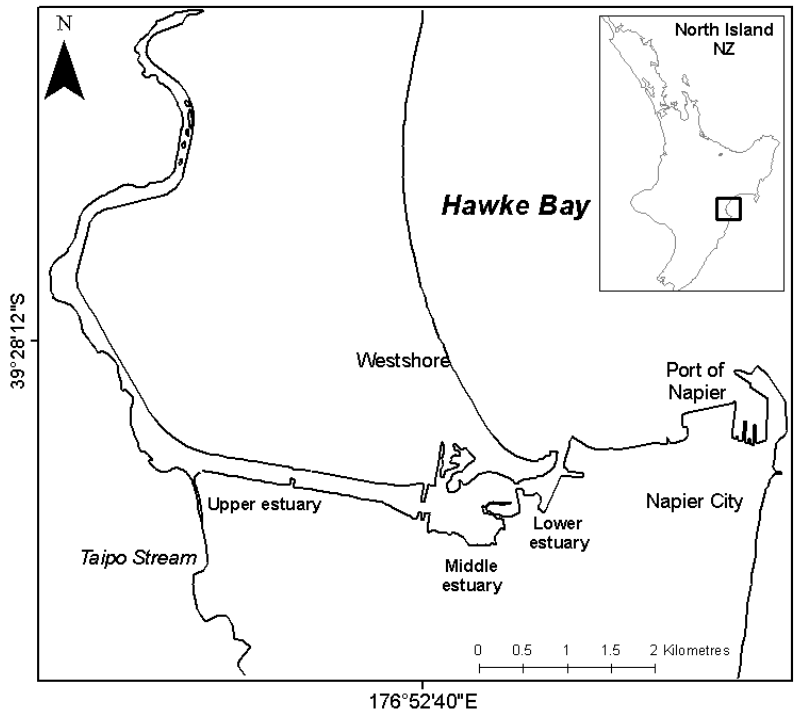

Figure 1. Ahuriri Estuary, located in Hawke Bay on the east coast of North Island, New Zealand (see inset). The estuary is divided into three parts for this study, the upper, middle and lower sub-estuaries.

3.0 Methods

3.1 Hydrodynamic model

The DHI Mike 21 modelling suite is used for simulating hydrodynamics and sediment transport. The 2-dimensional Mike 21 FM model is used to simulate tidal hydraulics. This solves the vertically integrated Saint-Venant equations for mass continuity and momentum in the horizontal dimensions using finite differencing to determine the water depth and velocities within each cell (DHI 2004). Frictional losses are parameterised in the model by bed roughness and eddy viscosity, which treat turbulent energy losses on a scale smaller than the grid resolution. The model is forced at an offshore boundary by a time series of tidal information from the National Institute of Water and Atmospheric Research (NIWA) free tide prediction service. Wave action is not included in this study as local wave generation and propagation of swell waves into the estuary are limited. Freshwater input is minimal and is considered unimportant in the hydrodynamic simulation of the estuary, therefore was not included in the hydrodynamic model forcing. An existing bathymetry was provided by Hawke's Bay Regional Council (HBRC). The highly channelised flow in the estuary and the narrow nature of the channels required a high-resolution grid of 10 m x 10 m. Such a resolution was viable in this study as computational time was low due to the small size of the study area.

3.2 Model Calibration

Three Sontek Triton-ADV current meters were deployed at 3 study sites (Fig. 2) to record pressure, current direction and speed during separate spring-tide and neap-tide deployments for a duration of 3 full tidal cycles.

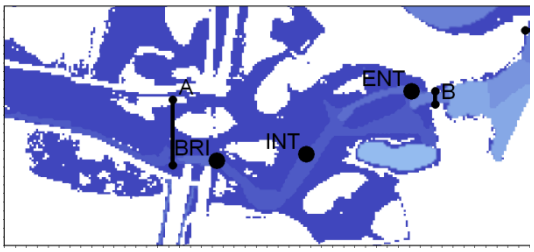

Figure 2. ADV deployment sites (ENT, INT and BRI) and lines of discharge calculation (A,B,C).

Modelled data were extracted for the time period corresponding to the field measurements. The best fit of modelled and measured currents was obtained with a Manning number of 38 $m^{1/3}.s^{-1}$ and an eddy viscosity of 1 $m^2.s^{-1}$ applied to the whole estuary. Modelled tidal current speed and direction were vector-averaged over two tidal cycles during spring tide conditions. The residual currents calculated can be used to indicate likely areas of erosion and accretion and to infer sediment transport pathways.

3.3 Mud Transport Model

The calibrated hydrodynamic model was used to force the DHI Mike 21 Mud Transport model. Sediment transport is based upon the advection-dispersion equation, which is vertically integrated for use in Mike 21 (Lumborg & Windelin 2003). Sediment transport, erosion and deposition are dependent on the bed shear stress, which in turn is calculated from the tidal currents extracted from the FM model. Whether sediment is eroded or deposited depends on the critical shear stress for erosion, τ_{ce}, and the critical shear stress for deposition, τ_{cd}. The model was initialised with parameters derived primarily from the literature (Table 1). Table 2 shows the parameters finally used in this study. The parameters for erosion were chosen such that under neap tides, fine sediments were brought into suspension in small concentrations in the channels. Such behaviour is noted in field studies under fairweather conditions (e.g. Green & Coco 2007).

For each grain-size, the settling velocity is specified according to the Stokes model (Equation 1).

$$W_s = \frac{(\rho_s - \rho) g d^2}{18\mu} \quad (1)$$

Table 1. Mike 21 Mud Transport model parameters used in previous studies.

Critical shear stress for deposition, τ_{cd} ($N.m^{-2}$)	**Critical shear stress for erosion, τ_{ce} ($N.m^{-2}$)**	**Erosion coefficient, α ($m.N^{-0.5}$)**	**Source**
0.05 – 0.3	0.19 – 0.8	6.5	Lumborg & Pejrup 2005
0.002 – 1.0	0.1 – 0.7	10-20	Lumborg & Windelin 2003
0.18 – 1.1	---	---	Mehta & Partheniades 1975
0.05	1.04	---	de Villiers & Basson 2007
0.02 – 0.8	0.02 – 0.8	---	Hu et al. 2009
---	---	10-20	van Rijn 1989
---	0.04-0.62	4.2-25.6	Parchure & Mehta 1985
$0.21 < \tau_{cd} < 0.37$	---	---	Haralampides et al. 2003

Table 2. Mike 21 Mud Transport model parameters used in this study

Parameter	Value
Sediment source concentration	25 $mg.l^{-1}$
Freshwater source discharge	5 $m^3.s^{-1}$
Critical shear stress for erosion	0.2 – 0.5 $N.m^{-2}$
Critical shear stress for deposition	0.05 – 0.3 $N.m^{-2}$

As only sediment dispersal patterns and the retention of sediment in the estuary are of interest, the initial sediment concentration and the thickness of the bed are both set to zero. Mud transport patterns were simulated under spring and neap tides, each for a period of 2 days. Two complete tidal cycles were extracted for analysis. To track sediment export from the estuary, discharge data were extracted from three lines in the model grid, A, B and C (Fig. 2). The lines divide the estuary into the upper, middle and lower estuaries. The total sediment input (kg) crossing each line was calculated to determine sediment budgets.

4.0 Results

A detailed analysis of the simulated hydrodynamics and sediment transport within the estuary has been carried out. Overall, a good calibration of the hydrodynamics was achieved (Fig. 3). Current direction was accurately simulated at all sites and the timing of current reversal is well predicted, within the accuracy of the forcing data, which is 5-10 minutes (NIWA 2008). The modelled tide arrived slightly early at the BRI site, which is furthest from the estuary mouth.

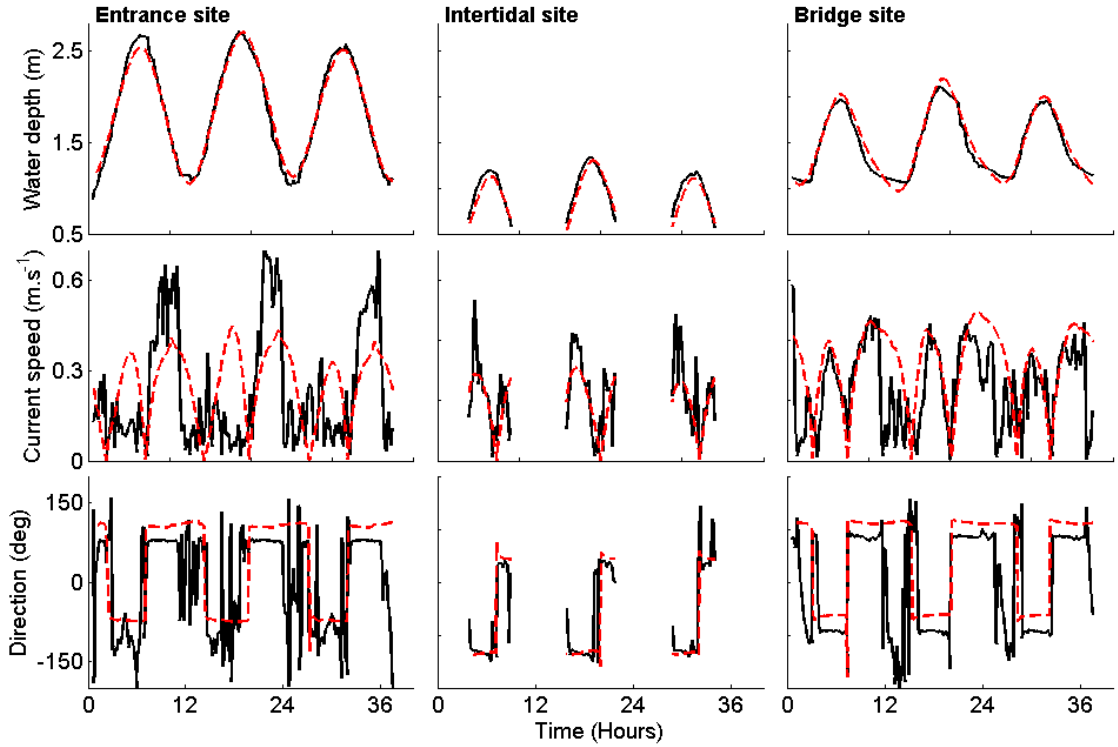

Figure 3. Measured and modelled water depth, current speed and direction at entrance, intertidal and bridge sites. Solid black lines indicate measured data and dashed red lines indicate modelled data.

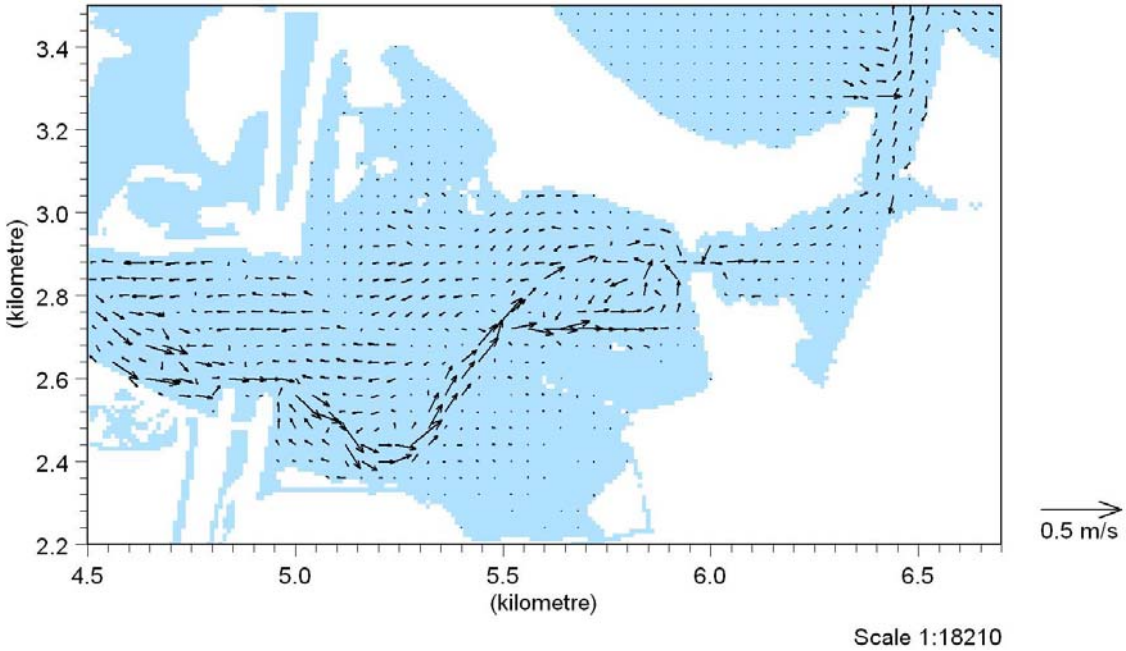

Figure 4. Residual surface elevation, current speed and direction for two tidal cycles during spring tide conditions. Vectors indicate residual current speed and direction (see reference vector for scale). White areas indicate dry land.

The residual circulation in Ahuriri Estuary was ebb-dominated (Fig. 4), which is set up by the asymmetry in the tidal current speeds seen in the measured and modelled data (Fig. 3). The residual current speeds are low throughout the intertidal regions (less than 0.1 $m.s^{-1}$), with the greatest residual current speeds in the channels. In the upper estuary, residual currents are relatively low. However, where the flow is constricted underneath the highway bridge, residual currents of up to 0.2 $m.s^{-1}$ were evident (Fig. 4). In the middle estuary, residual currents are generally restricted to the channels and are negligible elsewhere. The intertidal channel fringes show flood-dominated flows. This is expected, as during the flood tide with the water level rising, flow is still highly channelised and strongly directional. During the early stages of ebb tidal flow, currents are not restricted to the channels. This is reflected in the data measured by the ADV at the intertidal site. The ADV was situated near the channel edge, and it is evident that flood tidal currents are stronger than ebb tidal currents (Fig. 3). Relatively strong seaward-directed residual currents can be seen through the small inlet from the estuary into the boat harbour, with an eddy in the central area (Fig. 4). The location of this residual eddy coincides with previous dredging operations.

Figure 5 illustrates that the volume percentage of total sediment input discharged across each of the lines A, B and C is highly dependent on the sediment grain-size (and therefore settling speed). A large proportion of sediment crossing line A is transported downstream across lines B and C. Also of significant interest is the timing of sediment influx in the tidal cycle, which accounted for a difference in

sediment export from the upper estuary of up to 48 percent. Sediment released during mid-flood tide conditions was flushed further upstream, resulting in the greatest deposition upstream of the sediment release site. Sediment released during mid-ebb tide was transported downstream, and transported the greatest percentage through the estuary mouth. Following sediment release at mid-ebb tide, the suspended sediment plume progressing downstream at the time of tide reversal was halted and flushed back into the middle estuary, dispersing into intertidal areas. Net sediment accumulation was evident in these intertidal areas, however, the low settling velocity of mud resulted in low volumes of accumulation. Net accumulation was also apparent on the main channel banks. Coarse silt (60 µm) followed a similar transport regime to mud, although a greater fraction remained in the upper estuary. Fine sand (105 µm) was predominantly deposited in the upper estuary in close proximity to the sediment source site and was transported downstream in very low concentrations. There is a missing data-point in Figure 5 (C.) where no discernible flux of sediment was measured.

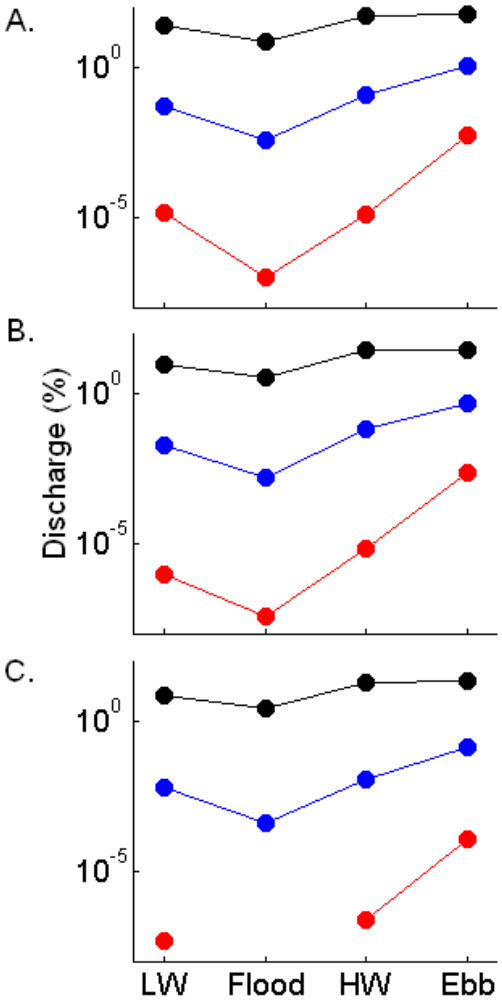

Figure 5. Percentage of total sediment input discharged across line sites A (A.), B (B.) and C (C.) for grain-size simulations of mud, 10µm (black line), coarse silt, 60µm (blue line) and fine sand, 105µm (red line). See Figure 3 for line site locations. Missing data indicates no flux measurement of sediment across line.

5.0 Discussion

The hydrodynamic simulation has been shown to accurately simulate the tidal hydraulics of the Ahuriri Estuary. Outgoing current speeds are slightly under-predicted during spring tides. This is thought to be an artefact of the drainage of the upper estuary being relatively restricted in the model, due to the difficulty of adequately representing the complex morphology in the model grid. However, it is not necessarily the actual current speeds that are of concern, but rather the accurate simulation of tidal asymmetry and residual currents, which will govern sediment-transport pathways.

Residual circulation patterns in the Ahuriri Estuary are shown to be ebb-dominated, which indicates a net downstream movement of sediment. The flow is highly channelised in the lower estuary, suggesting that sediment that is introduced into the estuary from the Taipo Stream is likely to be flushed from the estuary if it reaches the middle estuary. However, sediment that is in suspension in the middle estuary during the incoming tide has been shown to migrate into intertidal areas, which are a major sink for suspended sediments. Sediment cores taken in intertidal areas in other studies show lamination consistent with regular sedimentation (Dyer 1994). Tidal currents are low to negligible in these areas, and the limited fetch and sheltered nature of the estuary indicate that it is unlikely sediment will be resuspended.

As the residual currents in Figure 4 suggest, a significant proportion of sediment reaching the middle estuary was exported from the estuary to the coast across measurement site C (Fig. 5). Turbulent flows and mixing in the channels are likely to transport sediment further as the turbulence keeps sediment in suspension. For the finer sediment fractions, a significant proportion of the total sediment influx was transported from the model domain across the open ocean boundary. However, fine sand (105 μm) predominantly settled out of suspension in the upper estuary. Based on a settling velocity of 0.001 $m.s^{-1}$ for the fine sand and a mean water depth at the site of 1.2 m, it would take approximately 20 minutes for sediment to settle out of suspension in close proximity to the source. This results in negligible export of sediment into the lower estuary of fine sand.

Timing of release is an important factor controlling sediment fate and dispersal, accounting for a difference in sediment reaching the middle estuary of up to 48 percent. Fine sand released at high tide and during the ebb tide was flushed downstream to the middle and lower estuaries before settling out of suspension. The lower settling velocities of the fine fractions enabled the sediment to remain in suspension for sufficient duration to be transported with the outgoing tide, with a significant proportion lost from the model domain.

6.0 Conclusions

Differing grainsize resulted in significant differences in the volume of sediment export and locations of sediment accumulation within the upper, middle and lower sub-estuaries. The timing of sediment release in the tidal cycle also resulted in significant differences in the transport and ultimate location of deposition. Release upon high water slack and flood tide resulted in greater deposition upstream and in

close proximity to the source, whereas release upon low water slack and ebb tide conditions resulted in greater downstream transport. The different scenarios summarised in this paper suggest that sedimentation events differ in severity and location according to simulation conditions. Due to the range of conditions under which sedimentation events occur, it can be concluded that Ahuriri Estuary is vulnerable to sedimentation.

Acknowledgements
Thanks are given to the Hawke's Bay Regional Council and the (New Zealand) Foundation for Research, Science and Technology (contract CO1X0307, Effects-Based Protection and Management of Aquatic Ecosystems) for project funding and use of resources. Thank-you to Dirk Immenga of the University of Waikato for field and technical assistance. Thanks go to Anna Madarasz-Smith and Craig Goodier (HBRC) for assistance and advice.

References

Andersen, T.J., Fredsoe, J., and Pejrup, M. (2007) In situ estimation of erosion and deposition thresholds by Acoustic Doppler Velocimeter (ADV). *Estuarine, Coastal and Shelf Science,* Vol. 75, 327-336

Bass, S.J., Manning, A.J and Dyer, K.R. (2007) Preliminary findings of a study of the upper reaches of the Tamar Estuary, UK, throughout a complete tidal cycle: Part I: Linking hydrodynamic and sediment cycles. In Maa, J.P.Y, Sanford, L.P and Schoellhamer D.H. (Eds.) *Estuarine and Coastal Fine Sediment Dynamics.* Elsevier, pp. 1-14

Chagué-Goff, C., Nichol S.L., Jenkinson A.V. and Heijnis H. (2000) Signatures of natural catastrophic events and anthropogenic impact in an estuarine environment, New Zealand. *Marine Geology,* Vol. 167, 285-301

de Villiers, J.W.L., and Basson, G.R (2007) Modelling of long-term sedimentation at Welbedacht Reservoir, South Africa. *Journal of the South African Institution of Civil Engineering*, Vol. 49, No. 4, 10-18

DHI (2004) Mike 21: Coastal Hydraulics and Oceanography – User Guide. DHI Water and Environment.

Dolphin, T.J. (2004). Wave-induced sediment transport on an estuarine intertidal flat. PhD thesis, Earth Sciences, University of Waikato, New Zealand

Dyer, K. (1994) Estuarine sediment transport and deposition. In: K. Pye (Ed.), *Sediment transport and depositional processes*, Blackwell Scientific Publications, pp. 193-218.

Green, M.O., Black, K.P., and Amos, C.L. (1997) Control of estuarine sediment dynamics by interactions between currents and waves at several scales. *Marine Geology,* Vol. 144, 97-116

Green, M. O. and Coco, G. (2007) Sediment transport on an estuarine intertidal flat: Measurements and conceptual model of waves, rainfall and exchanges with a tidal creek. *Estuarine, Coastal and Shelf Science,* Vol. 72, 553-569

Haralampides, K., McCorquodale, J.A. and Krishnappan, B.G. (2003) Deposition Properties of Fine Sediment. *Journal of Hydraulic Engineering*, *ASCE*, Vol. 129, No. 3, 230-234

Hu, K., Ding, P., Wang, Z. and Yang, S. (2009) A 2D/3D hydrodynamic and sediment transport model for the Yangtze Estuary, China. *Journal of Marine Systems,* Vol 77, 114-136

Hume, T. (2003) Estuaries and tidal inlets. In J. Goff, S. Nichol & H. Rouse (Eds.), *The New Zealand coast Te Tai o Aotearoa*, Dunmore Press, pp. 191-214

Lal, R. (1998) Soil erosion impact on agronomic productivity and environment quality. *Critical reviews in plant science*, Vol. 17, No. 4, 319-464

Lumborg, U. and Pejrup, M. (2005) Modelling of cohesive sediment transport in a tidal lagoon—an annual budget. *Marine Geology,* Vol. 218, 1-16

Lumborg, U. and Windelin, A. (2003) Hydrography and cohesive sediment modelling: application to the Rømø Dyb tidal area. *Journal of Marine Systems,* Vol. 38, 287– 303

Manning A.J., Bass, S.J. and Dyer K.R. (2007) Preliminary findings of a study of the upper reaches of the Tamar Estuary, UK, throughout a complete tidal cycle: Part II: *In Situ* floc spectra observations. In Maa, J.P.Y, Sanford, L.P and Schoellhamer D.H. (Eds.) *Estuarine and Coastal Fine Sediment Dynamics.* Elsevier, pp. 15-33

Mehta, A.J. and Partheniades, E. (1975) An investigation of the depositional properties of flocculated fine sediments. Journal of Hydraulic Research, Vol. 13, No. 4, 361-381

NIWA (2008). Tide forecaster. Retrieved December 14, 2008 from http://www.niwa.co.nz/our-services/online-services/tides. National Institute of Water and Atmospheric Research

Parchure, T.M., and Mehta, A.J. (1985) Erosion of soft cohesive sediment deposits. *Journal of Hydraulic Engineering – ASCE,* Vol. 111, No. 10, 1308-1326

Pimentel, D., Harvey, C., Resosudarmo, P., Sinclair, K., Kurz, D., McNair, M., Crist, S., Shpritz, L., Fitton, I., Saffouri, R. & Blair, R. (1995) Environmental and economic costs of soil erosion and conservation benefits. *Science*, Vol. 267, No. 5210, 1117-1123

Sheffield, A., Healy, T. & McGlone, M. (1995) Infilling rates of a steepland catchment estuary, Whangamata, New Zealand. *Journal of Coastal Research*, Vol. 11, No. 4, 1294-1308

Thrush, S. F., Hewitt, J. E., Cummings, V., Ellis, J. I., Hatton, C. & Lohrer, A. (2004) Muddy waters: elevating sediment input to coastal and estuarine habitats. *Frontiers in ecology and the environment*, Vol. 2, No. 6, 299-306

van Rijn, L.C. (1989) Transport of cohesive materials. Delft Hydraulics H 461, 12.1-12.27

Walling, D.E. (2005). Tracing suspended sediment sources in catchments and river systems. *Science of the total environment*, Vol. 344, 159-184